
Ir-based nanoparticles for catalytic hydrogen generation using chemical hydrogen storage compounds

Thesis submitted in accordance with the requirements of Cardiff
University for the degree of Doctor of Philosophy by

Davide Motta

School of Chemistry

Cardiff University

2019



Supervisors

Dr. Ceri Hammond

Dr. Nikolaos Dimitratos

Dr Ulrich Hintermair

Abstract

The objective of this thesis is to present and evaluate hydrous hydrazine as a suitable liquid storage compound for the production of hydrogen that can be utilised for hydrogen fuel cells. Catalytic decomposition of hydrous hydrazine at mild conditions is considered for application for hydrogen generation in portable devices, focusing on the (I) productivity, (II) reusability of the catalysts and the yield of hydrogen and (III) avoiding the production of ammonia which is harmful to the fuel cell membrane. Ir-based nanoparticles were synthesised and deposited on a range of supports and different preparation methods were used to tune their structural and catalytic properties. Moreover, computational calculations were used to elucidate the mechanism of reaction and the interaction of the catalytic surface with the hydrazine and intermediates.

The catalytic performance of a synthesised Ir/CeO₂ as reference material is presented in order to optimise the reaction conditions for identifying the kinetic regime of the studied reaction. Characterisation techniques and computational calculations are used to provide possible reaction pathways for tuning the yield of the reaction toward hydrogen production. After the determination of the optimal reaction parameters the preparation methods of supported monometallic Ir nanoparticles were modified in order (I) to tune the catalytic properties of active metal, (II) explore possible metal-support interactions by using different metal oxides as support and finally (III) optimising the yield of the reaction towards hydrogen. ATR-IR studies were carried out in order to identify adsorbed species on the surface of the desired model catalyst in specific chosen reaction conditions and validate the possible mechanisms of the reaction. Once Ir-based catalysts were optimised Ni-based catalysts were subsequently investigated to perform hydrous hydrazine catalytic decomposition with higher yield toward molecular hydrogen. From the knowledge obtained by the catalytic and characterisation studies of monometallic Ir and Ni catalysts bimetallic Ir-Ni catalysts were synthesised and characterised in order to combine the higher selectivity and higher activity of the two monometallic catalysts. Characterisations were performed to investigate and elucidate the properties of the bimetallic materials synthesised. Finally, the main conclusions of the results are reported and a set of options to continue this research is presented.

Table of Contents

1. Introduction.....	1
1.1. Energy Overview	1
1.1.1. Alternative energy sources	1
1.1.2. Molecular Hydrogen	3
1.1.3. Fuel Cell systems	4
1.1.3.1. Types of fuel cells	5
1.1.3.2. Proton exchange membrane fuel cells.....	5
1.1.3.3. Alkaline fuel cells.....	6
1.1.3.4. Phosphoric acid fuel cells	7
1.1.3.5. Molten carbonates fuel cells.....	7
1.1.3.6. Solid oxide fuel cells	8
1.1.4. Hydrogen generation methods.....	9
1.1.4.1. Steam reforming	10
1.1.4.2. Hydrocarbon partial oxidation	13
1.1.4.3. Coal gasification	14
1.1.4.4. Electrolysis.....	16
1.1.5. Drawbacks of hydrogen usage.....	17
1.1.6. Alternative solutions to hydrogen storage	18
1.2. Catalysis.....	19
1.2.1. Type of catalysis.....	20
1.2.2. Bio-Catalysis	20
1.2.3. Homogeneous catalysis	21
1.2.4. Heterogeneous catalysis.....	21
1.2.5. Preparation of supported heterogeneous catalysts.....	24
1.2.5.1. Sol-immobilisation.....	25
1.2.5.2. Deposition-precipitation	27
1.3. Liquid-phase chemical hydrogen storage systems	28
1.3.1. Hydrous Hydrazine.....	30
1.3.1.1. Production of hydrazine	31
1.3.1.2. Hydrous Hydrazine decomposition	32
1.3.1.3. Heterogeneous catalysed hydrous hydrazine decomposition.....	32
1.4. Aims of the study	36
1.5. References.....	37
2. Experimental	44
2.1. Introduction	44
2.1.2. Equations	44
2.1.3. Reagents.....	46
2.2. Preparation of Supported Metal Nanoparticles	47
2.2.1. Colloidal methods	47
2.2.1.1. Sol-immobilisation with tetrakis(hydroxymethyl)phosphonium chloride (THPC) 48	

Table of Contents

2.2.2.	Deposition-precipitation methods.....	50
2.2.2.1.	Deposition-precipitation with NaOH	51
2.2.2.2.	Deposition-precipitation with Urea	52
2.2.3.	Solid-State grinding.....	52
2.2.4.	Heat Treatment Protocols	52
2.3.	Catalytic testing.....	53
2.3.1.	Volumetric quantification	53
2.3.2.	Pressure detection system.....	56
2.3.3.	Gas quantification via Mass spectroscopy.....	57
2.3.4.	Hydrous hydrazine quantification via colourimetric spectrophotometry.....	57
2.4.	Catalysts Characterisation	59
2.4.1.	Powder X-Ray Powder Diffraction (p-XRD).....	59
2.4.2.	X-ray Photoelectron Spectroscopy (XPS).....	61
2.4.3.	Electron Microscopy	63
2.4.3.1.	Scanning Electron Microscopy (SEM).....	65
2.4.3.2.	Energy Dispersive X-ray (EDX).....	67
2.4.4.	BET (Brunauer, Emmett and Teller) Surface Area Analysis	67
2.4.5.	Temperature Programmed Reduction Analysis (TPR).....	68
2.4.6.	Attenuate Total Reflectance (ATR) <i>in situ</i> Infrared spectroscopy	69
2.5.	Spectroscopic methods.....	70
2.5.1.	Ultraviolet/visible spectroscopy (UV/Vis).....	70
2.5.2.	Mass Spectrometry	71
2.5.2.1.	Inductively coupled plasma – Mass spectroscopy (ICP-MS).....	72
2.5.2.2.	Microwave Plasma-atomic Emission Spectrometry (MP-AES)	74
2.6.	Computational methods	74
2.6.1.	Density Functional Theory (DFT) studies	74
2.6.2.	Supercomputer and software.....	76
2.7.	References.....	77
3.	Catalytic decomposition of Hydrous Hydrazine over Ir/CeO₂.....	80
3.1.	Introduction	80
3.2.	Optimisation of reaction parameters	81
3.2.1.	Effect of the stirring rate.....	83
3.2.2.	Effect of the mass of catalyst.....	85
3.2.3.	Effect of NaOH concentration.....	87
3.2.4.	Effect of the reaction temperature	89
3.3.	Preliminary Reusability studies.....	90
3.4.	Characterisation of fresh and used catalysts.....	92
3.4.1.	BET (Brunauer-Emmett-Teller) method surface area.....	92
3.4.2.	Powder X-ray diffraction (p-XRD)	93
3.4.3.	Inductively Coupled Plasma - Mass Spectroscopy (ICP-MS).....	94
3.4.4.	Scanning Electron Microscopy (SEM) and Energy Disperse X-ray Spectroscopy (EDS)	95
3.4.5.	Transmission Electron Microscopy (TEM)	96
3.4.6.	Temperature Programmed Reduction (TPR)	98
3.4.7.	X-ray Photoelectron Spectroscopy (XPS).....	100

3.5.	Density Functional Theory (DFT).....	105
3.5.1.	Adsorption on the IrO ₂ Surface.....	105
3.5.2.	Adsorption on the Ir (111) Surface	106
3.5.3.	Hydrazine reaction pathways on Ir (111)	109
3.5.3.1.	Intramolecular dehydrogenation	109
3.5.3.2.	N-N bond cleavage	110
3.5.3.3.	Intermolecular dehydrogenation.....	112
3.5.3.4.	Intermolecular amides dehydrogenation	113
3.5.3.5.	NH _x dehydrogenation.....	114
3.5.4.	Desorption of the products.....	117
3.5.5.	Analysis of the Energy Profiles.....	117
3.5.6.	Simulated Infrared Spectra	119
3.6.	Conclusions	121
3.7.	References.....	124
4.	Optimisation of the supported Ir nanoparticles for the catalytic liquid-phase decomposition of hydrous hydrazine	126
4.1.	Introduction	126
4.2.	Results and discussion	128
4.2.1.	Influence of the preparation method	128
4.2.2.	Influence of the support material.....	131
4.2.3.	Effect of reduction and high-temperature treatment.....	137
4.2.4.	Homogeneous Ir catalysts.....	141
4.2.5.	Reusability tests	145
4.2.6.	Analysis of gaseous products by Mass Spectroscopy	148
4.3.	Characterisation of the catalytic materials.....	152
4.3.1.	Powder X-ray diffraction (p-XRD)	153
4.3.2.	Scanning Electron Microscopy (SEM) and Energy Disperse X-ray Spectroscopy (EDS)	156
4.3.3.	Inductively Coupled Plasma – Mass Spectrometry (ICP-MS)	161
4.3.4.	Transmission Electron Microscopy (TEM)	162
4.3.5.	X-ray Photoelectron Spectroscopy (XPS).....	169
4.3.6.	UV/Visible Spectroscopy	176
4.3.7.	<i>In situ</i> Attenuated Total Reflectance Infrared Spectroscopy (ATR-IR)	178
4.4.	Conclusions	182
4.5.	References.....	186
5.	Investigation of Ni nanoparticles for catalytic decomposition of hydrous hydrazine in aqueous solution	187
5.1.	Introduction	187
5.2.	Results and discussion	188
5.2.1.	Initial catalytic screening of Ni/CeO ₂ catalysts prepared by sol-immobilisation with THPC	188
5.2.2.	Effect of the Reduction Treatment	191

Table of Contents

5.2.3.	Influence of the preparation method on the catalytic activity of Ni/CeO ₂ catalysts	194
5.2.4.	Influence of the support material	196
5.2.5.	Effect of the reaction temperature	197
5.3.	Characterisation of the catalysts	199
5.3.1.	Temperature Programmed Reduction (TPR)	199
5.3.2.	Powder X-Ray Diffraction (p-XRD)	201
5.3.3.	Scanning Electron Microscopy (SEM) and Energy Dispersed X-Ray Spectroscopy	202
5.3.4.	X-Ray Photoelectron Spectroscopy (XPS)	206
5.3.5.	UV/visible spectroscopy	207
5.4.	Conclusions	208
5.5.	References	211
6.	Investigation of supported bimetallic Ir-Ni nanoparticles for the catalytic decomposition of hydrous hydrazine in aqueous solution	212
6.1.	Introduction	212
6.2.	Results and discussion	214
6.2.1.	Initial tests on IrNi/CeO ₂ prepared by sol-immobilisation with THPC	214
6.2.2.	Effect of the Ir:Ni ratio in the synthesis of nanoparticles	216
6.2.3.	Modifications of the catalyst preparation protocol	217
6.2.4.	Effect of the reaction temperature	220
6.2.5.	Preliminary reusability tests	221
6.3.	Characterisation of the catalysts	223
6.3.1.	Powder X-ray Diffraction (p-XRD)	223
6.3.2.	Scanning Electron Microscopy (SEM) and Energy Disperse X-ray Spectroscopy (EDS)	224
6.3.3.	Transmission Electron Microscopy (TEM) and Energy Disperse X-ray Spectroscopy (EDS)	226
6.3.4.	X-ray Photoelectron Spectroscopy (XPS)	229
6.3.5.	<i>In situ</i> Attenuated Total Reflectance Infrared Spectroscopy (ATR-IR)	234
6.4.	Conclusions	235
6.5.	References	238
7.	Conclusions and Recommended future work	240
7.1.	Conclusions	240
7.2.	Recommended future works	243
7.3.	References	245
	Publications	247
	Acknowledgements	248

1. Introduction

1.1. Energy Overview

Our modern-day society utilises a range of energy sources in order to an ever growing request. Every activity perform in the day-to-day life requires energy in a way or another, from charging a phone to driving to store to buy food, from travelling to new countries to keep a house warm in winter. In order to maintain the modern standard of living is vital to have a continuous and adequate source of energy. These energies sources ideally should be abundant and with low environmental impact, or in alternative they have to be possibly to be regenerated by some of these sources. From the data of the International Energy Agency, IEA, the world energy consumption in 2015 was 9358 Mtoe (million tonnes of oil equivalent).¹ The expected growth in global population, with 8.5 billion people estimated by the United Nations to be reached by 2040,² and increasing economic condition of populous countries, such as India and China, IEA estimated an increase of the total world energy consumption of 28% from 2015 to 2040.³

Until now humanity main sources of energy have been fossil fuels, therefore oil, coal and natural gas. IEA data indicates that in 2015 81% of the global energy production was derived from fossil fuels.¹ These sources are reaching their peak in demand, especially coal and crude oil by 2020,⁴ and are expected to be completely depleted by the end of the 21st century,⁵ with coal and crude oil to consumed already by 2060-2070.⁶ Besides, most of the reserve of fossil fuels are located in areas where political instability and conflicts lead to variability in price of the fuel. Furthermore, the combustion of fossil fuel generates gases and other volatile molecules which are linked to climate change and health problem, such as asthma, deteriorating the quality of life and, more importantly, posing a threat to the global environment.

1.1.1. Alternative energy sources

For these reasons (resource depletion, price instability and environmental cost) the search for new reliable and renewable energy source became vital.^{7,8} Over the years biomass plants, solar plants, wind plants and geothermal plants have become more efficient and common and in addition to the studies on alternative high energy fuels have been increased. A proof

of this trend is the worldwide investments in renewable energy technology which reached 286 billion US\$ in 2015 with all the major world economic leading the source for a sustainable future. Nonetheless, only a minor part of the world energy consumption is obtained by renewable energy sources, 19% as of data from 2015.⁹

Most of the renewable energy produced, 48% at 2017, derives from hydroelectric power plants, as shown in Figure 1.1.⁹ Hydroelectric energy is generated by the movement of water, usually it requires the construction of dams, since the energy amount of energy produced is related to the volume of moving water and the difference in altitude between the reservoir and the generator. Another major renewable source of energy is wind, which can move the large turbines used to produce energy, from 600 kW to 5 MW for each turbine. Solar energy is also a largely studied and applied field. Solar energy can be harvested in different ways as thermal energy, using concentrated solar thermal systems, or as electric energy, using photovoltaic panels. The conversion of solar energy to electrical energy can happen directly, such as with photovoltaic panels easy to install and versatile to use also in residential building, or pass through a thermal stage, like for concentrated solar power plant where solar light is concentrated in single point to overheat a medium that later is used to generate electricity, which more efficient and reliable but require large deployment space. Considering all its forms, solar energy plants constitute approximately 21% of renewable energy globally. Biomass refers to all the plant-based waste that can be used to produce energy, either by direct combustion or by the conversion to greener biofuels such as ethanol or biodiesel. These fuels allow to capture, at least partially, the CO₂ produced during the growth of the crops, even if large scale application would need large agriculture areas to be devoted to these productions. Geothermal energy plants take advantage of the higher temperature of the internal part of the Earth crust to produce energy.

Another main energy source adopted until now in order to reduce the usage of fossil fuel is nuclear energy, which has high energy output. Nuclear plants cover 2.3% of the total energy consumption. However, the future of nuclear energy plants seems to be limited due to the difficulties in the process and stock the dangerous radioactive waste and the general risk linked to accidents, of which the Fukushima Daiichi nuclear disaster in March of 2011 have been last reminder.¹⁰

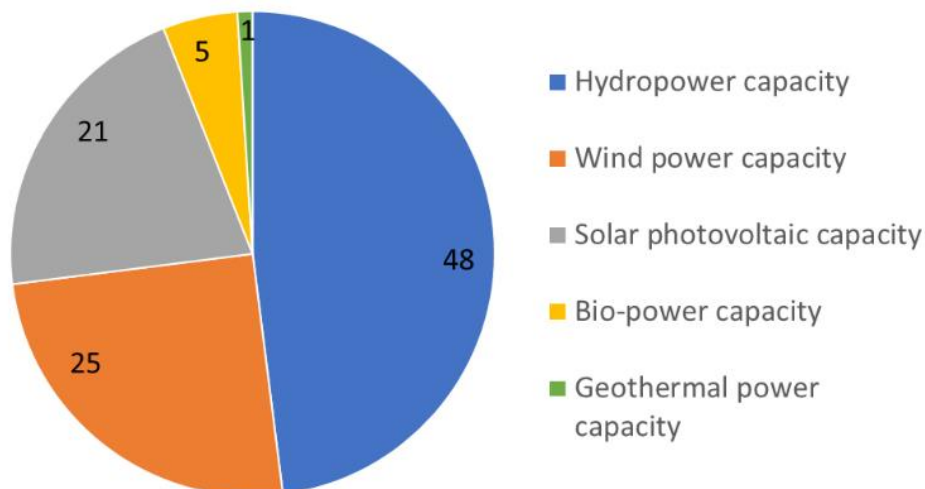


Figure 1.1. Overview of global renewable power production from hydroelectric, bio-mass, solar power, wind power and geothermal, data from Renewables 2019 global status report.⁹

The renewable energy sources listed here above have the potential to satisfy the future energy needs of humanity. The use of renewable energy can have a beneficial effect on human health and on the environment and climate. However, solar energy and wind are not constant during time, depending on weather and daylight time, and to this day one of the main challenges in the application of renewable energies is the development of an efficient way to store the energy produced by wind or solar light and to later use it whenever it is needed. Therefore, a lot of attention has been focused on battery technology and the synthesis of highly energetic fuels to store electrical energy as chemical energy.

1.1.2. Molecular Hydrogen

Hydrogen is commonly present in water, hydrocarbons and other organic and inorganic compounds bonded to other atoms. Hydrogen is, therefore, the tenth most abundant element on the crust of our planet, constituting 0.14% of its mass.¹¹ Since hydrogen in nature is found in compounds energy is required for the conversion to molecular hydrogen, which is consequently more appropriately considered an energy vector than an energy source.¹² The use of molecular hydrogen as vehicle fuel or in fuel cells to generate electricity was then investigated with crescent interest over the past few years as a potential means to accumulate and transport energy which can be released when it is necessary by the final user. The ideal is then to combine renewable sources dependent to external factor like wind and

solar to generate hydrogen during periods of high production and then use that hydrogen the production is energy production is low or to use it directly in proximity of the final user.¹³

Molecular hydrogen attractiveness as energy carrier comes from two main factors (I) high energy density, Table 1.1, and (II) harmless by-product produced during the conversion. The energy density of hydrogen molecules is 120 kJ g⁻¹ which the highest values among the fuel used, almost three times higher than petrol.¹⁴⁻¹⁶ Molecular hydrogen, either used as direct combustible or in fuel cell, undergoes to combustion with oxygen to create water molecules which are harmless for the environment.^{17,18}

Table 1.1. Energy density for different fuel considering the net calorific value for different solid, liquid and gas fuels.¹⁴⁻¹⁶

Fuel	Energy Density (kJ g ⁻¹)
Hydrogen	120
Methane	50
Natural gas	46
Petrol	44
Crude oil	43
Diesel	43
Ethanol	27
Coal	26
Methanol	20

1.1.3. Fuel Cell systems

Fuel cells are electrochemical devices which use catalysts in order to convert the chemical energy contained in specific fuel, such as molecular hydrogen, methanol or ammonia, into electrical energy via the reaction with oxygen. These devices can convert fuel into energy with higher efficiency than traditional internal combustion engines (ICE), without the production of harmful side-products like NO_x, CO₂ and particulate.^{7,19} Moreover, fuel cells produce less noise than ICE which can be a remedy to the acoustic pollution of which city suffer today. All these reasons have made, in recent year, fuel cells increasingly attractive alternative for portable devices and transportation.²⁰⁻²³ Nevertheless, to this day fuel cells still have a high

cost of manufacture and have lifetime issues, while molecular hydrogen has a problem related to its transportation and storage and there is still no profitable renewable way to produce it. These difficulties are limiting the application and commercialisation of fuel cells worldwide.^{19,24} The research reported in this thesis is focused on the solution of some these issues, such as safety and affordability of both storage and transportation of hydrogen.

1.1.3.1. Types of fuel cells

Commercially available fuel cells are divided into five major class of devices:

- Proton exchange membrane fuel cells (PEMFCs)
- Alkaline fuel cells (AFCs)
- Phosphoric acid fuel cells (PAFCs)
- Molten-carbonate fuel cells (MCFCs)
- Solid oxide fuel cells (SOFCs)

1.1.3.2. Proton exchange membrane fuel cells

These devices most commonly use molecular hydrogen as fuel, but the technology can be adapted to use low chain alcohols, such as methanol or ethanol, as fuel instead. In these devices, the fuel reacts on an anode to produce protons, H^+ , and electrons, e^- . The protons travel through a proton exchange membrane to reach the cathode where they then react with oxygen molecules. At the same time, the free electrons are forced into an electrical circuit where a load, i.e. an engine or battery, is present before reaching the cathode to complete the reaction of the fuel cell, as shown in Figure 1.2. Hydrogen PEMFCs can operate at temperatures as high as 150 °C with efficiency up to 60% producing only water, heat and electricity. On the other hand, direct methanol fuel cells operate up to 80 °C, using a solution of methanol in water to produce electricity, heat, water and CO_2 .¹⁹

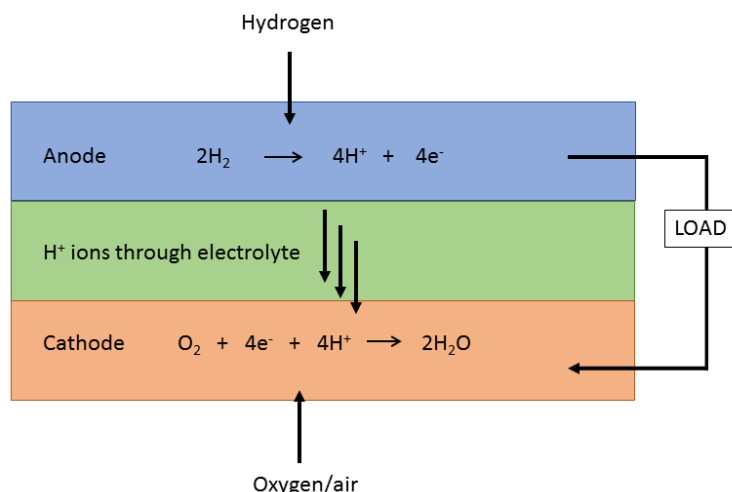


Figure 1.2. Schematic of proton exchange membrane fuel cell working with hydrogen, displaying flow of protons and electrons in the circuit.

This class of devices was developed in the 1960s for military and aerospace applications, but it was later abandoned due to the short lifetime of the devices and their high cost. Even if these limitations remain the main barrier to the large-scale commercialisation of these devices the interest around them is growing due to the possible application to a variety of system from smartphones to vehicles. The cost and durability issues of PEMFCs can be associated with the catalysts used at the anode of the electrochemical circuit. In order to achieve high hydrogen conversion in a short period of time, the anode is covered with Pt or Pt-based catalysts. Pt is one of the most expensive metals on the planet with limited availability, which drive up the cost of PEMFCs, and at the same time, Pt-based catalysts tend to be sensible to poisoning from a series of small molecules, most noticeably carbon monoxide, which limits the lifespan of the device. Therefore, the current researches are focused on the optimisation on the replacement of Pt to reduce costs and increase durability, or in the alternative, the optimisation of Pt-based catalysts in order to reduce the amount of Pt used and increase its stability in operating condition.

1.1.3.3. Alkaline fuel cells

AFCs are schematically similar to PEMFCs, with the reaction of hydrogen and oxygen happening on two electrodes separated by a medium which allows the transfer of ions to balance the chemical reaction, as shown in Figure 1.3. In this case at the anode molecular hydrogen reacts with hydroxyl ions to produce water and electrons which travel through an external electrical circuit. Hydroxyl ions are formed at the cathode by the reaction of oxygen

with water and electrons. The transfer of OH^- is possible by the presence between the electrodes of a porous material saturated with a solution of KOH . AFCs operate at temperature up to $80\text{ }^\circ\text{C}$ with an efficiency of 70% producing only water, heat and electricity. The main drawback of AFCs is that are sensitive to CO_2 which can transform the KOH in K_2CO_3 and, therefore, stopping the transfer of OH^- to the anode. Because of this the cathode has to be fed with pure oxygen, while PEMFCs can work with air as a source for oxygen decreasing cost of the fuel and volume of the device.^{19,20}

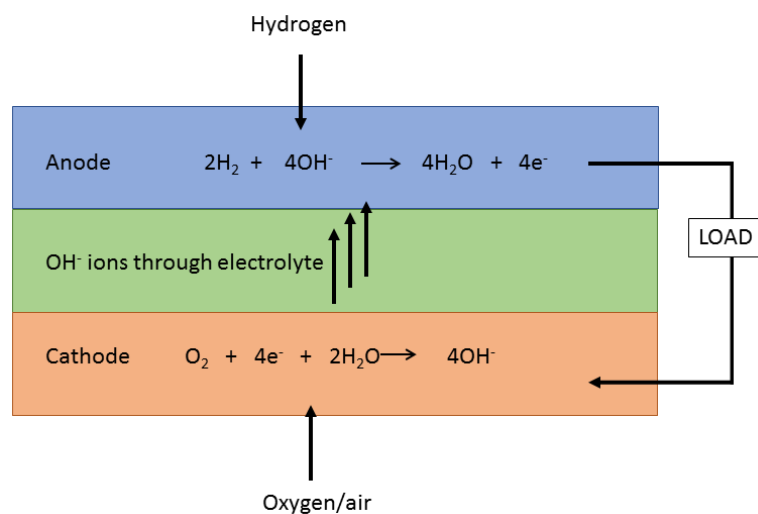


Figure 1.3. Schematic of an alkaline fuel cell, displaying flow of hydroxyl ions and electrons in the circuit.

1.1.3.4. Phosphoric acid fuel cells

PAFCs are systems similar to PEMFCs performing the same reactions on the two electrodes, while the transfer of protons, in this case, is done by the use of a silicon carbide matrix saturated with phosphoric acid concentrated. PAFCs have to be maintained above $42\text{ }^\circ\text{C}$ which is the freezing point of phosphoric acid, but they are more tolerant of CO_2 and CO until 1.5%. PAFCs have an efficiency of up to 50%, but when operated at a higher temperature, 150-200 $^\circ\text{C}$, the steam formed can be recovered and used boosting the efficiency to 70%. They can also be adapted to use fuel different from molecular hydrogen, such as gasoline. For these reasons PAFCs are becoming an appealing alternative to traditional power generation systems, to be used in banks, hospitals and computer facilities.^{19,20}

1.1.3.5. Molten carbonates fuel cells

MFCs semi-reaction are different from the ones reported before for the other fuel cells, as shown in Figure 1.4. At the anode, molecular hydrogen reacts with carbonate ions to form

water, carbon dioxide and electrons, which travel in an external electrical circuit. On the cathode oxygen reacts with carbon dioxide and electrons to produce carbonate ions, closing a zero net cycle of CO_2 . Like in the case of PAFCs the replenish of ions at the anode is performed by a liquid electrolyte in an inert matrix, in this case, molten alkaline carbonates in porous aluminium oxide. This system requires that the operating temperature of the fuel cells stay around $650\text{ }^\circ\text{C}$ in order to maintain liquid the carbonate salts. This higher operating temperature allows to use of non-precious metals as catalysts for the fuel cell and usually, Ni and NiO are used at the anode and cathode respectively. MCFCs can reach efficiency to 60%, and if combine to heat recovery systems the efficiency can increase to 85%. On the other hand, the use of molten carbonates is an issue due to the corrosion due to the salts on the fuel cells components.²⁰

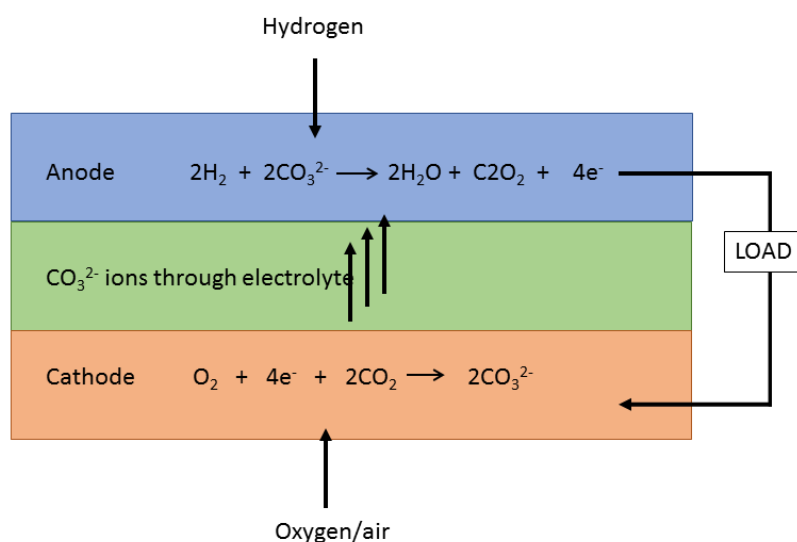


Figure 1.4. Schematic of molten carbonates fuel cell, displaying flow of carbonate ions and electrons in the circuit.

1.1.3.6. Solid oxide fuel cells

SOFCS, such as MCFCs, use an electrolyte to move negatively charged ions from one electrode to another, Figure 1.5. In the case of SOFCs at the anode molecular hydrogen reacts with O^{2-} ions coming through the electrolyte to produce water and electrons. At the cathode molecular oxygen reacts with the electron coming from the external electrical circuit to produce O^{2-} to replenish the electrolyte. The electrolytes in SOFCs are ceramic material opportunely doped in order to increase the transportation of the oxygen ions. Among the materials used as electrolyte there is zirconia, with yttrium or scandium up to 10%, and ceria,

with gadolinium doping. In order to increase the ion transfer the fuel cell as to operate at a temperature between 500 °C and 1000 °C and the start of operation is crucial to avoid fracture in the solid electrolyte due to thermal expansion. In order to reduce the mechanical stress due to the expansion the catalysts are directly deposited on the ceramic electrolyte and the most common is nickel for the anode and strontium-doped lanthanum manganite, $\text{La}_{1-x}\text{Sr}_x\text{MnO}_3$, for the cathode.²⁰

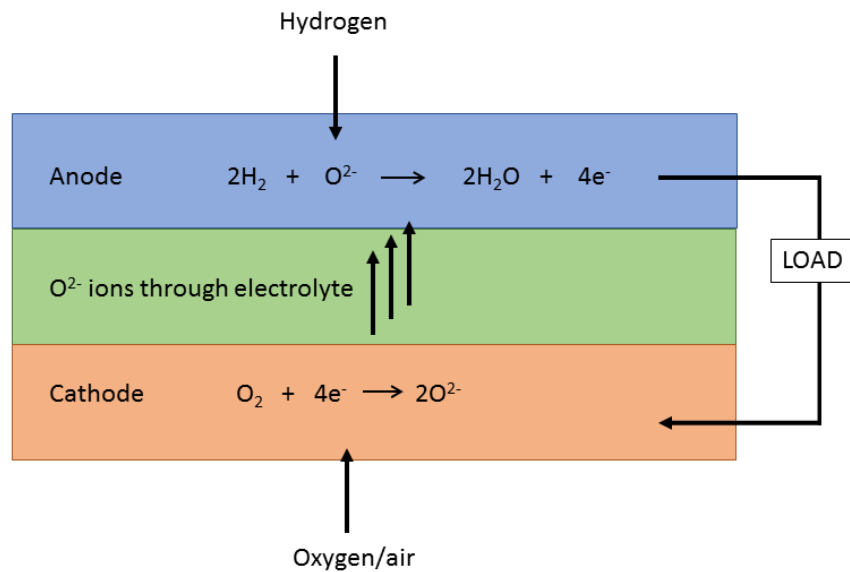


Figure 1.5. Schematic of solid oxide fuel cell, displaying flow of oxygen ions and electrons in the circuit.

1.1.4. Hydrogen generation methods

The most of fuel cell systems discussed before requiring the use as fuel of hydrogen and oxygen for the production of electricity. Therefore, the adoption of fuel cells has to be associated with the generation of hydrogen from another source locally available, since molecular hydrogen does not naturally occur.

Until this point in this thesis, the adoption of hydrogen fuel cells has been characterised as an alternative to fossil fuels. Nonetheless, 96% of hydrogen produced annually currently comes from treatment of fossil fuels, in particular, natural gas.²⁴

The production of hydrogen is currently performed by different processes: (I) Steam reforming of natural gas; (II) partial oxidation of oil; (III) coal gasification; (IV) and only 4% is produced by non-fossil fuel related processes, like electrolysis or biological processes. The distribution in the production between the different processes is shown in Figure 1.6.²⁵

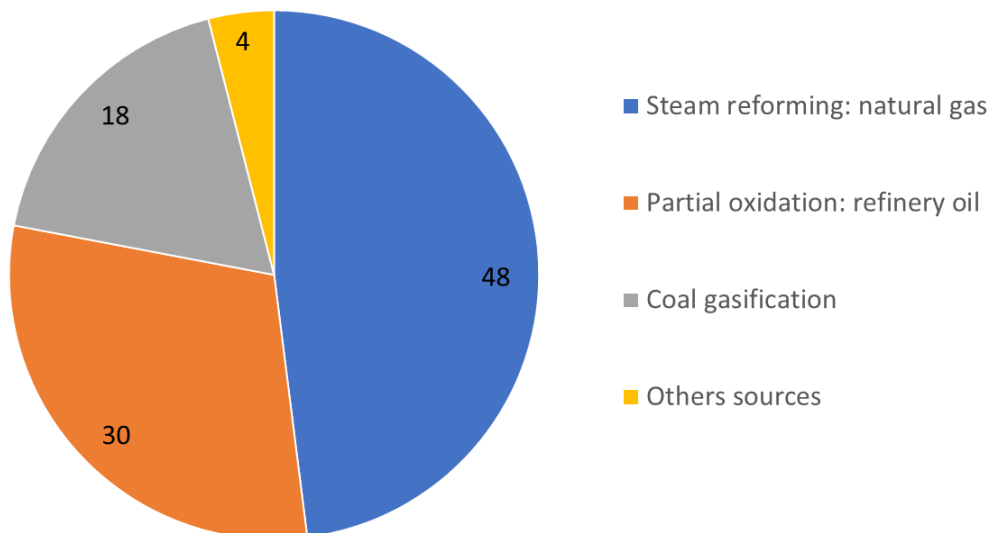


Figure 1.6. Hydrogen processes distribution in percentual by mass of hydrogen produced annually worldwide, data from Energy Technology Essentials.²⁵

From these data it can be deduced how, even if fuel cells are more environmentally friendly, nowadays they rely on fossil fuel for the generation of hydrogen, being, therefore, non-sustainable, expensive and less environmentally friendly than they may appear if considering only energy production unit.

1.1.4.1. Steam reforming

Steam reforming is currently the most common process for the production of hydrogen gas. The success of this process is due to its high efficiency and low cost, both for the material and the operations. Steam reforming converts natural gas, or more generally hydrocarbons, into CO and H₂ by reaction with water.

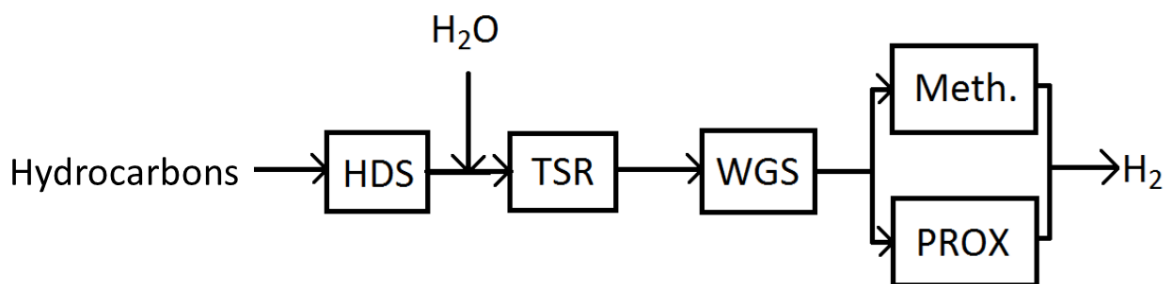


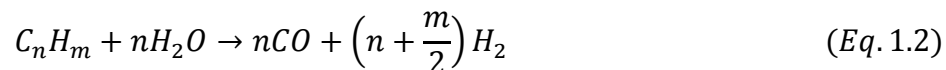
Figure 1.7. Representative schematic process of steam reforming of hydrocarbons, composed of hydrodesulphurisation, tubular stream reformer, water gas shift, methanation or preferential oxidation.

As shown in Figure 1.7, firstly the hydrocarbons undergo a hydrodesulphurisation process (HDS) in order to remove the sulphur compounds normally presents in hydrocarbons, especially H₂S. This step is crucial since catalysts used in successive step are sensible to S

poisoning which can lead to an early deactivation of the catalytic system.²⁰ HDS is performed by the absorption of H_2S on a bed of active carbon or ZnO , which reacts to form ZnS by the reaction:



Then the stream of hydrocarbons is mixed with aqueous steam to perform the steam reforming reaction. The reaction takes place in a tubular reformer (TSR) where the feed enters at a temperature between 450-650 °C and exits the reactor at 850-950°C.²⁶ At the exit of the TSR, the stream is composed of a mixture of H_2 and CO commonly known as syngas. Syngas composition varies depending on the hydrocarbon used as feed for the steam reforming by the Eq. 1.2, with methane giving a ratio $CO:H_2$ ratio of 1:3.



The reaction is catalysed by Group VIII elements both from the first row, like Ni, or from the third row, like Pt or Rh. The reaction is performed in severe conditions both for temperature and pressure, 30 bar can be reached during the process. For this reason, metal nanoparticles tend to grow and, therefore, deactivate over time and support have to carefully choose since they have to sustain the high pressure in the reactor.

The syngas is then treated in a catalytic converter where CO and H_2O react following the water-gas shift, WGS, reaction in order to eliminate CO from the stream and increase the yield in hydrogen, Eq. 1.3.



Two main WGS system are reported, which differ by the operation temperature used. A high-temperature shift which is performed at a temperature between 300-500 °C and which use as catalyst made of Fe_2O_3 , Cr_2O_3 and MgO , where iron oxide is the active species and chromium is used to stabilise it and prevent its sintering.²⁷ The low-temperature shift is performed at a temperature of 210-230 °C with a catalyst composed of CuO , ZnO and Cr_2O_3 containing 2 wt. % MnO and MgO and 5 wt. % Al_2O_3 .²⁷ In this case, copper oxide is the active catalyst while the other oxides are used as additives to increase the performances of the

catalysts, i.e. ZnO act both as support and as desulphurisation agent in order to prevent poisoning of copper.²⁷

The WGS reaction can occur at the same time as the steam reforming, due to the high temperatures used in the process. Nonetheless, the WGS reaction equilibrium is limited at high temperature, which prevents the conversion of CO below 1% of the total exiting feed. Since PEMFCs have to be used with a feed of hydrogen with a maximum content of 10-20 ppm in order to avoid poisoning of the anode catalyst the CO content of the gas has to be further reduced by performing preferential oxidation (PROX) or by methanation (meth.). PROX uses oxygen from the air to convert CO to CO₂, in order to reach 10 ppm of CO in the final gas mixture. However, oxygen can react to hydrogen to produce water and, thus, reducing the production of molecular hydrogen of the process. On the other hand, methanation uses part of the hydrogen produced to convert CO to methane reducing both CO and H₂ production. Consequently, PROX is currently usually used for the reduction of the CO content.²⁸

Reforming can also be performed in absence of steam, using CO₂ as a reagent for the reaction in a process called dry reforming or CO₂ reforming, Eq. 1.4. Dry reforming of methane, DRM, uses two greenhouse gases like CH₄ and CO₂ to produce valuable syngas.



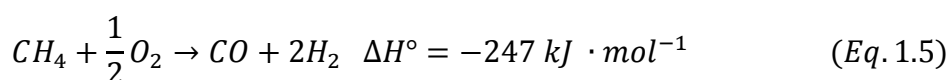
Mixed reforming has been developed using both steam and CO₂ to perform the reforming reaction. DRM and mixed reforming have energy and environmental advantages compared with traditional steam reforming, and they use similar nickel catalysts which undergoes rapid deactivation due to carbon deposit and sintering of Ni particles due to severe conditions of the reaction. An important parameter for the determination of the overall efficiency is the H:C molar ratio in the feedstock of the process. Higher H:C ratios lead to less CO₂ production and higher thermal efficiency of hydrogen generation by steam reforming, reaching 70–85 %.

Since the tubular nature of the reactors used the production can be scaled by adding more tubes with proportional costs. The production nowadays for steam reactor can reach 300000 Nm³h⁻¹ of hydrogen.^{26,28} This system is the most economically viable for small and medium-size plants at present date.

1.1.4.2. Hydrocarbon partial oxidation

Hydrocarbon partial oxidation is more economically viable at present for large scale plants and is used for 30% of the global production of hydrogen. The process uses O_2 to react with hydrocarbons in a combustion chamber producing a CO and H_2 , but also H_2O and CO_2 . Typical feed for this process is heavy oil fractions, but also lighter hydrocarbons can be used.

The partial oxidation can be performed as a non-catalytic process, POX, using oxygen and the gasified hydrocarbon as feed in the combustion chamber where the reaction is performed at 3-8 MPa of pressure and temperature of 1300-1500°C. Partial oxidation produces more CO than steam reforming, but it then converted through WGS reaction.²⁸



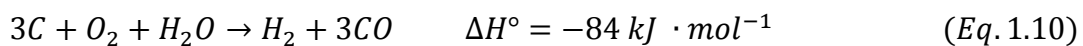
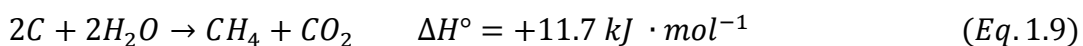
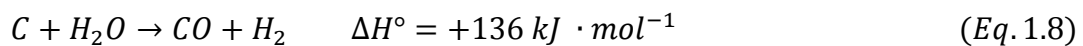
The partial oxidation of hydrocarbons is an exothermic reaction and it produces enough energy to sustain the process when started, for this reason it requires less added energy during the process than steam reforming in spite of the higher temperature used than the steam reforming.²⁹ Moreover, since POX does not use catalysts can be performed on heavier petroleum fraction without the necessity of hydrodesulphurisation to remove S compounds, usually present in large amount in these fractions. Nonetheless, this process is suitable only for large scale application and due to the exothermicity of the process is more difficult to hold at desired temperature than steam reforming.

The partial oxidation can be also performed in the presence of a catalyst, CPOX. Either first-row transition metals, such as Ni, and noble metal, such as Rh, can be used as a catalyst. Ni is cheaper than other metals and in metallic form can promote partial oxidation, however, Ni species with oxidation state ≥ 2 tend to catalyse the total combustion of hydrocarbons.³⁰ Ni also promotes the production of coke. A major issue for the catalyst is the presence of sulphur in the feed. In order to increase the stability of Ni catalysts many promoters, added as an alloy to Ni, have been studied, such as Co, Cu, Pt, Au and Pd.

CPOX works at temperature between 700-1000 °C and it is less efficient when compared to steam reforming producing less hydrogen per molecule of hydrocarbon, as can be seen from Eq. 1.2 and 1.6.²⁸ Thermal efficiency of CPOX is in the range of 60-75%. However, the absence of steam lead to a general simplification of the system which can make CPOX more appealing than steam reforming for some application, such as small-scale cogeneration plants, despite the lower efficiency.^{20,28,31}

1.1.4.3. Coal gasification

During the 19th century and the beginning of the 20th century a mixture of hydrogen, carbon oxides, organic liquids and residual coke, named town gas, was produced by coal gasification. Nowadays, the coal gasification has been improved to generate hydrogen by the reaction with steam and oxygen at high temperatures, 1. 8-1.10. The kind of products and their proportion is relative to various factor among which there are the type of coal, temperature and pressure of the reaction and amount of oxygen and steam used.³²



The process can be performed in different gasifiers. Firstly, moving bed gasifiers work at relatively low temperature, 450-650 °C. The coal feed and the oxidant flow move in opposite directions. The gases produced are mainly methane and ethane, while also a liquid stream gets produced containing naphtha, tars, oils and phenols with ratio varying from the composition of coal used as feed.

Entrained bed gasifiers use higher temperature, 1100-1500 °C, and pressure, 4 MPa. In this case, the feedstock and the oxidising agent are inserted in co-current. Since the residence time is of only few seconds, high temperature and small particle dimension are necessary. In order to avoid the formation of NO_x at high-temperature O₂ is preferred to air. The system produces a gas composed of hydrogen and carbon oxides, while the production of hydrocarbons is limited.³³

Fluidised bed uses an operating temperature between the two systems already discussed, 925-1050°C. In this gasifier, the feedstock is moved and mixed by the action of the flow of oxidising agent to increase heat and mass transfer.²⁰

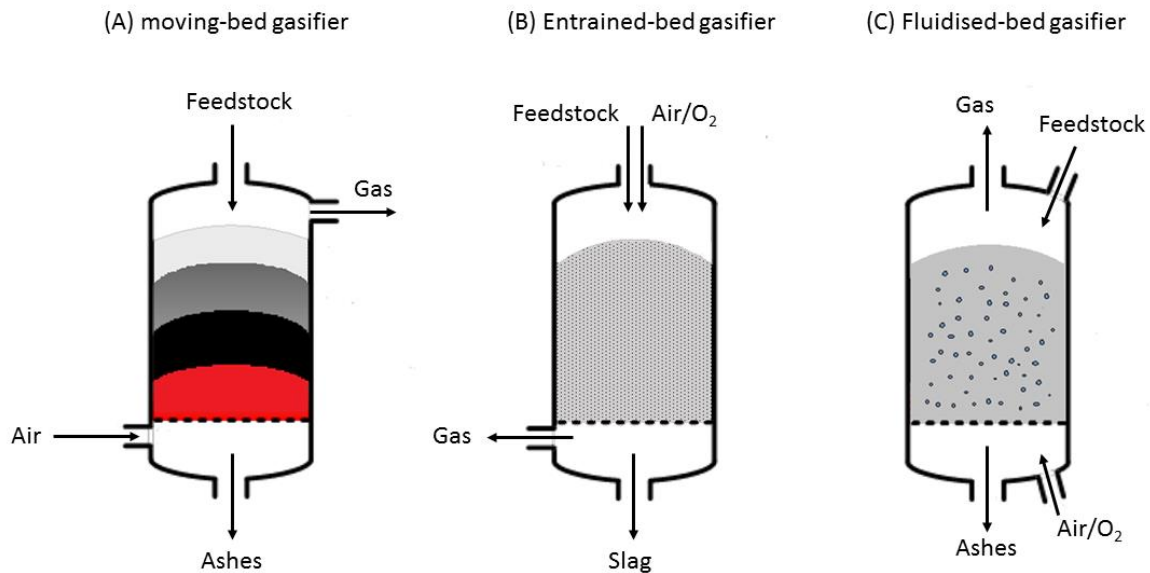


Figure 1.8. Representative schemes of different classes of coal gasifiers, which differ from each other for temperature, feeding position and exit of the products.

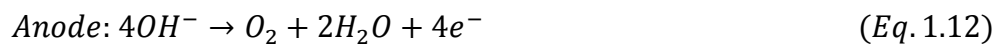
The heat required to carry out the reaction is provided by the partial oxidation of coal. Even if the gasification is performed commonly in the absence of a catalyst, many researches have been reported over the years about catalysts. Most elements of the periodic table have been tested from alkali and transition metals to noble metals and lanthanides.³⁴⁻³⁶ Nonetheless, due to the large variety of parameter which influences the gasification a consensus on an optimal catalyst has yet to be found.³²

The products of coal gasification have to be purified in order to remove contaminants to avoid the poisoning of the fuel cell catalyst. Moreover, WGS reaction has to be performed to decrease the content in CO of the gas stream. The condition of the gasification can also be optimised so that the H₂:CO ratio in the products increases.³²

Gasification process has a low heat efficiency, 35-50%, due to the vaporisation of moisture in the coal.^{25,28} This reason and the cost for O₂ separation necessary to avoid the formation of NO_x make coal gasification less economically viable than partial oxidation and steam reforming. Moreover, gasifier needs to be coupled with CO₂ capture scheme.³⁷

1.1.4.4. Electrolysis

Other technologies based on the conversion of fossil fuel mentioned above, the currently most used process for the production of hydrogen is electrolysis, constituting approximately 4% of the global hydrogen production.^{25,28} Electrolysis uses a direct current applied to two electrodes immersed in a water solution to split the O-H bonds of water and generate O₂ and H₂.



The reaction can be performed using sulphuric acid as electrolyte and platinum electrodes. However, in industrial application stainless steels and nickel-based electrodes are used immersed in a KOH solution at a temperature between 60-80°C.³⁸

The process is energy-intensive compared with the previously reported hydrogen production systems. However, electrolysis (I) produces high purity hydrogen, without the need of cleaning procedure or WGS reaction, (II) does not produce greenhouse gases and (III) produces pure oxygen which can be used for other industrial applications.

Theoretically, electrolysis can reach 85% energy efficiency,²⁵ but in commercial applications, the efficiency is lower, 50-75%, due to the optimisation of other parameters.²⁸

To increase the efficiency of the electrolysis, high-temperature and high-pressure systems have been tested. The high-temperature process reaches a temperature between 800-1000°C and uses the heat to provide part of the energy to the system instead of electricity. If the heat is recovered from another process the overall efficiency of the hydrogen production is increased. The high-temperature electrolysis consumes 5 kWh/m³ of hydrogen.

High-pressure electrolysis pressurises water to 120-350 bar, this pressurisation is less energy-intensive on the water than on hydrogen, therefore the water is pumped in the electrolyser at high pressure. As a consequence, the hydrogen gas produced is dissolved in water at high-pressure and can be separated after at the desired pressure. In this way, compressors for hydrogen after the electrolyser are no longer necessary and the overall efficiency is improved

by lower energy required for the pressurisation.³⁹ Normal and high-pressure electrolysis consumes 4-5 kWh m⁻³, require a voltage of 1.85-2.05 V to operate at temperatures between 70-90°C.

The hydrogen produced by electrolytic systems can reach 99.8% purity. Nonetheless, these systems require a large amount of energy to operate. In order to be commercially viable and sustainable electrolysis has to be coupled with large renewable sources (hydroelectric, solar or wind), and that explained the limited application of this system up to now.³⁸

Hereafter in Table 1.2 is an overview of the method of production of hydrogen feed for fuel cells.

Table 1.2. Hydrogen production technologies summary.

Technology	Feedstock	Thermal efficiency (%)
Steam reforming	Methane	70-85
Partial oxidation	Methane	60-75
Coal gasification	Coal	35-50
Electrolysis	Water + electricity	50–75 (Commercial)

1.1.5. Drawbacks of hydrogen usage

The abovementioned hydrogen production processes showed how industrial-scale manufacture is still limited by price and use of fossil fuels. Nonetheless, the main limitation to the extensive application of hydrogen as an energy carrier is the hydrogen storage technology, both for the restricted capacity of storage and safety issues associated to storage and transportation at mild conditions, which is a problem for widespread use of the technology.⁴⁰ The safety issues arise from the high flammability of hydrogen, which is flammable between 4.0% and 77.0% in volume in air at 1 atm, whereas in oxygen the upper limit rises to 94.0% in volume.²⁰

The energy density per unit of mass of hydrogen is the highest among the fuels currently used, but due to its gaseous state at standard condition, the energy of hydrogen per unit of volume is, therefore, lower than any liquid fuel. For this reason, hydrogen requires an ulterior energy-intensive process in order to modify its conditions (pressure, temperature or phase) so that it

can be used in technology similar by volume to the ones already existing that hydrogen application aims to replace. 1 kg of hydrogen at 15 bar occupies 800 L, which can explain why the traditional way to store hydrogen is under 800 bar of pressure in order to decrease the volume of the cylinder used for the storage or using liquified cryo-hydrogen, both methods require high-energy and specialised instrumentation for the usage.⁴¹ Moreover, if transported in pipelines, like it is done for natural gas, it would require 20-30% more energy per unit of energy transported due to pressure drops than the distribution of natural gas.⁴² This consideration leads to the conclusion that relative long distances, above 100 km, transportation of hydrogen has major economic drawbacks.⁴³

1.1.6. Alternative solutions to hydrogen storage

To overcome the issue linked to transportation and storage of hydrogen many researches currently try to address this problem by studying new systems to produce hydrogen *in situ*, close to the final users. These methods are focused on the use of portable devices, so are limited in many cases to small-scale applications.

In the first instance, the solutions can be classified into: physical processes and chemical processes, as shown in Figure 1.9. Among the physical processes used to store molecular hydrogen physisorption on porous material is the most researched. In this process, hydrogen is stored in the pores of a solid material such as zeolite,⁴⁴ carbon materials,^{44,45} metal-organic frameworks (MOFs)⁴⁶ or organic polymers.⁴⁷ The system is straight forward, but the amount of hydrogen that is possible to store is limited and there are issues over reusability and full desorption of gas from the porous material.⁴⁵

Chemical hydrogen storage systems with high hydrogen contents are able to store hydrogen by forming chemical bonds. Solid-state materials, such as metal and non-metal hydrides, may have a high capacity for hydrogen storage, but the kinetics of release is often slow and requires high temperature to match the requirements of fuel cells. Furthermore, these materials suffer from degradation after some cycles of use and require a completely new system of distribution and recharging.^{48,49} Liquid chemical storage systems show the great advantage to use the pre-existing recharging station system already in use for gasoline distribution.⁵⁰ Among these a lot of interest has been given to decomposition of hydrogen-rich small molecule like methanol,⁵¹ formic acid,⁵² hydrous hydrazine,⁵³ amines⁵⁴ and

borohydrates.⁴⁸ Since most of the liquid chemical storage material require the use of a catalysis in order to release their hydrogen content a deeper analysis of these systems is reported later in the chapter.

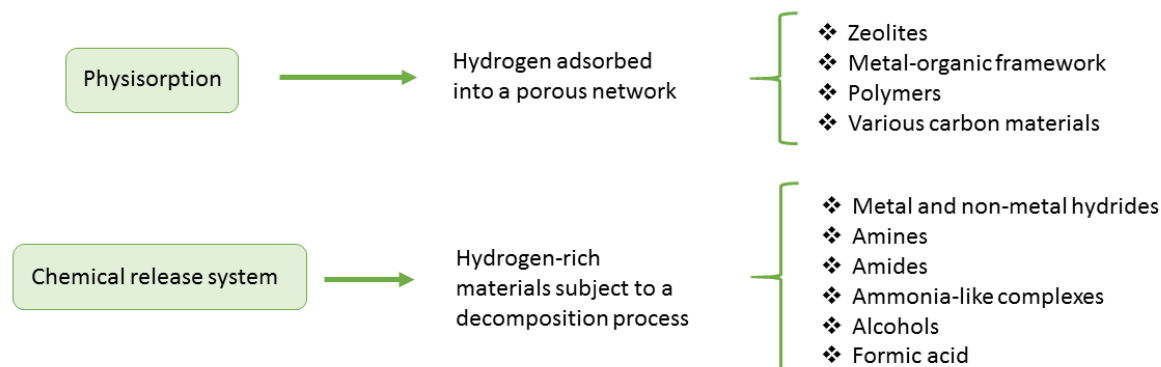


Figure 1.9. Scheme of most common hydrogen storage system and classification, main division being between physical methods and chemical methods.

1.2. Catalysis

IUPAC defines a catalyst as “a substance that increases the rate of a reaction without modifying the overall standard Gibbs energy change in the reaction; the process is called catalysis. The catalyst is both a reactant and product of the reaction”.⁵⁵ Therefore, the catalyst does not change the thermodynamic nor the final equilibrium of a reaction, but it provides an alternative reaction pathway with lower activation barrier, thus, increasing the rate of reaction without, for an ideal system, being consumed during the reaction.⁵⁶ Catalysis is of extreme importance for life since enzymes catalyse most of the reaction which takes place in biological cells. The importance of catalysts in lowering the energy requirement and increasing rate for reactions have been largely exploited also by industry. It is estimated that 85-90% of all the material produced require at least one catalysed step, both for economic and environmental reasons.^{56,57}

The general mechanism of reaction for catalysts follow a series of elementary steps that are common between the catalysts and can be summarised as: (I) a reaction between a reagent and the catalyst to form an intermediate species; (II) possible reaction between the intermediate and another reagent, that can also be bonded or not to the catalyst; (III) the split of the bond between the catalyst and the product. The increase in the rate of the reaction is

related to the lower maximum of activation energy required to complete the catalysed reaction compared to the non-catalysed reaction.

1.2.1. Type of catalysis

The catalytic processes are divided in class by the typology of catalyst used: bio-catalysis, homogeneous and heterogeneous.

1.2.2. Bio-Catalysis

Bio-catalysis is performed by large proteins called enzymes. Enzymes are naturally coded by living cells and are used to build-up protein and DNA, breakdown complex molecules and convert molecules like sugars to energy. Enzymes are highly specialised catalysts able to recognise specific groups thanks to the chain of amino acids constituting the active site, Figure 1.10, and they can achieve high efficiency and stability. For example, decomposition of hydrogen peroxide by enzymes can reach rates of 10^7 molecules per second per enzyme.⁵⁷ Nonetheless, enzymes are sensitive to the reaction condition since changes in temperature, pH or ions concentration can lead to denaturation of the protein, the modification of the 3D structure of the protein due to the weakening of the intramolecular bond in the protein. The modification of the 3D structure of the enzyme can lead to the modification of the active site.⁵⁷ The optimal conditions of utilisation of specific an enzyme usually are environmental conditions of the habitat of the cell that expressed the enzyme.

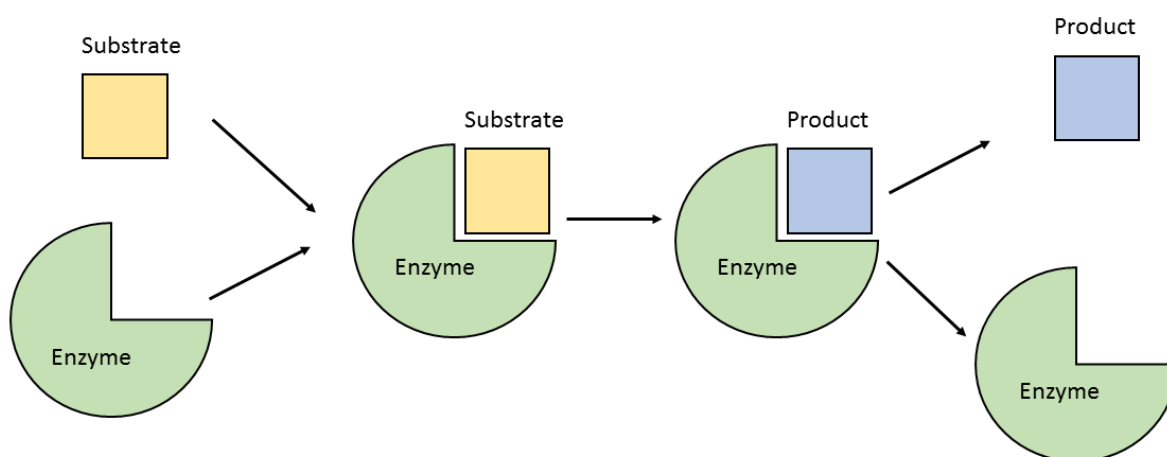


Figure 1.10. Representative scheme for enzymes-substrate reaction, passing through the formation of enzyme-substrate and enzyme-product complexes.

1.2.3. Homogeneous catalysis

Catalysis is classified homogeneous when reagents and catalysis are in the same phase (solid, liquid and gas), usually liquid. Among the most common homogeneous catalysts, there are acids and bases (both Brønsted and Lewis), porphyrin complexes and organometallic complexes. Organometallic catalysts, in particular, consist of one or more metal atoms coordinated with various ligands. The organometallic catalysts are highly influenced by the ligands used which are coordinated with metal atoms, so that it is possible to tune the selectivity of the reaction toward selected products by varying the ligands, i.e. reaction of butadiene with Ni catalysts in Figure 1.11.⁵⁸

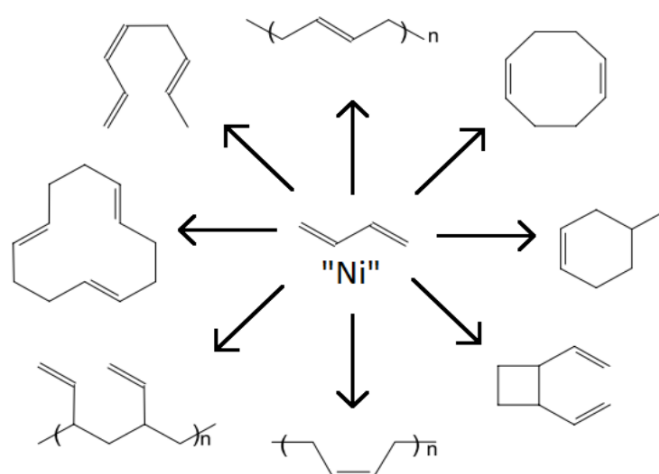


Figure 1.11. Products of the reaction of butadiene in the presence of nickel complexes with various ligands.

In the case of homogeneous catalysts almost all the atom of the active metal participates as an active site in the catalytic reaction, this increases the efficiency of the catalytic process and favour the economic aspects of the application. The absence of multiphase processes and the possibility of single-site mechanism allow a deeper understanding of the reaction mechanism and, therefore, a smarter design of the catalyst to fit better the reaction to be improved.⁵⁹ Nonetheless, since the catalysts and the products are in the same phase, for this kind catalysis, the separation and recovery of the catalysts at the end of the reaction is difficult and expensive, and it possible the contamination of the products by the catalysts.^{57,58}

1.2.4. Heterogeneous catalysis

It is classified as heterogeneous the catalytic process in which the catalyst is in a different phase than the reagents. Usually, in heterogeneous catalysis, the catalyst is solid while the

reagents are liquids or gases. The heterogeneous catalysis follows the same three steps stated for the general catalysis and the creation of a bond between the catalyst and the reagents is the adsorption on the surface, as shown in Figure 1.12.

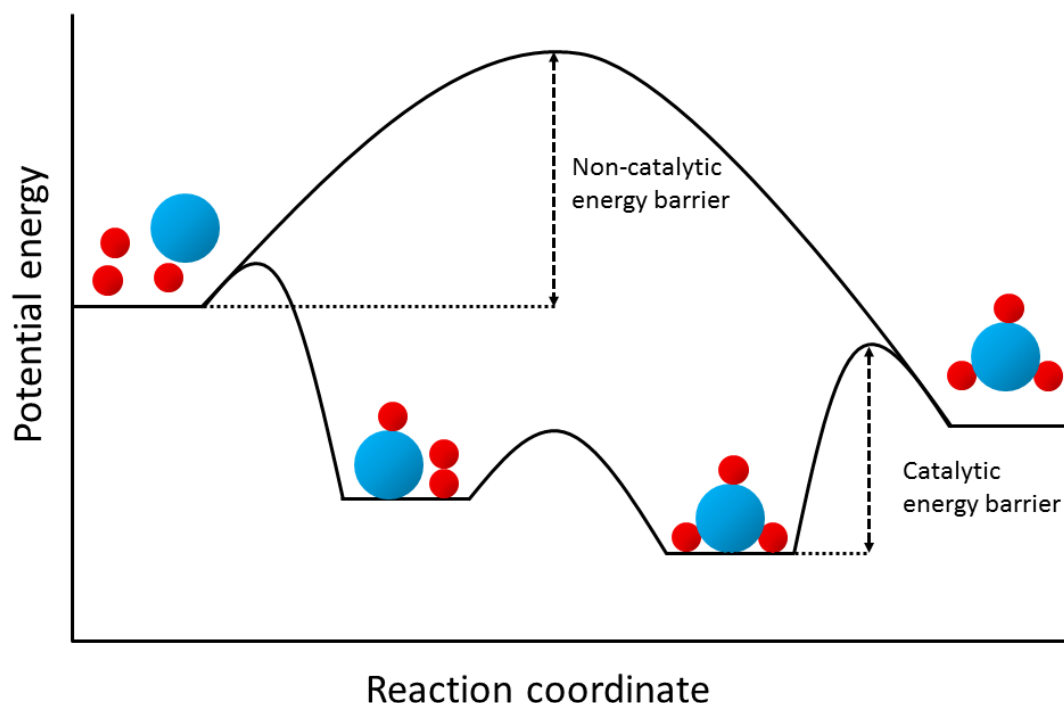


Figure 1.12. Representative mechanism of reaction during heterogeneous catalysis, following adsorption, reaction and desorption mechanism.

Among the various heterogeneous catalysts a classification can be done on the base of composition and conformation of the catalysts themselves: (I) unsupported or bulk catalysts; (II) supported catalysts; (III) coated catalysts.⁶⁰

Unsupported catalysts are used especially when the use of support can affect the reaction or absorb the products. Unsupported heterogeneous catalysts can be metal oxides, carbide, nitrides, insoluble salts or metals. Examples of oxides catalyst are NiO, used as cathode in some fuel cell, and perovskite (CaTiO_3), which are used for combustion reactions. Metal gauze and grid are used when the reactions are highly exothermic and it is desirable to contain the height of the catalytic bed, such as in the case of Pt-Rh gauze for ammonia oxidation during the production of nitric acid, or Ag grids, used in methane dehydrogenations. Carbides and nitrides, formed by the inclusion of C or N atom in interstitial position of metals, are good catalysts used for hydrogenation and anhydrous hydrazine decomposition.⁶⁰

Supported heterogeneous catalysts have a vital role in the economy of many industrial processes. The use of bulk precious metal can be a disadvantage for industrial processes, so the use of supported metal nanoparticles increases the effective surface area of the active metal allowing to use less metal. As support for the active metal is usually chosen an inert material like metal oxides, carbon or organic resins. Nonetheless, the support may display interaction with the active metal to meet two main objectives: (I) the stabilisation of specific nanoparticles structures, controlling the electronic properties of the particles and, therefore, modifying catalytic properties; (II) avoiding the agglomeration, which tend to happen at high temperature, and favour good dispersion on the surface in order to maintain a high value of surface area. This phenomenon is called strong metal-support interaction, SMSI, and it is key for the success of many catalytic processes.⁶⁰

In order to optimise catalytic processes bimetallic or multi-metallic nanoparticles can be used instead of monometallic ones. The use of a second metal can be necessary to increase the activity of a specific catalyst, to inhibit a specific side reaction or to enhance the stability toward agglomeration or poisoning. Moreover, using a non-precious metal to modify a precious metal nanoparticle the cost of the catalyst may be reduced. This is the case of Cu-Ni alloys, where the surface is rich in Cu due to its lower surface energy compared to Ni and the alloy offer more active sites per mass than bulk Cu.⁶¹

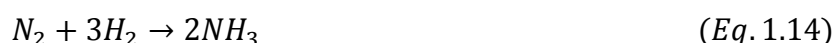
As mentioned before, support metal nanoparticles are largely used in industry, due to activity and simplicity of recovery after the reaction, but the cost of the metals may be a drawback. For this reason, discovering how to synthesise and tailor the nanoparticles size, morphology and composition has been the focus of many researches over the years.⁶²⁻⁶⁷

Coated catalysts, typically applied to monolithic honeycombs, are becoming more popular in recent years and they consist in the deposition of a thin layer of active species on an inert structure. The layer deposited on the surface of the inert material can be composed of the active metal directly or of a supported catalyst itself.⁶⁰

Heterogeneous catalysts in industrial application display many advantages such as (I) elimination of liquid waste and corrosion, due to free liquid acid; (II) Simple separation of the catalyst after the reaction; (III) stability at a wide range of condition.^{26,56,60} On the other hand heterogeneous catalysts (I) can suffer from mass transfer limitations, which can reduce the

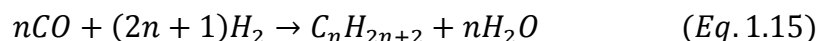
efficiency of the catalysts; (II) can lose active metal due to leaching; (III) can suffer of agglomeration of the nanoparticles overtime at the reaction conditions, giving problem of stability on long-term applications and (IV) in some cases it can induce pressure drop in the system which can be problematic for the entire process.^{26,56,60}

Successful examples of industrial heterogeneous catalysis are the Haber-Bosch method for ammonia and Fischer-Tropsch synthesis to produce hydrocarbons. The Haber-Bosch method converts N_2 and H_2 to ammonia using four catalytic bed at 400°C and 15MPa following Eq. 1.14:



The reaction is performed using iron as catalyst promoted with K_2O , CaO , SiO_2 and Al_2O_3 . Ru-based catalysts are a family of catalysts found to be potentially more active than iron, working at lower pressure. Nonetheless, the large amount of expensive catalyst required to compete with the Haber-Bosch process commercially makes the use of Ru-based catalysts less economically viable.⁶⁰ In fact, currently 450 million tonnes of nitrogen fertilisers every year are manufactured by the Haber-Bosch process.

Fischer-Tropsch synthesis proceeds by the Eq. 1.15



Industrially the reaction is performed at $220\text{-}240^\circ\text{C}$ and $2\text{-}4\text{ MPa}$ with catalysts that can be made of Fe, Co and Ru. Iron and cobalt catalysts are used more than ruthenium ones due to the lower cost of those metals. Iron catalysts are less sensitive to CO_2 in the feed due to the possibility to performed WGS reaction but are prone to inhibition by water molecules. Cobalt catalysts can operate at lower temperatures and are more stable than iron ones. Hence, cobalt-based catalysts can last up to five years in the reactor while iron-based catalysts need to be replaced every approximately six months, but cobalt is more expensive, so extensive analysis has to be performed in order to choose the most advantageous catalyst.⁶⁰

1.2.5. Preparation of supported heterogeneous catalysts

Small dimensions of nanoparticles, in the range of $1\text{-}10\text{ nm}$, by prediction of physicists should present particular electronic structure due to quantum size effect which give nanoparticles properties different from both bulk metal and molecular compounds. This effect appears

when de Broglie wavelength of the valence electrons and the particle itself are of the same order of size.⁶⁴ This means that nanoparticles present unique properties which can be tuned by adapting the size and shape of the particles through the application of different preparation methods.⁶⁸⁻⁷⁰ Moreover, the properties of nanoparticles can be tuned by the choice of the support material which through metal-support interaction can alter the dispersion of the metal on the surface and the particle size.^{68,71}

In researches like the one presented in this thesis, the catalysts are synthesised in small-scale batch reaction, which produces enough catalyst for the study to perform, is less expensive than continuous flow system for small amount of catalysts and the parameter can be modified to tailor the preparation more easily. However, for industrial application large-scale preparation are needed, which can raise issues due to inhomogeneity on among batches from heat and mass transport limitation associated with the larger volume used to scale up. For this reason, continuous flow preparations are studied in order to reduced heat and mass transfer issues and, therefore, obtain more homogeneous catalysts. Moreover, these systems can be automatised to increase efficiency.⁷²

Nanoparticles preparation can be classified as *top-down* or *bottom-up* approaches. Top-down methods use physical method to reduce the dimension of the particles starting from bulk metal. These methods can produce a large number of nanocrystals but control the particles size distribution and mean particle size is complex.^{73,74} On the other hand, bottom-up methods growth nanoparticles starting from individual atoms, from the nucleation and growth of the crystals. These methods allow better control over size and distribution of particles and, therefore, were chosen as principal methods to be used in this thesis, sol-immobilisation and deposition-precipitation.

1.2.5.1. Sol-immobilisation

This method consists in the immobilisation of preformed nanoparticles from a colloidal solution on the surface of the support material. This method provides great control over mean particle size, particle size distribution and shape of the nanoparticles, especially for the case of noble metals.⁶⁵ The preparation method generally requires to follow five main steps: (I) preparation of a aqueous or solvent-based solution of metal salt precursor and stabiliser; (II)

addition of a reducing agent; (III) addition of the support and immobilisation of the nanoparticles; (IV) removing the stabiliser by washing the catalyst and (V) drying the sample.

Sol-immobilisation is a family of preparation technique which differs primarily by the reducing agent and the stabiliser used for the preparation of the colloidal solution. Many reducing agents used and reported in the literature are many, for examples NaBH_4 , hydrous hydrazine and alcohols, and also thermal, electrochemical and photochemical processes can be used to achieve the reduction of the precursor salt.

The stabiliser role is to avoid that free nanoparticles in solution interact with each other and agglomerate to the collapse of the colloidal solution. For some metal, the production of a colloidal solution does not require the presence of a stabilizer. However, the use of stabilising agent helps to control particle size distribution and mean particle size and increase the stability of the colloidal metal solution over time. Three mechanisms of stabilisation are used in sol-immobilisation:

- Increasing charge density and/or surface potential by the adsorption of ions on the surface of the particles, which create a charged double layer around the particle that repel over particles, as shown in Figure 1.13. This mechanism is used by citrate and tetrakis(hydroxymethyl)phosphonium chloride;
- Adsorption of relatively rigid hydrophilic macromolecules on the surface, in this way, enhancing the interaction with the solvent by reducing the Van der Waals forces and reducing the interaction with other nanoparticles. This mechanism is used by dextrin and starch.
- Steric stabilisation by deposition on the surface of high molecular weight molecules which sterically impede the contact between particles, as shown in Figure 1.13. This mechanism is the main one displayed by polymers like PVA or PVP.

Since the metal nanoparticles are pre-formed by chemical reduction and then immobilised, in many cases the nanoparticles are already present at metallic state without the necessity for a further reduction step, especially for noble metal nanoparticles.⁷⁶ However, for more reducible metals the drying at mild temperature may induce oxidation of the surface of the nanoparticles. This method usually provides a good distribution of the nanoparticles on the surface.

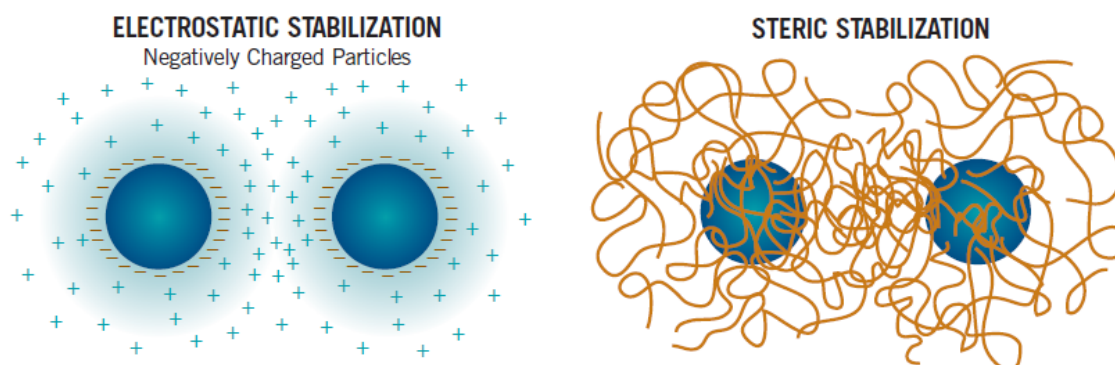


Figure 1.13. Representation of electrostatic, due to charges surrounding the nanoparticles, and steric stabilisation of nanoparticles, due to long chain polymers adsorbed on the surface.⁷⁵

However, sol-immobilisation faces challenges in the scale-up of the preparation method due to impurity introduced by the higher amount of reagents used possible inhomogeneity in the nucleation of the particles derived from the different stirring. Another issue is the limitation of the support that can be used for the preparation since the immobilisation is highly dependent on the point of zero charge (ZPC) of the support.^{77,78}

1.2.5.2. Deposition-precipitation

The deposition-precipitation method, DP, consist of the nucleation and growth of hydroxides and oxides nanoparticles on the surface of a support by the increase of the pH of the solution. The mechanism starts with the generation of hydroxy-metal complexes in solution, which then react to with other complexes to polymerise or with the hydroxyl groups on the surface of the support. Some reports indicate that the interaction with the surface is preferential with respect to the interaction with other hydroxyl complexes, so it creates nucleation centres where complexes can polymerise to grow the oxide nanoparticles.^{79,80}

The pH can be adjusted using different basic substances that act directly, such as alkaline hydroxide or carbonates, and indirectly, like urea that increases gradually the pH by generating in situ NH_3 by thermal decomposition.^{77,79,80} The morphology, particle size distribution and mean particles size can be controlled by the use of different precipitating agents, but also by the pH values and slow modification of values of pH during the preparation. After nucleation and growth processes the resulting particles may have a particle size too large and a more heterogeneous particle distribution. Therefore, the control of the

pH is crucial, while different counter ions can guide the growth in different way influencing the morphology of the particles.⁷⁷

This method requires only a system to control the pH and precipitation agents that are usually cheap and common chemicals, this made of DP one of the most well-known and used methods for supported catalysts preparation. Nonetheless, the deposition efficiency is affected by the characteristics of the support, especially its point of zero charge (PZC), so that the range of pH to be utilised is limited by the choice of the support.⁷⁷ Hence, this preparation method is sensitive to the reaction conditions (temperature, pH, ions concentration), therefore, the tuning and reproducibility of the catalysts are more complicated. Moreover, the nanoparticles produced by this method are oxides nanoparticles after the final drying step, this means that the catalysts have to be reduced by high-temperature reduction, or calcination in the case of gold, which can lead to the growth of the particles due to increased mobility of the particles and atoms.

A more detailed explanation of the protocols used for the catalyst preparations used in this Thesis is reported in Chapter 2, Section 2.2. .

1.3. Liquid-phase chemical hydrogen storage systems

As discussed in Section 1.1.6., a possible solution to overcome the issues regarding the safety and economy of hydrogen as an energy carrier is the use of liquid-phase chemical hydrogen storage systems. These systems are usually used in combination with homogeneous and heterogeneous catalysts in order to release efficiently hydrogen when necessary. The criteria for applicability of the systems are several from the cost to the charging/recharging system, the handling pressure and temperature and the gravimetric and volumetric capacity.^{81,82} Guidelines for hydrogen storage material applications have been redacted by several national and international organisations. Among them, the U.S. Department of Energy has set some targets, like reaching a target of 6.5 wt% as the gravimetric capacity and 50 g L⁻¹ as volumetric capacity.⁸³ In Table 1.3 some physical properties of liquid-phase hydrogen storage materials are reported.

Table 1.3. Physical properties for potential liquid-phase hydrogen storage materials.

Liquid chemical storage	Density at room temperature (g cm⁻³)	Hydrogen content (wt. %)	Ref.
Sodium borohydride	1.07	10.8	84
Lithium borohydride	0.67	18.4	85
Ammonia borane	0.74	19.6	84
Ammonia	0.73	17.6	85
Hydrous Hydrazine	1.03	7.9	85
Hydrazine borane	0.78	15.4	84
Methanol	0.79	12.5	85
Ethanol	0.79	13.0	86
Formic acid	1.22	4.4	87

One of the class of liquid compounds studied are borohydrates and boranes, especially sodium and lithium borohydrate, and ammonia and hydrazine borane. These systems are relatively safe and low-cost but tend to show difficulties into the recover or treatment of the waste produced.^{51,88-90}

C-based storage materials are also well studied, among them methanol, ethanol and formic acid. Methanol can be used as a reagent in direct methanol fuel cells, but it can also be treated with steam reforming process, at 200-300°C, to produced hydrogen, with a series of by-products.⁵¹ More interesting is the catalytic decomposition of methanolic sodium hydroxide which produces only molecular hydrogen and carbonates, reducing the waste, which is at the moment limited by the use of expensive homogeneous catalysts that need to be recovered.^{91,92}

Ethanol is currently used as “bio” alternative to gasoline in internal combustion engines in countries like Brazil and the USA, therefore, the distribution system for a future application as hydrogen storage is already operating. As for methanol, the main drawback for the catalytic decomposition is the use of homogeneous catalysts, such as Rh or Ru complexes.⁹³ In this case, another issue is the production of ethyl acetate and acetaldehyde that need to be treated before to be released in the environment.⁹⁴

Formic acid is also a potential candidate as liquid hydrogen storage material. Currently, it is produced as a by-product of several industrial processes, such as acetic acid production or conversion of cellulose to γ -valerolactone, and from the hydrolysis of methyl formate generated by the reaction between methanol and CO. Heterogeneous Pd-based and Au-based catalysts have been proven to be effective for the catalytic decomposition of formic acid.⁵²

C-based liquid storage materials tend to produce CO₂, a greenhouse gas, as a by-product of the hydrogen production. Nonetheless, they can also be produced by fermentation of a different kind of biomass so there is the possibility to use the CO₂ produced by the hydrogen generation creating a net-zero CO₂ cycle.

N-based liquid hydrogen storage material, like ammonia, amides and hydrous hydrazine, have been studied as well. Ammonia is a commodity product and its production from the Haber-Bosch process is well established. However, ammonia is really stable and high temperatures are necessary in order to perform its decomposition, temperatures of approximately 500 K are required in order to have good efficiency.⁹⁵

1.3.1. Hydrous Hydrazine

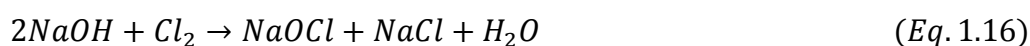
In this project, we are focusing our attention on the decomposition of hydrous hydrazine. Anhydrous hydrazine is a well-known monopropellant for rocket due to its rapid decomposition in particular on Ir/Al₂O₃ catalysts.⁹⁶ NH₂NH₂ has a high hydrogen content of 12.5 wt% and it is an oily liquid at room temperature. Anhydrous hydrazine easily decomposes on a series of different material from noble metals to metal carbides and nitrides producing a large volume of gas and potentially hydrogen if the temperature reached is high enough, increasing, therefore, the risk of fire and explosion during the storage.

In order to avoid any explosive danger related to the storing of hydrazine, the use of the monohydrate form is preferred to the anhydrous counterpart. Hydrazine monohydrate, despite the addition of one mole of water for each one of hydrazine, maintains a hydrogen content of 7.9 wt%, above most of the requirement for hydrogen storage material, and it is more stable and has the tendency to decompose to ammonia reducing the explosion risk during storing. NH₂NH₂·H₂O is liquid between -60 and 120°C, this characteristic makes it a

promising candidate for the replacement of gasoline in the already existent recharging networks for internal combustion engines.

1.3.1.1. Production of hydrazine

Currently, the production of hydrazine is one of the main drawbacks to the application of hydrazine monohydrate as suitable hydrogen storage material. The most common synthesis process used are ammonia oxidation processes, using chlorine or hydrogen peroxide as oxidants. These processes follow and adapt to the mechanism of Raschig synthesis. This follows the synthesis described by Eq. 1.16-1.18. As it can be seen as full conversion this process only utilised 2/3 of the moles of ammonia for hydrazine production, while the remaining is converted to ammonium chloride. Moreover, in this condition, 125-150°C, chloroamine and hydrazine are unstable, so low concentration, 1%, have to be maintained and the hydrazine need to be distillate.⁹⁷



The Bayer process produces the chloroamine by direct reaction of chlorine with ammonia and then uses it to form diaziridine three-membered ring by the reaction with imine, generate by the reaction of ammonia with a ketone. The diaziridine then reacts with a ketone molecule to form azine which is hydrolysed in acid to give hydrazine. This process can work at room temperature and at higher concentration. Due to the presence of acid hydrazine have to be extracted at the end of the reaction.⁹⁷

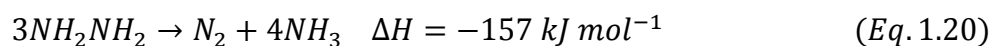
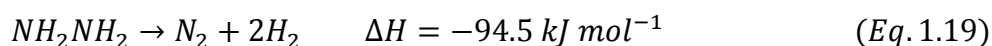
Ugine Kuhmann process is chlorine-free, using a combination of hydrogen peroxide and nitrile to oxidise the imine and create a three-membered oxaziridine, which later reacts with a ketone molecule and ammonia to form the azine intermediate. This process has the advantage to create less waste since the ketones and the nitrile can be regenerated, consuming only hydrogen peroxide.⁹⁷

An alternative to these processes over the years (I) radiolysis of ammonia, (II) glow discharge electrolysis of ammonia⁹⁷ and (III) nitrogen fixation processes have been studied.⁹⁷ Of particular interests for application as “green fuel” is the nitrogen fixation, therefore, the use

of molecular nitrogen to generate ammonia or hydrazine. The fixation can be done catalytically using homogeneous iron-based catalysts or electrochemically.⁹⁸ The possibility to generate ammonia from nitrogen and water applying electrical current,⁹⁹ open to the option of the generation of hydrazine using the excess of energy generated by renewable sources.

1.3.1.2. Hydrous Hydrazine decomposition

Hydrous Hydrazine easily decomposes following two main pathways: decomposition to molecular hydrogen, Eq. 1.19, and decomposition to ammonia, Eq. 1.20. The decomposition toward hydrogen is the desired reaction pathway for application in fuel cell, leading to the highest hydrogen yield without the formation of undesired and harmful ammonia. Ammonia interacts with proton membranes, like Nafion, poisoning them and leading to a premature deactivation of the fuel cell system.^{100,101} Nonetheless, as it can be seen the production of ammonia is thermodynamically favourite, so a kinetic control from the catalyst is required to achieve high yield toward hydrogen. Hydrous Hydrazine also as the great advantage that the complete decomposition produces as by-product only N_2 that can be dispersed in the atmosphere without any harms for the environment.¹⁰⁰



Hydrazine molecule presents only two types of bond: the N-H, with an energy of 84 kJ mol^{-1} , and N-N, with an energy 60 kJ mol^{-1} .¹⁰¹ This can indicate why achieving decomposition toward hydrogen at mild condition is a challenge.

1.3.1.3. Heterogeneous catalysed hydrous hydrazine decomposition

Catalytic studies on the decomposition of hydrous hydrazine have been performed using mainly heterogeneous catalysts. As a consequence, an overview on unsupported nanoparticles catalytic activity will be provided before to consider supported catalysts.

Singh et al. reported the activity of a series of monometallic nanoparticle (Rh, Co, Ru, Ir, Cu, Ni, Fe, Pt and Pd) as catalyst for hydrazine decomposition. Among those Cu, Ni, Fe and Pt were inactive for the decomposition while the other metals produced gases. However, while Co, Ir

and Ru showed only 7% of selectivity toward hydrogen, Rh nanoparticles were able to achieve 43.8% of selectivity to the desired reaction at 25°C.⁵³

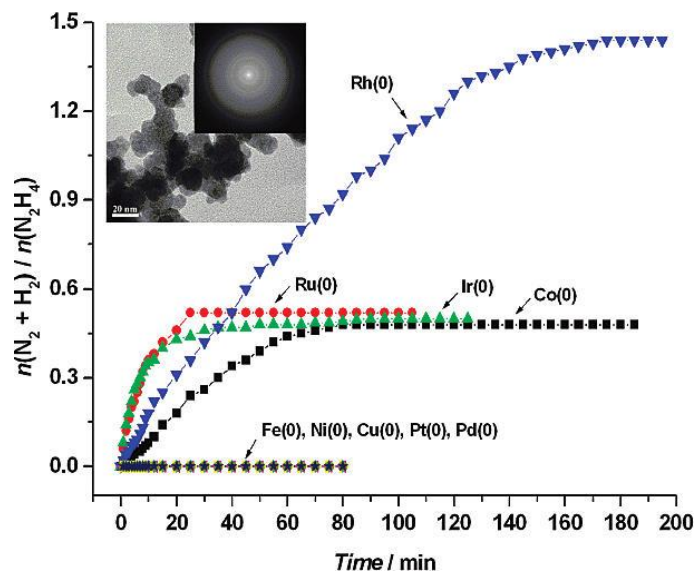


Figure 1.14. Time-dependent plots of hydrazine decomposition in aqueous solutions with different unsupported metal NPs as catalysts (metal/N₂H₄ = 1 : 10) 298 K, that show how Rh reaches highest yields, while Ru, Ir and Co are active, and Fe, Ni, Cu, Pd and Pt are inactive.⁵³

In a later paper Singh et al. have exhibited how Ni nanoparticles are able to decompose hydrous hydrazine increasing the temperature reaching 33% of selectivity to hydrogen at 50 °C.¹⁰² In this case, selectivity and activity increased with the increase of the temperature of the reaction. However, a different tendency was displayed by Rh nanoparticles for which the increase in temperature increased the activity but at the same time decreased the selectivity toward hydrogen, dropping from 43.8% at 25 °C to 34% at 70 °C.⁸⁸ The different behaviour of the two catalysts can be associated to different reaction mechanism¹⁰³ or to a stability problem of Ni nanoparticles which lead to modification of selectivity over time, therefore, the increase in activity due to the temperature preserve for longer during the reaction the most selective morphology of the nanoparticles.

Hydrazine is Brønsted base capable to accept a proton from the water. This interaction, eq. 1.3, with the reaction medium increases the presence in solution of N₂H₅⁺ which, after a first mechanist step of cleavage of the N-N, lead to a preferential formation of NH₃, competing with the deprotonation of hydrazine, Eq. 1.4.¹⁰⁴ For this reason in literature the use of a base as an additive to the reaction medium is often reported to increase the selectivity of the system to hydrogen generation. Moreover, the use of an alkaline solution increases the

basicity of the surface of the catalyst leading to an inhibiting effect on the formation of basic ammonia.¹⁰⁴

A few bimetallic nanoparticle catalysts formed by two noble metals have been tested for this reaction. One example is Ir-Pd alloy nanocages reported by Xia and co-workers, that were able to reach approximately 67% of selectivity toward molecular hydrogen.¹⁰⁵ More often bimetallic nanoparticles are composed by a noble metal, expensive and with higher rates, and a first-row transition metal, cheaper and slower to react but potentially more selective for the production of hydrogen. Rh-Ni nanoparticles have been studied in a series of paper in literature. Singh et al. reported that optimal atomic ratio between Ni:Rh of 4:1, with approximately 3 nm of diameter, is optimal for this bimetallic system reaching 100% selectivity to hydrogen at 25 °C, while at 70 °C more nanoparticles with different ratios achieved 100% selectivity, between atomic ratio of Ni:Rh of 2:8 to 9:1.^{88,106}

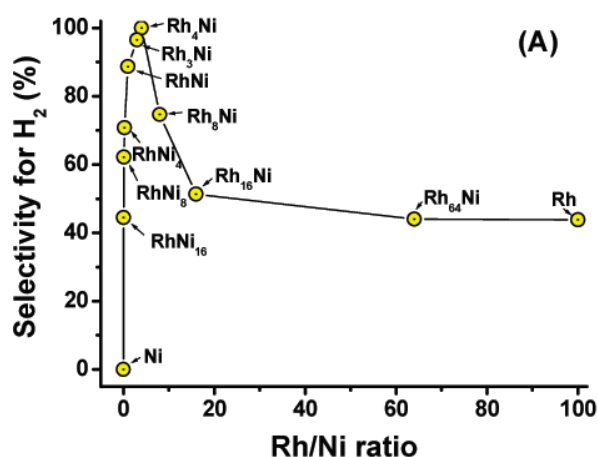


Figure 1.15. Selectivity for hydrogen generation from hydrous hydrazine catalysed by Rh_xNi_y with Rh/N_2H_4 1:10 at 25°C.¹⁰⁶

Another interesting bimetallic system is Ni-Pt which exhibited full conversion and 100% selectivity to hydrogen when the Pt content is between 7-31% of the molar composition of the nanoparticles.¹⁰⁷ In another study the best atomic ratio between the two metals was found to be Ni:Pt of 6:4 atomic ratio, with 1.1 ± 0.3 nm particles size, reaching 100% selectivity to hydrogen and a TOF of 150 h^{-1} .¹⁰⁸ To be noticed that both these metals as monometallic catalysts are reported to be inactive, however when are present as part of alloy bimetallic nanoparticles, they display optimal selectivity and high TOF.

Moreover, in the case of Ni-Pd alloy nanoparticles, with particles size between 2-4 nm, the optimal atomic ratio between the Ni:Pd is reported to be 6:4, like for Ni-Pt, reaching 100% selectivity in the presence of NaOH.¹⁰⁹ Finally, Ir-Ni nanoparticles are reported to have a trend closer to the one reported for RhNi nanoparticles, with 100% selectivity to hydrogen achieved only for low content of Ir, 5-10 mol.%.¹¹⁰

Other bimetallic nanoparticles of first-row transition metals with noble metals, were reported to be less successful than the Ni-based one. For example, CoRh₄ reached only 21.1% selectivity to molecular hydrogen and FeRh₄ reached 30% selectivity.¹⁰⁶ They Ir alternative reported even lower selectivity while no Cu-based catalyst with noble metal was able to perform the decomposition of hydrous hydrazine.

A series of noble metal-free nanoparticles have also been tested for the reaction. In contrast with bimetallic nanoparticles containing noble metals, these nanoparticles are inactive at 25°C, while Ni₁Fe₁, with 10 nm particle size and alloy structure, was able to reach 100% selectivity when the reaction was performed at 70°C. NiCo and NiCu in the same conditions only reached selectivity of 18% and 15% respectively.¹¹¹

Also, the influence of a metal oxide support has been studied over the years. For example, Haung et al. deposited small amount of CeO₂ on Ni nanoparticles which demonstrated the existence of strong metal-support interaction between Ni and CeO₂. CeO₂ presented a ratio Ce⁺³/Ce⁺⁴ of 1.33 indicating a high number of vacancies in the oxide, these vacancies perturb the electronic structure of Ni, therefore, modifying the interaction between nickel and hydrous hydrazine increasing the selectivity to molecular hydrogen to 99%. In the same work, CeO₂ was reported to have the best beneficial effects on the catalytic properties of Ni among other oxides such as La₂O₃, MgO and ZrO₂. All the systems mentioned above are examples of unsupported nanoparticles catalysts, these systems have the advantage of better contact between particles and reagents but are difficult to separate from the reaction mixture, for this reason, supported nanoparticles are usually preferred to the use.¹¹²

Supported monometallic nanoparticles, on the other hand, displayed more limitations to the catalytic performances of the active metals. Noble metals supported nanoparticles are reported to have low selectivity toward hydrogen. As shown by Dai et al, Ir/CeO₂ reported only 7% total selectivity to hydrogen at 50 °C,¹¹³ while only in 2018 Qiu et al. reported a

selectivity of 34% with a high TOF, 8571 h⁻¹, using a low substrate/metal molar ratio and high loading of iridium on the surface, by galvanic replacement with a particle size of approximately 3 nm.¹¹⁴

Ni-based catalysts, instead, displayed low activity requiring a long time to complete the reaction but achieving higher selectivity to hydrogen. Examples of this are Ni/Al₂O₃ or Ni/CeO₂ which reported 93% and 100% selectivity respectively.^{115,116}

More promising are bimetallic Ni-noble metal nanoparticles catalysts. Between the Ir-Ni supported catalysts can be reported Ir_{0.059}Ni/Al₂O₃¹¹⁶ and Ir₁₃Ni₈₇/meso-CeO₂, with a Ni@NiIr structure,¹¹⁴ that reached 99% and 100% selectivity respectively, and the latter had a calculated TOF of 343 h⁻¹. Moreover, also NiPt and NiRh catalysts were reported to be able to reach 100% maintaining a high level of activity, for example, Pt_{0.6}Ni_{0.4}/PDA-rGO 903 h⁻¹.¹¹⁷

Table 1.4. Catalytic data from literature for metal nanoparticles for hydrazine decomposition at mild conditions.

Catalyst	Temperature (°C)	TOF (h ⁻¹)	H ₂ selectivity (%)	Reference
Rh	25	2.5	43.8	53
Ni _{0.95} Ir _{0.05}	25	2.2	100	110
Ni ₈₈ Pt ₁₂ @MIL-101	50	350	100	118
Ni-0.08CeO ₂	30	51.6	99	112
Ir _{0.059} Ni/Al ₂ O ₃	50	n.d.	99	116
Pt _{0.6} Ni _{0.4} /PDA-rGO	30	903	100	117
Ir ₁₃ Ni ₈₇ /meso-CeO ₂	50	343	100	114
Ir/meso-CeO ₂	50	8571	34	114
Ir/CeO ₂	50	n.d.	7	113
Ni ₉₁ Ir ₉ /CeO ₂	50	94	100	113

1.4. Aims of the study

As seen in the literature review many potential candidates for the catalytic decomposition of hydrous hydrazine have been proposed. Nonetheless, large-scale application of this technology is still limited by the cost of the material, the mass of catalysts to be used (since most of the experiment reported substrate/metal ratio <20), selectivity/yield to hydrogen and overall stability.

Thus, the objectives of the following presented studies are:

- Study first the effect of reaction conditions on the activity and selectivity of the catalytic decomposition of hydrous hydrazine to hydrogen. Modifying parameters such as temperature, mass of catalyst, stirring speed and concentration of base, the optimal conditions of reaction, which allow performing the test in kinetically limited regime can be found, (Chapters 3).
- Study the adsorption of hydrous hydrazine molecules on Ir surface from experimental ATR-IR and theoretical calculation by computational studies in order to obtain information about the reaction mechanism and preferential reaction pathway in order to find an optimised structure and maximise selectivity/yield toward hydrogen, (Chapter 3 and 4).
- Synthesis of monometallic Ir-based and Ni-based monometallic supported nanoparticles on different supports in order to identify and understand possible strong metal-support interaction (Chapter 4 and 5).
- Comparison of different preparation methods, such as deposition-precipitation, sol-immobilisation and solid grinding; including different heat-treatment protocols to study the influence of mean particle size of Ir, oxidation state and surface coverage can influence the catalytic performances of monometallic catalysts (Chapter 4 and 5).
- Preparation and optimisation of bimetallic Ir-Ni catalysts to understand the influence on the catalytic performances and identify potential interaction of the two metal through characterisation, (Chapter 6).

1.5. References

- 1 International Energy Agency, Key world energy statistics, <http://svenskvindenergi.org/wp-content/uploads/2017/12/KeyWorld2017.pdf>, (accessed 11 September 2019).
- 2 United Nations, World Population to 2300, <https://www.un.org/en/development/desa/population/publications/pdf/trends/WorldPop2300final.pdf>, (accessed 20 September 2019).
- 3 U.S. Energy Information Administration, International Energy Outlook 2017 Overview, https://www.eia.gov/pressroom/presentations/mead_91417.pdf, (accessed 10 September 2019).
- 4 Carbon Tracker Initiative, Expect the Unexpected: The Disruptive Power Technology,

- <https://www.carbontracker.org/reports/expect-the-unexpected-the-disruptive-power-of-low-carbon-technology/>, (accessed 20 September 2019).
- 5 R. C. Saxena, D. K. Adhikari and H. B. Goyal, *Renew. Sustain. Energy Rev.*, 2009, **13**, 167–178.
 - 6 D. L. Klass, *Energy Policy*, 2003, **31**, 353–367.
 - 7 Y. Ren, G. H. Chia and Z. Gao, *Nano Today*, 2013, **8**, 577–597.
 - 8 A. Ahmed, N. Radenahmad, Q. Cheok, S. Shams, J. H. Kim and A. K. Azad, *Renew. Sustain. Energy Rev.*, 2016, **60**, 822–835.
 - 9 REN21, Renewables 2019 global status report, https://www.ren21.net/wp-content/uploads/2019/05/gsr_2019_full_report_en.pdf, (accessed 19 September 2019).
 - 10 D. G. IAEA, The Fukushima Daiichi Accident, <https://www-pub.iaea.org/MTCD/Publications/PDF/Pub1710-ReportByTheDG-Web.pdf>, (accessed 15 September 2019).
 - 11 M. Fleisher, Recent estimates of the abundances of the elements in this earth's crust, <https://pubs.usgs.gov/circ/1953/0285/report.pdf>, (accessed 20 September 2019).
 - 12 M. Grasemann and G. Laurency, *Energy Environ. Sci.*, 2012, **5**, 8171–8181.
 - 13 S. Sharma and S. Krishna Ghoshal, *Renew. Sustain. Energy Rev.*, 2015, **43**, 1151–1158.
 - 14 J. H. Lee, J. Cho, M. Jeon, M. Ridwan, H. S. Park, S. H. Choi, S. W. Nam, J. Han, T.-H. Lim, H. C. Ham and C. W. Yoon, *J. Mater. Chem. A*, 2016, **4**, 14141.
 - 15 I. Staffell, The Energy and Fuel Data Sheet, https://www.academia.edu/1073990/The_Energy_and_Fuel_Data_Sheet, (accessed 18 September 2019).
 - 16 Y. Demirel, *Energy Production, Conversion, Storage, Conservation, and Coupling*, Springer, 2012.
 - 17 S. Park, J. M. Vohs and R. J. Gorte, *Nature*, 2000, **404**, 265–267.
 - 18 T. N. Veziroglu and S. Sahin, *Energy Convers. Manag.*, 2008, **49**, 1820–1831.
 - 19 K. Kendall and B. G. Pollet, *Hydrogen and Fuel Cells in Transport*, Elsevier Ltd., 2015, vol. 4.
 - 20 J. Larminie and A. Dicks, *Fuel Cell Systems Explained*, 2003.
 - 21 H. Wu, *Appl. Energy*, 2016, **165**, 81–106.
 - 22 A. Ugurlu and S. Oztuna, *Int. J. Hydrogen Energy*, 2015, **40**, 11178–11188.
 - 23 A. Baroutaji, J. G. Carton, M. Sajjia and A. G. Olabi, *Materials in PEM Fuel Cells*, Elsevier Ltd., 2015.
 - 24 W. Stanek, A. Valero and G. Calvo, *Thermodynamics for Sustainable Management of Natural Resources*, Springer, 2017.

- 25 International Energy Agency, Energy Technology Essentials, https://nachhaltigwirtschaften.at/resources/pdf/iea_ete02.pdf?m=1469658531, (accessed 10 September 2019).
- 26 J. R. Rostrup-Nielsen, in *Handbook of Heterogeneous Catalysis*, Wiley-VCH, Weinheim, 2008, pp. 2882–2905.
- 27 K. O. Hinrichsen, K. Kochloefl and M. Muhler, *Water Gas Shift and CO₂ Removal*, 2004.
- 28 C. M. Kalamaras and A. M. Efstathiou, *Conf. Pap. Energy*, 2013, **2013**, 9.
- 29 S. Kim, Y. Kim, Y. Lim, M. Kim and H. Hahm, *Korean J. Chem. Eng.*, 2003, **20**, 1023–1025.
- 30 S. Sengodan, R. Lan, J. Humphreys, D. Du, W. Xu, H. Wang and S. Tao, *Renew. Sustain. Energy Rev.*, 2018, **82**, 761–780.
- 31 J. R. R. Nielsen, *Catal. Rev.*, 2004, **46**, 247–270.
- 32 L. R. Radovic, in *Handbook of Heterogeneous Catalysis*, Wiley-VCH, Weinheim, 2008, pp. 3037–3045.
- 33 F. Sanchez, D. Motta and N. Dimitratos, *Appl Petrochem Res*, 2016, **6**, 269–277.
- 34 W. L. Holstein and M. Boudart, *Fuel*, 1983, **62**, 162–165.
- 35 W. D. McKee, *Fuel*, 1983, **62**, 170–175.
- 36 S. Sampath, N. K. Kulkarni, M. S. Subramanian and N. C. Jayadevan, *Carbon N. Y.*, 1988, **26**, 126–137.
- 37 L. Zhu, L. Li, Z. Zhang, H. Chen, L. Zhang and F. Wang, *Chem. Eng. Technol.*, 2016, **39**, 1912–1920.
- 38 E. Zoulias, E. Varkaraki, N. Lymberopoulos, C. N. Christodoulou and G. N. Karagiorgis, *TCJST*, 2004, **4**, 41–71.
- 39 US Pat., US 2017/0088959 A1, 2017, 1–5.
- 40 S. Z. Baykara, *Int. J. Hydrogen Energy*, 2005, **30**, 545–553.
- 41 A. Züttel, *Mater. Today*, 2003, 24–33.
- 42 P. E. Dodds and S. Demoullin, *Int. J. Hydrogen Energy*, 2013, **8**, 7189.
- 43 K. Takahashi, *Encycl. Life Support Syst.*, 2000.
- 44 Z. Yang, Y. Xia and R. Mokaya, *J. Am. Chem. Soc.*, 2007, **129**, 1673–1679.
- 45 V. Meregalli and M. Parrinello, *Appl. Phys. A Mater. Sci. Process.*, 2001, **146**, 143–146.
- 46 H. Dai, B. Xia, L. Wen, C. Du, J. Su, W. Luo and G. Cheng, *Appl. Catal. B, Environ.*, 2015, **165**, 57–62.
- 47 H. Furukawa and O. M. Yaghi, *J. Am. Chem. Soc.*, 2009, **131**, 8875–8883.
- 48 J. Graetz, *Chem. Soc. Rev.*, 2009, **38**, 73–82.

- 49 W. Grochala and P. P. Edwards, *Chem. Rev.*, 2004, **104**, 1283–1315.
- 50 M. Yadav and Q. Xu, *Energy Environ. Sci.*, 2012, 9698–9725.
- 51 A. Iulianelli, P. Ribeirinha, A. Mendes and A. Basile, *Renew. Sustain. Energy Rev.*, 2014, **29**, 355–368.
- 52 F. Sanchez, D. Motta, L. Bocelli, S. Albonetti, A. Roldan, C. Hammond, A. Villa and N. Dimitratos, *J. Carbon Res.*, 2018, **4**, 26.
- 53 S. K. Singh, X. Zhang and Q. Xu, 2009, **131**, 9894–9895.
- 54 J. Shen, L. Yang, K. Hu, W. Luo and G. Cheng, *Int. J. Hydrogen Energy*, 2015, **40**, 1062–1070.
- 55 M. McNaught and A. Wilkinson, *IUPAC. Compendium of Chemical Terminology*, Blackwell Scientific Publications, Oxford, 2nd edn., 2014.
- 56 G. C. Bond, *Heterogeneous Catalysis: Principles and Applications.*, Oxford University Press, 2nd edn., 1987.
- 57 I. Chorkendorff and J. W. Niemantsverdriet, *Concepts of Modern Catalysis and Kinetics*, Wiley, Weinheim, 2005.
- 58 P. W. N. M. van Leeuwen, *Homogeneous Catalysis Understanding the Art*, Springer Netherlands, 1st edn., 2004.
- 59 B. Cornils and W. A. Herrmann, *J. Catal.*, 2003, **216**, 23–31.
- 60 O. Deutschmann, H. Knozinger, K. Kochloefl and T. Turek, *Heterogeneous Catalysis and Solid Catalysts*, Wiley-VCH, Weinheim, 2009.
- 61 W. M. H. Sachtler and R. Jongepier, *J. Catal.*, 1965, **4**, 665–671.
- 62 C. Della Pina, E. Falletta, L. Prati and M. Rossi, *Chem. Soc. Rev.*, 2008, **37**, 2077–2095.
- 63 A. Roucoux and H. Patin, *Chem. Rev.*, 2002, **102**, 3757–3778.
- 64 M. C. Daniel and D. Astruc, *Chem. Rev.*, 2004, **104**, 293–346.
- 65 M. Sankar, N. Dimitratos, P. J. Miedziak, P. P. Wells, C. J. Kiely and G. J. Hutchings, *Chem. Soc. Rev.*, 2012, 8099–8139.
- 66 L. Prati and A. Villa, *Acc. Chem. Res.*, 2014, **47**, 855–863.
- 67 M. Brust, M. Walker, D. Bethell, D. J. Schiffrin and R. Whyman, *J. Chem. Soc.*, 1994, 801–802.
- 68 N. Dimitratos, A. Villa, L. Prati, C. Hammond, C. E. Chan-thaw, J. Cookson and P. T. Bishop, *Appl. Catal. A Gen.*, 2016, **514**, 267–275.
- 69 S. M. Rogers, C. R. A. Catlow, C. E. Chan-thaw, D. Gianolio, E. K. Gibson, A. L. Gould, N. Jian, A. J. Logsdail, R. E. Palmer, L. Prati, N. Dimitratos, A. Villa and P. P. Wells, *ACS Catal.*, 2015, **5**, 4377–4384.
- 70 S. M. Rogers, C. R. A. Catlow, C. E. Chan-thaw, A. Chutia, N. Jian, R. E. Palmer, M.

- Perdjon, A. Thetford, N. Dimitratos, A. Villa and P. P. Wells, *ACS Catal.*, 2017, **7**, 2266–2274.
- 71 N. Dimitratos, C. Hammond, C. J. Kiely and G. J. Hutchings, *Appl Petrochem. Res.*, 2014, **4**, 85–94.
- 72 E. J. Roberts, S. E. Habas, L. Wang, D. A. Ruddy, E. A. White, F. G. Baddour, M. B. Gri, J. A. Schaidle, N. Malmstadt and R. L. Brutchey, *ACS Sustain. Chem. Eng.*, 2017, **5**, 632–639.
- 73 C.-J. Jia and F. Schuth, *Phys. Chem. Chem. Phys.*, 2011, **13**, 2457–2487.
- 74 P. Zhao, N. Li and D. Astruc, *Coord. Chem. Rev.*, 2013, **257**, 638–665.
- 75 M. Mitchnick, *Drug Dev. Serv. Tech. Br.*, 2009.
- 76 Z. Wei, J. Sun, Y. Li, K. Datye and Y. Wang, *Chem. Soc. Rev.*, 2012, **41**, 7994–8008.
- 77 L. Prati and A. Villa, *Catalysts*, 2012, **2**, 24–37.
- 78 A. Villa, D. Wang, G. M. Veith, F. Vindigni and L. Prati, *Catal. Sci. Technol.*, 2013, **3**, 3036–3041.
- 79 R. Zanella, L. Delannoy and C. Louis, *Appl. Catal. A Gen.*, 2005, **291**, 62–72.
- 80 P. Burattin, M. Che and C. Louis, *J. Phys. Chem. A*, 1998, **102**, 2722–2732.
- 81 D. Mori and K. Hirose, *Int. J. Hydrogen Energy*, 2009, **34**, 4569–4574.
- 82 M. Felderhoff, F. Schu and B. Bogdanovic, 2004, 2249–2258.
- 83 U. S. D. of Energy, DOE Technical targets for onboard hydrogen storage for light duty vehicles, <https://www.energy.gov/eere/fuelcells/doe-technical-targets-onboard-hydrogen-storage-light-duty-vehicles>, (accessed 12 September 2019).
- 84 M. Yadav and Q. Xu, *Energy Environ. Sci.*, 2012, **5**, 9698–9725.
- 85 U. B. Demirci and P. Miele, *Energy Environ. Sci.*, 2011, **4**, 3334–3341.
- 86 M. Trincado, D. Banerjee and H. Grutzmacher, *Energy Environ. Sci.*, 2014, **7**, 2464–2503.
- 87 K. Huang and J. Eppinger, *ACS Energy Lett.*, 2017, **2**, 188–195.
- 88 A. K. Singh, M. Yadav, K. Aranishi and Q. Xu, *Int. J. Hydrog. Energy*, 2012, **37**, 18915–18919.
- 89 Z. Wang, I. Tonks, J. Belli and C. M. Jensen, *J. Organomet. Chem.*, 2009, **694**, 2854–2857.
- 90 S. C. Amendola, S. L. Sharp-Goldman, M. S. Janjua, M. T. Kelly, P. J. Petillo and M. Binder, *J. Power Sources*, 2000, **85**, 186–189.
- 91 M. Nielsen, E. Alberico, W. Baumann, H. Drexler, H. Junge, S. Gladiali and M. Beller, *Nature*, 2013, **495**, 85–89.
- 92 L.-C. Yang, T. Ishida, T. Yamakawa and S. Shinoda, *J. Mol. Catal. A Chem.*, 1996, **108**, 87–93.

- 93 H. B. Charman, *J. Chem. Soc.*, 1970, 584.
- 94 M. Nielsen, A. Kammer, D. Cozzula, H. Junge, S. Gladiali and M. Beller, *Angew. Chemie - Int. Ed.*, 2011, **50**, 9593–9597.
- 95 A. K. Hill and L. Torrente-Murciano, *Appl. Catal. B Environ.*, 2015, **172–173**, 129–135.
- 96 V. Prasad and M. S. Vasanthkumar, *J. Nanoparticle Res.*, 2015, **17**, 398.
- 97 H. Hayashi, *Res. Chem. Intermed.*, 1998, **24**, 183–196.
- 98 S. Fukuzumi, *Joule*, 2017, **1**, 689–738.
- 99 R. Lan, J. T. S. Irvine and S. Tao, *Sci. Rep.*, 2013, **3**, 1–7.
- 100 E. W. Schmidt, *Hydrazine and Its Derivatives: Preparation, Properties, Applications*, Wiley-Interscience, 2nd edn., 1984.
- 101 B. Zhao, J. Song, R. Ran and Z. Shao, *Int. J. Hydrogen Energy*, 2012, **37**, 1133–1139.
- 102 S. K. Singh, Z. H. Lu and Q. Xu, *Eur. J. Inorg. Chem.*, 2011, **2011**, 2232–2237.
- 103 Y. Cheng and H. Xu, *Sustain. Energy Fuels*, 2019, **3**, 343–365.
- 104 S. K. Singh, A. K. Singh, K. Aranishi and Q. Xu, *J. Am. Chem. Soc.*, 2011, **113**, 19638–19641.
- 105 M. Liu, Y. Zheng, S. Xie, N. Li, N. Lu, J. Wang, M. J. Kim, L. Guo and Y. Xia, *Phys. Chem. Chem. Phys.*, 2013, **15**, 11822–11829.
- 106 S. K. Singh and Q. Xu, *J. Am. Chem. Soc.*, 2009, **131**, 18032–18033.
- 107 S. K. Singh and Q. Xu, *Inorg. Chem.*, 2010, **49**, 6148–6152.
- 108 A. K. Singh and Q. Xu, *Int. J. Hydrogen Energy*, 2014, **39**, 9128–9134.
- 109 D. Bhattacharjee, K. Mandal and S. Dasgupta, *J. Power Sources*, 2015, **287**, 96–99.
- 110 S. K. Singh and Q. Xu, *Chem. Commun.*, 2010, **46**, 6545–6547.
- 111 S. K. Singh, A. K. Singh, K. Aranishi and Q. Xu, *J. Am. Chem. Soc.*, 2011, **133**, 19638–19641.
- 112 L. He, B. Liang, L. Li, X. Yang, Y. Huang, A. Wang, X. Wang and T. Zhang, *ACS Catal.*, 2015, **5**, 1623–1628.
- 113 H. Dai, Y. Zhong and P. Wang, *Prog. Nat. Sci. Mater. Int.*, 2017, **27**, 121–125.
- 114 Y. Qiu, H. Yin, H. Dai, L. Gan, H. Dai, P. Wang, A. Y. Qiu, H. Yin, H. H. Dai, L. Gan and H. H. Dai, *Chem. Eur. J.*, 2018, **24**, 4902–4908.
- 115 L. He, Y. Huang, A. Wang, X. Wang, X. Chen, J. J. Delgado and T. Zhang, *Angew. Chemie Int. Ed.*, 2012, **51**, 6191–6194.
- 116 L. He, Y. Huang, X. Y. Liu, L. Li, A. Wang, X. Wang, C. Y. Mou and T. Zhang, *Appl. Catal. B Environ.*, 2014, **147**, 779–788.

- 117 F. Song, Q. Zhu and Q. Xu, *J. Mater. Chem. A Mater. Energy Sustain.*, 2015, **3**, 23090–23094.
- 118 N. Cao, J. Su, W. Luo and G. Cheng, *Int. J. Hydrogen Energy*, 2014, **39**, 9726–9734.

2. Experimental

2.1. Introduction

In this chapter, the materials and experimental methods used during the preparation methods and the evaluation of catalytic performance the catalysts are reported. Descriptions of the experimental procedures used and of the principles on which the characterisation techniques used to carry out this thesis work, are also reported in this chapter.

Hereafter are reported abbreviations, equations and material used throughout this Thesis.

2.1.1. Abbreviations

DP: deposition-precipitation

Sol-imm.: sol-immobilisation

THPC: tetrakis(hydroxymethyl)phosphonium chloride

PVA: poly(vinyl)alcohol

EDS: energy disperse (X-ray) spectroscopy

SEM: scanning electron microscopy

TEM: transmission electron microscopy

XPS: X-ray photoelectron spectroscopy

p-XRD: powder X-ray diffraction

TOF: Turnover frequency

FWHM: Full Width at Half Maximum

2.1.2. Equations

Here are reported some basic mathematical formulas and equations used during this thesis:

•Conversion

$$X_{substrate} = \frac{m_{substrate\ initial} - m_{substrate\ final}}{m_{substrate\ initial}} \quad (Eq. 2.1)$$

- Turnover frequency number (TOF)

$$TOF = \frac{n_{\text{substrate initial}} - n_{\text{substrate at time}}}{n_{\text{metal}} \cdot \text{time}} \quad (\text{Eq. 2.2})$$

- Ideal gas law

$$PV = nRT \quad (\text{Eq. 2.3})$$

- metal loading of catalysts

$$\text{metal loading \%} = \frac{m_{\text{metal}}}{m_{\text{metal}} + m_{\text{support}}} \cdot 100 \quad (\text{Eq. 2.4})$$

TOF defines the number of moles of substrate converted over time by moles of active site. Over the years, this value has been largely used to quantify the rate of the reaction catalysed and derives from biological studies. The use of turnover frequency also in heterogeneous catalysis is commonly accepted as a fast way to quantify the rate of reaction and compare the catalytic performances of materials with good approximation in well-defined conditions.¹ Nonetheless, many critiques can be done to the use of TOF in heterogeneous catalysis such as the fact that it is a function of the condition used, especially temperature and concentration of the reagents. The dependency of TOF from the concentrations leads to another critical aspect of its use, its dependency from the instantaneous conditions since during the reaction the substrate is consumed, not necessarily linearly, therefore TOF calculated as derivative of the turnover over time to reduce the averaging of the value over long period of time.² Moreover, in heterogeneous catalysis the number of active sites, in most of the cases, is not easily quantifiable since not all the metal used, for example for bulk metal or nanoparticles, is exposed to the reagent as surface atoms, likewise, not all the superficial metal atoms on a nanoparticles are active or have the activity since the catalytic proprieties can be linked to specific facet of a metal or edge atoms.^{2,3} The difficulties to quantify over time the species in solution over time during this project and the linearity of conversion of the substrate in the first part of the reaction (until 50% of the total conversion approximately) allowed to use TOF in this thesis work with a good degree of approximation maintaining constant the parameter of reaction.

Other equations are presented through the thesis where a deeper discussion and analysis are required for the explanation.

2.1.3. Reagents

Table 2.1. list of chemicals used throughout the thesis.

Name	Formula	Company (catalogue n°)	Purity	Use
Cerium (IV) oxide	CeO ₂	Sigma-Aldrich (544841)	N.d.	Catalysts support
Titanium (IV) oxide	TiO ₂ (aeroxide,P25)	Fisher Scientific (10646903)	≥99.5%	Catalysts support
Aluminium (III) oxide, gamma-phase	γ-Al ₂ O ₃	Alfa-Aesar (1344-28-1)	99.9%	Catalysts support
Magnesium aluminate, spinel	MgAl ₂ O ₃	Sigma-Aldrich (635073)	99.99%	Catalysts support
Dihydrogen hexachloroiridate	K ₂ IrCl ₆	Alfa-Aesar (11031)	99%	Metal precursor
Iridium (III) acetylacetonate	Ir(CH ₃ COCH ₂ COCH ₃) ₃	Sigma-Aldrich (333352)	97%	Metal precursor
Nickel (II) chloride	NiCl ₂	Alfa-Aesar (7718-54-9)	98%	Metal precursor
THPC solution	(HOCH ₂) ₄ PCI	Sigma-Aldrich (404861)	80% in H ₂ O	Reducing agent
Sodium borohydride	NaBH ₄	Sigma-Aldrich (480886)	99.99 %	Reducing agent
Sulphuric acid	H ₂ SO ₄	Sigma-Aldrich (258105)	95 – 98 %	pH corrector
Sodium hydroxide, pellet	NaOH	Fisher Scientific (1310-73-2)	≥97%	pH corrector
Urea	(NH ₂) ₂ CO	Sigma-Aldrich (U1250)	≥99.5%	pH corrector
Hydrazine monohydrate	N ₂ H ₄ · H ₂ O	Sigma-Aldrich (207942)'	98%	Reagent
Hydrazine-¹⁵N monohydrate	¹⁵ N ₂ H ₄ · H ₂ O	Sigma-Aldrich (492787)	98%	Reagent
Ethanol	CH ₃ CH ₂ OH	Fisher Scientific (13225483)	99.9%	Solvent

Hydrochloric acid	HCl	Sigma-Aldrich (7647010)	37%	pH corrector
4-(Dimethylamino) benzaldehyde	(CH ₃) ₂ NC ₆ H ₄ CHO	Sigma-Aldrich (156477)	99%	Reagent

2.2. Preparation of Supported Metal Nanoparticles

The catalytic performances of supported metal nanoparticles are influenced by the morphology and structure of the nanoparticles themselves, which in turn are related to the preparation methods utilised for the synthesis of the catalyst. The catalysts tested have to be reliable, therefore, the reproducibility of the method used, is of great importance. Throughout the thesis, three main preparation methods have been used: sol-immobilisation, deposition-precipitation and solid-state grinding.

2.2.1. Colloidal methods

In Chapter 1, it has been explained and discussed how the preparation of colloidal metal solutions allow to (I) control mean metal particle size and particle size distribution and (II) the morphology of the supported nanoparticles on the final catalysts. The colloidal methods tend to follow straightforward procedures, but in literature are reported many detailed studies on the relationship between the conditions used during the preparation method and the colloidal metal nanoparticles formed.⁴⁻¹¹ The colloidal method in principle, consists in the dissolution of a metal precursor salt in a solvent, either water or organic, and when reduced by a reducing agent (mild or strong reducing agent), like H₂ or NaBH₄, in the presence of a stabilising agent, electrostatic and/or steric, like PVA, THPC, citrate. The use of stabiliser is essential in order to avoid nanoparticle agglomeration and collapse of the metal nanoparticles in the solution. The colloidal metal nanoparticle solution is then immobilised on the support, usually by varying the pH of the colloidal metal nanoparticle solution and the support added, in order to increase the interaction between the preformed metal nanoparticles and the surface of the chosen support.

2.2.1.1. Sol-immobilisation with tetrakis(hydroxymethyl)phosphonium chloride (THPC)

Sol-immobilisation with THPC is a particular type of colloidal method in which the reducing agent acts also as a stabiliser.⁴ In fact, THPC in basic solution decomposes following the reaction pathways shown in the scheme in Figure 2.1. THPC in alkaline solution loses one of the hydroxymethyl group, that turns into formaldehyde, and reduces the P centre from P^V to P^{III}. P(CH₂OH)₃ then re-oxidises to tetrakis(hydroxymethyl)phosphonium oxide, THPO, using the oxygen from H₂O, in the process H₂ is formed. Both formaldehyde and H₂ can reduce the metal precursor to form metal nanoparticles.¹² The stabilisation of the nanoparticles is related to the adsorption of THPO on the surface (as a positive charge phosphonium centre) and it is balanced by chloride ions. This concentration of charges near the surface acts as an electrostatic barrier avoiding the contact between the nanoparticles in solution and it can be removed partially or completely, by washing the immobilised catalyst. In this way, the surface of the metal nanoparticles produced is more accessible to the reagent than when steric stabilisers are used.⁶

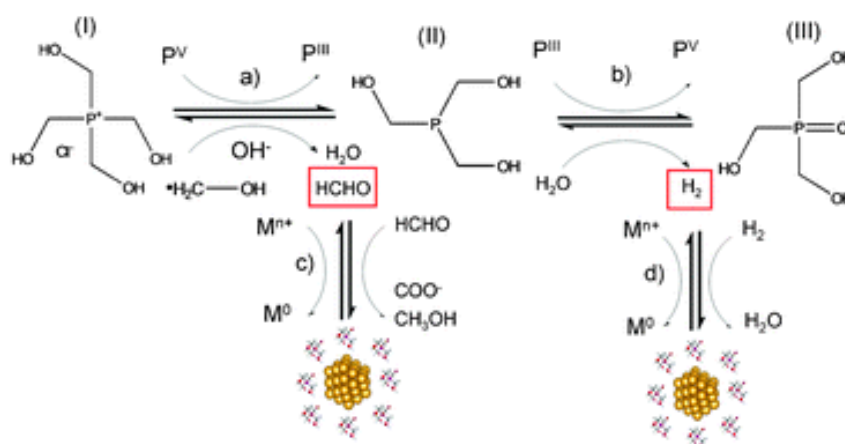


Figure 2.1. Scheme of reduction of metal for the production of nanoparticles by THPC.¹²

Figure 2.2 displays the experimental procedure followed for the preparation of the catalysts by sol-immobilisation. Typically, for the sol-immobilisation method with THPC the following experimental procedure was followed: in a 100 mL beaker deionised water was added with the final volume of 50 mL after the initial addition of reagents for the preparation of the colloidal metal solution, as shown in Table 2.2. Then, under stirring (750 rpm), a volume of 0.0675 M THPC, calculated in order to have metal:THPC molar ratio of 3:4, was added to the

aqueous solution with 0.2 M NaOH with a volume ratio of NaOH/THPC of 1.5. After the addition of THPC to the alkaline solution, the metal precursor solution was added and then left to react under continuous stirring for 30 minutes to achieve the complete reduction of the metal precursor. The reduction of the metal precursor to metal nanoparticles is accompanied by a modification of the absorption spectra in the UV/vis region which can be analysed and monitored by UV/vis spectroscopy. Therefore, after 25 minutes from the addition of the metal precursor, a UV spectrum was recorded in order to check the state of chemical reduction of the metal before the immobilisation.



Figure 2.2. Schematic representation of sol-immobilisation with THPC for Ir catalysts used in this thesis.

Immobilisation was then performed by adding the support, (for 1 g of 1 wt. % the mass of the support is 0.99g), to the colloidal metal solution under stirring. Depending on the support (point of zero charge of support) used an acidification step may be required. In case acidification is needed, 1-1.5 mL of H₂SO₄ concentrated, 98%, was added in order to decrease the pH of the slurry dispersion to a value of 2. The dispersion was left under stirring for 1 h before it was filtrated and washed, with 1 L of deionised water in order to remove the residues of the reduction reaction. Finally, the filter was collected and dried in an oven at 90°C overnight and the filtrated solution was collected for analysis with ICP-MS.

Bimetallic Ir-Ni catalysts were also prepared by this method. The standard procedure for bimetallic catalysts followed the same steps as the experimental procedure for the monometallic Ir catalysts, using an aqueous solution containing both the desired precursor salts. This method should favour the contemporaneous reduction of both metals, leading, if possible, to the formation of alloy metal nanoparticles. The two-step reduction, instead, used two separate metal precursor solutions which are reduced in two phases. First, one of the metals was reduced using a specific volume of THPC solution and NaOH solution proportionate to the moles of the first metal used; after 30 minutes of stirring and the confirmation of the first metal reduction, an additional amount of the same reducing agent and the second metal precursor were then added. The principle of the method is that the

second metal uses the metal nanoparticles already formed in the first colloidal metal solution as a nucleation preferential site leading to the formation of nanoparticles of the second metal on the surface of the preformed colloidal metal nanoparticles. Therefore, the possibility to partially or fully covering the surface of the initial solution of metal nanoparticles and creating core-shell structures could be achieved. Finally, the two-step immobilisation procedure consisted of two separated sol-immobilisation procedures of the same methodology. During each preparation method, a monometallic colloidal metal solution was produced and then immobilised onto the support. The immobilisation of the first metal colloid was done on a bare support like in the normal methodology discussed. However, the immobilisation of the second metal colloid was carried out on the previously produced supported metal catalyst. This procedure can produce structures like bimetallic alloy nanoparticles, core-shell structure and segregated monometallic.

Table 2.2. Volume of precursor solutions and reducing agent used during the preparation of 1 wt. % supported metal nanoparticles. $[H_2IrCl_6] = 3.25 \text{ mg/dm}^3$, $[NiCl_2] = 9.73 \text{ mg/dm}^3$ and $[THPC] = 0.0675 \text{ M}$.

Catalysts	Ir loading (wt.%)	Ni loading (wt.%)	Volume of THPC used (cm^3)	Volume of Ir precursor used ($\text{cm}^3/\text{g}_{\text{cat}}$)	Volume of Ni precursor used ($\text{cm}^3/\text{g}_{\text{cat}}$)
Ir/support	1.0	-	1.02	3.08	-
Ni/ support	-	1.0	3.36	-	1.03
Ir₉Ni₁/ support	0.97	0.03	1.10	2.98	0.03
Ir₃Ni₁/ support	0.91	0.09	1.24	2.79	0.09
Ir₁Ni₁/ support	0.76	0.24	1.575	2.36	0.24
Ir₁Ni_{3.3}/ support	0.5	0.5	2.19	1.54	0.51
Ir₁Ni₉/ support	0.27	0.73	2.74	0.81	0.75

2.2.2. Deposition-precipitation methods

Deposition-precipitation methods consist of the precipitation of metal oxide particles by the use of a precipitating agent followed by a heat treatment step to form metallic or oxide forms of metal nanoparticles, depending on the choice of gas (H_2 /air) and temperature during heat treatment. In particular, the precursor salt in solution at higher pH form hydroxide species

that interacting with the oxo- and hydroxy- species on the surface of the support, leading the precipitation of the metal hydroxide on the surface.¹³ Due to the possible electrostatic repulsion between the hydroxy- species that prevent the aggregation or the deposition on the negatively charged surface. Deposition-precipitation methods tend to follow simple and practical manufacture procedure and, therefore, are commonly used for industrial applications. Nonetheless, these methods are sensitive to the small variation of pH and ions concentration both in terms of final loading of metal and mean particle size.^{4,14-16} For this reason, these methods tend to be more difficult to reproduce than others.

2.2.2.1. Deposition-precipitation with NaOH

This method follows a simple preparation procedure. Firstly, in a 100 mL beaker, 50 mL of water and the support are added and stirred. The dispersion of the support in water is then treated with a NaOH solution of 0.1 M dropwise until the desired pH is reached, in this project usually 10. When the pH of the dispersion is stable, the metal precursor is added. The pH is adjusted to 10 by adding NaOH aqueous solution dropwise and it is kept constant at that value, for the time necessary for the full theoretical deposition in this thesis the duration was 8 hours. This method is sensitive to parameters like the variation of pH kept during the experimental procedure and the use of different precipitation agents, such as KOH and Na_2CO_3 . Therefore, continuous control has to be maintained during the preparation of the catalysts, in order to maintain the same $\text{M}(\text{OH})_x\text{Cl}_y$ throughout the preparation. In the case of Ir this method was not able to deposit all the metal used as a precursor, therefore, deposition-precipitation with urea was used to achieve better deposition.⁴

The catalyst was then filtered, dried in an oven at 80 °C and finally reduced at high-temperature to obtain metallic nanoparticles.



Figure 2.3. Schematic representation of the deposition-precipitation method with NaOH for Ir catalysts used in this thesis, particular importance is covered by the reaction under stirring at controlled pH.

2.2.2.2. Deposition-precipitation with Urea

Deposition-precipitation with urea follows the same principles of the DP with NaOH, but the method is modified since in this case the precipitation agent is slowly produced through the preparation, this method allows to deposit higher amount of active metal compared with other DP methods. First, the support was added with the salt precursor to 400 mL of deionised water and then the dispersion was heated to 80°C and kept at that temperature, as shown in Figure 2.4. When the temperature was constant the desired amount of urea was then added and left to react for 3 hours after pH 7 was finally reached. Urea in acidic solution hydrolyses producing ammonia that gradually raises the pH to a value of 7 and acts as a precipitation agent, as illustrated in Eq. 2.5. The catalyst was then filtered and dried in an oven at 80°C. In order to remove ammonium by-products of the hydrolysis of urea the material needed to be calcined before the reduction in H₂ at high temperature.

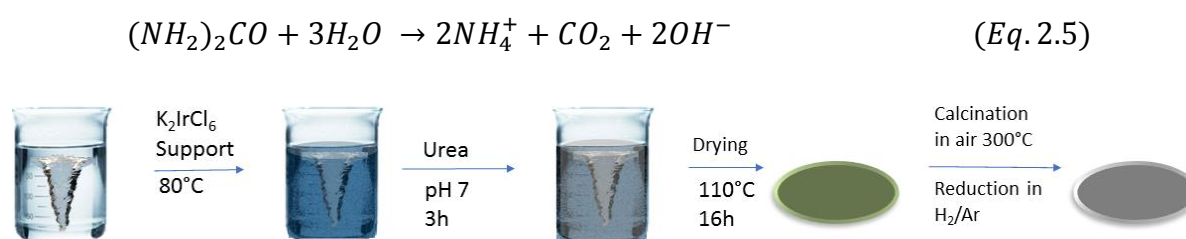


Figure 2.4. Schematic representation of deposition-precipitation with urea for Ir catalysts used in this thesis, particular importance is covered by the reaction under stirring at controlled pH.

2.2.3. Solid-State grinding

Solid-state grinding is a dry preparation technique since it does not require the use of any solvents.⁴ Typically, 0.99 g of support required was added in a mortar and it was ground manually for 30 minutes using 26.6mg of Ir(acac)₃. The solid mixture, without a mesh selection, was then calcined in order to decompose the organic counter-ion of the Ir precursor, acetylacetonate. The material was then reduced at 600°C to obtain metallic Ir particles.

2.2.4. Heat Treatment Protocols

The catalysts prepared by the aforementioned methods need high-temperature treatment in order to be activated and produce metal nanoparticles. Two heat treatment procedures have been followed: (I) calcination and (II) reduction. The heat treatments, when necessary, were performed in a horizontal furnace, equipped with a quartz tube, capable to reach

temperatures as high as 800°C using a calcination boat in ceramic to contain the catalyst powder during the treatment. Calcination was performed under a flow of air, 120 mL min⁻¹, with a temperature increase of 10°C/min until a heat-treatment temperature of 300°C, or 400°C and 500°C to be reached. The chosen temperatures were chosen in order to vary and study the effect of the growth of the nanoparticles and activate metal-support interaction. After reaching the final heat-treatment temperature the sample was kept at the desired temperature for 3 h. The furnace was then let to cool down to room temperature without external aids. Similar parameters were used for the reduction, but instead air a 10% H₂ in Ar flowed, 70-80 mL min⁻¹, in the furnace during the heat treatment. Particular attention was focused on the removal of the sample since if the temperature of the material was still high the surface of the catalyst can then be easily re-oxidised by the atmospheric air outside the furnace when the calcination boat is extracted. Therefore, the sample as left in reducing gas flow until a temperature near to ambient was reached in the furnace.

2.3. Catalytic testing

The typical catalytic tests were performed in a sealed batch reactor, Figure 2.5 and Figure 2.6. The decomposition of hydrous hydrazine was followed either by the volume of gas produced and then collected or by the pressure changes inside a completely sealed reactor. Batch reactions were performed to obtain kinetics data in an accurate and reproducible way.

2.3.1. Volumetric quantification

The main catalytic test protocol used in this thesis is the decomposition of hydrous hydrazine in sealed batch reactor and quantification by volumetric water displacement.

The set-up, that is displayed in Figure 2.5, is composed by a single-neck sealed cap round bottom flask used as reactor. The typical experimental protocol for the reaction was the following: The weighted mass of the desired catalyst was added in the reactor with 8 mL of a NaOH solution in water and a magnetic stirrer bar. The reactor is placed in an oil bath on a magnetic stirring hot plate, which was set to reach a chosen temperature. The temperature of reaction varied, throughout this thesis, between 30°C and 70°C, and the magnetic stirring was initiated. While the reactor was warming the valve on the lid was kept closed to avoid evaporation of the aqueous solution. When the reaction temperature was reached and was stable the magnetic stirrer was shortly stopped to allow the addition of 0.3 mL of 3.3 M

hydrous hydrazine solution. Then, the system was purged with N_2 gas in order to eliminate O_2 and, therefore, maintain the gas mixture outside the explosion limits of H_2 . The valve on the lid of the reactor was then connected via flexible tubes to a washing bottle filled with 1 M HCl solution and, after, to a burette filled with water where the gasses can be collected. Parameters like temperature of the reaction, stirring rate, mass of catalyst and concentration of NaOH have been optimised for the reaction and results are presented in Chapter 3.

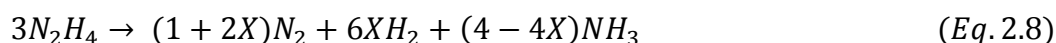


Figure 2.5. Photograph of the reaction set-up used for the volumetric quantification of hydrous hydrazine decomposition.

Once the lid is connected to the gas collection system, the valve on the lid was open and the stirring was initiated again in order to start the reaction. The acid washing bottle was used to trap possible ammonia generated during the decomposition and evaporated so that the volume read from the displacement is related only to H_2 and N_2 . The volume of gas produced was quantified using a burette filled with water and rotated upside-down in a beaker filled with water. When the gas is collected in the burette, it displaces the water, therefore from the variation in the position of the meniscus in the burette the total volume of gas produced can be quantified. From the volume of gas produced using the ideal gas law, as shown in Eq. 2.3, it is possible to calculate the moles of H_2 and N_2 . Van der Waals corrections have been tried too, but these corrections did not vary significantly the number of moles calculated at the working condition of the set up. The reaction was then performed more than once in

order to guarantee the reproducibility of the reaction. At the end of the reaction, the remaining hydrous hydrazine in solution was quantified by colourimetric method, as it is presented in Section 2.3.3.

The yield of the reaction was then calculated by a formula derived from the two stoichiometric reactions, Eq. 2.6-2.8.



Where X is the selectivity of the reaction to hydrogen, with a value of 1 for complete decomposition to hydrogen. Since ammonia, if produced, is trapped using the washing bottle filled acid and the moles N₂ and H₂ have to be considered as moles of total gas, since it is not possible to distinguish the moles of the two gasses from the volume collected, Eq. 2.10, the moles of gas are quantified and, therefore, ammonia is then removed from the equation, Eq. 2.9.



Later calculating the moles of gas produced, n(H₂+N₂), from the moles of hydrazine consumed, n(N₂H₄).

$$\frac{n(N_2H_4)}{3} = \frac{n(H_2 + N_2)}{(1 + 8X)} \quad (Eq. 2.11)$$

$$(1 + 8X) = 3 \frac{n(H_2 + N_2)}{n(N_2H_4)} \quad (Eq. 2.12)$$

When decomposition is completed, the n(H₂+N₂)/n(N₂H₄) parameter reaches a value of 1/3, in case of complete decomposition to ammonia (X = 0), and 3, in case of complete decomposition to hydrogen (X = 1), as it can be calculated from Eq. 2.10. At the same time, the selectivity to hydrogen, X, at full conversion is equivalent to the value of the yield to hydrogen, γ .¹⁷

$$Y = \frac{3 \frac{n(H_2 + N_2)}{n(N_2H_4)} - 1}{8} \quad (\text{Eq. 2.13})$$

For the analysis of the gas produced by the decomposition reaction, the reactor was connected to a gas sealed bag instead that the gas burette so that the gas could be fed later to the portable mass spectrometer and analysed by the method described in section 2.3.3. .

Reusability tests were performed following the same experimental procedure of the batch reaction quantified by the volumetric method. From the second reaction, fresh hydrous hydrazine solution was added in order to restart the experimental test, while the catalyst was kept in the reaction solution between the reaction cycles.

2.3.2. Pressure detection system

The experimental tests with homogeneous catalysts due to the smaller volume involved were performed using a sealed pressure round bottom flask which lid was equipped with a pressure sensor, as shown in Figure 2.6. The lid has mounted on top a 3-way valve that can be switched between two positions (180°). In one position the flask connects to the exterior so that it can be purged with N₂. In the other position the flask connects to the pressure sensor, therefore the system is closed.



Figure 2.6. Photograph of the reaction set-up used for the volumetric quantification of hydrous hydrazine decomposition used for test homogeneous catalysts.

The reaction was performed by placing 8 mL of 0.5 M NaOH solution and the selected amount of catalyst in the pressure round bottom flask with a magnetic stirring bath. The reactor was sealed and purged with N₂ before being placed in the oil bath where heat and stirring are provided. Once the temperature reached the desired value of 50°C and the pressure inside the reactor was stable 0.1 mL of 3.3M hydrous hydrazine solution were injected with a syringe through a septum that closes the second neck of the reactor. The solution was then let react until the pressure inside the reaction was stable again, indicating the end of the decomposition reaction.

2.3.3. Gas quantification via Mass spectroscopy

The yield to hydrogen calculated by volumetric quantification was then validated by repeating some representative experimental tests in which the gases were analysed by MS technique. As mention before, the gases for the MS analyses were collected in a sealed gas bag and then injected into a mass spectrometer Hiden analytical atmospheric gas analysis-quadrupole gas analyser (QGA). Argon gas was used as carrier during the analyses.

Using a standard mixture of H₂/N₂ at fixed ratios the internal sensitivity parameters were corrected, therefore, ulterior external calibration was not required to obtain a correct quantification of H₂ and N₂.

The analyses were performed using fragment at $m/z = 2$ and 28 as reference for the quantification of hydrogen and nitrogen respectively. Contribution from water at the fragment $m/z = 2$, were taken in consideration for the quantification of hydrogen. While the fragment at $m/z = 32$, oxygen, was used as a reference to compensate possible contribution from air to the nitrogen quantification.

2.3.4. Hydrous hydrazine quantification via colourimetric spectrophotometry

At the end of the gas evolution from the reaction mixture, to control the final conversion of hydrous hydrazine, a sample of the solution was treated in order to perform a colourimetric quantification of the undecomposed reagent.^{18,19}

22.25 mL water were placed in a 50 mL beaker and then 2.5 mL of p(dimethyl)-aminobenzaldehyde in 1:1 (vol/vol) EtOH/HCl solution was added. 1.5 mL of the solution from

the reactor was taken and centrifuged to separate the catalyst. Then, 1 mL was collected in a 50 mL volumetric flask with 6 drops of concentrated HCl and it was made up to 50 mL with deionised water. 0.25 mL of the diluted solution was then added to the solution in the beaker and left to stir for 10 minutes. 1 mL was then collected to record the UV spectrum taken in order to determine the concentration of hydrous hydrazine at the end of the reaction.

$$A = \varepsilon \cdot l \cdot c \quad (\text{Eq. 2.14})$$

The absorption of the *p*-(dimethyl)aminobenzaldehyde azine in the UV/Vis region was quantified and calibrated, at the maximum peak at 456 nm, using the Lambert-Beer law, as shown in Eq. 2.14. *A* is the absorbance at the chosen wavelength, ε is the extinction coefficient at that wavelength ($\text{cm}^{-1} \text{M}^{-1}$), *l* is the optical pathway (cm) and *c* is the species concentration (M). To confirm the absence of response from ammonia, 1 mmol of ammonia instead of hydrous hydrazine was added in the reaction mixture and tested, as shown in Figure 2.7. The calibration showed a linear response between the concentration of 0 and $3.16 \cdot 10^{-5} \text{M}$, at the wavelength of the maximum of the peak, which cover the range of concentration used during the tests after the dilution, as shown in Figure 2.8.

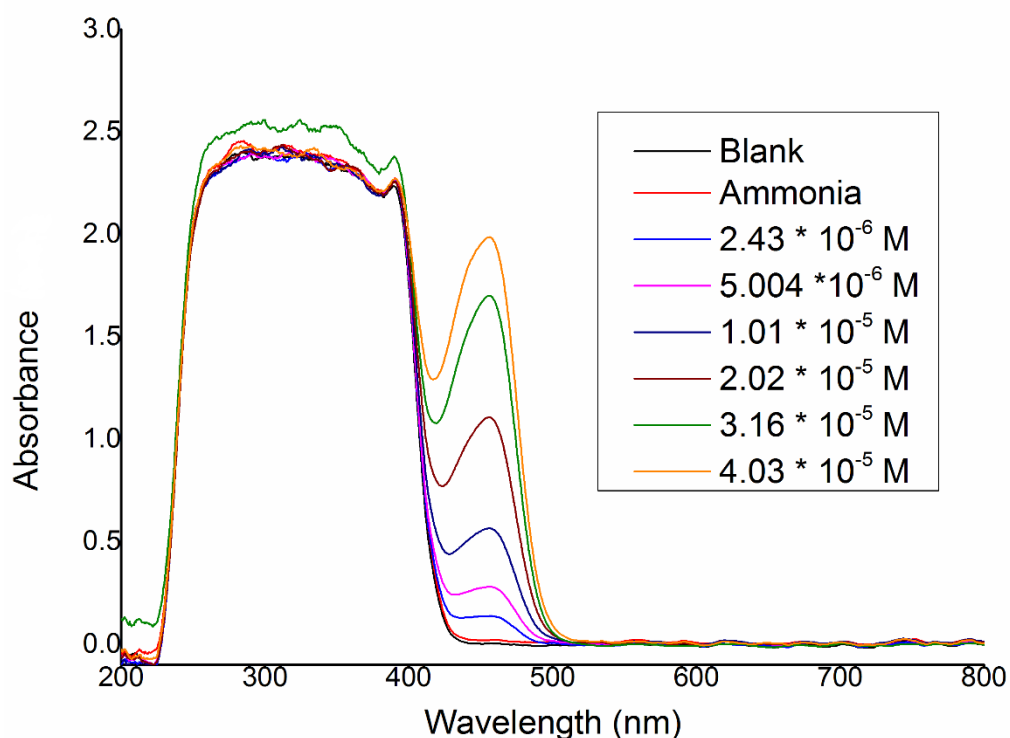


Figure 2.7. UV/Vis spectra of different concentration of *p*-(dimethyl)aminobenzaldehyde azine.

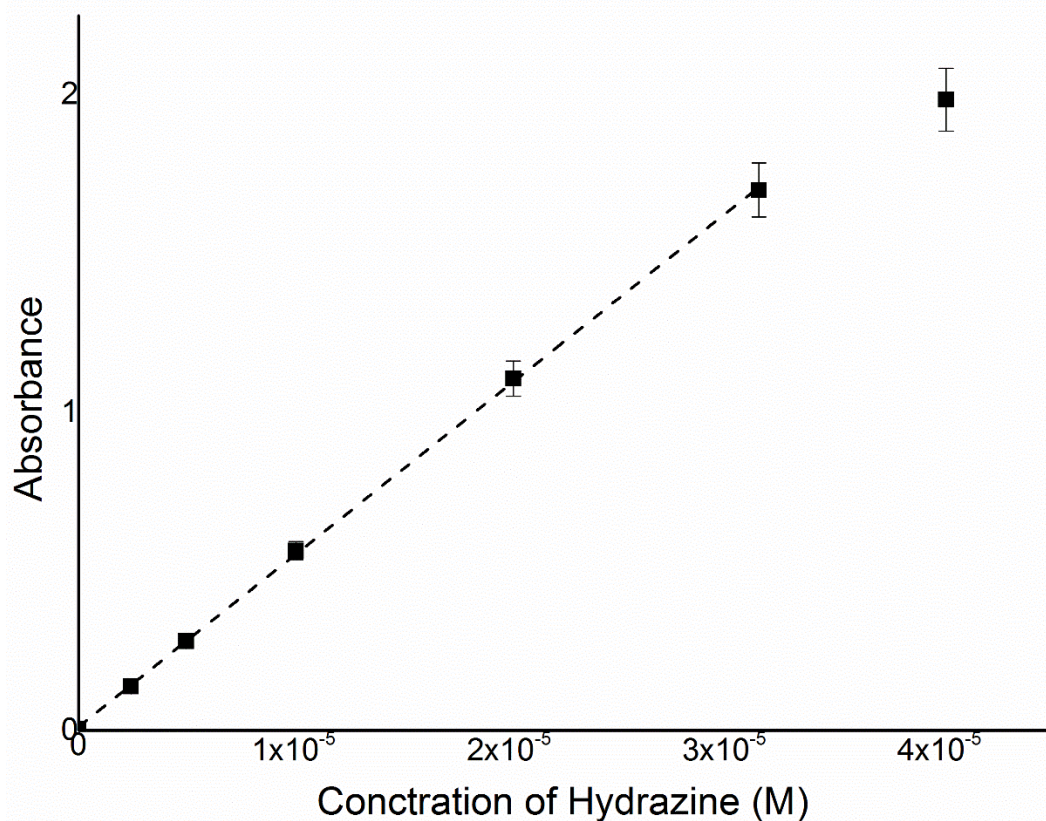


Figure 2.8. Absorbance at 456 nm versus concentration of hydrous hydrazine functionalised as *p*-(dimethyl)aminobenzaldehyde azine.

2.4. Catalysts Characterisation

2.4.1. Powder X-Ray Powder Diffraction (p-XRD)

Powder X-Ray diffraction is a considered “non-destructive” crystallographic technique for bulk material, while on nanoparticles can affect the oxidation state of the metal nanoparticles. Its main use is for the determination of crystalline species present on the analysed sample by the study of diffraction patterns. The sample to be analysed is exposed to an X-ray beam which is scattered by the interaction with the material in all the directions, these scattered radiations are therefore cancelled by destructive interference. Nevertheless, when the X-ray beam hit the sample with certain angles, constructive interferences are generated and can be detected and analysed, as shown in Figure 2.9. These constructive interactions produce a pattern which provides structural information about the sample. A diffractogram is then created which displays the intensity of the diffracted X-rays against the angle, 2θ , at which the constructive interference is detected. The pattern is related to the

crystalline phase and chemical composition of the crystal; therefore, it can be used for the identification of the sample using specialised databases.

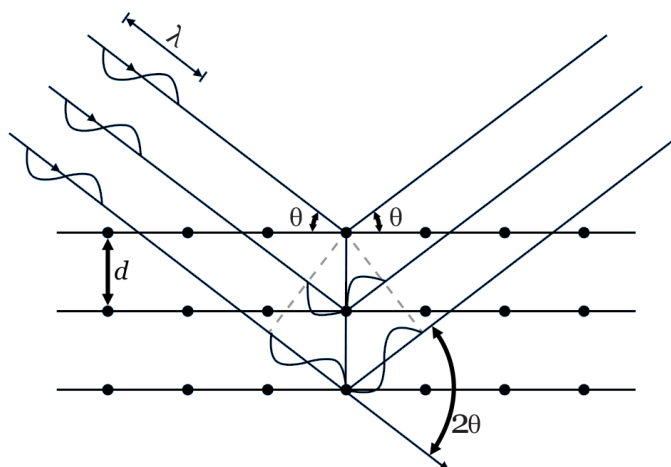


Figure 2.9. Illustration of constructive interferences and Bragg's law.²⁰

The angles at which constructive interferences occur can be calculated by Bragg's Law, Eq. 2.15.²¹

$$2d \sin \theta = n\lambda \quad (\text{Eq. 2.15})$$

where d is the spacing between planes of the crystalline structure, θ is the angle of the incident X-ray radiation, n is an integer and λ is the wavelength of the incident X-ray radiation.

A unit cell is the smallest assembly of atoms that constitute the repeating pattern in a lattice. A unit cell is defined by three integers and three angles, which are called unit cell parameters. The repetitive translation of the unit cell along its vectors creates the crystal lattice. The lattice planes are sets of equally spaced and parallel defined by Miller indices, h,k,l .²²

Another important information that can be extrapolated from the diffractogram produced by p-XRD is the size of crystallite, regions with identical and continuous crystalline structure. This crystallite size can be estimated using the Scherrer equation, Eq. 2.16, which is related to the broadening of the peak with the crystallite size.

$$D = \frac{K \cdot \lambda}{\beta \cdot \cos \theta} \quad (\text{Eq. 2.16})$$

where D is the crystallite size, λ the X-ray wavelength, β the FWHM of the peak in 2θ , K a correction factor related to crystallite shape usually taken as 0.9 and θ the angle of the

maximum of reflection. As can be noted, peaks broaden with the decrease of the mean crystallite size, therefore, for small crystallites, the peaks cannot be distinguished by the background of the analysis. This limit is usually around a crystallite size of 5 nm.

PANalytical X'PertPRO X-ray diffractometer using the Cu K α radiation ($\lambda = 0.154098$ nm), operated at 40 kV and 40 mA, was used to collect X-ray diffraction (XRD) data at ambient temperature. X-ray diffraction patterns were recorded in the range 10-80° 2 θ at a step size of 0.017°. Samples were mounted on sample holders.

2.4.2. X-ray Photoelectron Spectroscopy (XPS)

To obtain information on the elemental surface composition and the oxidation state of the elements of the surface XPS was used, which is a surface sensitive technique. This spectroscopic technique irradiates the sample surface with a monochromatic X-ray beam in ultra-high vacuum conditions. The irradiation causes the atoms of the sample to emit photoelectrons from their core energy levels which are then measured. XPS is surface sensitive because the maximum depth from which electrons are emitted is of approximately 5 nm. Of these photoelectrons can be measured kinetic energy and from that is possible to determine the binding energy of the atoms according to Eq. 2.17.

$$E_{kin} = h\nu - E_{bin} - \Phi \quad (Eq. 2.17)$$

Where E_{kin} is the kinetic energy (KE), h is Planck's constant, ν is the frequency of the X-ray beam, E_{bin} is the binding energy and Φ is the work function of the spectrometer, which is the gap between the vacuum energy level and the Fermi energy level, as shown in Figure 2.10.

XPS spectra are reported as plots of the intensity of the electrons emitted, usually as electron counts, versus the energy of the electrons, usually as binding energy. Every element emits photoelectrons at characteristic binding energies associated with each core atomic orbital and this allows the identification of the species on the surface of the sample.

Electron peaks are identified by the quantum numbers (n , l and s) of the orbital which emits the electrons, i.e. for Ir the most common peaks analysed are the one emitted by 4f orbital. Quantum number n is an integer ≥ 1 , l is orbital momentum which can be in integer between 0 and $n-1$, it is also called as $s = 0$, $p = 1$, $d = 2$, $f = 3$, s is the spin momentum and can be either $+1/2$ or $-1/2$, and the total momentum is $j = |l + s|$.²¹ Therefore, every orbital, except for s

orbitals, have two sublevels associated with j leading to the formation of a doublet of peaks. Thus, the Ir 4f level gives two peaks, $4f_{7/2}$ (with $j = 3 + 1/2$) and $4f_{5/2}$ (with $j = 3 - 1/2$).

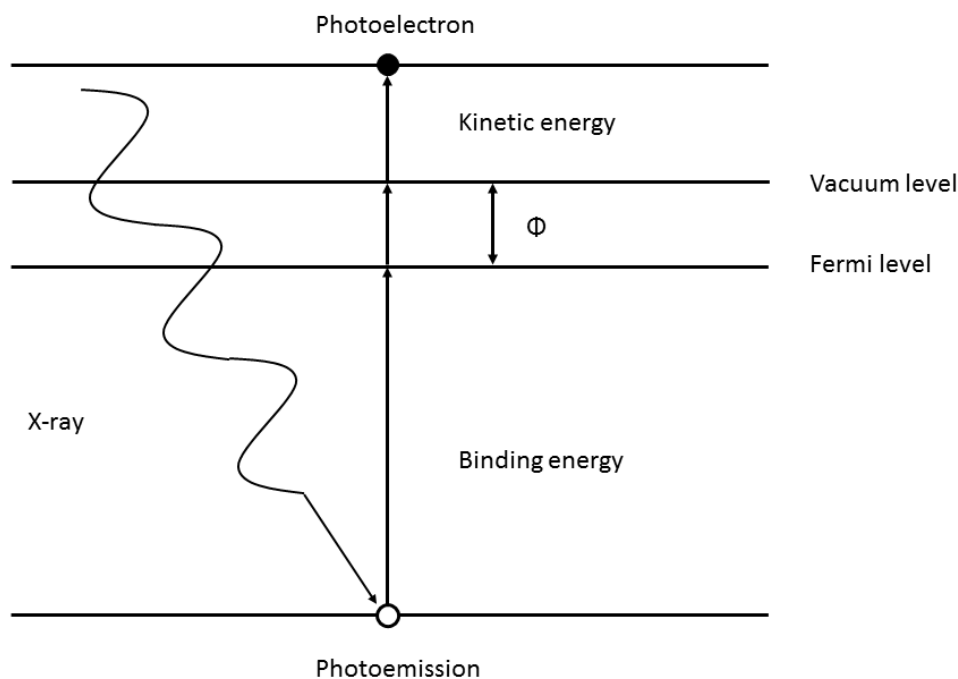


Figure 2.10. Illustration of the photoemission performed during XPS analysis.

Thermo Scientific K-alpha+ spectrometer was used to perform X-ray photoelectron spectroscopy (XPS) analyses. The spectrometer uses a monochromatic Al X-ray source operating at 72 W (6 mA x 12 kV). The signal was averaged on an oval-shaped area of approximately 600 x 400 microns. Data was recorded using pass energies of 150 eV for survey scans and 40 eV for high-resolution scans with a 1eV and 0.1 eV step respectively. Charges on the samples were neutralised using a combination of low energy electrons and argon ions (less than 1 eV) in order to have a C 1s binding energy for adventitious carbon of 284.8 eV. The experimental spectra were fitted after subtraction of Shirley^{23,24} or U2 Tougaard background using CasaXPS (v2.3.17 PR1.1) and Scofield sensitivity factors with an energy exponent of -0.6. The Ir 4f region, more characteristic, presents two doublets $4f_{7/2}$ and $4f_{5/2}$, both for metallic and oxidised Ir species. The second peak has the same width as first and 3/4 of the area of the $4f_{7/2}$ due to their multiplicities proportional to $2j+1$, which results in 8:6. $4f_{5/2}$ has binding energy 3 eV higher than $4f_{7/2}$.²⁵ Ni2p are the most characteristic peaks for Ni. Due to the satellite peaks related to the shake-up of the main 2p peak the shape of Ni2p is

not clearly defined and model have been created in order to obtain accurate fitting of the oxidised species. Also, only Ni2p_{3/2} was analysed since Ni2p_{1/2} is fully proportional to the other peak.²⁶

2.4.3. Electron Microscopy

Allowing to distinguish features until approximately 1 μm , due to the long wavelength of visible light, optical microscopy is not useful in the characterisation of the surface of a catalyst. To overcome this limitation electron microscopy was developed. Due to the small wavelength of electrons, this technique nowadays can reach magnifications on the order of one million times and resolutions of approximately 0.1 nm. Electron Microscopy can be used to determine the nanoparticle size, shape and morphology of heterogeneous catalysts. The analysis of the electrons emitted by the interaction of the sample with the electron beam can give important information about the composition of the sample. Depending on the kind of electron detected and analysed, as shown in Figure 2.11, various electron microscopy techniques can be classed. In this thesis, Transmission Electron Microscopy and Scanning Electron Microscopy have been used.

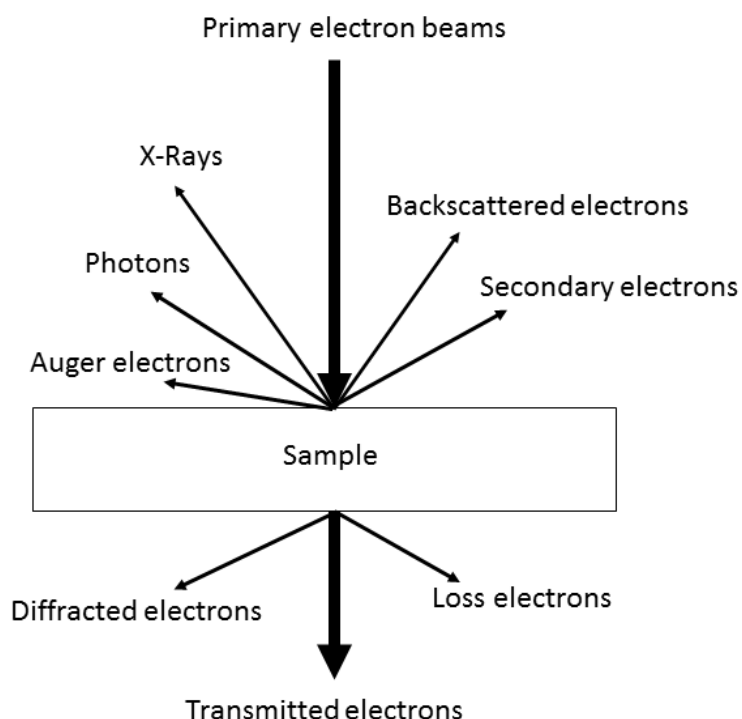


Figure 2.11. Interaction between the electron beam and the sample during electron microscopy, the position of the detector and of the lenses with respect of the beam can allow to select specific electron or radiation emitted.

2.1.1.1. Transmission Electron Microscopy (TEM)

Transmission Electron Microscopy uses an electron gun that emits a primary electron beam at high energy and intensity which is passed through a condenser to obtain parallel beams that are focused on the sample. Only a fraction of the electrons passes through the sample without energy loss and are called transmitted electrons. Like in optical microscopy, a two-dimensional projection of the sample is created by the transmitted electrons, which are later magnified by electromagnetic lenses. Finally, a bright-field image is formed when the transmitted electron beam hits a fluorescent screen. Dark-field images can be also collected if, instead of the transmitted electrons, diffracted electrons are magnified and focused on the fluorescent screen. If the particles are oriented towards the beam, the electrons can offer crystallographic information.

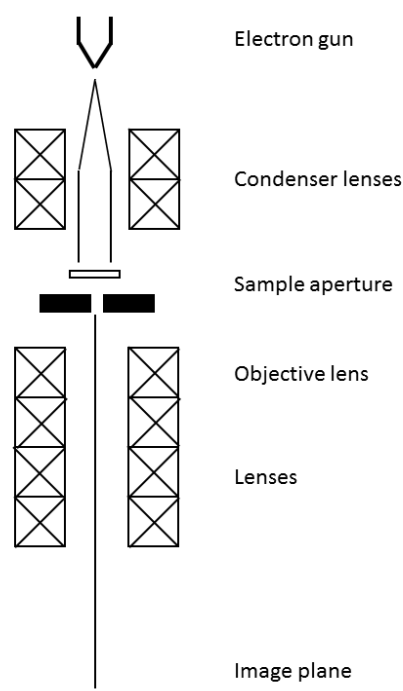


Figure 2.12. Schematic design of a transmission electron microscope.

Particle size distributions and mean nanoparticle size was obtained performing Transmission Electron Microscopy using a JEOL JEM 2100 TEM operating at 200 keV. For examination, powder samples were dispersed in high purity ethanol and a drop of the suspension was deposited on a holey carbon film supported by a 300-mesh copper TEM grid and then let evaporate. In order to obtain a reliable mean nanoparticle size of the desired metal

nanoparticles and particle size distributions determination at least 200 particles from different areas were measured.

TEM performed in Leeds by Dr Tom Chamberlain group were prepared by the following experimental procedure. The samples were dispersed in 10 mL of isopropanol and sonicated for 10 minutes. Then 3 drops of this solution were deposited on carbon-coated copper TEM grids. HRTEM and STEM were performed at 200 kV (Leeds Electron Microscopy and Spectroscopy Centre, LEMAS). Nanoparticles sizing was performed by measuring a statistically valid number of individual NPs using the TEM data. EDX mapping was performed in STEM mode.

The analyses performed at Lehigh University by prof. Chris Kiely group were analysed in a JEOL ARM 200CF analytical electron microscope equipped with a 4th order ASCOR probe corrector and a JEOL Centurio silicon drift detector XEDS system operating at 200 kV. Images were collected in the HAADF-STEM mode. STEM image acquisition and interpretations were performed in DigitalMicrograph. XEDS data were acquired and analysed using Thermo Scientific NSS software.

2.4.3.1. Scanning Electron Microscopy (SEM)

SEM can be used to obtain information about the macroscopic morphology of the catalyst. In this technique, the electrons are produced by a metallic filament, usually tungsten due to the high melting point, by the application of a voltage under vacuum. The electron beam hitting the sample emits secondary and backscattered electrons which are then detected as a function of the position of the primary beam, as shown in Figure 2.13.

Backscattered electrons are generated deeper in the sample, they have higher energy, and have different response based on the atom that emits them, with heavier atoms having higher response resulting in brighter region in the final image.

Secondary electrons are generated from the surface atoms and have lower energy. To amplify the response from these electrons they get collected and fired at a scintillator that releases flashes of light into a photomultiplier. This amplified signal is then displayed as an intensity distribution pattern. The intensity of the signal in each region depend on the number of electrons detected. The orientation of surface influence, therefore, the intensity of the signal.

If the surface directly faces the detector, it will collect more electrons, resulting brighter than surfaces pointing to other directions.

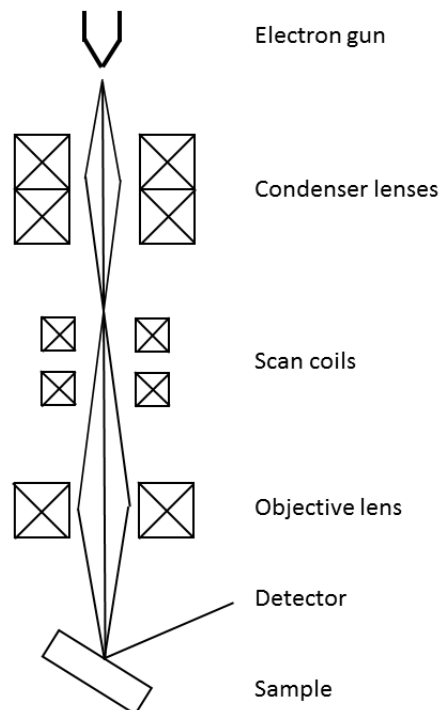


Figure 2.13. Schematic of a scanning electron microscope.

After exposing the main difference in functioning between SEM and TEM, as to be also noted that the maximum resolution range is 1-10 nm for SEM analyses, while with TEM it is possible to reach sub-nanometre resolution.

Powders were dispersed on an Al-stub and examined in a Hitachi TM3030PLUS SEM equipped using 15kV to generate the electron beam with a Quantax70 energy-dispersive X-ray spectrometer.

A range of selected samples for which TEM analyses resulted problematic were analysed by Scanning Electron Microscopy performed on a Tescan Maia3 field emission gun scanning electron microscope (FEG-SEM) fitted with an Oxford Instruments XMAXN 80 energy dispersive X-ray detector (EDX). Images were acquired using the secondary electron and backscattered electron detectors. Samples were dispersed as a powder onto 300 mesh copper grids coated with holey carbon film.

2.4.3.2. Energy Dispersive X-ray (EDX)

EM techniques are often coupled with an energy-dispersive X-ray spectrometer (EDX) detector so that elemental composition can be analysed. In EDX detector, a solid-state device consisting of lithium-doped silicon, X-rays are absorbed and turned into electron by ionisation. This process dissipates kinetic energy creating electron-hole pairs in the semiconductor. The pulse heights of the current, which is proportional to the number of electron-hole pairs, are measured to know the kinetic energy of the photoelectrons and, therefore, the energy of the X-ray emitted by the sample. This energy is characteristic for each element and in this way, elements can be recognised and the image mapped element by element. EDX as a limitation in the recognition of the species on the surface due to the proximity of energy of X-ray emitted by atoms with similar electronic structure.²¹

The relative elemental composition can be assessed by EDX since the quantity of X-rays emitted at specific energy values is proportional to the amount of each specific atom.

2.4.4. BET (Brunauer, Emmett and Teller) Surface Area Analysis

Since heterogeneous catalysis is performed on the surface of the catalytic material the extension of its surface area plays a relevant role in defining the catalyst activity. Gas adsorption is used in order to measure the surface area of the materials used and the size and volume of its pores if the material presents porosity. For this technique, an inert gas, at its condensation temperature, is physically adsorbed on the surface of the material analysed. The typical choice for the inert gas is N₂, since it is abundant and cheap, and its condensation temperature can be achieved immersing the sample in liquid nitrogen. Brunauer–Emmett–Teller (BET) equation describes multilayer absorption and it is derived from the Langmuir model for monolayer molecular adsorption and, with some assumptions, it can be used for an assessment of the surface area of the sample. However, some assumptions have to be done: (I) the gas molecules adsorb in layers on a solid, (II) the interaction between each adsorption layer is negligible, (III) the Langmuir theory can be applied to each layer and (IV) the enthalpy of adsorption of the first layer is greater than for the second and other layers, which is the liquefaction energy. The result of the analysis of an isotherm function of the volume of the gas adsorbed versus the relative pressure, as illustrated in Eq. 2.18.²⁷

$$\frac{1}{v \left[\left(\frac{\rho}{\rho_0} \right) - 1 \right]} = \frac{c - 1}{v_m \cdot c} \cdot \left(\frac{\rho}{\rho_0} \right) + \frac{1}{v_m \cdot c} \quad (\text{Eq. 2.18})$$

Where ρ and ρ_0 are the pressure of adsorbates at equilibrium and saturation, v is the volume of adsorbed gas, v_m is the volume of adsorbed monolayer gas and c is the BET constant. This equation is only valid for partial pressure value, ρ/ρ_0 , between 0.05 and 0.30, where the BET plot is linear and if the value of c is high enough to set the intercept to approximately 0.²⁷ In these conditions for non-porous materials is reached a near complete adsorbed monolayer without the adsorption of successive layers. From a graphical representation, the volume of the monolayer, v_m , can be calculated and, from it, the specific surface area from Eq. 2.19.

$$A_s = \left(\frac{v_m}{22414} \right) \cdot N_A \cdot \sigma \quad (\text{Eq. 2.19})$$

where N_A is Avogadro's number, v_m is the volume of adsorbed monolayer gas and σ is the area covered by one nitrogen molecule, 0.162 nm².^{22,28}

BET surface area was measured from the adsorption-desorption of N₂ at liquid nitrogen temperature, 77 K, using a Quantachrome NOVA 2200e. Samples were degassed for 3 h under vacuum at 500 K before the BET analysis. The total surface area was determined using the BET (Brunauer–Emmett–Teller) equation and the multi-point method.

2.4.5. Temperature Programmed Reduction Analysis (TPR)

Temperature-programmed (TP) analysis is a class of techniques in which a chemical reaction or desorption is monitored while the is progressively increased temperature. In this class of analysis are collected Temperature Programmed Desorption (TPD), Temperature Programmed Reduction (TPR) and Temperature Programmed Oxidation (TPO), which are commonly used for the characterisation of heterogeneous catalysts. During this thesis, TPR was performed. The technique passes a flow of H₂/Ar through the sample under well-defined conditions and quantifies the gases produced over time during the reduction. Different species reduces at different temperature and in the case of metal nanoparticles can give information about the nanoparticles structure and the interaction between the nanoparticles and support.²⁹

TPR was performed using a Quantachrome ChemBET TPR/TPD chemisorption analyser with a TCD. During the pre-treatment step 50 mg of sample, in a U-shaped quartz tube, is heated at 15 °C/min up to 130 °C left at that temperature for 1 h with a flow of He at 120 ml/min, in order to remove physisorbed species on the surface. The sample was then cooled down to room temperature with He flow. The last step is the reduction of samples by heating up to 800°C (at 10°C/min) in 10% H₂/Ar, monitoring the evolution of reduction product with a Thermal Conductivity Detector (TCD) at attenuation 1 and current 180 mV.

2.4.6. Attenuate Total Reflectance (ATR) *in situ* Infrared spectroscopy

Infrared radiation is capable to excite particular modes of vibration of the chemical bonds present in molecules. This excitation happens when the IR radiation incident to a material has an energy that matches a mode of vibration of a bond present in the material irradiated, which, therefore, absorbs the radiation. Since the energy required to excite a bond depends from the nature of the atoms who constitute the bond and the length of the bond, related to its strength, IR spectroscopy is of particular interest for the study of chemical species and their modification through a reaction. IR spectroscopy usually is focused on the mid-IR region of the spectrum, between 600 to 4000 cm⁻¹.

ATR-IR is a technique used to obtain information about liquids or solids in contact with the crystal used during the analysis. In fact, this technique utilises the effect called evanescent wave to perform the analysis. First, an IR light source is used to generate a beam that passes through a crystal so that it is reflected off the internal surface at least once, the reflection creates an evanescent wave which extends itself from the external surface of crystal that is in contact with the sample.³⁰ The penetration depth of the evanescent wave is typically few μm, depending on the wavelength of light, the angle of incidence and the indices of refraction for the ATR crystal and the samples to analyse. The beam is collected at the exit of the crystal and then focused on a detector in order to analyse the IR radiation. Since the penetration of the evanescent wave is limited to few μm or less, ATR-IR allows to record spectra of medium that usually would strongly attenuate the IR radiation. In heterogeneous catalysis, ATR-IR can be performed depositing a thin layer of catalyst and flow a solution containing the reagents on the catalyst. This *in-situ* spectroscopy can give insights on the most stable intermediates created during the reaction and from that information on the mechanism of reaction.^{31,32}

In-situ/operando infrared spectroscopy measurements were carried out in the attenuated total reflection mode (ATR-IR) using a Vertex 70V spectrometer (Bruker) at the Paul Scherrer Institut equipped with a liquid N₂-cooled HgCdTe detector and a commercial mirror accessory (6 reflections attachment 11244, Specac). All spectra were acquired by averaging 20 interferograms at 4 cm⁻¹ resolution and 10 kHz scanner velocity. The collected data are then elaborated using a Fourier transformation. An aqueous suspension of the sample (10 mg) was dropped on a parallelogram ZnSe internal reflection element (IRE; 45°, 50x20x2 mm³) and dried in ambient air to generate a homogeneous layer. The coated IRE was mounted within the walls of a homemade cell heated using a heating foil and connected to a peristaltic pump (Ismatec) by Teflon tubings, and the analyses were performed at 50 °C. The cell was connected to a washing bottle enabling separation of liquid and gas components.

2.5. Spectroscopic methods

2.5.1. Ultraviolet/visible spectroscopy (UV/Vis)

UV/Vis spectroscopy is a quantitative and qualitative technique which analyses the sample via the interaction of the samples with a light beam. As a matter of fact, molecules containing π -electrons or nonbonding electrons, n-electrons, are capable to adsorb photons and in this way exciting these electrons to higher antibonding molecular orbitals.

The spectrophotometer quantifies the intensity of light passing through the sample (I) and then relates it to the intensity of light generated by the source (I_0). The I/I_0 ratio is the transmittance. Nonetheless, absorbance A , defined as $-\log_{10}T$, is commonly used to quantify the portion of light absorbed by the sample. Using the Lambert-Beer equation, Eq. 2.14, and keeping the optical path fixed, usually 1 cm, and knowing the extinction coefficient ϵ is possible to quantify the concentration of UV/Vis active species.

The more common UV/Vis spectrophotometers use light sources which provide a radiation spectrum in the range of UV/Visible. This beam passes through a monochromator, which selects a specific wavelength at the time, and is then focused alternative through the sample cell and the reference cell till it reaches the detector which converts the photons into an electrical signal which can be measured and recorded with a computer.

In this thesis was used a single-beam spectrophotometer. In this case, the reference spectrum and the sample spectrum are recorded at different times and then the reference spectrum was subtracted from the sample spectrum by the computer. The spectra were then recorded in transmission mode.

UV/Vis was used to control the reduction of the metal precursors by the change of colour of the solution and, if possible, the creation noble metal nanoparticles by the exhibition of typical surface plasmon resonance absorptions. These resonances are due to the free conduction electrons collective oscillation provoked by the interaction with electromagnetic radiation.^{33,34} UV/Vis spectroscopy was also used to quantify the amount of hydrous hydrazine remain in the reaction solution.

UV/Vis spectroscopic analyses were performed cuvette using in-situ AvaSoft UV-Vis Spectrometry set-up displayed in Figure 2.14 in a 1 cm² quartz. The solution to be analysed was placed in the quartz cuvette, at room temperature, and the UV-vis spectrum (200-900 nm) of the solution was recorded.



Figure 2.14. (Up-left) AvaLight-DH-S deuterium halogen source, (up-right) AvaSpec-ULS2048XL EVO spectrometer and (bottom) CUV-UV/VIS-TC temperature-controlled cuvette holder.

2.5.2. Mass Spectrometry

Mass spectrometry (MS) is a class of analytical techniques used to detect, quantify and identify molecules and ions and that can be associated with separation technique, such as gas and liquid chromatography, in order to analyse the isolated compounds, as shown in Figure 2.15. The analysis performed the measures by the mass to charge ratio m/z of the detected

fragments versus the intensity of the signal generated by the fragment. The first step of the analysis is the ionisation of the molecules and atoms in the sample. The ionisation is usually accomplished by bombarding the sample with a high energy beam of particles, depending from the energy source. The ions source used is one of distinction between the different MS technique, since more energetic sources produce smaller fragment, and less energetic ones are able to maintain larger fragments of the molecules, therefore, the fragmentation signature of the same molecule change based on the source energy. The selection of the fragments is then achieved by accelerating the ions in a beam which is accelerated by either a magnetic or electric field and then selected by speed (i.e. lighter and more charged ions are faster), time-to-flight, or by selectively focusing specific m/z to the detector. The detector is typically an electron multiplier.

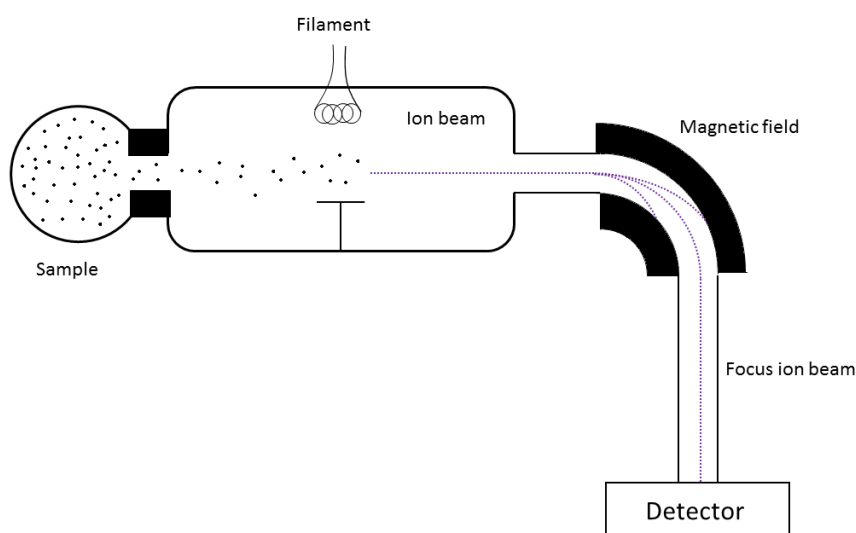


Figure 2.15. Diagram of a representative Mass Spectrometer, the sample is injected into a low pressure chamber where it is ionised using an high energy source, it is then focused using magnetic field before the detector.

2.5.2.1. Inductively coupled plasma – Mass spectroscopy (ICP-MS)

An inductively coupled plasma is an ions source that uses a plasma of inert gas, usually Ar, inductively heated by an electromagnetic to temperatures in the range 8000 - 10000 K. The plasma generated in this way can generate ions and electrons making it electrically conductive, keep the total neutral charge of the plasma.³⁵ The energy of plasma is high

enough to atomise every molecule so that the fragments detected are related to the total elemental content of the sample, as shown in Figure 2.16.

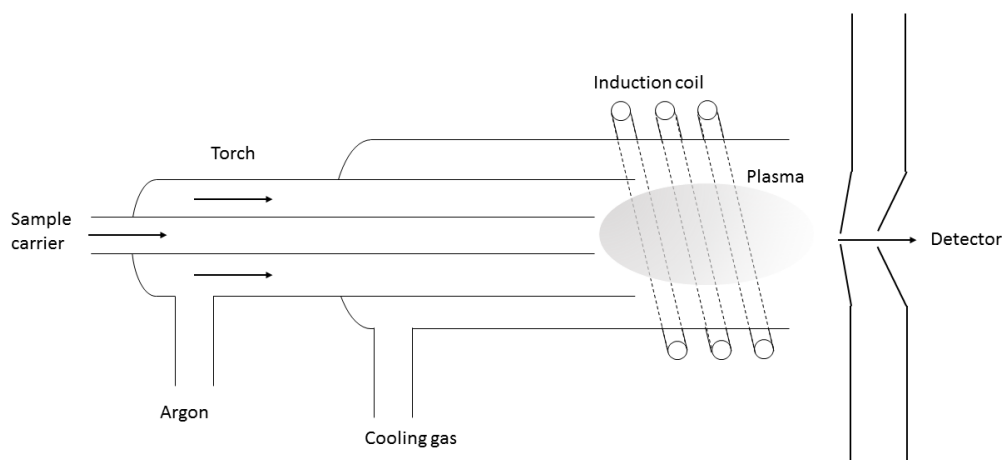


Figure 2.16. Diagram of the ion source and interface in the ICP instrument.

The torch is constituted of three concentric quartz tubes that are placed inside an induction coil which is supplied with a radio-frequency electric current. An electric spark generates free electron in the Ar gas flowed between the two outermost tubes, the radiofrequency magnetic field then accelerates the electron in gas changing the directions based on the high frequency of the electric current. These electrons accelerated by the magnetic field interact with Ar atom creating new electron and Ar^+ which are also accelerated. This process continues until the rate of recombination of electron and Ar^+ matches the rate of release of new electrons. When the plasma is generated the sample to be analysed is introduced through the central tube as gas or nebulised solution.³⁶

ICP-MS analyses of solutions of the preparation of catalyst, after the filtration and separation of the solid catalyst, was performed to quantify the amount of metal that was not immobilised/deposited during the preparation of the catalysts and, therefore, remained in solution. The analysis was performed on an Agilent 7900 ICP-MS with full calibration for Ir (1mg L^{-1} , 0.1mg L^{-1} , 0.01mg L^{-1} , 0.001mg L^{-1} and blank) prepared with certified standards from Waters. The analyses have been performed on the collected filtrated solution after washing the solid with an exact amount of deionised water so that the total volume is known. Therefore, the amount of metal remained in solution can be calculated by multiplying the volume of the solution by the concentration found by the ICP-MS analyses.

2.5.2.2. Microwave Plasma-atomic Emission Spectrometry (MP-AES)

The microwave plasma was used in combination with Atomic emission spectroscopy (AES) as a detection method. AES identify and quantify atom species by analysing the spectra of the photons emitted by the atoms from the sample. The identification is performed by comparing the wavelength of the photons emitted from the sample with the atomic spectral line characteristic of each element. The intensity of the radiation is directly proportional to the concentration of that particular atom in the sample, which allows the element quantification.

The microwave plasma ions source operates with a principle similar to the aforementioned ICP. In this case, a N₂ plasma is created in the torch by a concentrated axial magnetic field generated through excitation by microwaves. The plasma produced is toroidal with a temperature of approximately 5000 K to the external part and a cooler central channel where the liquid samples are nebulised. MP-AES using a N₂ plasma and AES detection method, require lower operating costs and can operate at higher maximum concentration than the ICP-MS. As withdrawal MP-AES as a higher detection limit that makes it less useful in case of traces elements.

MP-AES analyses were performed to control the concentration of the metal precursor solution. The analysis was performed on an Agilent 4100 MP-AES with full calibration for Ir (5mg/l, 3mg/l and 1mg/l) and for Ni (10mg/l, 5mg/l and 1mg/l) from standard solution provided by Agilent.

2.6. Computational methods

2.6.1. Density Functional Theory (DFT) studies

DFT calculations were done to support the mechanistic studies obtained from ATR-IR spectroscopy and MS gas analysis of the decomposition of ¹⁵N labelled hydrazine monohydrate. DFT calculations permit to estimate the adsorption energy of each intermediate on Ir surface and potential energy of the elementary steps for the decomposition of hydrazine. The transition states of the elementary steps were also calculated to obtain kinetic information about the reaction on Ir surface, such as energy barriers for the forward and reverse reaction. This information is crucial to the determination

of the optimal surface for the decomposition of hydrous hydrazine reducing to the minimum the production of ammonia which detrimental for the stability of fuel cells.

The calculations were carried out through the Vienna Ab-initio Simulation Package (VASP) using spin-polarized density functional theory (DFT).^{37,38} Perdew-Burke-Ernzerhof (PBE)³⁹ form of the generalized gradient approximation (GGA)⁴⁰ was used to calculate the exchange-correlation energy, and the effect of inner cores, including non-spherical contributions to the gradient corrections, were characterised by the projector augmented wave (PAW).^{41,42} The Van der Waals (VdW) corrections by employing the zero damping DFT-D3 method of Grimme,⁴³ which has been proven to be an enhancement on several systems, was utilised to improve the description of the long-range interaction.⁴⁴⁻⁴⁶ Plane wave basis sets were used with a kinetic energy cut-off of 500 eV. Optimised structures were converged in a limit of internal forces smaller than 0.02 eV/Å with the conjugate gradient algorithm and an electronic relaxation limit of 10⁻⁵ eV.

In good agreement with the experimental value of 3.839 Å, lattice parameter for iridium were calculated as 3.843 Å.⁴⁷ The Ir surface was simulated by a p(4x4) supercell slab model with 5 atomic layers, with the three more superficial fully relaxed, while the two on the bottom are fixed at the bulk lattice. Different slab thicknesses were tested until convergence was achieved within 1 meV per atom. The Brillouin zone was tested by a Γ -centered 3x3x1 Monkhorst-Pack grid with Methfessel-Paxton smearing broadening of $\sigma = 0.2$ eV to obtain a precise account of the total energy. A vacuum space of 15 Å was insert perpendicular to the surface in order to prevent false interaction with periodic images of the slap. In addition to molecular interaction, dipole correction along the z-axis was applied to improve the energy convergence. All adsorbates were relaxed during structural optimization.

Hydrazine in the gas phase can assume three main conformations: gauche, trans and eclipsed. Of these conformations, gauche is the most stable, while the energy of trans and eclipsed conformations have energies higher than the gauche conformation by 0.13 and 0.36 eV respectively.⁴⁸ Therefore, the energy of the gauche conformation was used as the gas-phase hydrazine energy reference to calculate the adsorption energy of hydrazine and the relative energy values of intermediates species along with the energy profiles of reaction, calculated by Eq. 2.20.

$$E_{N_yH_x}^{\text{ads}} = \left(E_{N_yH_x}^{\text{surf}} + (4 - x)E_{\text{H}}^{\text{surf}} + (2 - y)E_{\text{N}}^{\text{surf}} \right) - \left(((4 - x) + (2 - y) + 1)E^{\text{surf}} + E_{\text{N}_2\text{H}_4}^{\text{gas}} \right) \quad (\text{Eq. 2.20})$$

Where $E_{N_yH_x}^{\text{surf}}$ is the total energy of the adsorbed N_yH_x on a surface, $E_{\text{H}}^{\text{surf}}$ and $E_{\text{N}}^{\text{surf}}$ are the total energies of single adsorbed atom of hydrogen and nitrogen, on the surface, respectively. Additionally, E^{surf} is the energy of the bare surface and $E_{\text{N}_2\text{H}_4}^{\text{gas}}$ is the energy of an isolated hydrazine molecule in gas phase.

The climb-image nudged elastic band, ci-NEB,^{49,50} and the improved dimer method, IDM,⁵¹ were used together in order to find the saddle point of the transition states, TS, ensuring that the imaginary frequency along with the reaction coordinate is unique. The energy of reaction, E_r , is calculated by the difference between the energy of the final state, FS, and the energy of initial state, IS, as reported in Eq. 21. Exothermic reactions are characterised by negative values for E_r . Activation energy barriers, E_a , both forward and reverse, is calculated as the energy gap between the TS and the IS and the FS, respectively, as reported in Eq. 2.22 and Eq. 2.23.

$$E_r = E_{FS} - E_{IS} \quad (\text{Eq. 2.21})$$

$$E_a(\text{forward}) = E_{TS} - E_{IS} \quad (\text{Eq. 2.22})$$

$$E_a(\text{reverse}) = E_{TS} - E_{FS} \quad (\text{Eq. 2.23})$$

The adsorption energies calculated during the DFT analysis were used to create thermodynamic profiles of reactions for the most representative reaction pathways. The E_a were then used to study the kinetic aspects of each elementary step, giving a deeper comprehension of the mechanism of reaction for hydrous hydrazine decomposition on Ir surface.

2.6.2. Supercomputer and software

The Advanced Research Computing at Cardiff (ARCCA) Division which provides the support to develop research using computing services for the University, in particular through the Raven supercomputing cluster, was used to perform DFT studies.

VESTA software was used to visualise the 3D structural models.

2.7. References

- 1 M. Boudart, *Chem. Rev.*, 1995, **95**, 661–666.
- 2 S. Kozuch and J. M. L. Martin, *ACS Catal.*, 2012, **2**, 2787–2794.
- 3 C. Costentin, S. Drouet, M. Robert and J. Saveant, *J. Am. Chem. Soc.*, 2012, **134**, 11235–11242.
- 4 L. Prati and A. Villa, *Catalysts*, 2012, **2**, 24–37.
- 5 N. Dimitratos, C. Hammond, C. J. Kiely and G. J. Hutchings, *Appl Petrochem. Res.*, 2014, **4**, 85–94.
- 6 F. Porta, L. Prati, M. Rossi, S. Coluccia and G. Martra, *Catal. Today*, 2000, **61**, 165–172.
- 7 C.-J. Jia and F. Schuth, *Phys. Chem. Chem. Phys.*, 2011, **13**, 2457–2487.
- 8 M. Sankar, N. Dimitratos, P. J. Miedziak, P. P. Wells, C. J. Kiely and G. J. Hutchings, *Chem. Soc. Rev.*, 2012, **41**, 8099–8139.
- 9 A. Villa, D. Wang, G. M. Veith, F. Vindigni and L. Prati, *Catal. Sci. Technol.*, 2013, **3**, 3036–3041.
- 10 Y. Zhao, L. Jia, J. A. Medrano, J. R. H. Ross and L. Le, *ACS Catal.*, 2013, **3**, 2341–2352.
- 11 N. Dimitratos, A. Villa, L. Prati, C. Hammond, C. E. Chan-thaw, J. Cookson and P. T. Bishop, *Appl. Catal. A Gen.*, 2016, **514**, 267–275.
- 12 J. L. Hueso, V. Sebastian, A. Mayoral, L. Uson, M. Arruebo and J. Santamaria, *RSC Adv.*, 2013, **3**, 10427–10433.
- 13 R. Zanella, L. Delannoy and C. Louis, *Appl. Catal. A Gen.*, 2005, **291**, 62–72.
- 14 C. Bianchi, F. Porta, L. Prati and M. Rossi, *Top. Catal.*, 2003, **13**, 231–236.
- 15 L. Prati and G. Martra, *Gold Bull.*, 1999, **32**, 96–101.
- 16 R. Zanella, S. Giorgio, C. H. Shin, C. R. Henry and C. Louis, *J. Catal.*, 2004, **222**, 357–367.
- 17 L. He, Y. Huang, X. Y. Liu, L. Li, A. Wang, X. Wang, C. Y. Mou and T. Zhang, *Appl. Catal. B Environ.*, 2014, **147**, 779–788.
- 18 M. George, K. S. Nagaraja and N. Balasubramanian, *Talanta*, 2008, **75**, 27–31.
- 19 G. W. Watt and J. D. Chrisp, *Anal. Chem.*, 1952, **24**, 2006–2008.
- 20 VEQTER, X-Ray Diffraction, <http://www.veqter.co.uk/residual-stress-measurement/x-ray-diffraction>, (accessed 15 September 2019).
- 21 J. W. Niemantsverdriet, *Spectroscopy in Catalysis: An Introduction*, Wiley-VCH, Weinheim, 2007.
- 22 M. Che and J. C. Védriném, *Characterization of solid materials and heterogeneous catalysts. From structure to surface reactivity*, Wiley-VCH, Weinheim, 2012.
- 23 H. Jiang, X. Sun, Y. Du, R. Chen and W. Xing, *Chinese J. Catal.*, 2014, **35**, 1990–1996.

- 24 D. A. Shirley, *Phys. Rev. B*, 1972, **5**, 4709–4714.
- 25 S. J. Freakley, J. Ruiz-Esquius and D. J. Morgan, *Surf. Interface Anal.*, 2017, **49**, 794–799.
- 26 M. C. Biesinger, B. P. Payne, L. W. M. Lau and R. S. C. Smart, *Surf. Interface Anal.*, 2009, **41**, 324–332.
- 27 S. Brunauer, P. H. Emmett and E. Teller, *J. Am. Chem. Soc.*, 1936, **407**, 309–319.
- 28 S. Partyka, F. Rouquerol and J. Rouquerol, *J. Colloid Interface Sci.*, 1979, **68**, 21–31.
- 29 M. Trepanier, A. K. Dalai and N. Abatzoglou, *Appl. Catal. A Gen.*, 2010, **374**, 79–86.
- 30 A. J. Mcquillan, *Adv. Mater.*, 2001, **13**, 1034–1038.
- 31 G. Chiarello, D. Ferri and E. Selli, *Appl. Surf. Sci.*, 2018, **450**, 146–154.
- 32 A. Villa, D. Ferri, S. Campisi, C. E. Chan-thaw, Y. Lu, O. Krçcher and L. Prati, *ChemCatChem*, 2015, **7**, 2534–2541.
- 33 S. Link and M. A. El-sayed, *J. Phys. Chem. B*, 1999, **103**, 4212–4217.
- 34 J. M. Sanz, D. Ortiz, J. M. Saiz, A. S. Brown, M. Losurdo, H. O. Everitt and F. Moreno, *J. Phys. Chem. C*, 2013, **117**, 19606–19615.
- 35 L. Balcaen, E. Bolea-fernandez, M. Resano and F. Vanhaecke, *Anal. Chim. Acta*, 2015, **894**, 7–19.
- 36 A. T. Cawley and U. Flenker, *J. Mass. Spectrom.*, 2008, **43**, 854–864.
- 37 G. Kresse and J. Furthmüller, *Comput. Mater. Sci.*, 1996, **6**, 15–50.
- 38 T. Bucko, J. Hafner, S. Lebegue and J. G. Angyan, *J. Phys. Chem. A*, 2010, **114**, 11814–11824.
- 39 J. P. Perdew, K. Burke and M. Ernzerhof, *Phys. Rev. Lett.*, 1996, **77**, 3865–3868.
- 40 J. P. Perdew, A. Ruzsinszky, I. Csonka, O. A. Vydrov, G. E. Scuseria, L. A. Constantin, J. P. Perdew, A. Ruzsinszky, X. Zhou and K. Burke, *Phys. Rev. Lett.*, 2008, **100**, 1–4.
- 41 G. Kresse and D. Joubert, *Phys. Rev. B*, 1999, **59**, 1758–1775.
- 42 P. E. Blochl, O. Jepsen and O. K. Andersen, *Phys. Rev. B*, 1994, **49**, 16223–16233.
- 43 S. Grimme, S. Ehrlich and L. Goerigk, *J. Comput. Chem.*, 2011, **32**, 1456–1465.
- 44 S. S. Tafreshi, A. Roldan, N. Y. Dzade and N. H. de Leeuw, *Surf. Sci.*, 2014, **622**, 1–8.
- 45 N. Y. Dzade, A. Roldan and N. H. de Leeuw, *Minerals*, 2014, **4**, 89–115.
- 46 A. Roldan and N. H. de Leeuw, *Phys. Chem. Chem. Phys.*, 2017, **19**, 12045–12055.
- 47 H. P. Singh, *ACTA cryst.*, 1968, **24**, 469–471.
- 48 S. S. Tafreshi, A. Roldan and N. H. de Leeuw, *Phys. Chem. Chem. Phys.*, 2015, **17**, 21533–21546.
- 49 G. Mills and H. Jonsson, *Phys. Rev. Lett.*, 1994, **72**, 1124–1127.

- 50 G. Mills, H. Jonsson and G. K. Schenter, *Surf. Sci.*, 1995, **324**, 305–337.
- 51 A. Heyden, A. T. Bell and F. J. Keil, *J. Chem. Phys.*, 2005, **123**, 1–14.

3. Catalytic decomposition of Hydrous Hydrazine over Ir/CeO₂

3.1. Introduction

As it has been discussed in Chapter 1 the goal of this research project is to study the catalytic decomposition of hydrous hydrazine in the liquid phase using metal nanoparticles (NPs) as the active material to produce gaseous hydrogen, Eq. 3.1. As mentioned previously anhydrous hydrazine is too reactive to a future safe well-spread use, for this reason the tests have been performed on more diluted forms of Hydrazine, in particular, hydrazine monohydrate (N₂H₄·H₂O) has been selected as the reagent to conduct the catalytic tests hereafter.

The project started investigating the activity of a well-known active and selective metal, Iridium. Iridium catalysts have been benchmark materials for hydrazine propelled thrusters for many years, but researches on liquid phase hydrous hydrazine decomposition have shown that where Ir nanoparticles maintain high activity and their selectivity shift toward the generation of ammonia, an undesirable side product, Eq.2.



To better study the kinetics of the decomposition reaction and compare a range of different catalysts or experimental conditions, mass transfer (external and internal) limitations have to be avoided to obtain kinetic data from the reactions performed. Kinetic regime is achieved when the determining step for the reaction rate is reaction on the surface, while when the rate is determined by the diffusion of reagents and product from the bulk solution to the surface and vice versa the regime is of external mass transfer. Finally, if the catalytic material present porous structure and the rate is determined by the diffusion through the pores of reagents and products the reaction is under internal mass transfer regime. An Ir/CeO₂ catalyst

prepared by deposition precipitation has been used as reference catalytic material to determinate the influence of internal and external mass transfer effects in the batch reactor used to perform the catalytic tests.

Reusability tests have also been performed to confirm the activity and stability of the catalyst used and explore a possible future real-world application studying the long-term performance of the catalyst.

Moreover, periodic density functional theory (DFT) calculations have been performed to help to identify the lower energy reaction pathway on the most common Iridium surface, the (111) facet.

3.2. Optimisation of reaction parameters

In order to provide accurate and reproducible sets of kinetic data, the hydrous hydrazine decomposition tests were performed in a batch reactor under optimised reaction conditions. The tests were monitored by collecting the gases produced, H_2 and N_2 , during the reaction and, as explained in Chapter 2 Section 2.3.1., quantifying the moles of gaseous product produced during the catalytic test. The optimisation of the reaction conditions was performed using as catalysts Ir/CeO₂ with a nominal loading of 1 wt.% prepared following the deposition precipitation (DP) method with NaOH and reduced at 600°C in 5 %H₂/Ar flow for 3 hours (Ir/CeO₂ DP 600 3h) or 6 hours (Ir/CeO₂ DP 600 6h). Due to the large amount of catalyst required for the tests and limited amount of catalyst prepared with this method, 2 grams per batch, the effect of the stirring rate was studied using 1 wt.% Ir/CeO₂ DP reduced at 400°C in 5% H₂/Ar flow (Ir/CeO₂ DP 400 3h). Since the evaluation of the kinetic data relies on the volumetric quantification of evolved gases, a study of the evaporation of reaction mixture and variation of pressure inside the sealed reactor due to the effect of the temperature is necessary in order to reduce the experimental error on the analyses performed and ensure a high level of reproducibility. The evaluation of the impact of these factors on the final value of the volume of gas collected was carried out by blank reactions carried out using the same experimental reaction conditions in the absence of catalyst. In Figure 3.1, is displayed the volume of gas collected over the reaction time at the different reaction temperatures, 30-70°C, used during the experiments conducted in the successive part of the project. In addition, catalytic tests

on deionised water were performed to be certain that the reagent did not undergo quantifiable thermal decomposition in the batch reactor.

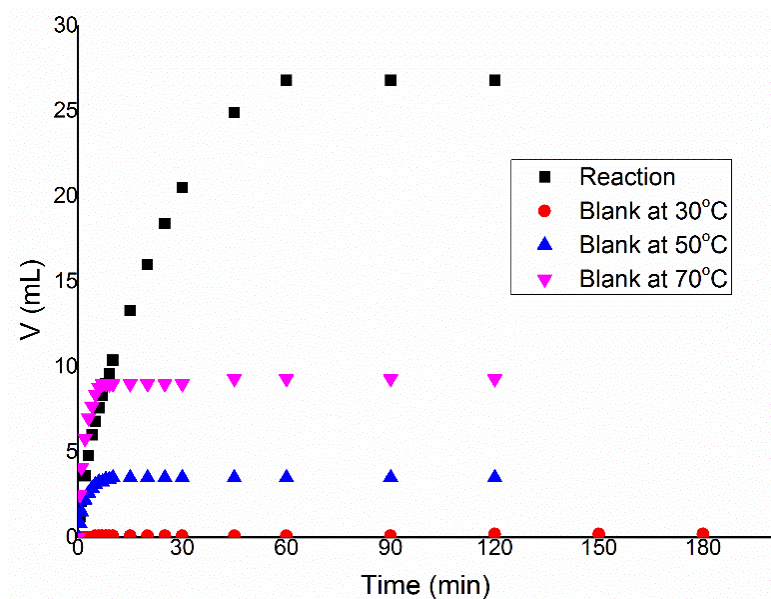


Figure 3.1. Volume of gas generated from reactor versus reaction time for 8.3 ml of hydrous hydrazine solution containing 1mmol of NH_2NH_2 in presence of catalyst at 50°C and blank reaction at 30°C, 50°C and 70°C.

To ensure that the tests were reproducible, the reactions were performed in the same reaction condition twice or three times, as exemplified in Figure 3.2, where the value of $n(\text{H}_2+\text{N}_2)/n(\text{N}_2\text{H}_4)$ is plotted against the reaction time.

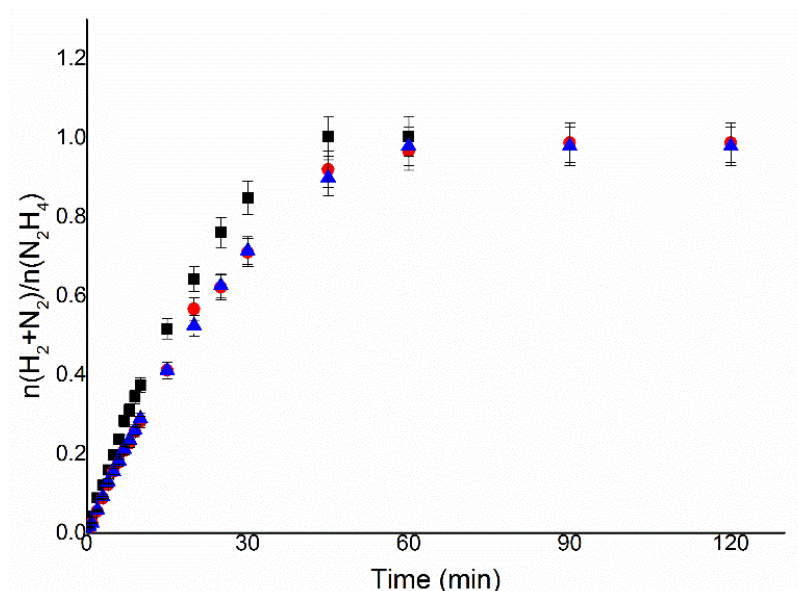


Figure 3.2. $n(\text{H}_2+\text{N}_2)/n(\text{N}_2\text{H}_4)$ versus time for reaction of 0.3 mL, 3.3 M of hydrazine monohydrate in 8 mL 0.5 M of NaOH solution using 152.4 mg of Ir/CeO₂ DP 600 3h, at 50°C and 1050 rpm of stirring rate.

As it can be observed, the initial values of $n(\text{H}_2+\text{N}_2)/n(\text{N}_2\text{H}_4)$ are the most affected by the experimental error of measurements. This is due to both a larger effect of the experimental error of the blank reaction, which tends to be more stable on longer reaction times, and a general larger relative error that decrease when the value of the measurement increase, remaining the absolute error on the measurement the same over the duration of the reaction. During the project, the reactions were compared by the value of final yield, the time for the complete decomposition of the reagent and using the turnover frequencies (TOF) at 50 % of total conversion in order to limit the influence of the error on the initial readings on the catalytic comparison of different samples tested.

An accurate evaluation of the catalytic activity of a material requires the confirmation that the reaction has been performed under kinetic conditions, which means that the reaction rate is dependent only on the surface reaction rate without influences from internal and external mass transfer effects. The external mass transfer is the diffusion of reactant from the bulk solution to the surface of the material and the migration of the products from the surface to the solution, this phenomenon is influenced by the concentration of the reagents, the stirring rate, the amount of catalyst and the temperature of the solution. Whilst, the internal mass transfer is the migration in and out of the pores of the materials of reagents and products, that is influenced by the concentration of the reagents on the surface, the amount of catalyst used and the temperature.

3.2.1. Effect of the stirring rate

External mass limitations are related with the diffusion of the reactants through the interphase layer between liquid and solid, this is influenced by three main factors: the surface of the interphase, the concentration of the species on the two phases and the thickness of the interphase itself. The surface is strictly linked with the amount of catalyst used and the dimension of the particles, that can be considered constant for the same catalyst and amount. As explained in Chapter 2, the initial concentration of the hydrous hydrazine in the solution have been kept constant for reason related to the experimental set up used. On the other side increasing the stirring rate on the reactor decreases the thickness of the interphase, allowing, therefore, faster diffusion of the reactants. The stirring rate was consequently varied in the range between 600 and 1200 rpm, whereas the temperature and

substrate/metal molar ratio were kept at 50°C and 250:1 substrate/metal molar ratio and 0.3 mL of 3.3 M hydrous hydrazine solution in 8 mL of 0.5 M NaOH were used. From the comparison of the TOF_{50%} using different stirring rates, Figure 3.3, a plateau was reached for values above 900 rpm, confirming the achievement of kinetic regimes above this stirring rate.

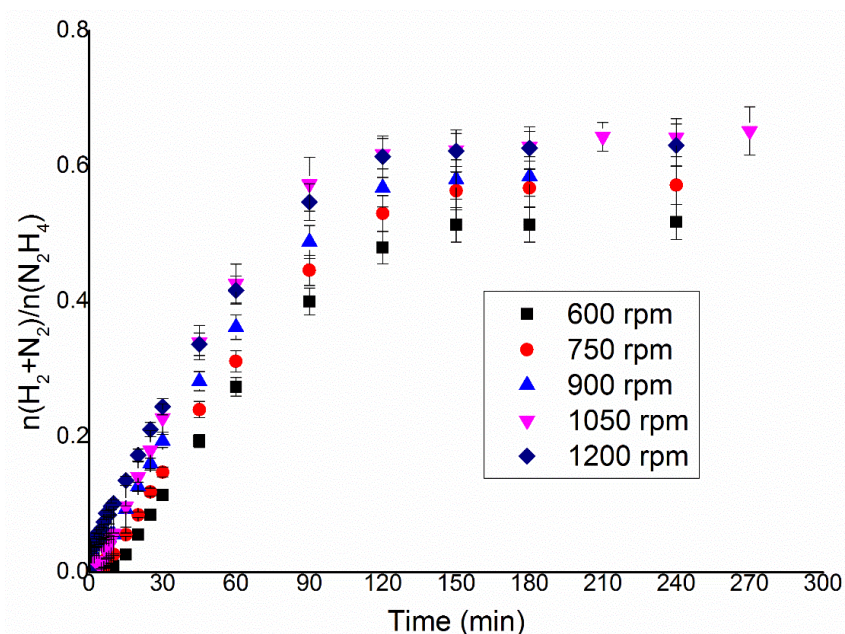


Figure 3.3. $n(\text{H}_2+\text{N}_2)/n(\text{N}_2\text{H}_4)$ versus time for hydrous hydrazine decomposition over Ir/CeO_2 DP 400 3h using 0.3 mL of 3.3 M hydrazine monohydrate in 8 mL 0.5 M of NaOH solution, at 50°C and 152.4 mg of catalyst, varying the stirring rate from 600 to 1200 rpm.

The gas evolution over time, displayed in Figure 3.3, showed how in this case the variation of the stirring rate did not affect only the rate of the reaction, but at lower stirring rate the final yield toward molecular hydrogen of the system was lower. For both parameters, such as reaction rate and selectivity, 1050 and 1200 rpm were equally feasible stirring rates to be used in the hydrous hydrazine decomposition catalytic tests, as it is shown in Figure 3.4. To decide which of the two rates to use in the succeeding tests the stability of the rotation of the stirrer during the reaction was considered. Higher rotation speed decreases the stability of the magnetic stirrer on the rotation axis which can lead to droplet of the solution on the walls of the reactor and general instability of the stirrer bar. For these reasons, 1050 rpm was chosen as the optimal stirring rate for the following catalytic tests.

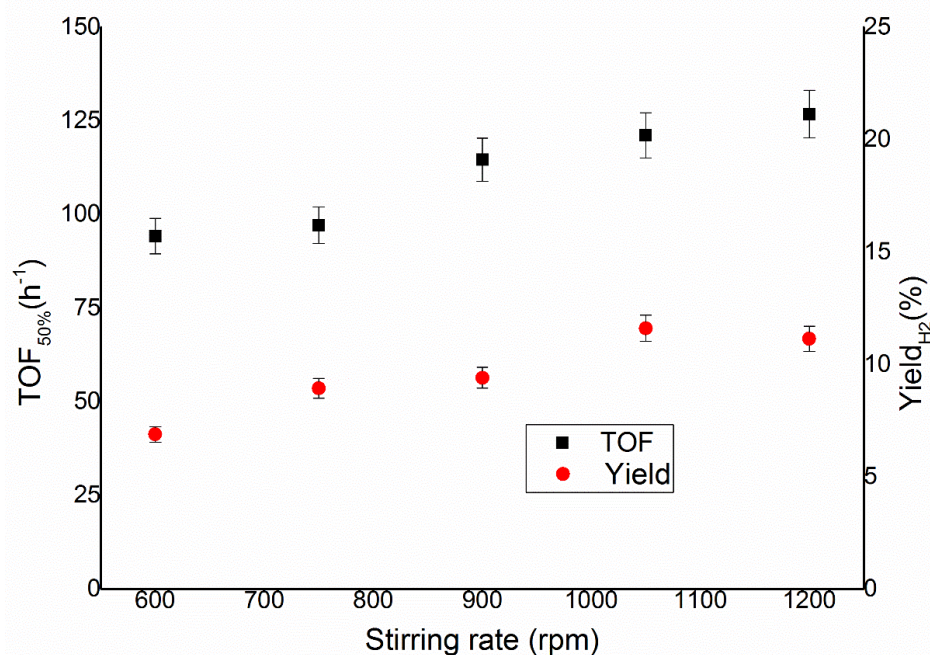


Figure 3.4. Turnover frequency, left y axis, and yield toward hydrogen, right y axis, of the reaction over Ir/CeO₂ DP 400 3h at different stirring rates.

3.2.2. Effect of the mass of catalyst

In a purely kinetically limited reaction, the rate of reaction is proportional to the number of active sites, for this reason varying the amount of catalyst used in the reaction, therefore the number of active sites, is one of the primary tests to identify the presence of mass transfer limitations. In the latter case modifying the amount of catalyst lead to a non-proportional variation on the activity of the catalysts since in this situation the reaction is controlled by the speed of the diffusion of the reactant from the bulk solution through the interface between the liquid and solid and, if the material present pores, the diffusion in and out of the pores. The preliminary tests on the influence of the mass of the catalyst used a temperature of reaction of 50°C, 0.3 mL of hydrous hydrazine 3.3 M in 8 ml of 0.5 M NaOH solution, as described in Chapter 2, and Ir/CeO₂ DP 600 3h as catalyst. The reaction mixture was left to react until the production of gases was stopped for at least 30 min. The stirring rate used for these tests was set to a value of 1050 rpm after the study reported in the previous section. These catalytic tests were performed varying the amount of catalyst used from 38.1 mg to 152.4 mg, which correspond to a substrate/metal molar ratio of 500:1 to 125:1. This range of values was chosen for two reasons, firstly, molar ratios lower than 125:1 requires high amounts of catalyst which would have precluded the possibility of higher the number of catalytic tests on

these catalysts, secondly, for molar ratios lower than 500:1, following the trend demonstrated by the catalytic tests performed, would have required a longer reaction time to record good readings of the data in the final stages of the reaction. The reaction profiles of these catalytic tests, displayed in Figure 3.5, demonstrate that the amount of catalyst used did not have any sensible influence on the final yield of the reaction at the specific studied range. However, in order to identify a possible influence of mass transfer effect the value of $\text{TOF}_{50\%}$ was calculated in order to weight the activity of the reaction with the amount of active metal used in the reaction. These $\text{TOF}_{50\%}$ have been calculated to be 297.6, 358.3 and 366.0 h^{-1} for the ratio 125:1, 250:1 and 500:1 respectively, whereas the final yields are 24.5%, 23.9% and 24.1%, which can be considered constant within the experimental error of the measurement. These data showed that as expected the final yield of the reaction is independent from the mass of catalysts used in the reaction, but the activity increases between the ratios 125:1 and 250:1, while the difference in TOF between 250:1 and 500:1 stay within the error of the analyses. The observed catalytic behaviour indicated the higher amount of catalysts (ratio 125:1) tend to limit the diffusion of the reagent in the solution whereas the kinetic regime was achieved above the 125:1 molar ratio.

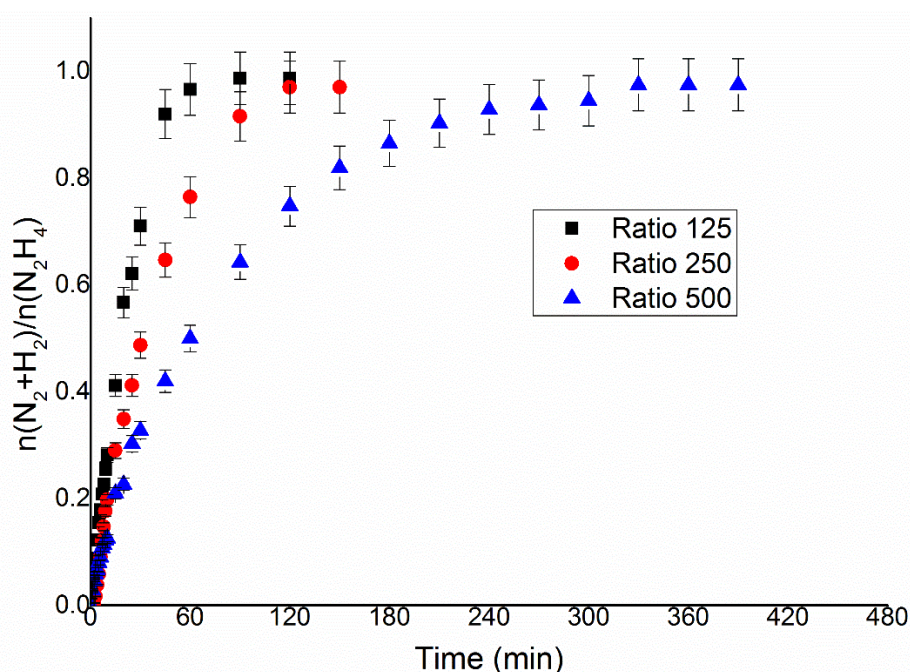


Figure 3.5. $n(\text{H}_2+\text{N}_2)/n(\text{N}_2\text{H}_4)$ versus time for hydrous hydrazine decomposition over Ir/CeO_2 DP 600 3h using 0.3mL of 3.3M hydrazine monohydrate in 8mL 0.5M of NaOH solution, at 50°C and 1050 rpm of stirring rate, with different amount of catalyst 38.1, 76.2 and 152.4mg for the ratio 500:1, 250:1 and 125:1 respectively.

The 250:1 substrate/metal molar ratio, corresponding to 76.2 mg in the case of 1 wt.% Ir catalysts, was chosen as optimal value of the following catalytic tests, as a reasonable compromise between the time of reaction and the amount of catalyst used, allowing to perform at least two catalytic reactions per day per experimental set up and more than 10 reactions per batch of catalyst synthesised.

3.2.3. Effect of NaOH concentration

As the final step of the optimisation process, the influence of the concentration of sodium hydroxide on the reaction solution was studied. As previous works in literature have displayed that the presence of NaOH in the decomposition of hydrous hydrazine in aqueous solution has a beneficial effect on the selectivity of the reaction, and in some cases also on the activity of catalysts.¹⁻³ This effect is most probably related to the formation, in neutral solutions, of the protonated form of hydrazine (N_2H_5^+). A deeper analysis of the reaction pathway will be discussed later in this chapter, but the presence in N_2H_5^+ of a third hydrogen atom bonded to a nitrogen probably leads, to the direct formation on the surface of the metal of ammonia which is more stable than other species derived from N_2H_4 and therefore decreasing the formation molecular hydrogen. Hence, the effect of the concentration of NaOH in solution was studied varying its value between 0 M and 1 M, and results are presented in Figure 3.6, using the previously optimised values of substrate/metal molar ratio, 250:1, and stirring rate, 1050rpm, at 50°C and using Ir/CeO₂ DP 600 6h as the reference catalyst. Figure 3.7 displays the increase in final yield with the concentration of sodium hydroxide, till a plateau is reached around a concentration value of 0.5M, whereas the activity of these catalysts decreases with the decrease of the concentration of sodium hydroxide.

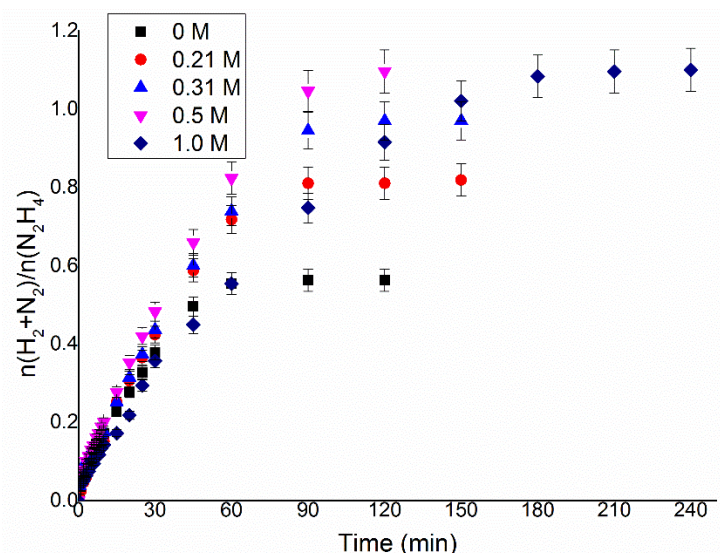


Figure 3.6. $n(\text{H}_2+\text{N}_2)/n(\text{N}_2\text{H}_4)$ versus time for hydrous hydrazine decomposition over Ir/CeO_2 DP 600 6h using 0.3mL of 3.3M hydrazine monohydrate in 8mL of NaOH solution with a concentration between 0 and 1.0 M, at 50°C, 1050 rpm of stirring rate and 250:1 substrate to meta molar ratio.

The observed catalytic behaviour can be due to different explanations, such as (I) the lower rate of adsorption of the reagents and/or (II) the slower individual elemental steps. With the aim of achieving the highest selectivity possible from the catalytic system using the lowest possible amount of additive, to increase the economy of the system itself, it was decided to perform the consequent tests with a NaOH concentration of 0.5M, since this was the lowest value on plateau of the yield versus concentration as showing in the following graph.

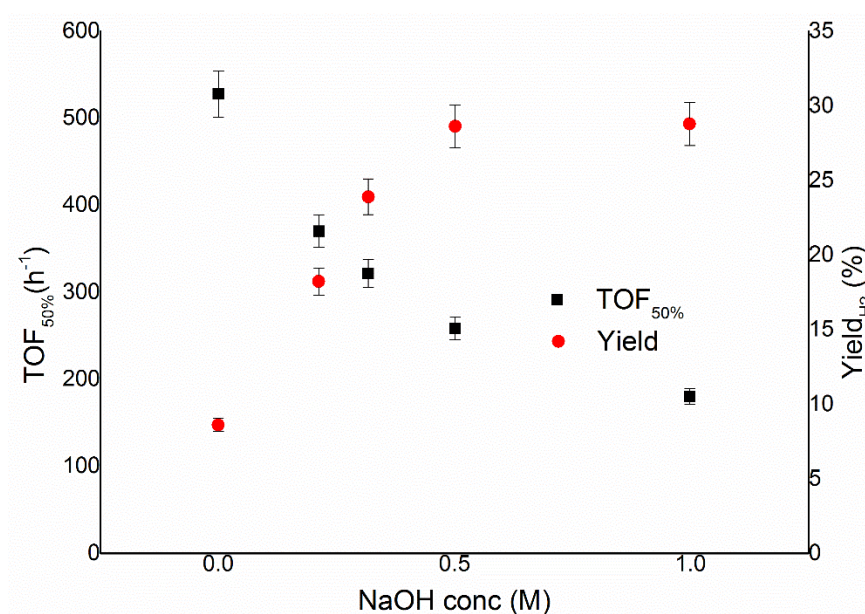


Figure 3.7. Turnover frequency, left y axis, and yield toward hydrogen, right y axis, of the reaction over Ir/CeO_2 DP 600 6h as function of the concentrations of NaOH.

3.2.4. Effect of the reaction temperature

The last parameter to optimise for the liquid phase catalytic decomposition of hydrous hydrazine was the temperature of the reaction. In literature is reported that for many catalysts the increase of the temperature of the reaction mixture led to a decrease in the final yield of hydrogen of the system, whereas the activity increased.^{4,5} To confirm this trend, the reaction was performed at 30, 50 and 70°C with the experimental conditions optimised in the previous reported catalytic tests, as shown in Figure 3.8.

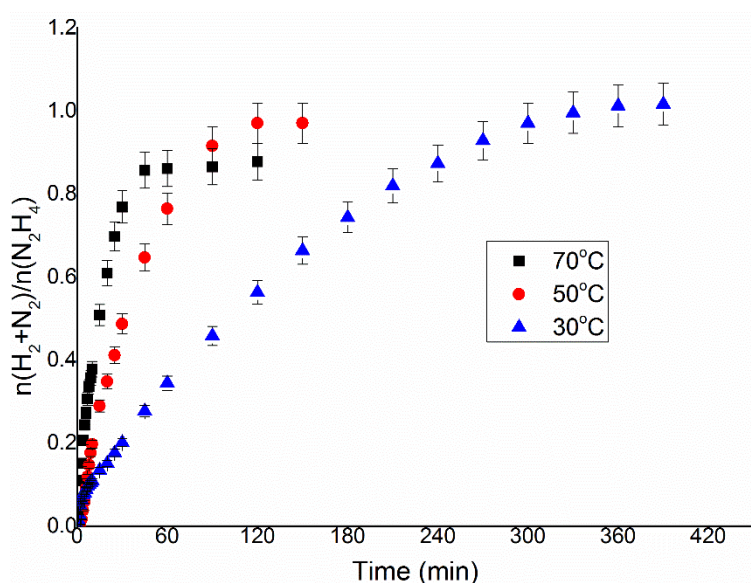


Figure 3.8. $n(\text{H}_2+\text{N}_2)/n(\text{N}_2\text{H}_4)$ versus time for hydrous hydrazine decomposition over Ir/CeO₂ DP 600 3h using 0.3mL of 3.3M hydrazine monohydrate in 8mL of 0.5M NaOH solution at 1050 rpm of stirring rate and 250:1 substrate to metal molar ratio and temperature of 30°C, 50°C and 70°C.

Figure 3.9 displays that the tendency of the decrease of selectivity is respected also in the case of Ir/CeO₂ DP 600 3h where the final yield decreased from 25.6% at 30°C to 20.4% at 70°C. On the other hand, the TOF_{50%} of this reaction went from 107.3 h⁻¹ to 923.0 h⁻¹, for 30 and 70 °C. The temperature chosen for the succeeding tests was 50 °C, which showed values of activity and selectivity intermediate, permitting to test also catalysts with lower activity, without sacrificing much in terms of selectivity.

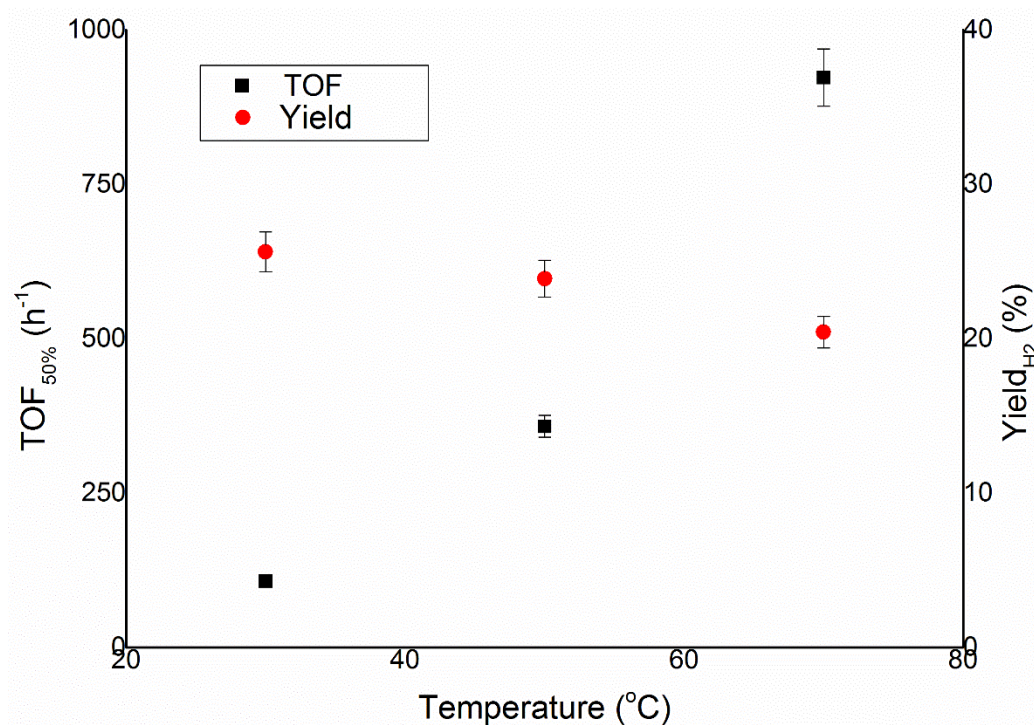


Figure 3.9. Turnover frequency, left y axis, and yield toward hydrogen, right y axis, of the reaction over Ir/CeO₂ DP 600 3h as function of temperatures.

3.3. Preliminary Reusability studies

In order to assess the stability of the catalytic material under the experimental reaction conditions, a preliminary reusability test was performed on Ir/CeO₂ DP 600 3h. Reusability tests were conducted, as described in Chapter 2, by adding a fresh hydrous hydrazine solution of known concentration, when gases stop to evolve from the reaction mixture, which is considered a signal of complete decomposition of hydrous hydrazine (100% conversion). The same catalyst has been used up to five reaction cycles, as can be seen in Figure 3.10.

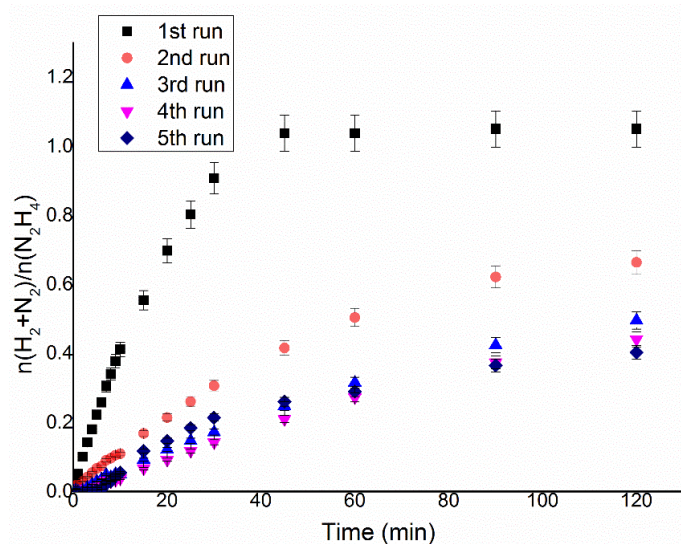


Figure 3.10. $n(\text{H}_2+\text{N}_2)/n(\text{N}_2\text{H}_4)$ versus time for hydrous hydrazine decomposition over Ir/CeO₂ DP 600 3h using 8mL of 0.5M NaOH solution at 50°C, 1050 rpm of stirring rate and 250:1 substrate to metal molar ratio, 0.3mL of 3.3M hydrazine monohydrate was added before each reaction.

The final yield toward molecular hydrogen of the reaction decreases after each run, whereas the activity measured by the TOF_{50%} reaches a minimum in the third run and increases in the fourth and fifth run, as shown in Figure 3.11. Firstly, to be noticed is that the reaction restarts when new aqueous solution of hydrous hydrazine is added in the sealed reactor, indicating a preliminary proof in this way that at the end of the gas evolution is related to a complete decomposition of the reagent, this assumption was later verified during the project by colourimetric quantification of hydrazine in the reaction mixture, reported in Chapter 4 Section 4.3.6. . Secondly, the variations in terms of activity and the decrease in final yield during the subsequent reactions can indicate a possible change of the catalytic species presented on the surface of the support. The aqueous catalytic decomposition of hydrous hydrazine can take multiple pathways also for the production of the same products, so the poisoning of specific catalytic sites⁶ or the reconstruction⁷ of the surface can vary specific pathways with respect to the others. The increase of the TOF, between the third and fourth and fifth runs, strongly suggest a mechanism of modification of the surface since the creation of the type of catalytic active species on the surface of the nanoparticles would agree with a change on reaction pathway for the production of hydrogen like the one exhibited by the Ir/CeO₂ catalyst in this specific reaction test. This modification of the nanoparticles would agree with the comparison among preparation methods that produce small mean particle

size and larger mean particle size, in which the latest show higher activity but lower selectivity than the material with smaller mean particle size, as reported in Chapter 4 Section 4.2.1. .

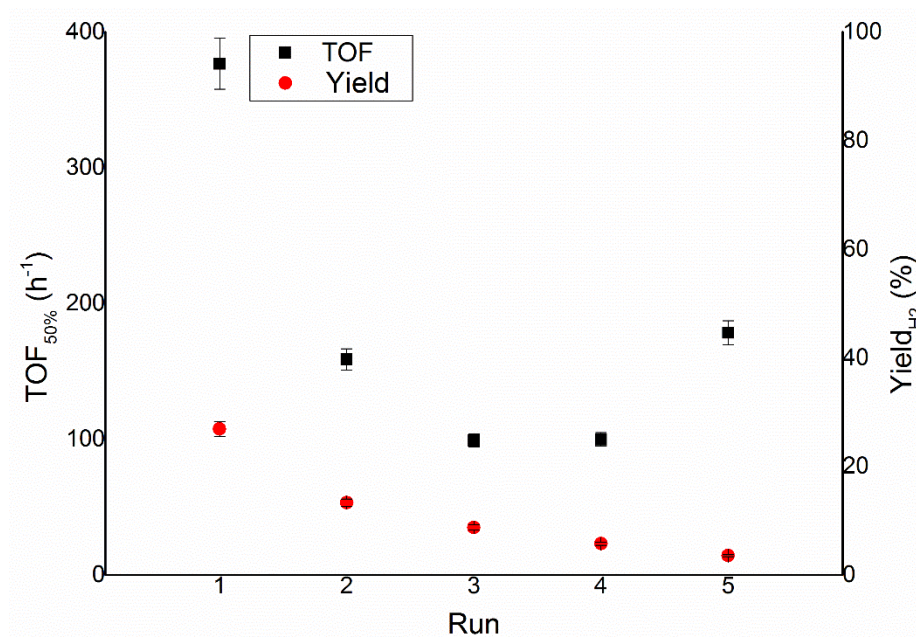


Figure 3.11. Turnover frequency, left y axis, and yield toward hydrogen, right y axis, of the reaction over Ir/CeO₂ DP 600 3h at during the reusability tests.

3.4. Characterisation of fresh and used catalysts

In order to better understand the catalytic materials tested, a series of different characterisation techniques and measurements have been conducted. Hereafter are reported some of the preliminary characterisations of Ir/CeO₂ DP 400 and Ir/CeO₂ DP 600 3h performed to measure specifically (I) surface area, (II) mean particle size and particle size distribution, (III) superficial oxidation state and surface coverage and (IV) thermal reduction profile.

3.4.1. BET (Brunauer-Emmett-Teller) method surface area

As explained in Chapter 2, the total surface area of the samples can be determined from the BET equation.^{8,9} Bare CeO₂ have been analysed besides Ir/CeO₂ DP 600 3h in order to assess possible change on the total surface area of the catalyst occurred during the preparation of the samples. The total surface area for the bare support has been calculated as 44 m² g⁻¹ and the Ir/CeO₂ catalyst one as 49 m² g⁻¹. Firstly, to be noticed is that the bare support has value of high surface area for a non-porous oxide, similar to the value reported for TiO₂ P25 (≈50 m² g⁻¹), confirming that the support was composed by nanoparticles of CeO₂. Secondly, even

if there is an increase in the surface area between the support and the catalyst, the increase of the value is at the limit of the 5% experimental error range of the analytical instrument used so no clear determination on the extent of the surface area of the Ir nanoparticles deposited on the support. For this reason, other characterisation techniques, like XRD and TEM, have been employed from hereafter to determine crystalline phase, crystallite/particle size and dispersion of Ir nanoparticles.

3.4.2. Powder X-ray diffraction (p-XRD)

X-ray diffraction analyses were performed on the catalysts in order to define the crystal structure of the different chemical species in the samples and their mean crystallite size by the use of the Scherrer equation (Eq. 2.16). In this chapter are studied Ir/CeO₂ catalysts so CeO₂ and different Ir species are used as a reference. For the CeO₂ main characteristic diffraction peaks to assign, are related with the (111), (200), (220) and (311) planes, which tend to have the higher intensities, at $2\theta = 29.3^\circ$, 33.1° , 47.5° and 57.6° , respectively.¹⁰ On the other hand, Iridium can be presented on the surface both as metallic Ir and IrO₂, the most common and stable oxide form. The first of these species, Ir⁰, shows diffraction peaks at $2\theta = 40.8^\circ$, 47.2° , 69.1° and 83.6° corresponding to the (111), (200), (220) and (311) planes,¹¹ on the other hand IrO₂ diffraction peaks at $2\theta = 28.1^\circ$, 35.0° , 39.8° and 55.3° respectively for (110), (101), (200) and (211) planes.¹²

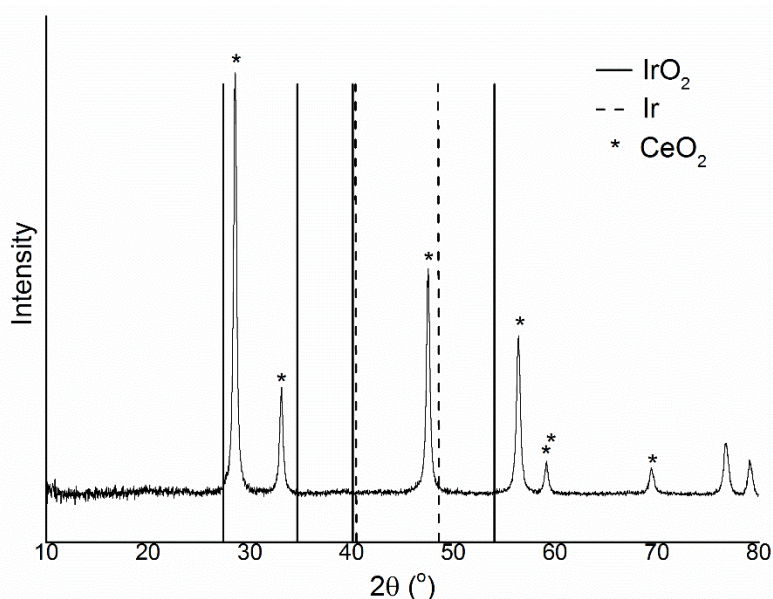


Figure 3.12. XRD pattern of Ir/CeO₂ DP 400 recorded between 10° and 80°.

Figure 3.12, the X-ray pattern of Ir/CeO₂ DP 400 used as example, exhibits the characteristic diffraction peaks of CeO₂, and it can be observed that the diffraction peaks are not narrow and sharp. This phenomenon is related with the nanometric size, 25 nm nominally, of the CeO₂ powder used, since as it can be seen from the Scherrer equation the width of the diffraction peak is inversely related to the dimension of the crystallite, this dimension can be calculated as 21.6 nm through the Scherrer equation (0.38° of full wide of maximum for the peak at 28.6°). Most of the more intense peaks for the Iridium species are in the range of less than 2° to some diffraction peaks of CeO₂. Due to the small amount of Iridium present on the catalysts, 1 wt.%, the best region where to look for the presence of Ir species is around 40° where Ir(111), 40.8°, and IrO₂(220), 39.8°, are located. From Figure 3.13 it is evident there is no presence of diffraction peaks in the 40°-42° region, which can be attributed to the following explanations: first the crystallite size of the Ir particles is small (≤ 5 nm) so that the broadening of the diffraction peak and the low intensity due to the small amount present, make the peak undistinguishable from the baseline of the analysis; second the Iridium can be an oxide but amorphous, in this way not having a discrete diffraction pattern at the X-ray analysis.

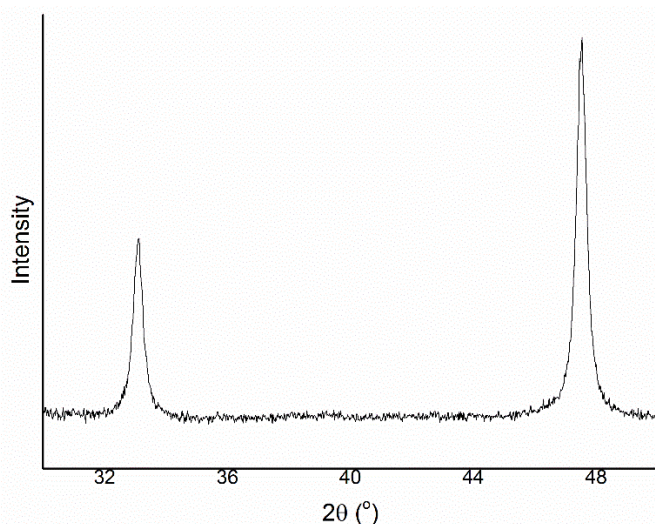


Figure 3.13. XRD pattern of Ir/CeO₂ DP 400 magnified in the 30°-50° region.

3.4.3. Inductively Coupled Plasma - Mass Spectroscopy (ICP-MS)

ICP-MS was used to quantify the amount of Ir immobilised/deposited on CeO₂ support during the immobilisation/deposition step of the preparation method. A part of the filtrated solution, 5 ml of 500ml, was collected before the final washing of the catalysts for ICP-MS

analysis. The used of ICP as ionisation method coupled with the mass spectrometer permit to analyse ppb and ppt level of concentration of metal. The result of the analysis, after dilution of the filtrate solution, is a concentration of Ir of 12.06 mg L^{-1} . Considered a total volume of the solution of 500 mL, this indicates that 6.03 mg of Ir were not immobilised on the surface, with respect to the 20 mg used for the synthesis, giving a deposition efficiency of 69.9 wt.%. The metal loading calculated by ICP-MS is therefore used to calculate the substrate/metal molar ratio and TOF values.

3.4.4. Scanning Electron Microscopy (SEM) and Energy Disperse X-ray Spectroscopy (EDS)

Different typologies of electron microscopy techniques are used in material characterisation. One of the most used among them is SEM. This technique allows the imaging of the surface of the material and therefore the detection of macroscopic changes on the morphology of the catalyst, especially the support. SEM is often coupled with an Energy Disperse X-ray detector (EDX) in order to analyse the X-ray emitted by samples under the electron beam during the analyses. Since each element emits X-ray with a precise energy signature EDS combined the mapping of the surface gives an elemental mapping sample. With the elemental mapping of the sample dispersion of the different elements can be investigated and also the total amount of the different elements can be quantified inside a certain degree of confidence.

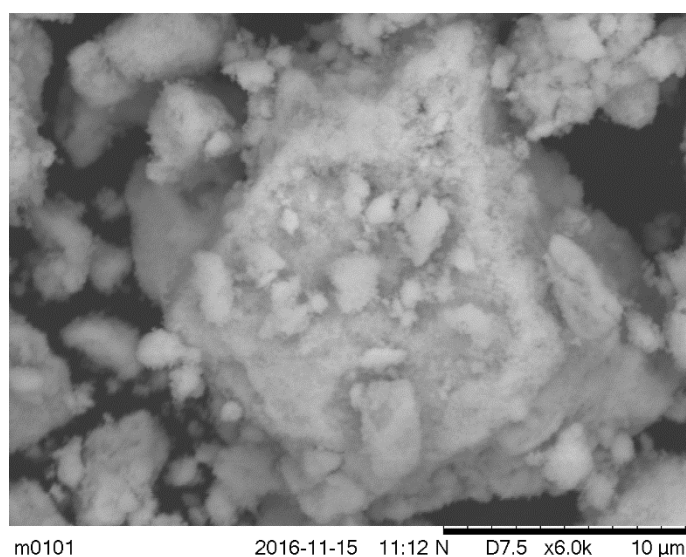


Figure 3.14. Example of SEM Imaging of Ir/CeO₂ DP 600 Gh with an x6.0k magnification.

Figure 3.14 shows a representative image of Ir/CeO₂ DP 600 6h catalyst morphology on the 10 μm scale. Figure 3.15 instead shows some surface mapping of Ir/CeO₂. From the EDX the average total value of Ir loading onto the support, is 0.70 wt.% ± 0.1 with a good dispersion over the sample, with no empty zone of Ir nanoparticles in the Ir map. The 0.70 wt.% is lower than the calculated 1.0 wt.% by the amount of precursor used during the preparation of the catalyst, but it agrees with the ICP-MS analyses reported before. This lower loading is probably related to the deposition-precipitation method employed for the synthesis which can be greatly influenced by pH, temperature and time of deposition. For this reason, the deposition-precipitation catalysts have been used with a calculated loading of 0.7 wt.% instead of the nominal 1%.

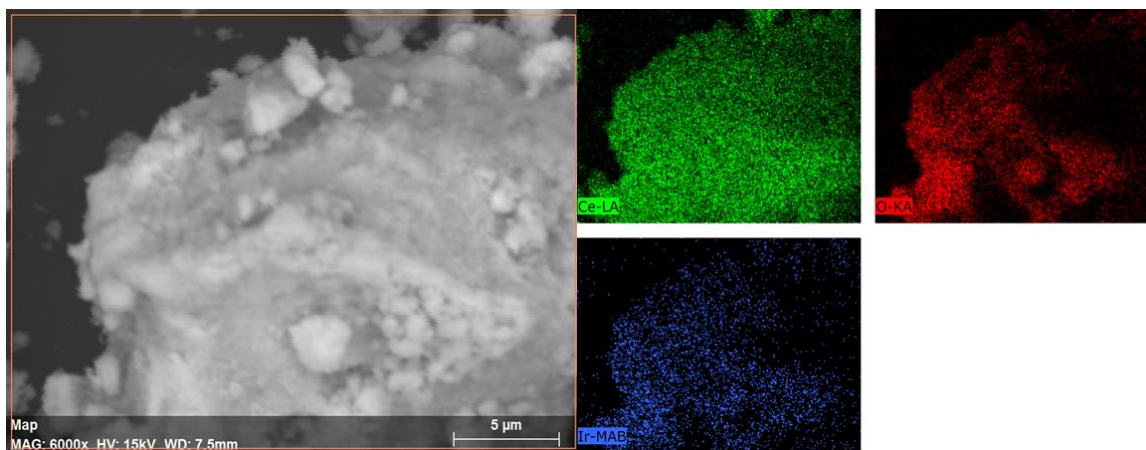


Figure 3.15. SEM-EDX mapping of a portion of Ir/CeO₂ DP 600 6h sample, that displays and homogeneous distribution of Ce, O and Ir across the material as expected.

3.4.5. Transmission Electron Microscopy (TEM)

For the characterisation of metal nanoparticles in terms of mean particle size and particle size distribution, the use of transmission electron microscopy is of primary importance for the characterisation of the catalytic species. This technique allows the measurement of individual nanoparticle size from which statistical data such as mean particles size and distribution can be obtained. Ir/CeO₂ DP 400 was analysed both before (fresh) and after (used) the reaction. One of the requirements, in order to achieve a good resolution of the images, is the difference in atomic mass of the metal of nanoparticles and the other elements in the sample since heavier element diffract the electron beam more than lighter ones, therefore, creating darker 2-D projection on the fluorescent screen. Even if Ir has an atomic mass higher than Ce the

difference of the diffraction between the elements is not high, which can lead to a more difficult count e measurement of the Ir nanoparticles over the cerium oxide support.

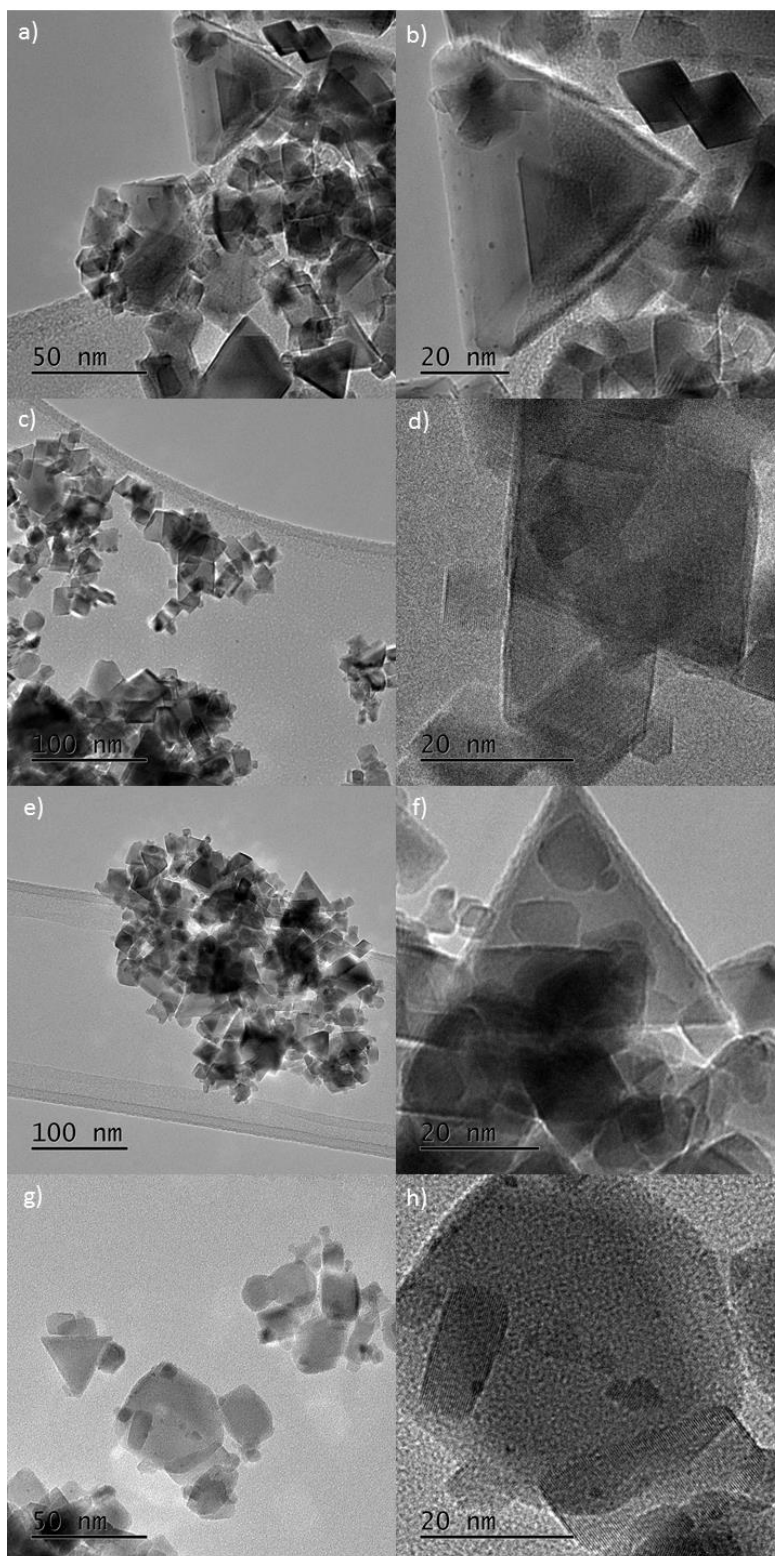


Figure 3.16. TEM images of Ir/CeO₂ DP 400 fresh, a-d, and used, e-h. Ir nanoparticles can be seen as dark spots in the higher magnification images, while grey larger particles are the CeO₂ support.

In Figure 3.16, representative images of the fresh and used catalysts are displayed. As can be seen, the CeO₂ is present as crystals in the range of 10-50 nm. On the other hand, only few nanoparticles of Ir can be distinguished from the background due to low contrast with the support, so only nanoparticles on a thin layer of oxide or on the edge of its particles, and also because their dimensions are small. CeO₂ tends to get charged on the surface during the analysis, with effect to increase interferences and therefore it makes more difficult the acquisition of high magnification pictures, which are required to see the presence of very small nanoparticles (below 2 nm). For these reasons the amount of Ir nanoparticles measured was not enough to obtain a statistically valid sample pool, but this can be used as a first indication for nanoparticles size before the measurement of other catalysts with different supports or preparation method, and so more easily analysable.

The fresh catalyst, Ir/CeO₂ DP 400, has a mean particle size of 0.9 ± 0.2 nm (counting 33 nanoparticles for this sample), whereas the same catalyst after being used has a mean particle size of 1.2 ± 0.4 nm (with a 21 particles sample). This indication can help us explaining why XRD analysis did not show the presence of diffraction peak that could be related with Ir species since >1nm particles have very broad diffraction peaks that could merge with the background of the analysis. The difference between the mean particle size of fresh and used catalysts is in the range of the error of the analyses.

Because of the poor contrast and the very small dimension of the nanoparticles, no lattice fringes have been found during the analysis of the samples, therefore no information on the Ir species planes have been discovered.

3.4.6. Temperature Programmed Reduction (TPR)

Temperature programmed reduction has been performed on the catalysts before the reduction at high temperature in H₂/Ar flow in order to optimise the experimental protocol and after that to characterise the synthesised material.

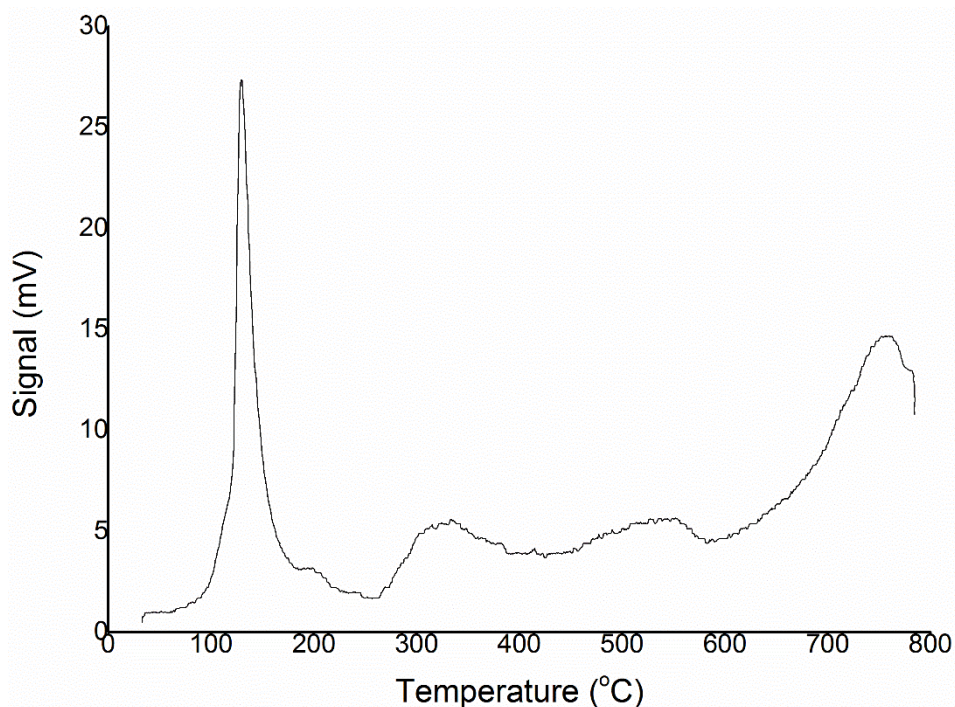


Figure 3.17. TPR analysis of fresh Ir/CeO₂ DP before utilising high-temperature H₂ treatment, showing reduction of Ir at 130°C, and of CeO₂ at 350 and 550°C.

In Figure 3.17 and 3.18 are reported the profile of reduction for Ir/CeO₂ DP 600 3h before reduction with H₂ at high temperature and after this treatment. The untreated catalyst shows an intense and quite narrow peak centred at 130°C which can be identified as the reduction of IrO₂ even if at a lower temperature than what is reported in literature (200°C).¹³ The low reduction temperature of the Iridium nanoparticles can be explained by their small nanoparticle size but also by the use of CeO₂. CeO₂ is known to be a reducible oxide that acts in synergy with the presence of metal nanoparticles on its surface during many redox processes and reduction of the NP itself can be among these processes. To be noticed on the untreated Ir/CeO₂ DP 600 6h are also the two broad peaks at around 320°C and 540°C.¹⁴ These peaks are reported in the literature to be related to the reduction of the CeO₂ close to the metal NPs. This is particularly interesting since it is evidence of a strong metal support interaction (SMSI), which is very important for affecting activity, selectivity and stability. On the bare support the reduction of the oxide is achieved only at higher temperature (>800°C), the lower reduction temperature for some of the CeO₂ is due to the interaction of the O species with NP that can facilitate the reduction. Moreover, the O in the CeO₂ lattice can move more freely than on other metal oxides that lead to migration of O toward the edge of the nanoparticles at higher temperature in order to compensate the vacancy on the lattice left by

the reduction, this can lead to reduction not only of CeO_2 next the particles but also a broader “neighbourhood” region gives a more distinct reduction peak in the TPR analysis.

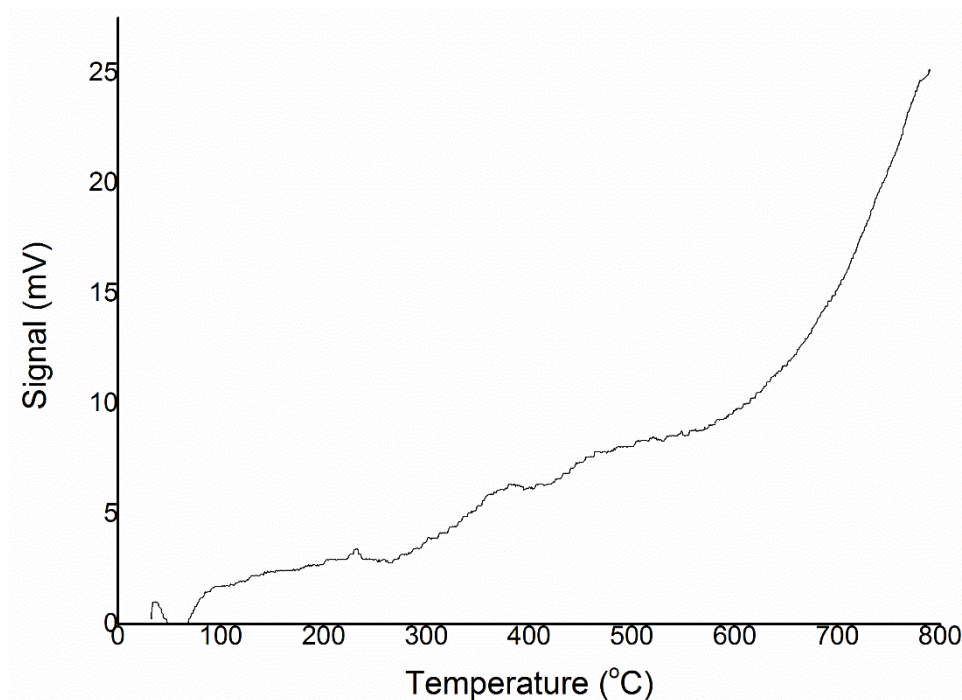


Figure 3.18. TPR analysis of Ir/CeO_2 DP 600 3h after employing high-temperature H_2/Ar treatment, which does not display significant reduction peaks.

On the other hand, the analysis of the reduced catalyst does not exhibit particular peaks, with the exception of two small and very broad peak at 380°C and 480°C, Figure 3.18. These can be related to the CeO_2 reduction, as explained for the untreated sample, probably due to the partial re-oxidation of the CeO_2 by the exposition to air at room temperature, a condition in which the samples have been stored.

3.4.7. X-ray Photoelectron Spectroscopy (XPS)

XPS analysis offers information on the quantitative surface composition (surface metal coverage), presence of impurities and the oxidation state of the different atoms of the surface. These kind of information in catalysis are of paramount importance for the understanding of the catalytic behaviour of the materials. XPS analyses have been performed on different Ir/CeO_2 prepared by deposition precipitation method that had undergone different reduction treatment, as it is shown in Figure 3.19. Also, Ir/CeO_2 DP 600 3h, Ir/CeO_2 prepared by deposition-precipitation with NaOH , was tested before and after the reaction and also at the end of the reusability study, so after a cycle of 10 reactions in row, Figure 3.20.

The main analytical parameters used for the deconvolution of the Ir 4f are the one reported in Chapter 2, Section 2.4.2. . All the iridium species in the Ir 4f region display doublet spins due to the spin-orbit splitting that lead to the creation of the Ir 4f_{7/2}, in the range 60.8-62.8 eV, and Ir 4f_{5/2}, in the range of 63.8-65.8 eV. Moreover, the area of the two peaks of the doublet are related by a specific ratio that in the case of the 4f orbital is 3:4 for 5/2:7/2 peaks. In particular, using as reference the Ir 4f_{7/2}, in literature metallic Ir is reported to have a binding energy of 60.9-61.2 eV, where else IrO₂ has a binding energy of 61.9-62.5 eV and IrCl₃ has one of 62.2-62.6 eV.¹⁵ In the case of Ce 3d, the analysis of the XPS spectrum is more difficult because due to the shake down of the peaks that lead to the formation of two satellite peaks at lower energies for each one of the peaks of the doublet. Therefore, in order to simplify the analyses, fitting for Ce⁺³ and Ce⁺⁴ have been prepared on standard materials, commercial CeO₂ and a reduced CeO₂, and after applied on the XPS spectra.

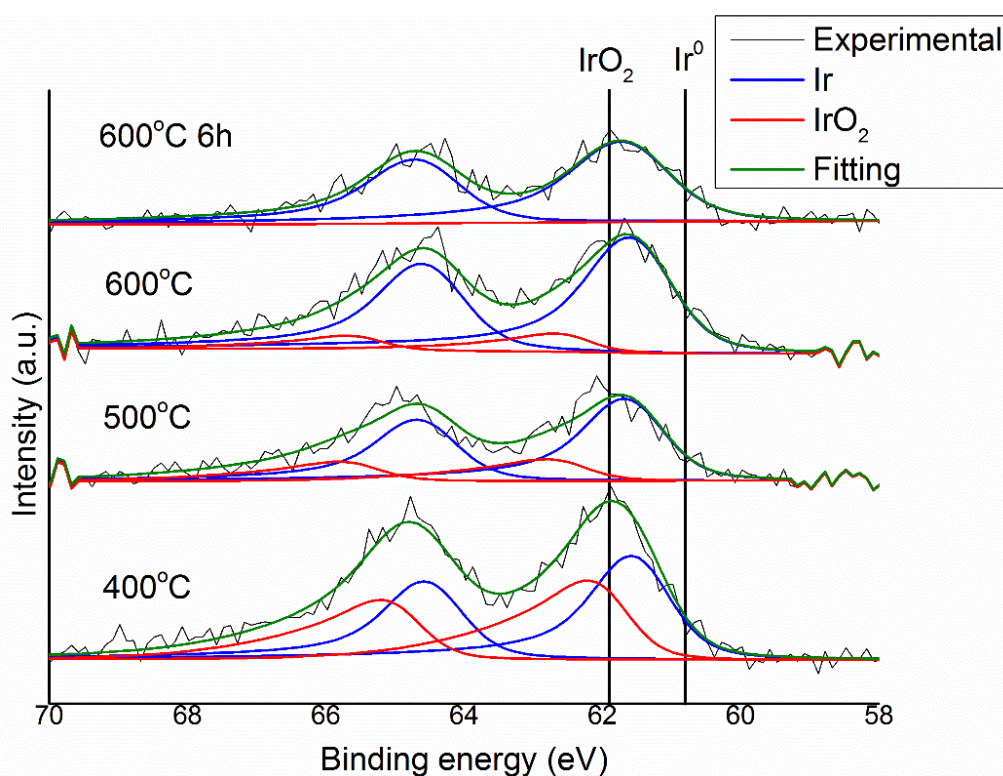


Figure 3.19. XPS experimental spectra and fitting of Ir 4f for Ir/CeO₂ DP 400, Ir/CeO₂ DP 500, Ir/CeO₂ DP 600 3h and Ir/CeO₂ DP 600 6h, Ir/CeO₂ prepared by deposition-precipitation with NaOH treated under H₂ flow at different temperatures, from bottom to top, with the deconvolution of peaks.

In Figure 3.19 are reported the spectra of different Ir/CeO₂ prepared by deposition-precipitation treated in H₂/Ar flow at different temperature (400°C, 500°C and 600°C) and time (3h and 6h). For these XPS spectra, the unfitted data showed a peak for the Ir 4f_{7/2} at

61.6-61.8 eV that can mislead to the assignment of this as IrO₂, but that would be in contrast with the TPR data discussed earlier that confirm the high degree of reduction of the iridium precursor. Therefore, they were fitted with two different peaks and the range of binding energies used were enlarged at higher values than the ones reported in the literature in order to get a more precise fitting of the signal. The best fitting gives two peaks one in the range 61.5-61.8 eV and the other 62.5-62.9 eV that have been assumed to be Ir⁰ and Ir⁺⁴ which are higher than the literature values. A similar phenomenon, but with a down shift, can be noticed frequently during the analyses of Au NPs where small nanoparticles due to partial negative charges on the surface induced by the small particle dimensions. Consequently, the peaks at 61.5-61.8 eV, that undergo an up shift, have been assigned to metallic iridium nanoparticles with partial positive charges due to the small dimensions and interaction with the support, the peaks at 62.5-62.9 eV have been assigned to IrO_x species. The comparison between the catalysts shows similar binding energies for the same two doublet peaks of the two Ir species, but the samples have different ratio between metallic Ir and IrO₂. The atom surface coverage exhibits an increase in the quantity of metallic Ir with the increase of temperature and duration of the reduction treatment, as can be seen in Table 3.1. The presence of oxidised form of Ir in the samples reduced below 600°C can be linked to the peaks of reduction at high temperature that were seen with the TPR analyses, so a partial re-oxidation of the Ir NPs can be due to the action of the support close to the edge of these and higher temperature treatment help to stabilise the metallic form of Ir.

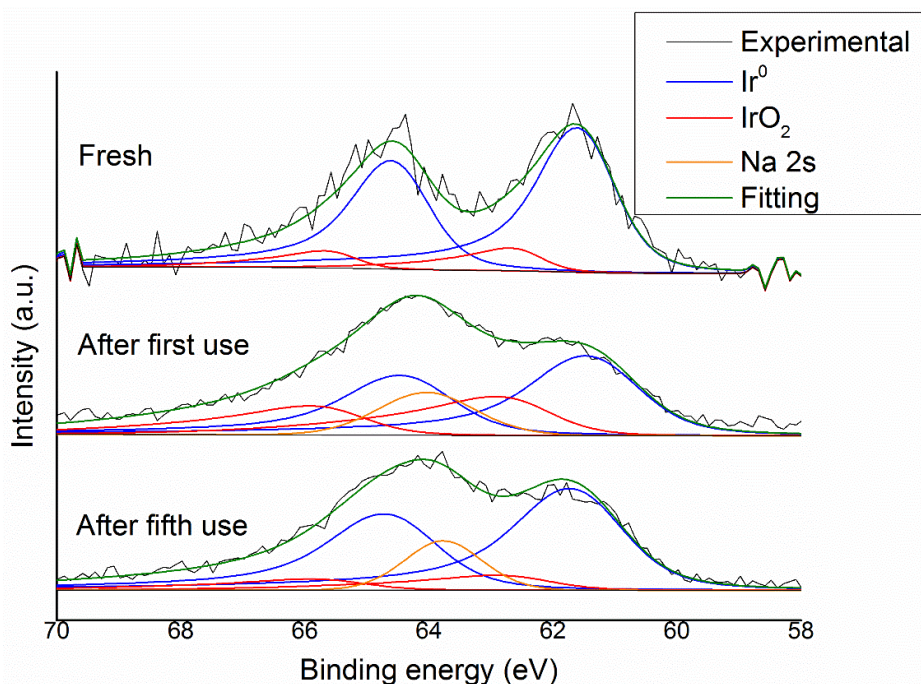


Figure 3.20. XPS experimental spectra and fitting of Ir 4f for Ir/CeO₂ DP 600 3h fresh and after one and five uses with the deconvolution of the peaks.

The comparison between fresh and used catalyst, as shown in Figure 3.20, is less accurate due to the presence of traces of Na on the samples that derive from the NaOH used in the catalytic reaction. Na 2S orbital has a broad single peak at 63.0-64.0 eV this overlap with the Ir 4f region and therefore a precise quantification of the different Ir species is not possible, but the presence of peaks at 61.6-61.4 eV can be found also on the used samples. This small down-shift for the used samples may indicate that aggregation may have occurred and, therefore, an increase in the mean particle size. Taking into account the aforementioned observations, no final and ultimate conclusion can be derived due to the overlapping of the elements.

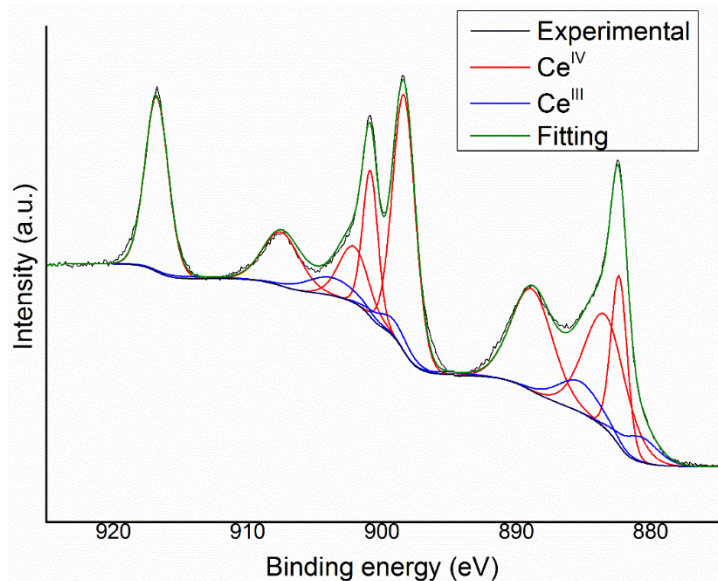


Figure 3.21. XPS experimental spectra and fitting of Ce 3d region for Ir/CeO₂ DP 600 3h with the deconvolution of the peaks.

Figure 3.21 shows the spectra of the Ce 3d region for the different spectra, these are similar and only traces of Ce³⁺ have been detected and most of the Ce is present as Ce⁴⁺, CeO₂.

Table 3.1. XPS values for the Ir species binding energy (BE), ratios on the total Ir and total atom surface coverage of Ir for Ir/CeO₂ prepared by deposition precipitation with NaOH reduced at 400°C, 500°C, 600°C and 600°C for 6h.

Sample	Ir 4f _{7/2} (eV)		Metal coverage (%)		Ir atomic surface coverage (%)
	Ir ⁰	Ir ^{IV}	Ir ⁰	Ir ^{IV}	
IR/CEO ₂ DP 400	61.6	62.1	42.9	57.1	0.53
IR/CEO ₂ DP 500	61.5	62.5	87.6	12.4	0.40
IR/CEO ₂ DP 600 3H	61.6	n.d.	100	-	0.28
IR/CEO ₂ DP 600 6H	61.6	62.3	77.9	22.1	0.35

Table 3.1 reports the value of atom surface coverage for the different elements on the samples analysed. The difference among the values remain in the range of the error the technique, which can be at 10% for such small amount, so can be concluded that the thermal treatment at higher temperature in H₂/Ar flow does not lead at a higher rate of aggregation of the nanoparticles in the range tested for the reduction of Ir precursor.^{16,17}

3.5. Density Functional Theory (DFT)

The decomposition of hydrazine, as described by Eq. 3.1 and Eq. 3.2, can produce N₂, H₂ and NH₃ following two different stoichiometric reactions and each of these reactions can follow different possible pathways formed by several individual elemental steps. DFT calculations were performed to calculate the absorption energies of the possible intermediate formed during the reaction and the transition states of the elementary steps. All this information can be used to get insights about the preferential pathway of reaction on specific Ir surfaces, calculating the free energy and the activation energy of each individual step. DFT calculation combined with *in-situ* ATR-IR, reported in Chapter 4 Section 4.3.7., and the experimental data can give crucial information for the intelligent design of new more Ir catalysts more efficient for the decomposition of hydrous hydrazine to hydrogen.

In the first place, the adsorption of the different species was calculated on the most stable facet IrO₂ and metallic Ir. Adsorption energy (E_{ads}), Eq. 3.3, of reagents and products can be used to probe the viability of the reactions, while looking at the adsorbed species (from here on referenced with * after the molecule) E_{ads} and the activation energies, E_a , involved in each elemental step gives information about the possible reaction pathways.

$$E_{ads} = E_{mol+surf} - (E_{mol} + E_{surf}) \quad (Eq. 3.3)$$

Where $E_{mol+surf}$ is the energy of the molecule adsorbed on the surface, E_{surf} is the energy of the surface alone, E_{mol} is the energy of the molecule.

3.5.1. Adsorption on the IrO₂ Surface

During the collaboration with Dr Alberto Roldan's group in Cardiff, the IrO₂ surface energy for different surfaces were calculated to find out which surface has the lowest energy, therefore which one is the most stable. The calculations reveal this stability order: (101)>(110)>(100)>(001)>(111). Consequentially the most stable surface (101), (110) and (100) have been optimised and the molecules, N₂H₄ and NH₃, and atoms, H and N, were adsorbed on non-equivalent sites and their E_{abs} have been calculated following the Eq 3.

The adsorption energies reported in Table 3.2 can be deduced that the species studied have an irreversible binding on the surfaces of IrO₂ simulated. This behaviour would bring the

surface to be rapidly covered by the adsorbates and therefore to saturation of the oxide surface and the end of the catalytic activity of the material.

Table 3.2. Adsorption energies calculate for N_2H_4 , H, N and NH_3 on the most stables IrO_2 surfaces (101, 110 and 100).

Adsorbate	Lattice plane (eV)		
	101	110	100
N	-3.16	-3.65	-3.92
H	-3.13	-3.57	-3.46
NH_3	-2.02	-2.46	-2.69
N_2H_4	-2.35	-3.24	-3.98

3.5.2. Adsorption on the Ir (111) Surface

As a typical representation of the metallic Ir surface, the surface (111) was used since it is the most stable and it presents a close-packed plane of the fcc structure. In this facet, atoms are arranged in a hexagonal lattice in which neighbouring atoms are separated by 2.692 Å. The interaction of different species with this particular surface was calculated and the most stable conformation has been found to be the one represented in Figure 3.22 and the E_{ads} values and bond distances are reported in Table 3.3.

Table 3.3. Adsorption energies, E_{ads} , calculated for reagent, product and intermediate on Ir (111) and bond length, d , and coordination, η . Hydrazine gaseous is added as a comparison.

Adsorbate	E_{ads} (eV)	$d(Ir-N^1)$ (Å)	$d(Ir-N^2)$ (Å)	$d(N^1-N^2)$ (Å)	$d(N^1-H)$ (Å)	$d(N^2-H)$ (Å)
N_2H_4 gas	--	--	--	1.450	η (2); 1.020	η (2); 1.020
N_2H_4	-2.70	2.158	2.159	1.650	η (2); 0.977	η (2); 0.977
N_2H_3	-2.97	2.119	η (2); 2.160	1.417	η (2); 1.067	1.016
HNNH	-2.47	η (2); 2.110	η (2); 2.110	1.533	0.963	1.073
NNH ₂	-2.79	η (3); 2.080	-	1.341	-	η (2); 1.101

NNH	-3.06	2.059	2.011	1.330	1.005	-
NH ₃	-1.95	2.130	-	-	η (3); 1.037	-
NH ₂	-3.72	2.104	-	-	η (2); 1.022	-
NH	-4.31	η (3); 2.044	-	-	1.025	-
N ₂	-1.14	1.927	-	1.128	-	-
H ₂	-0.53	-	-	-	-	-
N	-0.56	η (3); 2.005	-	-	-	-
H	-0.86	-	-	-	-	-

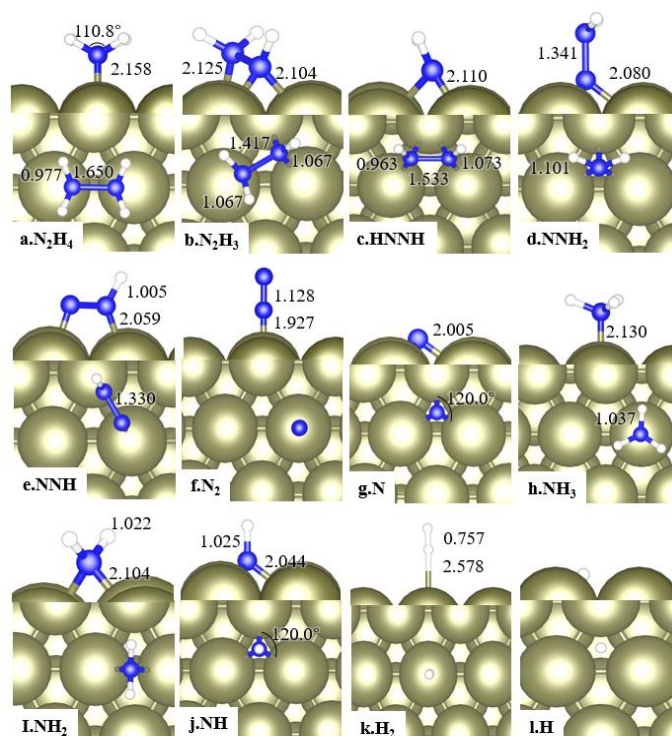


Figure 3.22. Schematic representation of N_2H_x ($x = 0-4$), NH_x ($x = 0-3$) and H_2 on the surface (111) of Ir. Ir atoms are large yellow spheres, N atoms are blue spheres and H atoms are white spheres. The distances are reported in Å.¹⁸

N_2H_4 can be placed in four different: top, bridge, fcc hollow and hcp hollow. The most stable conformation is the binding of hydrazine through the N atoms almost parallel to the surface in bridge site, Fig. 3.22a. In this conformation the average Ir-N distance is of 2.158 Å, while the N-N bond was stretched from 1.450 Å to 1.650 Å and the N-H bonds were shortened from 1.024 Å to 0.977 Å. This adsorption is an exothermic process with an E_{ads} of -2.70 eV.

N_2H_3 formation derives from the dehydrogenation of hydrazine and has preferential adsorption with the NH part on the hcp site, where the N bridges two Ir atoms, $\eta_{(2)}$, with a bond distance of 2.160 Å, Fig. 3.22b. The NH_2 , on the other side, sits on the Ir atom with an Ir-N length of 2.125 Å. The resulting N-N bond is stretched to 1.417 Å and the adsorption energy of this species is -2.97 eV.

Two different isomers of N_2H_2 could be formed during the reaction, HNNH and NNH_2 , Fig. 3.22c and Fig. 3.22d. The HNNH bind almost parallel to the surface on hcp hollow sites with both N with an adsorption energy of 2.47 eV. On the other hand, NNH_2 adsorbs on a hcp site with a single N atom perpendicularly to the surface and an $E_{ads} = -2.79$ eV. The two intermediates have different N orbitals conformation that is related also on the N-N bond length of 1.533 and 1.341 Å, for HNNH and NNH_2 respectively.

N_2H derives from the dehydrogenation of both the N_2H_2 isomers. This intermediate bind strongly on the surface, $E_{ads} = -3.06$ eV, on a bridge site, Fig. 3.22e. The N-N bond length is 1.330 Å and it is shorter than the other intermediates discussed above, remaining longer than the gas phase N_2H which is 1.150 Å, showing that the bond order is increased.

The most stable adsorption site of N_2 is a top site with perpendicular adsorption of the molecule and an Ir-N distance of 1.927 Å and the N-N bond is 1.128 Å compared with 1.098 Å, Fig. 3.22f. The E_{ads} calculated for this process is 1.14 eV.

N atoms are adsorbed on the surface preferentially on hcp hollow sites binding three Ir atoms releasing 0.56 eV from the adsorption from the gas phase. The average bond length is 2.005 Å between Ir and N, Fig. 3.22g.

The most stable adsorption of ammonia on Ir(111) is on top site, with Ir-N distance of 2.130 Å, and releases 1.95 eV due to interaction between the lone pair electrons and the electrons in the orbital 3d of Ir, Fig. 3.22h.

NH_2 adsorbs on the bridge site of the Ir surface with an average Ir-N distance of 2.104 Å, Fig. 3.22i. The E_{ads} calculated for this intermediate is -3.72 eV which lower than any N_2H_x adsorbed reported before.

Similarly, to N atoms, NH is adsorbed on hcp hollow site with an Ir-N $\eta_{(3)}$ bond length of 2.044 Å and a distance of 1.33 Å from the surface, Fig. 3.22j. The adsorption energy, -4.31 eV, and the Ir-N distance are shown to be negatively correlated.

H₂ physisorbs on top site o hcp hollow site releasing 0.52 eV, exhibiting long-range interaction, with Ir-H distances of 2.578 and 2.190 Å for top and hcp position respectively, Fig. 3.22k.

As N atoms, also H atom bind in hcp hollow site with a distance Ir-H $\eta_{(3)}$ 1.042 Å releasing 0.81 eV in the process, Fig. 3.22l.

These bond lengths are similar to works previously reported in literature for other metal surfaces.¹⁹⁻²¹

3.5.3. Hydrazine reaction pathways on Ir (111)

In this section, elementary reaction steps are studied for each possible intermediate, in order to understand the mechanism of the catalytic decomposition of hydrazine on Ir (111). The comparison between competitive elementary step was made by mean of the reaction energies (E_r) and the activation energy (E_a) of the steps in both directions. Here on each elemental step will be presented in five main mechanisms and discussed.

3.5.3.1. Intramolecular dehydrogenation

This mechanism considers the dehydrogenation of hydrazine by the progressive cleavage of the N-H bond from hydrazine molecules and their successive intermediates. The first N-H bond severing process, as shown in Figure 3.23a, is an endothermic step, $E_r = 0.18$ eV, with an E_a of 1.08 eV. Following this step N₂H₃ can be dehydrogenated in a symmetrical or asymmetrical way. The formation of HNNH is an endothermic process, $E_r = 0.54$ eV, with a high energy barrier of 1.77 eV. On the other hand, NNH₂ formation is endothermic as the symmetrical isomer, $E_r = 0.57$ eV, but the activation energy is lower, 1.02 eV. Further dehydrogenation of the N₂H₂ isomers have reaction energies close to 0, $E_r = -0.19$ and 0.11 eV for symmetric and asymmetric one respectively, and with E_a of 0.70 eV, symmetrical isomer, and 0.83 eV, asymmetrical isomers, to produce NNH. The final dehydrogenation of NNH to N₂ and H is lightly exothermic, $E_r = -0.02$ eV, but with a relatively high energy barrier, $E_a = 1.31$ eV, so that this process is energetically not favourable.

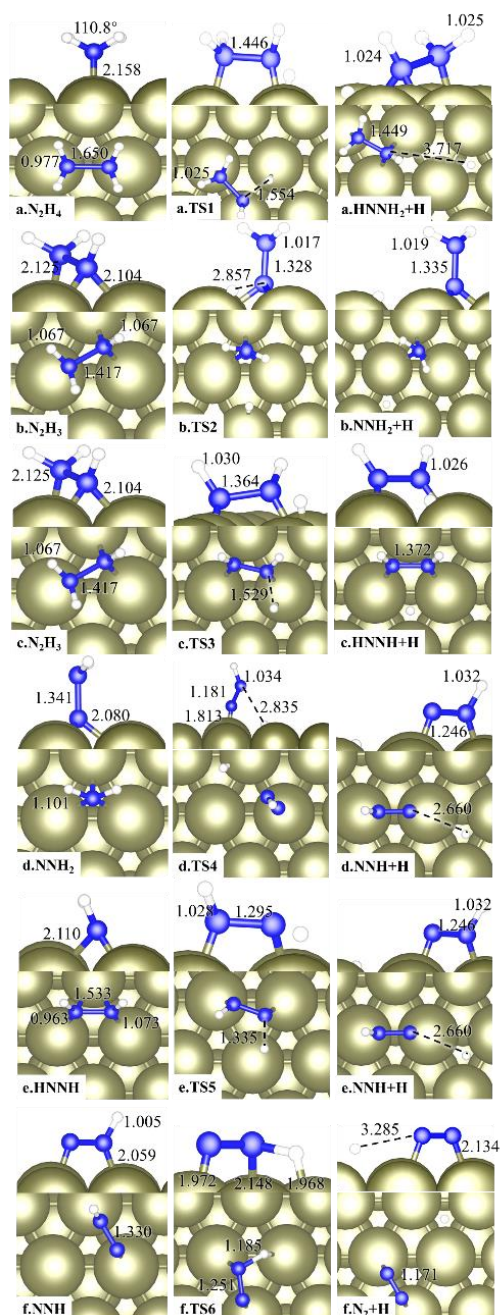


Figure 3.23. Schematic representation of initial, transition and final state for the reaction: a)hydrazine dehydrogenation; b) N_2H_3 asymmetrical dehydrogenation; c) N_2H_3 symmetrical dehydrogenation; d) NNH_2 dehydrogenation; e) $HNNH$ dehydrogenation; f) NNH dehydrogenation. Ir atoms are large yellow spheres, N atoms are blue spheres and H atoms are white spheres.¹⁸

3.5.3.2. N-N bond cleavage

The cleavage of the N-N bond of the $N_2H_4^*$ is an exothermic reaction, -0.52 eV, with an activation energy of 0.71 eV and lead to the formation of two amide species on the surface, NH_2^* , Figure 3.24. Compared with the mechanism of dehydrogenation reported previously, this reaction pathway is more energetically favourable, in agreement with studies already

present in literature. Any of the dehydrogenated intermediates shown before could possibly undergo to this mechanism. N_2H_3 can split forming NH^* and NH_2^* with an energetic gain, $E_r = 0.71$ eV, and an activation energy similar to the hydrazine cleavage, $E_a = 0.78$ eV. In the case of the N_2H_2 isomers the reaction energies are different for the two species, -0.53 and -1.49 eV for asymmetrical and symmetrical isomer respectively, due to the products since symmetrical HNNH produce two NH^* , while the asymmetrical NNH₂ lead to the formation of N^* and NH_2^* . The isomers N-N cleavage have similar E_a , 0.73 eV. The dissociation of NNH is exothermic, $E_r = -1.21$ eV, but very activation energy, 1.43 eV, limit the formation of N^* and NH^* .

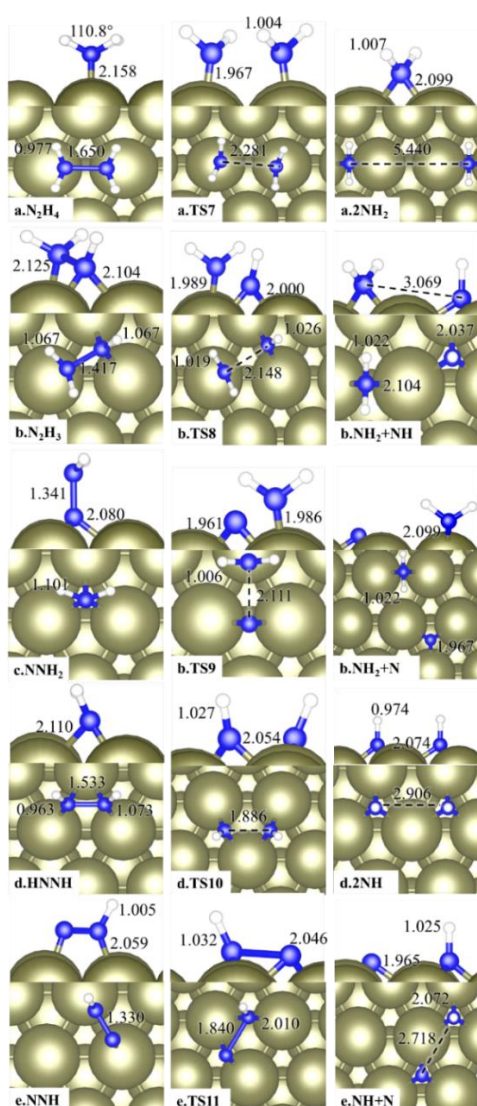


Figure 3.24. Schematic representation of initial, transition and final state for the reaction: a)hydrazine N-N bond cleavage; b) N_2H_3 N-N bond cleavage; c)NNH₂ N-N bond cleavage; d)HNNH N-N bond cleavage; e)NNH N-N bond cleavage. Ir atoms are large yellow spheres, N atoms are blue spheres and H atoms are white spheres.

3.5.3.3. Intermolecular dehydrogenation

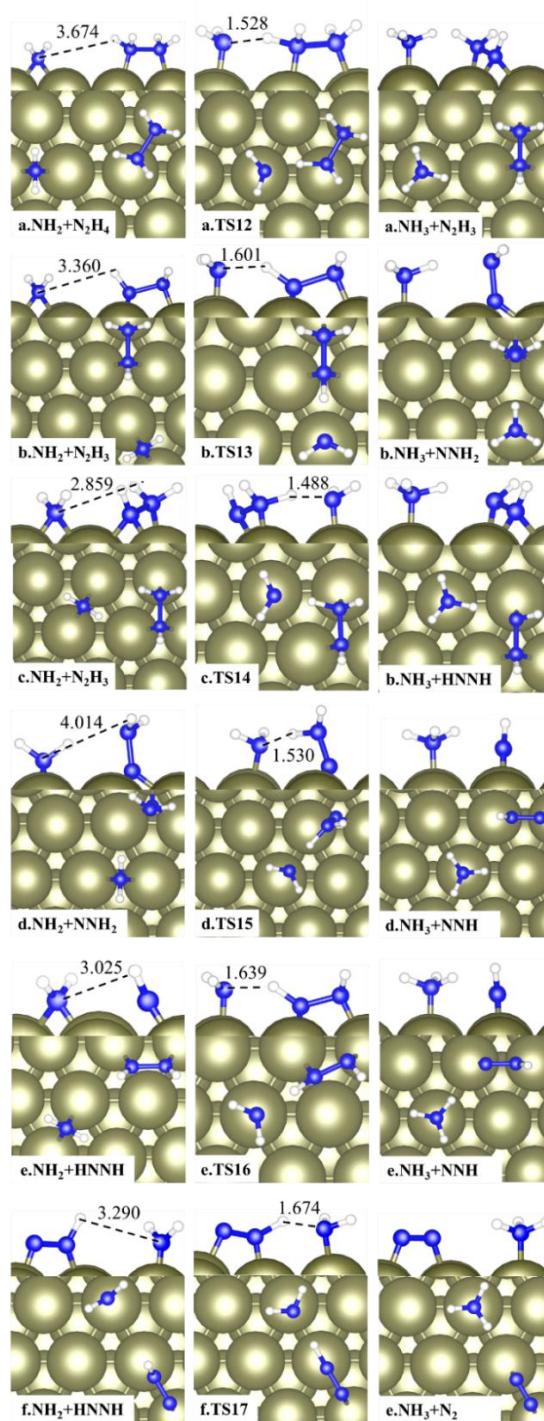


Figure 3.25. Schematic representation of initial, transition and final state for H abstraction by NH_2 : a) N_2H_4 ; b) N_2H_3 asymmetrical reaction; c) N_2H_3 symmetrical reaction; d) NNH_2 ; e) HNNH ; f) NNH . Ir atoms are large yellow spheres, N atoms are blue spheres and H atoms are white spheres.¹⁸

Once NH_x ($x = 0-2$) are formed on the surface following the aforementioned N-N cleavage mechanism, this species can dehydrogenate the co-adsorbed species been more nucleophilic than N_2H_x ($x = 1-4$) species driving, therefore, the proton transfer, Figure 3.25.

The adsorption of N_2H_4 in presence of NH_2^* destabilise the system by 0.13 eV respect to the isolated species. This dehydrogenation has low activation energy, 0.20 eV, and is exothermic, $E_r = -0.47$ eV. All these N_2H_x interaction with NH_2 similarly destabilise the surface by 0.2 eV and they have small energy barriers below 0.60 eV, except for the asymmetrical NNH_2 which have $E_a = 1.02$ eV. The low activation energies and energy gains suggest that this mechanism is the most likely to happen once NH_2 is present on the surface. This is also driven by the formation of NH_3 .

3.5.3.4. Intermolecular amides dehydrogenation

In Figure 3.26, similar dehydrogenation process can occur between NH_2^* and NH_x^* ($x = 1-2$) to form NH_3 . The reaction between two NH_2^* has small activation energy, 0.34 eV, and a favourable reaction energy of, -0.59 eV. On the contrary, the NH^* and NH_2^* interaction is more energetically driven, $E_r = -0.91$, but the energy barrier to overcome is higher, $E_a = 0.98$. Since the minimum activation energy required for the formation of NH^* is 0.71 eV is less probable the reaction of N_2H_4 with NH^* then with NH_2^* .

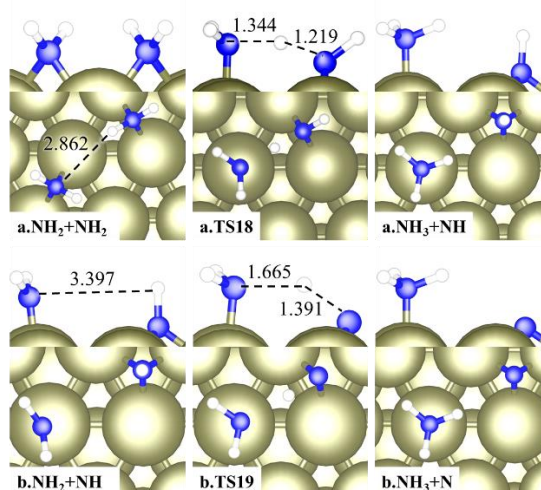


Figure 3.26. Schematic representation of initial, transition and final state for the reaction of NH_2 with a) NH_2 and b) NH . Ir atoms are large yellow spheres, N atoms are blue spheres and H atoms are white spheres.¹⁸

3.5.3.5. NH_x dehydrogenation

Similarly to the dehydrogenation of hydrazine, also NH_x^* ($x = 1-3$) species may react with the surface leading to the severing of the N-H bond and the formation of ad-atom H and N, Figure 3.27. These atoms on the surface can recombine further to produce H_2 and N_2 . The steps of dehydrogenation of NH_x are endothermic processes with a minimum value of 0.07 eV when NH^* is the starting point. Moreover, this mechanism is kinetically impeded by high activation energies higher than 1 eV.

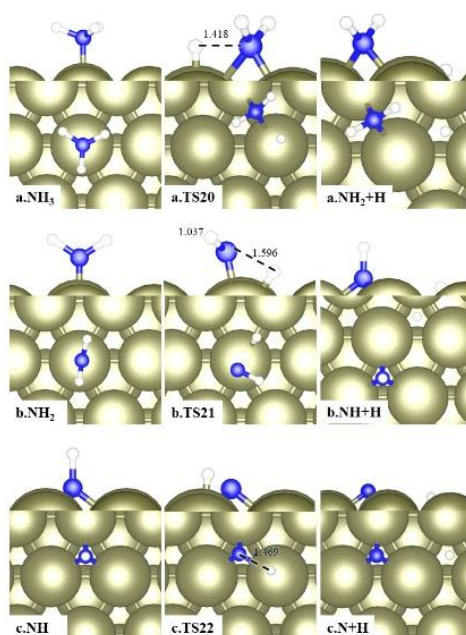


Figure 3.27. Schematic representation of initial, transition and final state for the reaction: a) NH_3 dehydrogenation; b) NH_2 dehydrogenation; c) NH dehydrogenation. Ir atoms are large yellow spheres, N atoms are blue spheres and H atoms are white spheres. ¹⁸

From all these analyses can be deduced that the more favourable mechanisms to occur on Ir(111) are the initial N-N cleavage followed by the intermolecular dehydrogenation of hydrazine by the NH_2^* created by the severing of the N-N bond of some hydrazine molecules.

Table 3.4. Reaction (E_r) and activation (E_a) energies for the forward and reverse elemental steps. E_r values of the adsorption and desorption processes are equal to the E_{ads} values (i.e. relative to the gas-phase), and ν is the imaginary frequencies of the intermediates.

		Iridium (111)			
Reactions	E_r (eV)	E_a	E_a	$\nu(\text{cm}^{-1})$	
		forward (eV)	reverse (eV)		
<i>Adsorption-desorption</i>					
R1	$\text{N}_2\text{H}_4 \rightleftharpoons \text{N}_2\text{H}_4^*$	-2.7			
R2	$\text{NH}_3^* \rightleftharpoons \text{NH}_3$	1.95			
R3	$\text{N}_2^* \rightleftharpoons \text{N}_2$	1.14			
R4	$\text{H}_2^* \rightleftharpoons \text{H}_2$	1.37			
<i>Dehydrogenation</i>					
R5	$\text{N}_2\text{H}_4^* \rightleftharpoons \text{N}_2\text{H}_3^* + \text{H}^*$	0.18	1.08	956.9	
R6	$\text{N}_2\text{H}_3^* \rightleftharpoons \text{HNNH}^* + \text{H}^*$	0.54	2.05	1126.8	
R7	$\text{N}_2\text{H}_3^* \rightleftharpoons \text{NNH}_2^* + \text{H}^*$	0.57	1.02	482.8	
R8	$\text{HNNH}^* \rightleftharpoons \text{NNH}^* + \text{H}^*$	-0.19	0.70	1115.8	
R9	$\text{NNH}_2^* \rightleftharpoons \text{NNH}^* + \text{H}^*$	0.11	0.83	386.1	
R10	$\text{NNH}^* \rightleftharpoons \text{N}_2^* + \text{H}^*$	-0.02	1.31	910.2	
<i>N-N dissociation</i>					
R11	$\text{N}_2\text{H}_4^* \rightleftharpoons 2\text{NH}_2^*$	-0.52	0.71	154.3	
R12	$\text{N}_2\text{H}_3^* \rightleftharpoons \text{NH}_2^* + \text{NH}^*$	-0.71	0.78	356.9	
R13	$\text{NNH}_2^* \rightleftharpoons \text{NH}_2^* + \text{N}^*$	-0.53	0.73	398.7	
R14	$\text{HNNH}^* \rightleftharpoons 2\text{NH}^*$	-1.49	0.73	549.7	

R15	$\text{NNH}^* \rightleftharpoons \text{NH}^* + \text{N}^*$	-1.21	1.43	2.64	571.9
<i>Intermolecular dehydrogenation</i>					
R16	$\text{N}_2\text{H}_4^* + \text{NH}_2^* \rightleftharpoons \text{N}_2\text{H}_3^* + \text{NH}_3^*$	-0.47	0.20	0.67	335.8
R17	$\text{N}_2\text{H}_3^* + \text{NH}_2^* \rightleftharpoons \text{HNNH}^* + \text{NH}_3^*$	-0.13	0.23	0.36	268.3
R18	$\text{HNNH}^* + \text{NH}_2^* \rightleftharpoons \text{NNH}^* + \text{NH}_3^*$	-1.03	0.19	1.22	322.9
R19	$\text{N}_2\text{H}_3^* + \text{NH}_2^* \rightleftharpoons \text{NNH}_2^* + \text{NH}_3^*$	-0.28	0.37	0.64	252.5
R20	$\text{NNH}_2^* + \text{NH}_2^* \rightleftharpoons \text{NNH}^* + \text{NH}_3^*$	-0.49	1.02	1.5	654.9
R21	$\text{NNH}^* + \text{NH}_2^* \rightleftharpoons \text{N}_2^* + \text{NH}_3^*$	-1.35	0.55	1.89	1291.0
<i>NH_x (x = 1,2,3) dehydrogenation</i>					
R22	$\text{NH}_3^* \rightleftharpoons \text{NH}_2^* + \text{H}^*$	0.76	1.79	1.03	1229.5
R23	$\text{NH}_2^* \rightleftharpoons \text{NH}^* + \text{H}^*$	1.66	1.96	0.30	1274.3
R24	$\text{NH}^* \rightleftharpoons \text{N}^* + \text{H}^*$	0.07	1.18	1.12	1154.5
<i>Interaction of NH₂ intermediates</i>					
R25	$2\text{NH}_2^* \rightleftharpoons \text{NH}^* + \text{NH}_3^*$	-0.59	0.34	0.93	124.1
R26	$\text{NH}^* + \text{NH}_2^* \rightleftharpoons \text{N}^* + \text{NH}_3^*$	-0.91	0.98	1.89	213.9
<i>N₂ generation</i>					
R27	$2\text{N}^* \rightleftharpoons \text{N}_2^*$	-0.59	2.02	2.61	568.3
<i>H₂ generation</i>					
R28	$2\text{H}^* \rightleftharpoons \text{H}_2^*$	0.31	0.51	0.20	271.1

3.5.4. Desorption of the products

Some of the processes described above lead to the production of ad-atoms N and H on the Ir(111), that can later recombine to form molecular hydrogen and nitrogen. N_2 formation is exothermic, $E_r = -0.59$ eV, but it has a high activation energy, $E_a = 2.02$ eV. The recombination of H atoms, instead, is an endothermic process, $E_r = 0.36$ eV, with a really accessible energy barrier, $E_a = 0.20$ eV. These data are in agreement with the literature about the decomposition of hydrazine over Ir, where temperature above 200°C are reported to be necessary to achieve high yields toward H_2 production.

The desorption of the products H_2 , N_2 , and NH_3 from the Ir surface is an endothermic process with E_{des} of 1.37, 1.14 and 1.95 eV respectively. Both decomposition reactions are overall exothermic processes, therefore the energy required for the desorption of the products can be provided by the exothermic steps of the reaction.

3.5.5. Analysis of the Energy Profiles

In this section, the energy profiles of the three reaction mechanisms are discussed as displayed in Figure 3.28, Figure 3.29 and Figure 3.30.

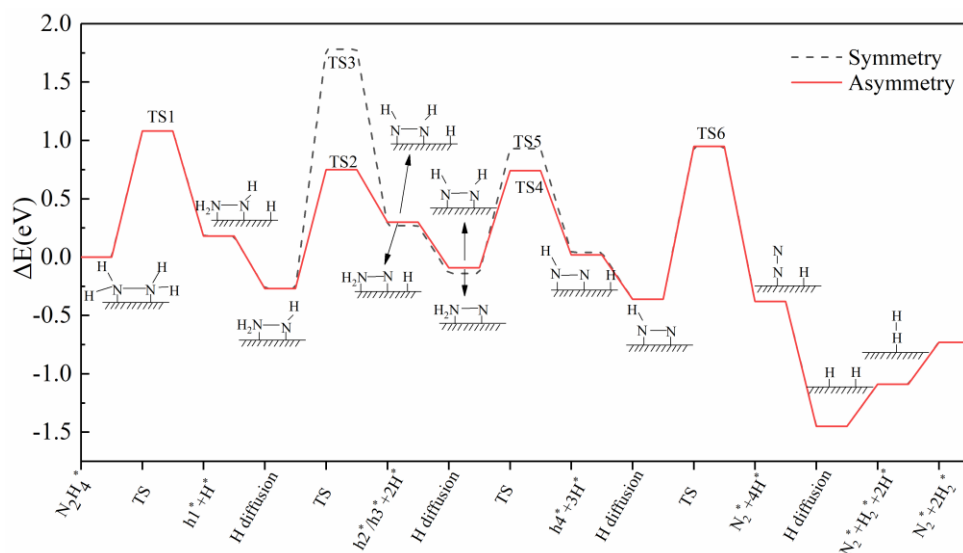


Figure 3.28. Intramolecular dehydrogenation pathways for the decomposition of N_2H_4 over Ir(111) surface. These pathways produces nitrogen and hydrogen.¹⁸

Figure 3.28 summarises the two reaction pathways that follow the intermolecular dehydration. From the values reported in Table 3.4 and that can be seen in Figure 3.28, R6 is the limiting step for the symmetric dehydrogenation pathway with an energy barrier of 2.05

eV. R10 is the main energetic barrier in asymmetrical pathway with an $E_a = 1.37$ eV. Moreover, H_2 desorption on Ir(111) is an endothermic process. For these reasons on this surface, these pathways may be less likely to happen than other pathways considered in the study.

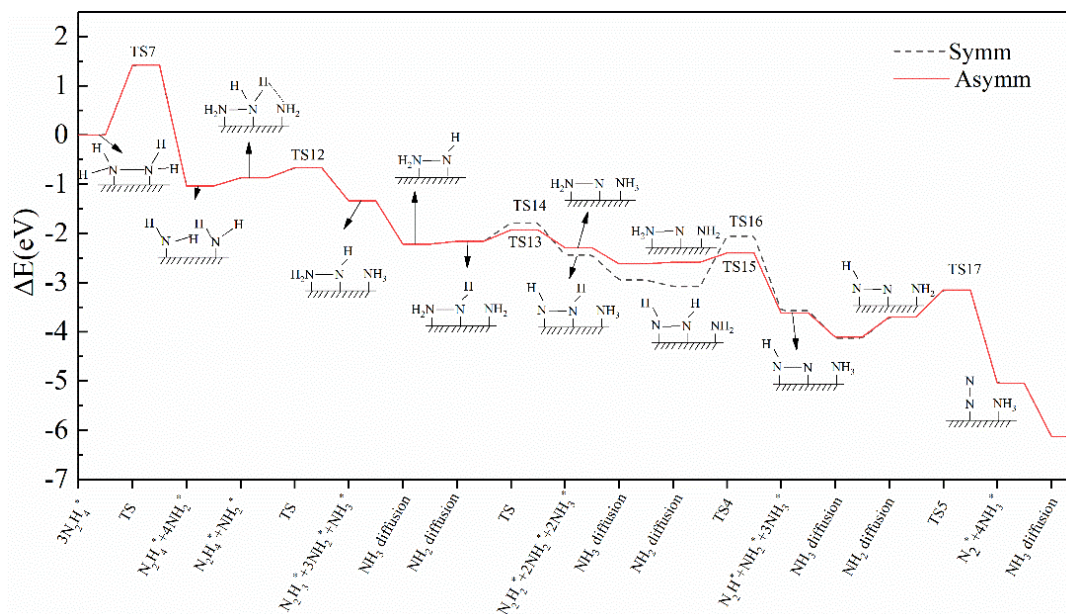


Figure 3.29. Intermolecular hydrazine dehydrogenation pathways for the decomposition of N_2H_4 over Ir(111) surface. This pathways produces nitrogen and ammonia.¹⁸

The thermodynamic suggests that N_2H_x species adsorbed on the surface undergo to break of the N-N bond as preferential pathway during the decomposition process, Figure 3.29. R11 lead to the formation of NH_2^* which later assist the dehydrogenation of hydrazine molecules co-adsorbed in the surface. Moreover, N-N bond breaks of other N_2H_x species like R12, R13 and R14 can lead to the formation of NH_2^* , NH^* and N^* with relatively low energy barrier and small energy gains. On the other hand, successive dehydrogenations of NH_2^* by the surface are limited by the high activation energies, as shown in Figure 3.30.

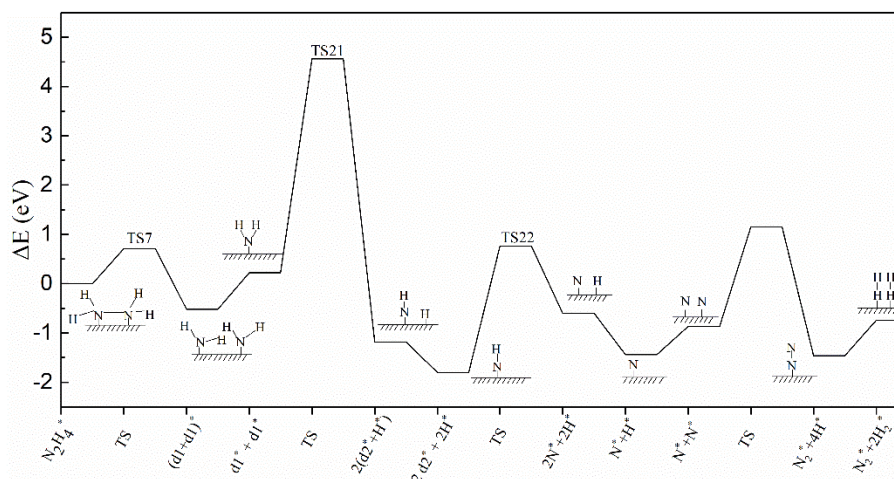


Figure 3.30. Amide dehydrogenation pathway for the decomposition of N_2H_4 over Ir(111) surface. This pathways produces nitrogen and hydrogen.¹⁸

The large energy required to dehydrogenate NH_3^* , R22, and the low relatively low energy barrier of all the intermolecular dehydrogenation of all the N_2H_x assisted by NH_2^* , which produces NH_3 , increase the yield toward it. Between the two pathways, the symmetrical pathway as a maximum E_a value of 0.55 eV, R21, while the asymmetrical pathway reaches 1.02 eV in R20, therefore the symmetrical intermolecular dehydrogenation is the most probable pathway to be followed during the decomposition of hydrazine over Ir(111).

From these calculations, it can be seen that on the Ir(111) surface the first elemental step to take place is the breaking of the N-N bond of the hydrazine creating NH_2 adsorbed species on the surface which later assist to the decomposition of hydrazine molecules adsorbed on the surface leading to the formation of N_2 and NH_3 . The dehydrogenations by the surface of NNH_x and NH_x are impeded by high activation energies of these steps, while the final selectivity toward hydrogen production is limited by the thermodynamics of the reaction, $\Delta G = -1.46$ eV against the $\Delta G = -1.72$ eV of the reaction to ammonia and the stability on the surface of ammonia which pushes the selectivity toward ammonia production. Therefore, the strategies should be to decrease energies barrier selectively of the pathways that lead to the production of hydrogen to have a kinetic control other the reaction to overcome the thermodynamic limitations of the hydrogen production.

3.5.6. Simulated Infrared Spectra

Having simulated the adsorption of the most common intermediate species it is possible to calculate the simulated infrared spectra for these species. These spectra are important to the

characterisation of the iridium catalysts since in combination with experimental IR analyses it can help to identify the species more presents on the surface and, therefore, they give information about the mechanism of reaction on the actual catalytic material. In Figure 3.31 are reported the simulated spectra of the N_2H_x species adsorbed on the surface. It can be seen that the strength of the hydrogen vibration decreases with dehydrogenation of the hydrazine, the N-N bond frequency increases indicating the decrease in length of the bond and its increase in strength and stability, in agreement with the dissociation energies reported for reaction R11-R15.

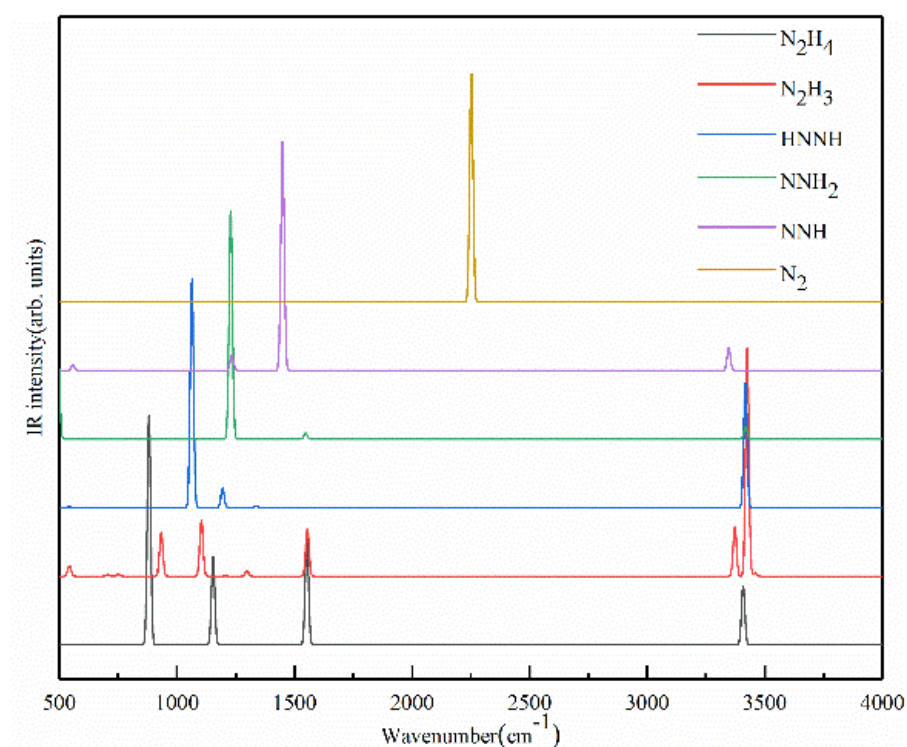


Figure 3.31 Infrared spectra for adsorbate hydrazine (N_2H_4), intermediate species (N_2H_3 , N_2H_2 , NNH) and N_2 .¹⁸

In Figure 3.32 displays the IR spectra for NH_x species adsorbed on the surface. Ammonia has a distinctive stretching at 1011 cm^{-1} .²² This distinctive vibrational frequency shifts to lower wavenumbers for the dehydrogenated species, and it becomes IR-active at 750 cm^{-1} for NH intermediate. Also, the H-N-H scissoring vibration decrease in wavenumber from ammonia to NH_2 , from 1569 cm^{-1} to 1466 cm^{-1} .

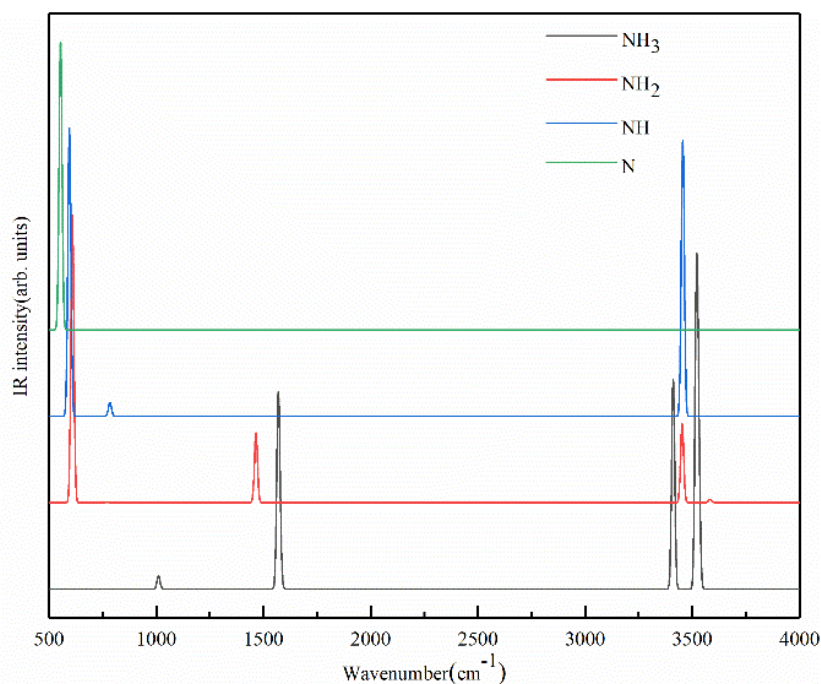


Figure 3.32. Simulated infrared spectra for adsorbed ammonia and intermediate species (NH_2 , NH and N).¹⁸

Table 3.5. Imaginary infrared frequencies of adsorbed reagent, products and intermediate species on Ir(111).

Species	Wavenumber (cm^{-1})					
N_2H_4	881	1154	1552	3408		
N_2H_3	543	933	1104	1555	3372	3425
HNNH	1064	1194	3417			
NNH_2	1229	1550	3418			
NNH	1232	1449	3348			
N_2	2251					
NH_3	1569	3411.2	3521			
NH_2	609	1466	3452			
NH	595	786	3456			
N	554					

3.6. Conclusions

In this chapter, Ir/CeO₂ catalysts prepared by deposition-precipitation method were used as initial reference materials for the studies on the feasibility of Ir as suitable catalytic material for the decomposition of hydrous hydrazine in an aqueous environment with the production of molecular hydrogen, reported as the preferential product only at higher temperature in

gas phase reaction. Ir/CeO₂ deposition-precipitation were used after for the optimisation of the reaction conditions in order to obtain kinetic data excluding the presence of limitations by mass transfer effects in solution or on the surface of the catalyst. The optimal reaction conditions were found to be a substrate/metal molar ratio of 250:1 or higher, NaOH concentration of 0.5M and stirring rate of 1050 rpm. At these experimental conditions, Ir/CeO₂ DP reduced at 600°C for 3h, presented a final yield toward molecular hydrogen of 23.9% toward the production of H₂ and a TOF_{50%} of 1018 h⁻¹.

To establish a potential structure/activity relationship and lay the ground for future catalytic improvement a series of different characterisation methods have been deployed. Firstly, BET analyses have not displayed a apparent increase in surface area after the deposition of the Ir nanoparticles, 44 to 49 m² g⁻¹. The increase of the surface area is too small to permit us to quantify the surface area of the nanoparticles in an accurate way. Particles size dimensions were therefore studied by other methods, like XRD or TEM. The XRD diffractogram did not exhibit the presence of diffraction peaks characteristic of metallic Ir or IrO₂, the two most stable species at normal conditions. The absence of Ir diffraction peaks is an indication of (I) the presence of amorphous Ir on the surface, (II) Ir nanoparticles deposited onto the surface of the support have small mean particles size, so that the characteristic diffraction peaks from XRD analysis are broadened and it is difficult to distinguish them from the background of the analysis, < 5 nm. To obtain a definitive measurement of the Ir nanoparticle size, TEM technique was employed. Due to the difficulties to obtain clear images of the Ir NPs, related to the support used and the dimension of the particles, it was not possible to capture a pool of data large enough to be statistically valid. However, TEM analysis gave a clear indication that Ir nanoparticles were present and with small nanoparticle size and narrow particle size distribution, < 2 nm.

To confirm the presence of metallic Ir, TPR and XPS analyses were performed on the samples in order to identify the oxidation state, surface coverage and ratio of Ir species and finally tendency towards reduction of Ir/CeO₂. From these analyses can be deduced that under H₂ atmosphere the Ir is readily reduced at a temperature around 130°C. Ir nanoparticles seems to be partially re-oxidised over time in contact with air, also at mild conditions, due to the interaction between the particles and the oxide support. The thermal treatment plays a

crucial role in the stabilisation of the metallic species with metallic Ir ratio passing from 43% to 100% as the reduction temperature increases from 400°C to 600°C and the time of the treatment doubles. The XPS spectra also display a shift of the Ir⁰ at higher energy, indicating a partial charge of the Ir surface due to the small dimensions and interaction with the support.

ICP-MS analysis and SEM-EDX mapping showed that the deposition-precipitation method is not capable to deposit all the Ir on the surface leading to a real loading of about 70% of the theoretical metal loading. Iridium is one of the most expensive metal on earth, therefore a preparation method that does not deposit all the metal put a limitation to the economical availability of all the system. Therefore, the study of additional preparation methods which may replace the deposition-precipitation displaying similar catalytic activity and better deposition efficiency has been pursued. The SEM-EDX also confirmed a good distribution of Ir nanoparticles on the surface of CeO₂ in the catalysts used for the reaction optimisation process.

A preliminary reusability test exhibits that after an initial high activity and good selectivity a rapid deactivation of the catalyst occurs. The yield in particular decrease from 26.9% to 3.6%, this result indicates the poor catalytic stability of Ir catalysts for possible application for hydrogen production systems. Therefore, it is important to search for alternative methodologies and identify the cause of deactivation.

To identify the causes of deactivation, TEM and XPS analysis was used. In terms of XPS analysis, high concentration of sodium used during the reaction to regulate the pH, make difficult to analyse the used sample. In the Ir 4f region, Na 2s has a strong response that precludes a clear analysis of the spectra, but the position of the peak seems to exclude the aggregation of metallic NPs. The TEM suggests that the particles only slightly increase, still in the margin of error of the technique, during the reaction. Therefore, possible causes of the deactivation of the catalysts are (I) the irreversible adsorption of some products, (II) modification of the active surface of iridium, (III) aggregation of the nanoparticles.

The DFT calculations were performed to study the thermodynamics of the reaction involved and the different elemental steps on IrO₂ and Ir(111) surfaces. The oxide surface irreversibly binds with reagent and products which would lead to rapid deactivation of the catalyst. On the Ir(111), three main catalytic mechanisms were studied (intramolecular hydrazine

dehydrogenation, intramolecular amide dehydrogenation and intermolecular hydrazine dehydrogenation), with five reaction pathways, including adsorption, activation energies and thermodynamics of each step. From these calculations, the first step to take place is the cleavage of the N-N bond of the hydrazine adsorbed on Ir(111) lead to the formation of NH_2^* species. Afterwards, NH_2^* may interact with different N_2H_x ($x = 1-4$), assisting the extraction of H and producing, therefore, NH_3^* and subsequently leaving N_2^* . Another possible mechanism is the interaction between NH_2^* and NH_x^* ($x = 1-2$) to produce NH_3^* and ad-atom N on the surface. On Ir(111) the recombination of ad-atoms H has a high energy barrier that limits the production of molecular hydrogen on this particular surface at mild conditions.

3.7. References

- 1 H. Wang, L. Wu, Y. Wang, X. Li and Y. Wang, *Catal. Commun.*, 2017, **100**, 33–37.
- 2 J. Wang, X.-B. Zhang, Z.-L. Wang, L.-M. Wang and Y. Zhang, *Energy Environ. Sci.*, 2012, **5**, 6885–6888.
- 3 S. K. Singh, A. K. Singh, K. Aranishi and Q. Xu, *J. Am. Chem. Soc.*, 2011, **113**, 19638–19641.
- 4 S. K. Singh, Z. H. Lu and Q. Xu, *Eur. J. Inorg. Chem.*, 2011, **2011**, 2232–2237.
- 5 A. K. Singh, M. Yadav, K. Aranishi and Q. Xu, *Int. J. Hydrog. Energy*, 2012, **37**, 18915–18919.
- 6 C. Keresszegi, T. Mallat and A. Baiker, *New J. Chem.*, 2001, **25**, 1163–1167.
- 7 S. Wunder, F. Polzer, Y. Lu, Y. Mei and M. Ballauff, *J. Phys. Chem. C*, 2010, **114**, 8814–8820.
- 8 M. Che and J. C. Védrinem, *Characterization of solid materials and heterogeneous catalysts. From structure to surface reactivity*, Wiley-VCH, Weinheim, 2012.
- 9 S. Partyka, F. Rouquerol and J. Rouquerol, *J. Colloid Interface Sci.*, 1979, **68**, 21–31.
- 10 Y. H. Liu, J. C. Zuo, X. F. Ren and L. Yong, *Metalurgia*, 2014, **53**, 463–465.
- 11 X. Yan, T. Ai, X. Su, Z. Wang, G. Sun and P. Zhao, *MATEC Web Conf.*, 2016, **2**, 1–5.
- 12 D. F. Abbott, D. Lebedev, K. Waltar, M. Povia, M. Nachtegaal, E. Fabbri, C. Coperet and T. J. Schmidt, *Chem. Mater.*, 2016, **28**, 6591–6604.
- 13 V. Pfeifer, T. E. Jones, J. J. Velasco Vélez, C. Massué, M. T. Greiner, R. Arrigo, D. Teschner, F. Girgsdies, M. Scherzer, J. Allan, M. Hashagen, G. Weinberg, S. Piccinin, M. Hävecker, A. Knop-Gericke and R. Schlögl, *Phys. Chem. Chem. Phys.*, 2016, **18**, 2292–2296.
- 14 J. Jehng and C. Chen, *Catal. Letters*, 2001, **77**, 147.

- 15 S. J. Freakley, J. Ruiz-Esquiús and D. J. Morgan, *Surf. Interface Anal.*, 2017, **49**, 794–799.
- 16 P. E. Sobol and J. Chastain, *Handbook of X-ray Photoelectron Spectroscopy*, Perkin-Elmer Corporation, Eden Prairie, Minnesota, 1992.
- 17 D. Andreeva, T. Tabakova, V. Idakiev, P. Christov and R. Giovanoli, *Appl. Catal. A Gen.*, 1998, **169**, 9–14.
- 18 X. Lu, S. Francis, D. Motta, N. Dimitratos and A. Roldan, *Phys. Chem. Chem. Phys.*, 2020, **22**, 3883–3896.
- 19 K. P. Huber and G. Herzberg, *Molecular spectra and Molecular Structure IV. Constants of Diatomic Molecules*, 1978.
- 20 J. A. Pople and L. A. Curtiss, *J. Chem. Phys.*, 1991, **95**, 4385.
- 21 S. S. Tafreshi, A. Roldan and N. H. de Leeuw, *Phys. Chem. Chem. Phys.*, 2015, **17**, 21533–21546.
- 22 T. H. Koops, T. Visser and W. M. A. Smit, *J. Mol. Struct.*, 1983, **96**, 203–218.

4. Optimisation of the supported Ir nanoparticles for the catalytic liquid-phase decomposition of hydrous hydrazine

4.1. Introduction

In the previous Chapter 3, we demonstrated the catalytic performance of Ir/CeO₂ as a potential catalyst for the liquid-phase decomposition of hydrous hydrazine at mild conditions. Characterisation of these catalysts have provided valuable structural information about both bulk and superficial features of the material, such as particle dimensions and oxidation state of the surface species, that can give insights on possible structure/activity relationships. These insights are hereafter used to tune the formation of nanoparticles to better accomplish the goal of the thesis.

Changes in surface and bulk characteristics, even the slightest, may have a drastic impact on the final catalytic activity of similar materials. For this reason, in this chapter different experimental parameters during the preparation of the catalysts were employed in order to tune the catalyst selectivity, rate of reaction, reusability and economic profitability. These are the main factors on which the attention was focused to improve the final yield toward hydrogen gas by Ir-based catalysts in this thesis, overcoming the thermodynamic limitation by mean of a kinetic control of the reaction by the catalytic material.

For example, nanoparticles can be produced following a number of different experimental procedures, for example, they can be formed on the surface by deposition method or immobilised by a preformed colloidal metal solution. Moreover, the formation of metal nanoparticles may be assisted by protecting ligands, such as PVA or PVP, or not, and different additives tend to cover the surface in different ways. All these factors lead to the possibility of tuning the particle size of the metal nanoparticle that can be achieved but also can

influence the amount of active metal loaded onto the surface of the support with respect to the nominal amount of metal deposited. Also, the choice of the material used as support has a great influence on the final catalyst, from cost to effectiveness of the preparation method and catalytic performance. Metal oxides have different properties from wettability to point of zero charge (PZC) and surface area. Some of these supports are inert while others can play a role in the activity of the catalyst by influencing the oxidation state of the active metal and activating the oxygen species.¹

In the previous chapter the experimental reaction conditions have been optimised for a series of Ir/CeO₂ catalysts prepared by deposition-precipitation method, and in principle parameters like substrate/metal molar ratio and stirring should be optimised for each of catalysts tested. Since the optimisation of the reaction for each single catalyst would have required a large amount of time and catalyst and since the materials chosen have similar properties, the reaction conditions have been set at the optimal one for Ir/CeO₂ prepared by deposition precipitation, while the most active was subject to a further optimisation of the experimental condition for their synthesis.

To find the best catalyst for this reaction, a number of experimental parameters, such as different preparation method, medium, high-temperature heat treatment of the catalytic materials and choice of support have been used. All these materials have been analysed by a number of different analytical techniques like scanning electron microscopy, transmission electron microscopy, X-ray photoelectron spectroscopy, powder X-ray diffraction, BET and temperature-programmed reduction. In addition, computational calculations based on density functional theory on specific Ir surfaces have been performed in order to better understand better the mechanical aspects of the reaction and preference toward each reaction pathway. Attenuate total reflectance infrared spectroscopy, ATR-IR has been performed with the goal to better understand which are the most stable intermediate species on the surface. Finally, mass spectrometry was performed on the gas phase produced during the reaction performed with some of the most significant catalysts and combined with used of N¹⁵ labelled hydrazine monohydrate in order to confirm the experimental yield values and possibly identify reaction pathways.

4.2. Results and discussion

The experimental tests to compare the catalytic performances were performed following the same experimental protocol presented in Chapter 2, Section 2.3., and the optimised experimental conditions were presented in Chapter 3 and, therefore, were applied also in the hereinafter catalytic tests. In summary: an aqueous solution 0.5M of NaOH was warmed at 50°C in the presence of the catalyst and when the desired temperature was reached at the reactor, the desired amount of hydrous hydrazine solution was added, without stirring, and the reactor was purged with N₂. Once purged, the reactor was connected to the gas collection system and the stirring initiated. The volume of gas collected was calculated at specific periodical times and more frequently at the beginning of the reaction.

4.2.1. Influence of the preparation method

Initially, the preparation method was varied in order to synthesise systematically supported Ir nanoparticles with different Ir particle size and how the presence of stabilisers can influence Ir particle size and the final catalytic performance. Using Ir/CeO₂ catalysts prepared by deposition-precipitation (DP) with NaOH as the chosen pH modulator as reference material, the comparison was made with other Ir/CeO₂ materials. One the catalysts prepared by deposition-precipitation with urea as pH modulator and two catalysts prepared by sol-immobilisation (sol-imm.) with tetrakis(hydroxymethyl)phosphonium chloride (THPC) method and an adapted version of the well-known polyvinyl alcohol/sodium borohydride sol-immobilisation method.²⁻⁴ All the samples were reduced at 600°C of temperature under H₂/Ar flow since it was demonstrated in Chapter 3 the importance of this heat treatment to improve the catalytic performance. Of the aforementioned methodology, the sol-immobilisation PVA did not produce a reliable catalytic material. In fact, this method in order to immobilise the particles on the surface of the support requires the use of H₂SO₄ to decrease the pH and increase the interaction between particles and support. Using with CeO₂, as the chosen support, the acidification, by addition of H₂SO₄, has to be avoided since also small amount of the acid lead to the dissolution of the support. Therefore, the acidification step can lead to an uncontrolled increase in the final metal loading and decrease in the final mass of catalyst produced. For these reasons a non-acidified immobilisation has been attempted but it has provided a really low efficiency of the immobilisation of the nanoparticles on the surface as

demonstrated by the presence of Ir plasmonic peak in solution. Consequently, the method has not been considered suitable for catalytic application in these particular experimental conditions.

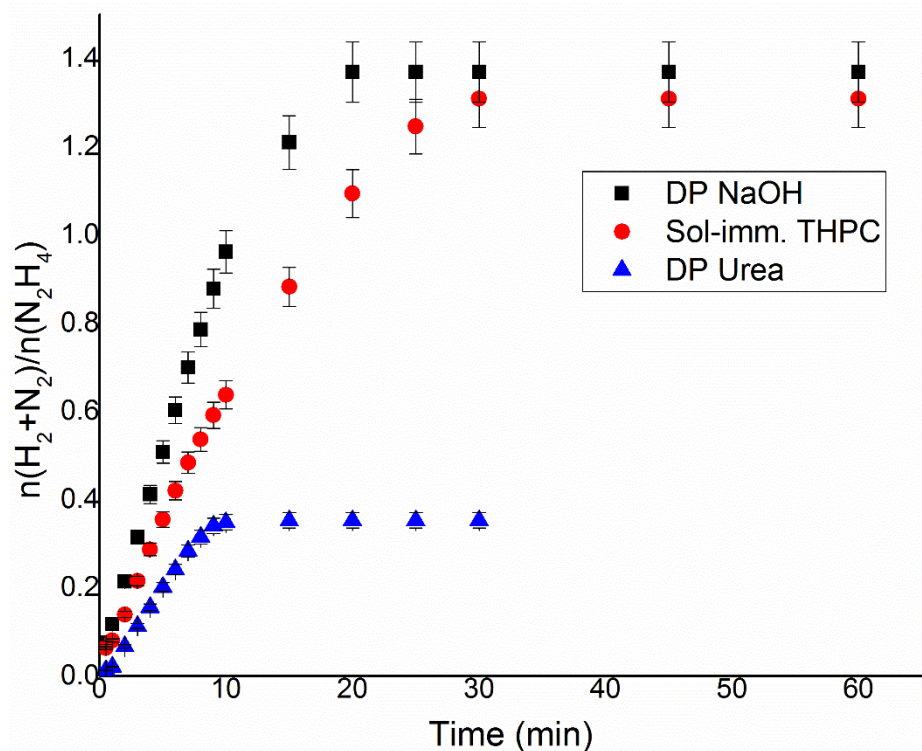


Figure 4.1. $n(\text{H}_2+\text{N}_2)/n(\text{N}_2\text{H}_4)$ versus time for hydrazine decomposition over Ir/CeO_2 DP 600 6h, Ir/CeO_2 urea 600 6h and Ir/CeO_2 THPC 600 6h, using 0.3mL of 3.3M hydrazine in 8mL 0.5M of NaOH solution, at 50°C and 76.2 mg of catalyst, with a stirring rate of 1050 rpm.

In Figure 4.1 the catalytic activities of the materials prepared by different experimental methods are displayed. As it can be seen the Ir/CeO_2 synthesised by deposition-precipitation method with NaOH as precipitation agent, while having a yield toward hydrogen similar to the one prepared by the sol-immobilisation, 38.9% and 36.6% respectively calculated as reported in Chapter 2 Section 2.3.1., it has a higher activity compared to this one, Table 4.1. Interestingly the sample prepared by deposition-precipitation by urea exhibited a final yield toward molecular hydrogen of only 0.7%, largely below the value of the other Ir/CeO_2 compared to this section, but it exhibits higher activity toward the decomposition of hydrous hydrazine, 1712 h^{-1} against 1564 h^{-1} (DP NaOH) and 727 h^{-1} (sol-imm THPC) in aqueous solution. The main difference between these methodologies, as reported in Chapter 2 Section 2.2., is the utilisation of an additional heat treatment step, a calcination step in air at 300°C before the high-temperature reduction in H_2/Ar flow, in the case of the deposition-

precipitation method with urea.^{1,5,6} This calcination step is necessary in order to remove volatile adsorbed species that can be generated by the decomposition of urea. As reported in the previous chapter, the high-temperature reduction treatment seems to have little or no effect on the mean particle size, probably due to the presence of H atoms adsorbed on the surface of the NPs acting as a stabilizer during the heat treatment. On the other hand, heat treatment in the presence of oxygen is well known to lead to particle sintering or agglomeration. Therefore, the difference in yield presented by the sample prepared by deposition-precipitation by urea may be related to an increase in of mean particle size due to the extra calcination step necessary during this preparation method.

Table 4.1. Comparison between Ir/CeO₂ catalysts prepared by different experimental methods by yield to H₂, TOF_{50%} and loading of iridium on the surface from SEM-EDX analyses.

Catalysts	Preparation method	Final yield to H ₂ (%)	TOF _{50%} (h ⁻¹)	Ir loading (wt.%)
<i>Ir/CeO₂ DP 600 6h</i>	DP NaOH	38.9	1564	0.7 ± 0.10
<i>Ir/CeO₂ THPC 600 6h</i>	Sol-imm. THPC	36.6	727	1.04 ± 0.13
<i>Ir/CeO₂ urea 600 6h</i>	DP urea	0.7	1712	0.98 ± 0.06

In a purely academical study for the choice of the best catalytic material, some important parameters should be taken into account, such as activity, yield and stability. Nonetheless, another important parameter of the catalyst that has to be taken into consideration is the efficiency of the deposition of iridium onto the surface of the support. As reported in Chapter 3, the deposition-precipitation with NaOH method displayed that only 70% of the total active metal used during the synthesis of the material was successfully deposited on the surface of the support in agreement with previous reports in the literature.^{1,3} On the other hand, both the sol-immobilisation and the deposition-precipitation with urea methods exhibit nearly total Ir deposition efficiency, 100% and 98% respectively, as it will be presented later in this chapter. Taking into account the high price per gram of iridium, 105 £/g for the precursor which contain 38-42% Ir, and the low deposition efficiency with this method, such as 70%, a serious issue for the utilisation of this material in a future industrial application is challenging, since it may require the implementation of extra operation of recovery and purification of the Ir precursor that can increase the cost of the material. On a smaller lab-scale synthesis, such

as the one used in this thesis, the recovery of the precious metal is more difficult and less efficient than in industrial-scale manufacture. For this reason, in spite of the higher TOF displayed by the Ir/CeO₂ prepared by DP with NaOH, it was decided to use the sol-immobilisation method with THPC as a preferential method for the preparation of supported iridium NPs materials.

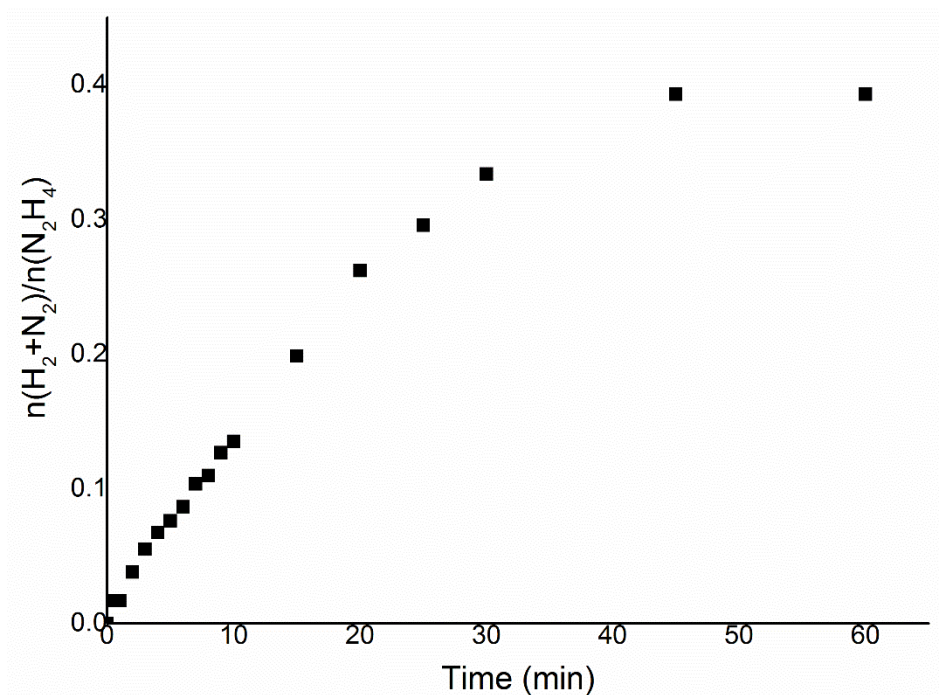


Figure 4.2. $n(\text{H}_2+\text{N}_2)/n(\text{N}_2\text{H}_4)$ versus time for hydrazine decomposition over Ir/CeO₂ SS 600, using 0.3 mL of 3.3 M hydrazine in 8 mL 0.5 M of NaOH solution, at 50°C and 76.2 mg of catalyst, with a stirring rate of 1050 rpm.

An alternative to these wet syntheses, a dry methodology has been explored. As reported in Chapter 2 Section 2.2.3., this solid-state technique is based on the grinding in absence of water of a mixture of metal oxide support and organic iridium precursor, Ir(acac)₃. This material was calcined at 300°C, to remove the organic anion of the precursor and then it was reduced at 600°C to form the Ir NPs, hereafter called Ir/CeO₂ SS 600. As displayed in Figure 4.2, the catalyst prepared by this method exhibited poor catalytic performance both in terms of activity and yield, 2.2% and 5023 h⁻¹, respectively.

4.2.2. Influence of the support material

Other than the active metal and the preparation method chosen for the synthesis of a catalyst, an important role in its final catalytic performance is played by the choice support on which the nanoparticles are deposited. The support employed can be selected among a

large range of materials, from resins to metal oxides, passing through activated carbons. In this thesis, the attention has been focused on metal oxides, which usually have lower surface area than other supports like activated carbons, but they offer a more consistent reference and their properties can be tuned more easily, like the SMSI displayed by Ir/CeO₂ system that is activated by high-temperature reductions, which are only possible on stable oxides.⁷⁻⁹ Different metal oxides present different species on the surface such as hydroxyl groups, oxygen bridges, vacancies and carbonates among them. Even if the same functional group is present on two different oxides the properties of the metal, like its electronegativity, may vary in a significant way the properties of the same functional group.

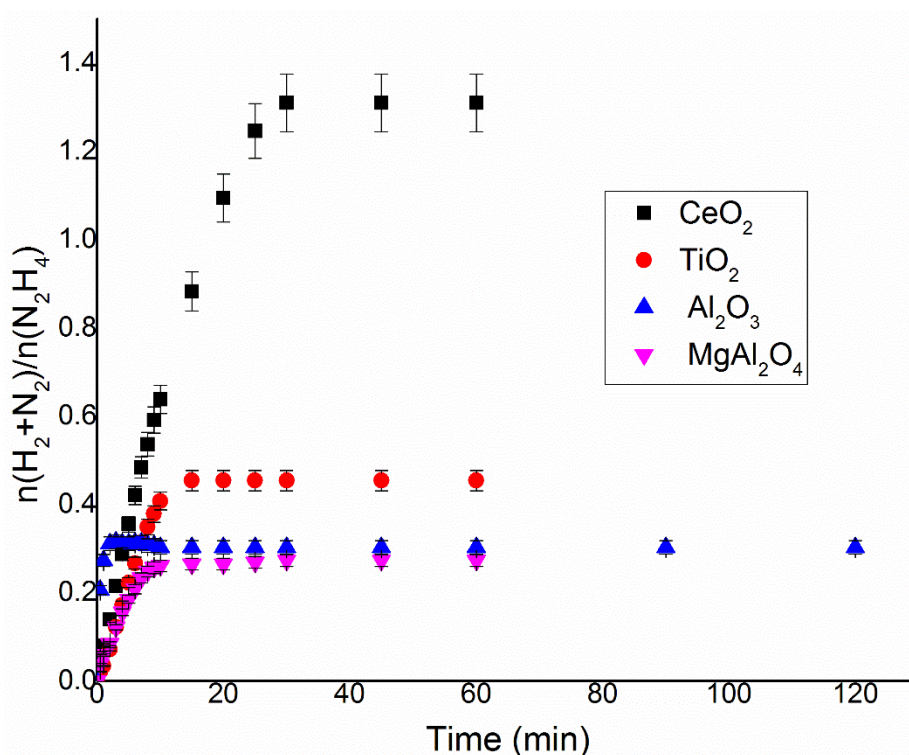


Figure 4.3. $n(\text{H}_2+\text{N}_2)/n(\text{N}_2\text{H}_4)$ versus time for hydrazine decomposition over Ir/CeO₂ THPC 600 6h, Ir/Al₂O₃ THPC 600 6h, Ir/TiO₂ THPC 600 6h, and Ir/MgAl₂O₄ DP 600 6h using 0.3mL of 3.3M hydrazine in 8mL 0.5M of NaOH solution, at 50°C and 76.2 mg of catalyst, with a stirring rate of 1050 rpm.

A series of Ir-based catalysts were prepared by sol-immobilisation THPC method. CeO₂, the reference oxide material, has been compared with TiO₂, γ -Al₂O₃ and MgAl₂O₄ in order to better identify if the catalytic performances of the material tested are related to its acid-base properties. Considering the point of zero charge, PZC, reported in literature for these oxides we can classify TiO₂ as the more acidic support, with PZC of 2-3, and MgAl₂O₄ as the more basic one, with PZC of 10-12, while CeO₂ and Al₂O₃ can be considered more neutral, with PZC

of 6-8. As it can be seen in Figure 4.3 and Table 4.2 none of the tested supports allowed to match the high yield to hydrogen achieved by the Ir NPs deposited on CeO₂. Ir/TiO₂ displayed slightly better yield than the other oxides tested aside CeO₂, while the Ir/Al₂O₃ has the best activity. It should be noticed is that the immobilisation step in the case of Al₂O₃ and MgAl₂O₄ for the sol-immobilisation by THPC synthesis is hindered by the interaction of the NPs with the surface, thus also modifying the method used adjusting the pH with H₂SO₄. These experimental difficulties are demonstrated by the lower Ir amount deposited on the surface, 70.4% and 36.0% for Al₂O₃ and MgAl₂O₄ respectively, as confirmed by the characterisations done on these samples and that will be reported later in this chapter.

Table 4.2. Catalytic performances of Ir catalysts prepared by deposition precipitation with urea and sol-immobilisation with THPC on various support materials for the catalytic decomposition of hydrous hydrazine in solution, using 0.3mL of 3.3M hydrazine monohydrate in 8mL 0.5M of NaOH solution, at 50°C and 76.2 mg of catalyst, with a stirring rate of 1050 rpm.

Catalysts	Final yield to H ₂ (%)	TOF _{50%} (h ⁻¹)	Ir loading (wt. %)
Ir/CeO ₂ THPC 600 6h	36.6	727	1.04 ± 0.13
Ir/CeO ₂ urea 600 6h	0.7	1712	0.98 ± 0.06
Ir/Al ₂ O ₃ urea 600 6h	-2.0	3487	1.06 ± 0.10
Ir/MgAl ₂ O ₄ urea 600 6h	0.0	1555	1.00 ± 0.11
Ir/TiO ₂ THPC 600 6h	4.5	1473	0.89 ± 0.08
Ir/Al ₂ O ₃ THPC 600 6h	0.0	5209	0.70 ± 0.05
Ir/MgAl ₂ O ₄ THPC 600 6h	0.0	2231	0.26 ± 0.12

For this reason, deposition-precipitation with urea has been also tested in order to obtain more reliable data on the effect of support on which the sol-immobilisation by THPC did not provide a complete deposition of Ir. The urea method was chosen for comparison since it uses milder conditions and works on a wider range of support.^{1,3} Figure 4.4 compares the catalytic behaviour of the catalysts prepared by deposition-precipitation with urea on CeO₂, Al₂O₃ and MgAl₂O₄. From the values presented in Table 4.2 it can be concluded that, as for the case of the sol-immobilisation with THPC, the CeO₂ exhibits a higher final yield toward molecular hydrogen respect the other supports.

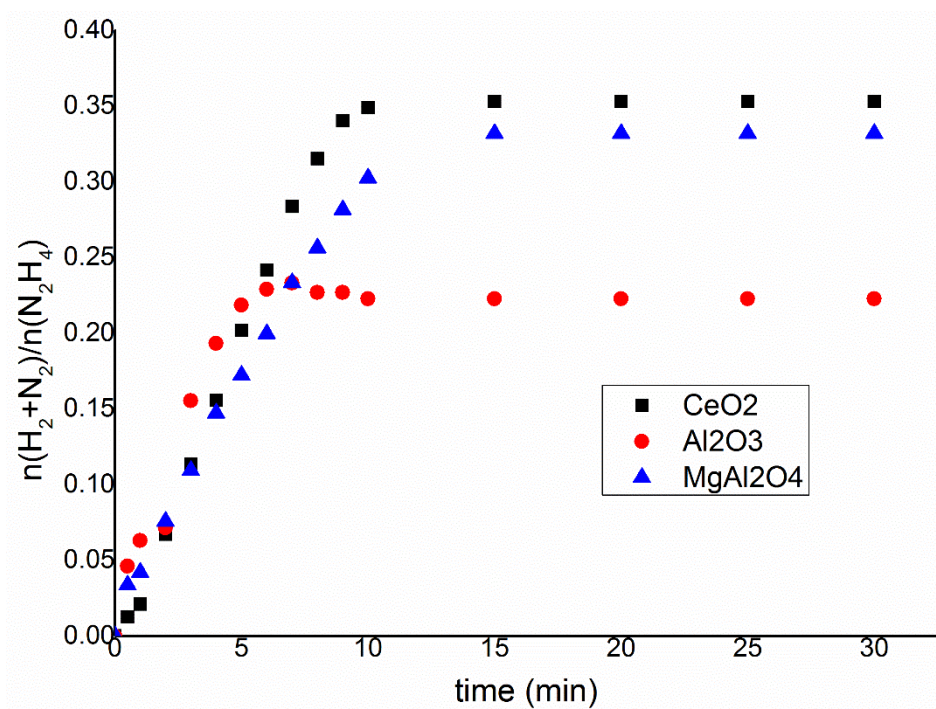


Figure 4.4. $n(\text{H}_2+\text{N}_2)/n(\text{N}_2\text{H}_4)$ versus time for hydrazine decomposition over Ir/CeO_2 urea 600 6h, $\text{Ir}/\text{Al}_2\text{O}_3$ urea 600 6h and $\text{Ir}/\text{MgAl}_2\text{O}_4$ urea 600 6h using 0.3mL of 3.3M hydrazine monohydrate in 8mL 0.5M of NaOH solution, at 50°C and 76.2 mg of catalyst, with a stirring rate of 1050 rpm.

It is the comparison made between the samples prepared by different experimental methods, Sol-immobilisation with THPC and deposition-precipitation with urea, on $\text{Ir}/\text{Al}_2\text{O}_3$ and $\text{Ir}/\text{MgAl}_2\text{O}_4$. As it can be seen in Figure 4.5 on support others than CeO_2 the differences in final hydrogen yield and total time of reaction are within the margin of error of the experimental procedure. This kind of catalytic behaviour may be another indication of the synergistic effect between Ir nanoparticles and CeO_2 during the reaction of liquid-phase decomposition of hydrous hydrazine.

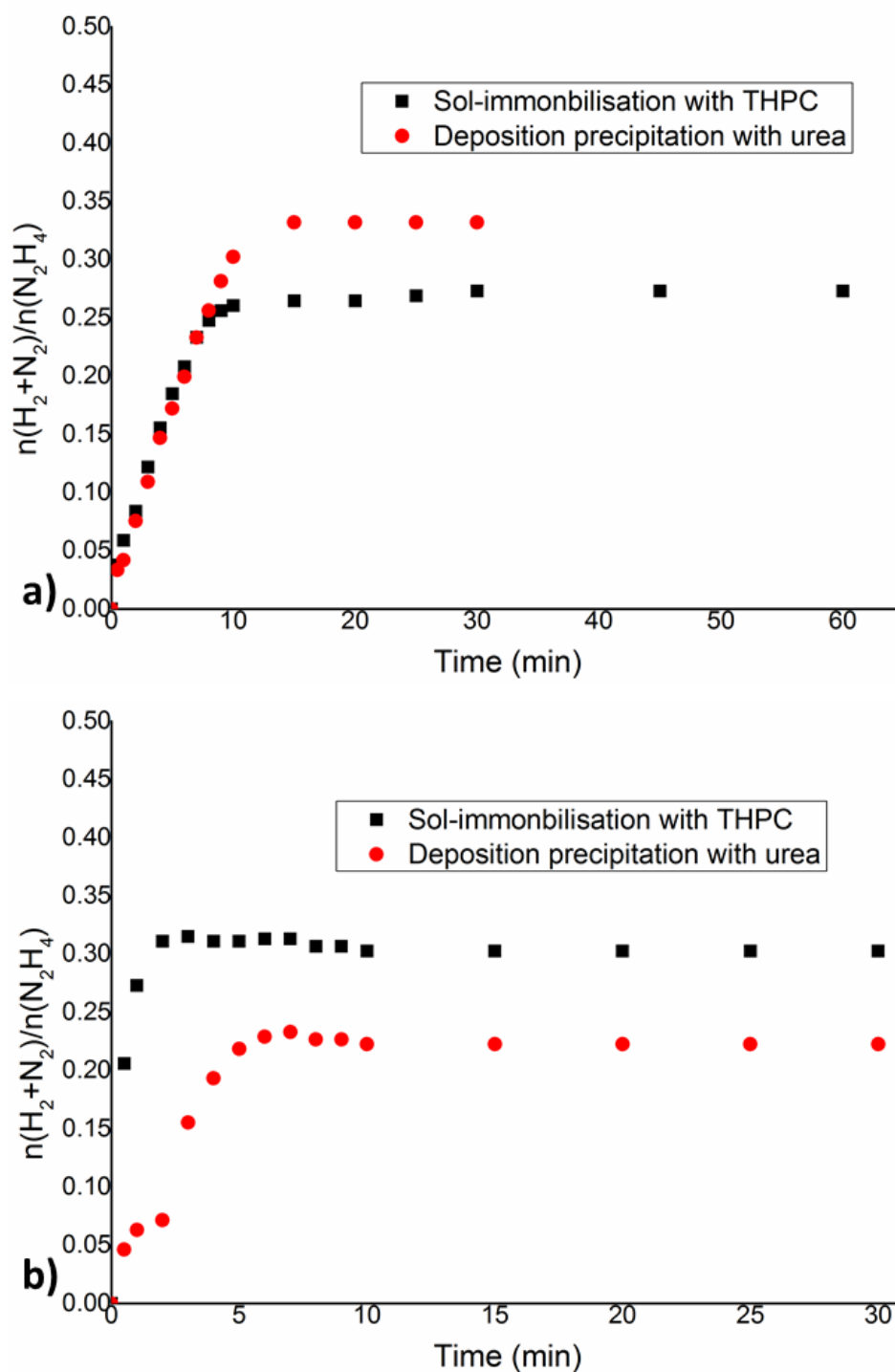


Figure 4.5. $n(\text{H}_2+\text{N}_2)/n(\text{N}_2\text{H}_4)$ versus time for hydrazine decomposition over a) Ir/MgAl₂O₄ urea 600 6h and Ir/MgAl₂O₄ THPC 600 6h and b) Ir/Al₂O₃ urea 600 6h and Ir/Al₂O₃ THPC 600 6h using 0.3mL of 3.3M hydrazine monohydrate in 8mL 0.5M of NaOH solution, at 50°C and 76.2 mg of catalyst, with a stirring rate of 1050 rpm.

NiO was considered as another option for the use as support and the deposition of Ir nanoparticles. Metallic nickel is reported in literature, like other first-row transition metal, to be active for the liquid-phase decomposition of hydrous hydrazine, with reported higher yield toward H₂ production than Ir but significant lower activity.¹⁰⁻¹² For this reason, bare NiO and

NiO samples were heat-treated like the Ir/NiO catalyst and they have been tested in order to exclude activity from the support during the experimental tests. Heat treatment under H₂/Ar flow in the case of NiO is limited at a maximum temperature of 170 °C in order to avoid the reduction of the NiO, since reduced NiO powder has magnetic properties which makes it interact strongly with the magnetic stirrer bar in the reactor and, in this way, it compromises the dispersion of the catalyst in the reaction mixture. The bare NiO support has been proven to be inert during the reaction and therefore the catalytic performance of a synthesised 1 wt.% Ir/NiO was assessed. In Figure 4.6 the catalytic results are reported; the gas production as a function of time of Ir/NiO and NiO samples is showed. Ir/NiO presented a final yield toward hydrogen of 84.2%, more than double of the one exhibited by the similarly prepared Ir/CeO₂_{THPC} (36.6%), and a TOF_{50%} of 132 h⁻¹, lower than the aforementioned Ir/CeO₂_{THPC} (727 h⁻¹). These catalytic performances are interesting since, in spite of lower activity, the higher yield of hydrogen make it more appealing for practical application reducing the waste of hydrous hydrazine for production of hydrogen. These catalytic proprieties can be related to the inclusion of Ni atom into the Ir nanoparticles, since from literature is reported that bimetallic Ir-Ni nanoparticles display the higher values of yield to molecular hydrogen for this reaction. The inclusion of Ni atom can either happen during (I) the immobilisation step, due to a small dissolution of the support in the medium, or (II) the heat treatment, when surface atoms are more mobile. Detailed characterisation is required to solve the real nature and structure of these nanoparticles, therefore Ir/CeO₂ prepared by sol-immobilisation with THPC has been used as reference material for Ir monometallic catalysts.

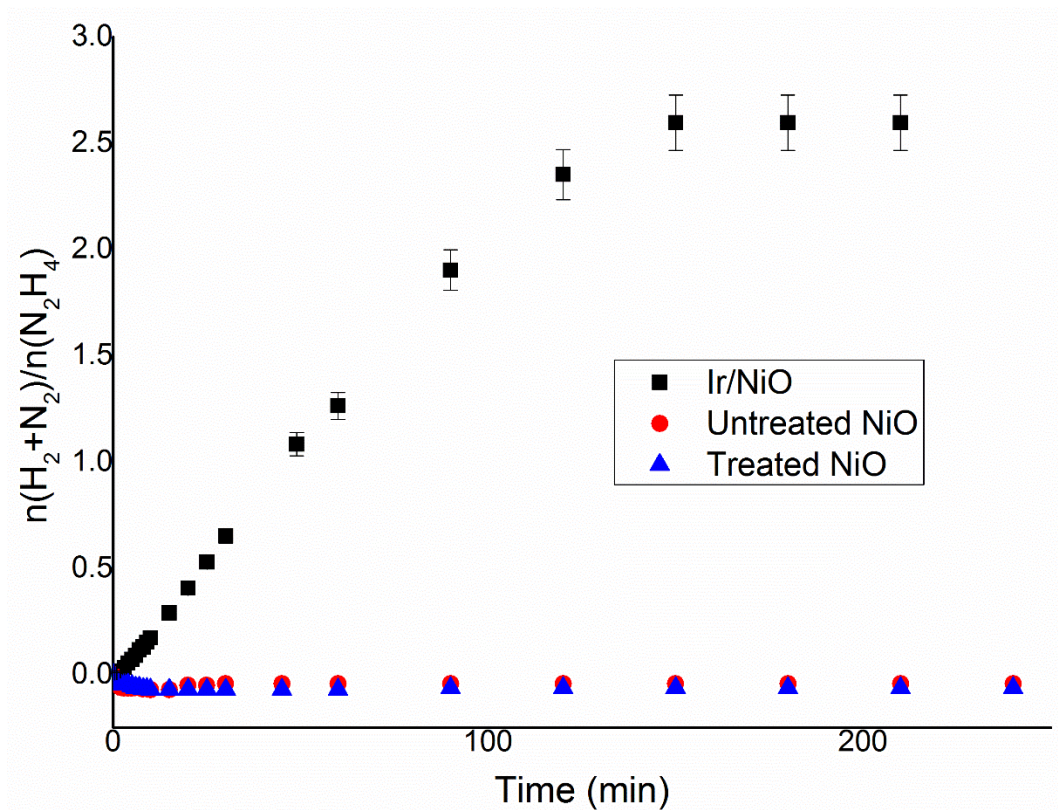


Figure 4.6. $n(\text{H}_2+\text{N}_2)/n(\text{N}_2\text{H}_4)$ versus time for hydrous hydrazine decomposition over Ir/NiO_{THPC 170 6h}, and NiO thermally treated at 170°C under flow of H₂/Ar and untreated NiO using 0.3mL of 3.3M hydrazine monohydrate in 8mL 0.5M of NaOH solution, at 50°C and 76.2 mg of catalyst, with a stirring rate of 1050 rpm.

4.2.3. Effect of reduction and high-temperature treatment

From the preliminary experimental tests on Ir/CeO₂ prepared by deposition-precipitation with NaOH and characterisation reported in Chapter 3, it was suggested the influence of the reduction treatment on the nature of the iridium species on the surface and catalytic behaviour of the material. For this reason, a study on the effect of the different temperature of reduction under H₂/Ar flow, calcination under air flow or chemical reduction with NaBH₄ was further investigated.

In Figure 4.7 the catalytic results are displayed. $n(\text{H}_2+\text{N}_2)/n(\text{N}_2\text{H}_4)$ of Ir/CeO₂ prepared by deposition precipitation with NaOH reduced at different temperature under H₂/Ar flow, reduced with NaBH₄ and non-reduced. As can be seen, the dried only sample was practically inert, as demonstrated by no gas produced over a reaction time of 4 hours, while the reaction catalysed by Ir/CeO₂ chemically reduced by NaBH₄ the gas yield, $n(\text{H}_2+\text{N}_2)/n(\text{N}_2\text{H}_4)$ of 0.097, is below the value of the of a complete decomposition of hydrous hydrazine toward ammonia, 0.33. For these samples, a high percentage of IrO₂ on the surface was observed, as described

by XPS analyses, reported later in the chapter 4.3.5. These catalytic performances can be explained by the tendency of IrO₂ to strongly absorb ammonia on the surface, as confirmed by computational studies reported in Chapter 3, Section 3.5.1. .

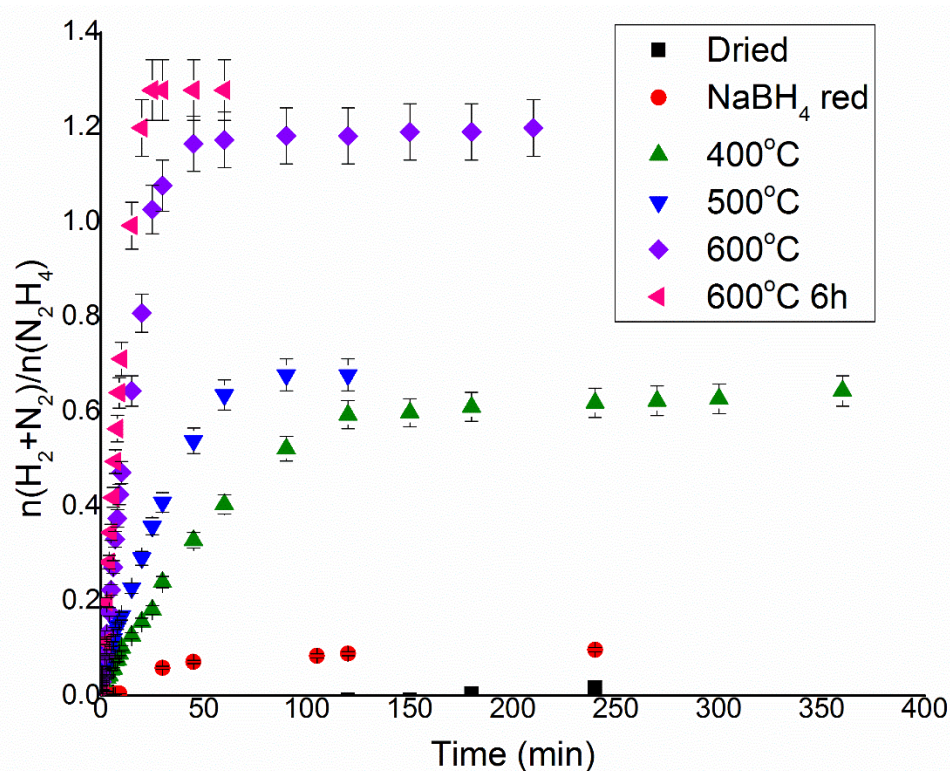


Figure 4.7. $n(\text{H}_2+\text{N}_2)/n(\text{N}_2\text{H}_4)$ versus time for hydrous hydrazine decomposition over Ir/CeO₂ DP dry, Ir/CeO₂ DP NaBH₄, Ir/CeO₂ DP 400, Ir/CeO₂ DP 500, Ir/CeO₂ DP 600 and Ir/CeO₂ DP 600 6h, using 0.3mL of 3.3M hydrazine monohydrate in 8mL 0.5 M of NaOH solution, at 50°C and 76.2 mg of catalyst, with a stirring rate of 1050 rpm.

The results of the samples reduced under H₂/Ar flow, contrary to the chemically reduced and dried samples, exhibit good final yield toward molecular hydrogen, between 11.6% and 38.9% where the chemically reduced did not completely decompose the hydrous hydrazine. In particular, it can be seen from the Table 4.3 how both activity and final yield increase when the reduction was conducted at a temperature of at least 600°C and at longer time of the heat treatment also gave a further increase of the catalytic performances of the Ir/CeO₂ prepared by deposition precipitation with NaOH, from 11.6% to 38.9% of final yield toward hydrogen and TOF_{50%} 244 h⁻¹ to 834 h⁻¹. This catalytic trend can be related to the oxidation state of the Ir nanoparticles and reducibility of the support, CeO₂. As reported in Chapter 3, temperature-programmed reduction, TPR, reported two reduction peaks at 320°C and 540°C that can be correlated to the reduction of CeO₂ around the Ir nanoparticles, this is a possible indication of strong metal-support interaction (SMSI). The XPS analyses, Chapter 3 Section 3.4.7.,

displayed how with higher temperature of reduction and longer duration of the reduction step the amount of metallic Ir increased, which is probably related to a stabilisation of metallic Ir promoted by the larger reduction of CeO₂ around the Ir nanoparticles. The improvement of the catalytic performances displayed by the samples reduced at higher temperature can be linked to (I) the SMSI between Ir and a partially reduced form of CeO₂ or (II) higher amount metallic Ir on the surface of the nanoparticles or a combination of these two causes.

Table 4.3. Catalytic performances of Ir/CeO₂ prepared by deposition precipitation with NaOH treated with various reduction processes for the catalytic decomposition of hydrous hydrazine in solution, using 0.3mL of 3.3M hydrous hydrazine in 8 mL 0.5 M of NaOH solution, at 50°C and 76.2 mg of catalyst, with a stirring rate of 1050 rpm. *Reaction did not consume completely the reagent, which gives problems with the calculation of activity and yield indicator.

Catalysts	Reduction treatment	Final yield to H ₂ (%)	TOF _{50%} (h ⁻¹)
<i>Ir/CeO₂ DP dry</i>	Dried only	n.d.*	n.d.*
<i>Ir/CeO₂ DP NaBH₄</i>	NaBH ₄ reduction	n.d.*	n.d.*
<i>Ir/CeO₂ DP 400</i>	400°C in H ₂ /Ar 3h	11.6	243
<i>Ir/CeO₂ DP 500</i>	600°C in H ₂ /Ar 3h	32.4	776
<i>Ir/CeO₂ DP 600 6h</i>	600°C in H ₂ /Ar 6h	38.9	834
<i>Ir/CeO₂ DP 600</i>	500°C in H ₂ /Ar 3h	12.9	459

In order to verify the influence of IrO₂ on the catalytic performances of supported Ir nanoparticles, a series of IrO₂/TiO₂ samples prepared by Dr Jonathan Ruiz Esquius were tested as reference materials. The samples were prepared by deposition-precipitation using different bases to control the pH (NaOH, K₂CO₃, Li₂CO₃) and they were used both fresh and calcined. As displayed in Figure 4.8, the only IrO₂/TiO₂ that exhibited a catalytic activity is the fresh sample prepared by NaOH and this is probably due to an in situ reduction of the IrO₂ on the surface by the hydrazine itself, indicated also by the increase in activity, as the reaction proceeded. Therefore, these tests indicate the inactivity of IrO₂ towards the decomposition of hydrazine, also toward the production of ammonia, as predicted by the DFT calculations.

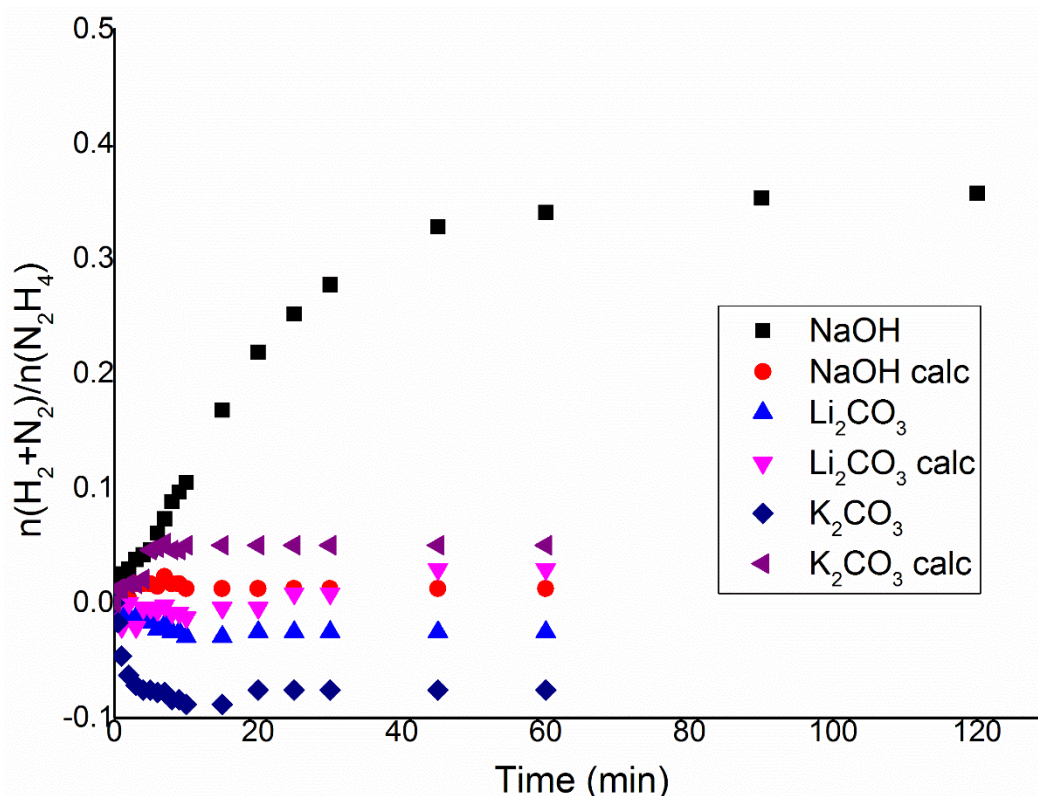


Figure 4.8. $n(\text{H}_2+\text{N}_2)/n(\text{N}_2\text{H}_4)$ versus time for hydrous hydrazine decomposition over $\text{IrO}_2/\text{TiO}_2$ prepared by DP with NaOH dried only and calcined, with Li_2CO_3 dried only and calcined and with K_2CO_3 dried only and calcined using 0.3 mL of 3.3 M hydrazine monohydrate in 8 mL 0.5 M of NaOH solution, at 50°C and 2.5 mg of catalyst, with a stirring rate of 1050 rpm.

To conclude the study on the effect of the thermal treatment, knowing from the previous catalytic tests the importance of metallic Ir on the surface a calcination followed by a reduction under H_2/Ar flow was preferred than to simple calcination step for increasing the percentage of metallic Ir. This test was performed on Ir/CeO_2 prepared by sol-immobilisation with THPC. In order to achieve a better comparison the 1g dried catalyst was divided into two equal parts and then one part was firstly calcined at 500°C under air flow for 3 hours and finally was reduced at 600°C under H_2/Ar flow for 6 h, while the other half was simply reduced under the same conditions. Figure 4.9 presents the results and shows that, while the activity increased in the sample that was calcined and reduced, the final yield toward hydrogen suffered by the use of the calcination step, decreasing from 29.5% to 7.4%. XPS analyses on the samples reported later in the chapter, showed that the main structural difference between the calcined-reduced and simply reduced Ir/CeO_2 prepared by sol-immobilisation with THPC is the absence of the upshift of the Ir^0 peak that was found in non-calcined Ir/CeO_2 . The upshift in the binding energy of metallic Ir can be related to the presence of a small mean

particle size value which probably induces a partial positive charge on the surface the active metal, due to the different coordination of the Ir-Ir structure.⁷⁻⁹ The difference in mean particle size suggested from the XPS was also confirmed by the SEM and TEM analyses presented in the following sections. Therefore, it can be concluded that the calcination facilitates the growth of the Ir nanoparticles; this is detrimental for the yield toward the production of molecular hydrogen.

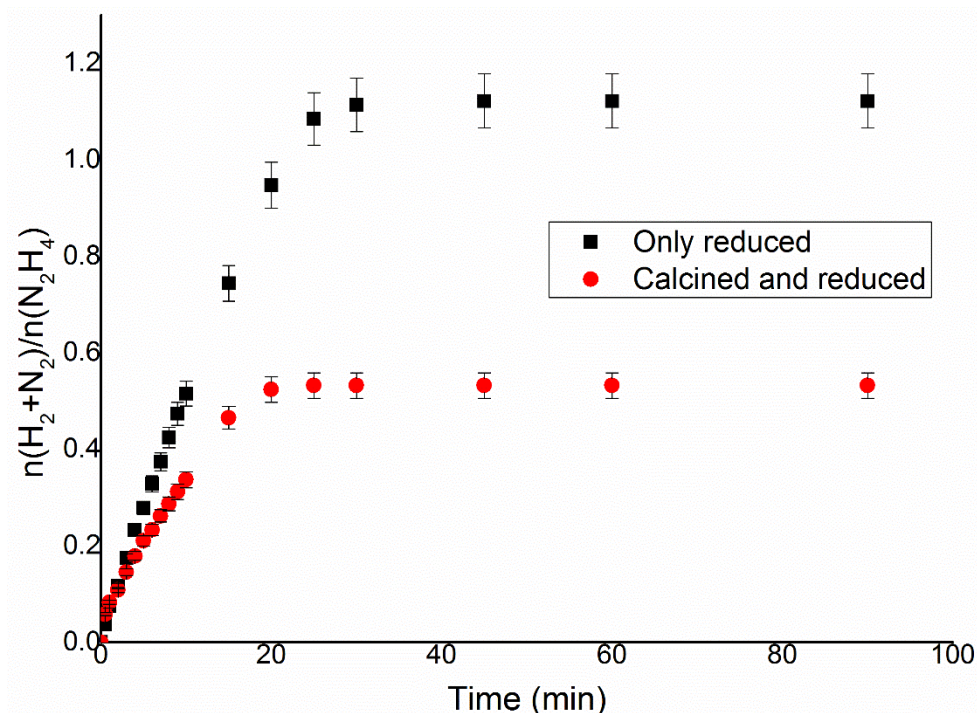


Figure 4.9. $n(\text{H}_2+\text{N}_2)/n(\text{N}_2\text{H}_4)$ versus time for hydrous hydrazine decomposition over Ir/CeO₂ prepared by sol-imm. with THPC reduced at 600°C under flow of H₂/Ar for 6 h and the same catalysts but calcined at 500°C in flow of air for 3 hours before the reduction using 0.3mL of 3.3M hydrazine monohydrate in 8mL 0.5M of NaOH solution, at 50°C and 76.2 mg of catalyst, with a stirring rate of 1050 rpm.

4.2.4. Homogeneous Ir catalysts

To further study the influence and nature of iridium species (oxidation state, ligand) in the catalytic activity for the liquid-phase decomposition of hydrous hydrazine, a series of Ir chloride salts and Ir complexes have been used as homogeneous catalysts. As part of the collaboration with Dr. Hintermair group from Bath University, IrCl₃, K₂IrCl₆, IrO₂, Cp*Ir(H₂O)₃ and (Cp*IrCl₂)₂ have been tested since they are respectively two soluble Ir salts of the stable Ir ions (Ir^{III} and Ir^{IV}), the most stable oxide to confirm that it is inert and two water-soluble complexes (Ir^I and Ir^{III}). The tests were conducted in a specialised batch reactor equipped with a pressure detector on the head space; this change in the reactor was necessary due to the

difficulty to slow the reaction rate at the beginning and allowing to operate in safety by purging the system before the gasses started to evolve from the reaction mixture. In the pressurised reactor the initial amount of hydrous hydrazine was decreased to 0.33 mmol to make sure to maintain an internal pressure lower than 1.5 bar, maximum safe operating pressure, even in the case of complete decomposition of hydrous hydrazine toward molecular hydrogen. As reported in Chapter 2 Section 2.32., firstly the Ir catalysts were warmed in the presence of an aqueous solution under N_2 environment inside the reactor and only when a stable temperature was achieved the aqueous solution of hydrous hydrazine was injected through a sealed septum. In this way the all the reaction was followed at steady conditions from the injection of the reagent as shown in Figure 4.10.

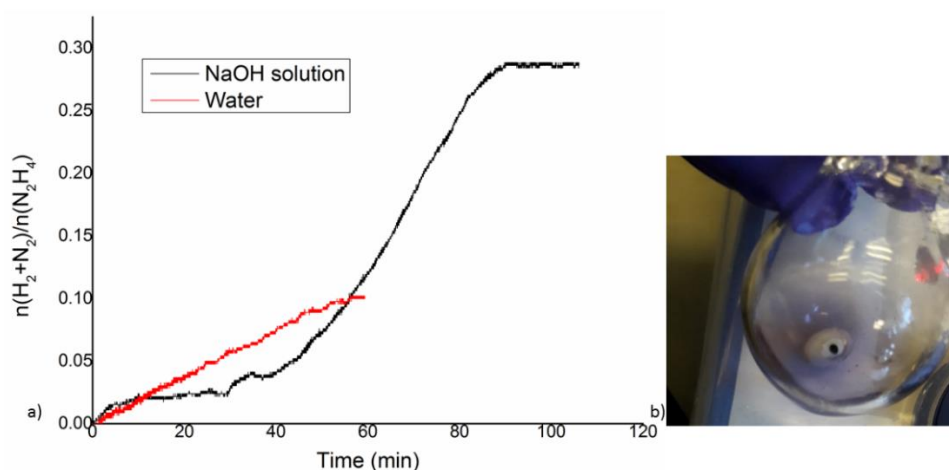


Figure 4.10. a) $n(H_2+N_2)/n(N_2H_4)$ versus time for hydrous hydrazine decomposition over $IrCl_3$ using 0.1 mL of 3.3 M hydrazine monohydrate in 8 mL of water or 0.5 M NaOH solution, at 50°C and 2 mg of catalyst, with a stirring rate of 1050 rpm. b) Reaction solution at the end of the reaction in the presence of a base.

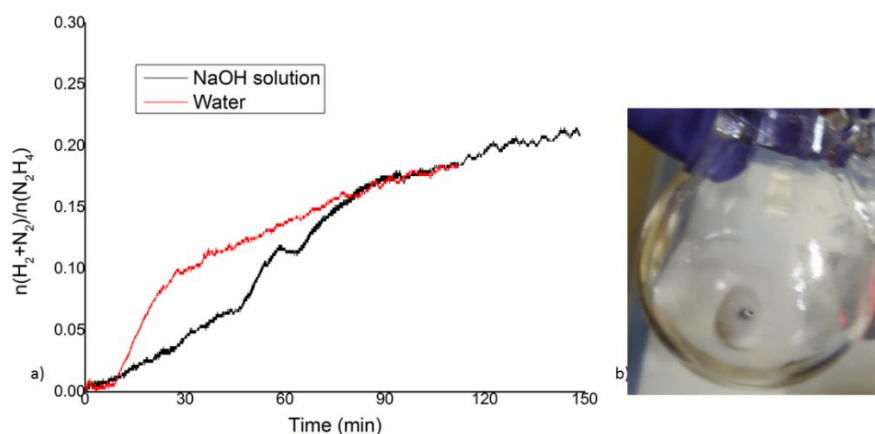


Figure 4.11. a) $n(H_2+N_2)/n(N_2H_4)$ versus time for hydrous hydrazine decomposition over K_2IrCl_6 using 0.1 mL of 3.3 M hydrazine monohydrate in 8 mL of water or 0.5 M NaOH solution, at 50°C and 2 mg of catalyst, with a stirring rate of 1050 rpm. b) Reaction solution at the end of the reaction in the presence of a base.

The Ir catalysts were tested in the presence of NaOH aqueous solution and deionised water as solvent, with the exception of the complexes which were only soluble in base. As in can be seen in Figure 4.10a and 4.11a, IrCl_3 and K_2IrCl_6 are active for the liquid-phase decomposition of hydrous hydrazine, in both base and neutral solutions. To be noticed is that the reaction tends to have an induction time before to start or increase the evolution of gas from the reaction mixture. This phenomenon is related to the formation of Ir nanoparticles due to the reducing action hydrous hydrazine as confirmed by the change of colour of the solution.

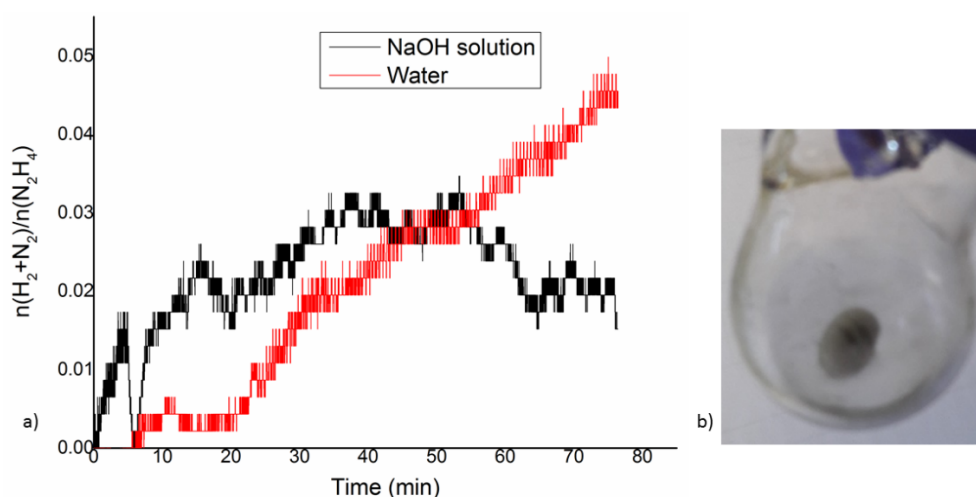


Figure 4.12. a) $n(\text{H}_2+\text{N}_2)/n(\text{N}_2\text{H}_4)$ versus time for hydrous hydrazine decomposition over IrO_2 using 0.1 mL of 3.3 M hydrazine monohydrate in 8 mL of water or 0.5 M NaOH solution, at 50°C and 2 mg of catalyst, with a stirring rate of 1050 rpm. b) Reaction solution at the end of the reaction in the presence of a base.

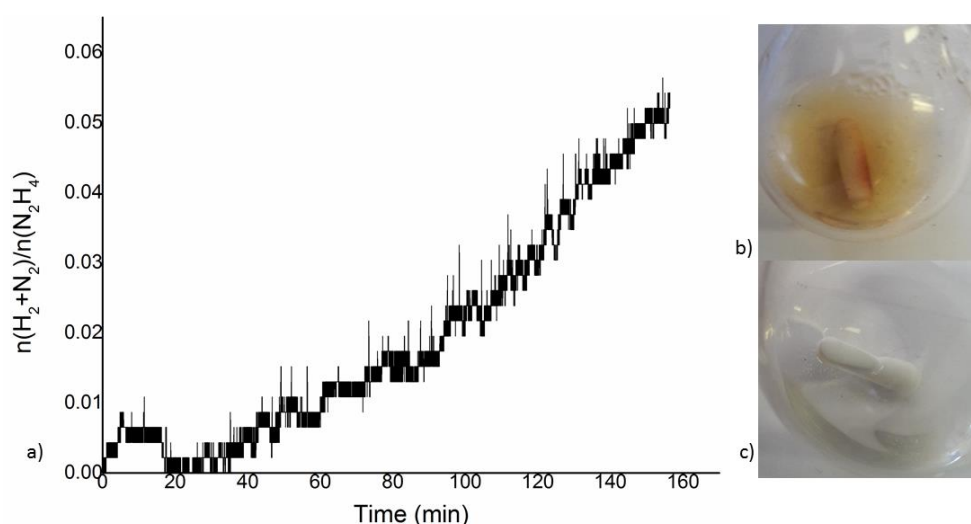


Figure 4.13. a) $n(\text{H}_2+\text{N}_2)/n(\text{N}_2\text{H}_4)$ versus time for hydrous hydrazine decomposition over $(\text{Cp}^*\text{IrCl}_2)_2$ using 0.1 mL of 3.3 M hydrazine monohydrate in 8 mL of water or 0.5 M NaOH solution, at 50°C and 2 mg of catalyst, with a stirring rate of 1050 rpm. b) Reaction solution before the reaction in the presence of a base. c) Reaction solution at the end of the reaction in the presence of a base.

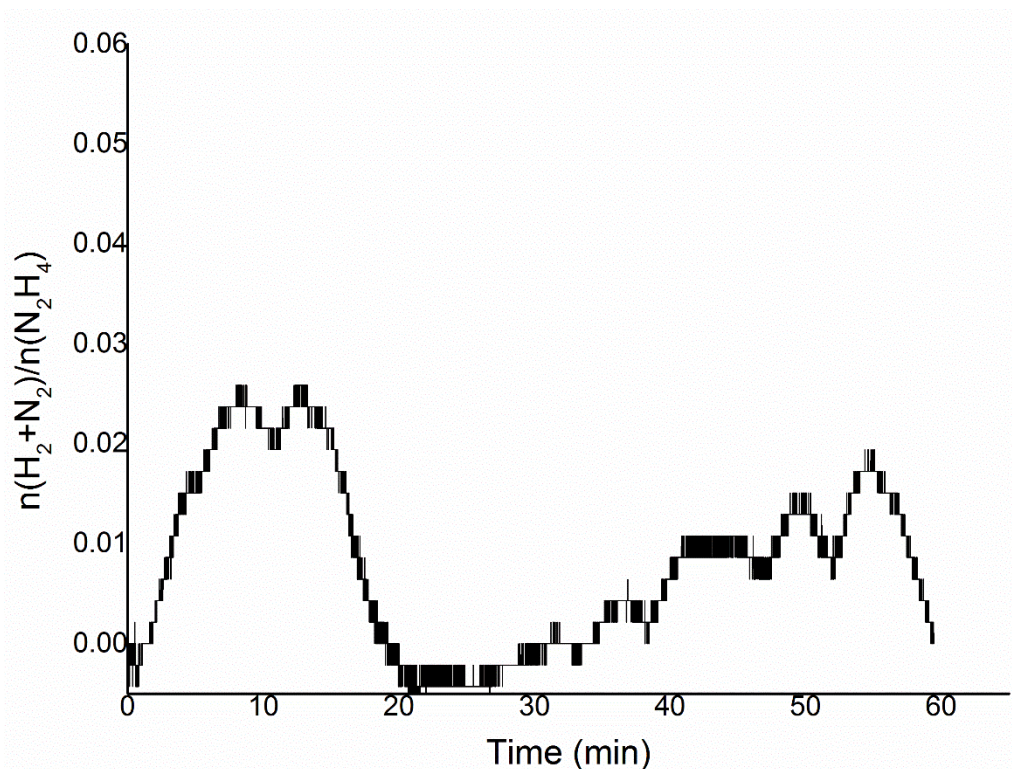


Figure 4.14. $n(\text{H}_2+\text{N}_2)/n(\text{N}_2\text{H}_4)$ versus time for hydrous hydrazine decomposition over $\text{Cp}^*\text{Ir}(\text{H}_2\text{O})_3$ using 0.1 mL of 3.3 M hydrazine monohydrate in 8 mL of water or 0.5 M NaOH solution, at 50°C and 2 mg of catalyst, with a stirring rate of 1050 rpm.

IrO_2 was only active (Figure 4.12a) in the absence of the base and the only Ir complex that displayed activity for the liquid-phase decomposition of hydrous hydrazine was $(\text{Cp}^*\text{IrCl}_2)_2$, as shown in Figure 4.13a, while the catalytic activity of $\text{Cp}^*\text{Ir}(\text{H}_2\text{O})_3$, is presented in Figure 4.14. These catalytic behaviours did not show a clear catalytic trend, especially there is not a clear relationship between the presence of a base and activity like in the case of heterogeneous catalysts. An explanation to this can be found by simple examinations of the reaction mixtures through reaction time. In fact, Ir salts dissolved in water assumed typical yellow-brownish colour, while IrO_2 is blue-purple and the complexes studied are yellow-oranges, the colourisation of the solution remained unaltered only in the case of the reaction that did not exhibit catalytic activity, as it is shown in Figure 4.13b. While the active samples tended to change to colourless solution when the induction period ended, therefore indicating a change in the nature of the Ir species in solution and that is linked with the activity of the metal, as shown in Figures 4.11b, 4.12b and 4.13c. In particular, Ir colloidal nanoparticles in aqueous solution tend to display an adsorption peak in the near UV or vis, <400 nm, with the colour of the Ir colloidal nanoparticles solution to show a light-yellow colour or absent colourisation.

Hydrous Hydrazine is a known reducing agent used in the synthesis of metallic colloidal nanoparticles, therefore, the production of Ir nanoparticles during the liquid-phase decomposition of hydrous hydrazine from salts and complexes is possible and coherent and could explain the induction time during the reaction as the time for the formation of the Ir nanoparticles in the aqueous solution and that maybe the active material. Moreover, in Figure 4.10b is shown the final reaction solution for the IrCl_3 in the presence of a base and it can be observed the formation of a purple powder, that can be identified as IrO_2 since Ir powder is black and Ir nanoparticles are colourless. It can be assumed that complete consumption of the hydrous hydrazine will facilitate the synthesis of Ir^0 nanoparticles and in the presence of the base and in the absence of protective agents and support the Ir nanoparticles will aggregate and oxidise. The worst catalytic performance of $\text{Cp}^*\text{Ir}(\text{H}_2\text{O})_3$ is probably related to the higher stability compared to the other complexes tested, shielding more efficiently the Ir centre from the reduction activity of hydrous hydrazine.

The catalytic activity of Ir^{III} and Ir^{IV} presented from these tests is mainly due to the chemical reduction that takes place by the reducing action of hydrous hydrazine, as it was verified again the inactivity of IrO_2 toward the decomposition of hydrous hydrazine under the same reaction conditions. Moreover, the chemical stability of Ir^{III} and Ir^{IV} chlorides was low in the presence of a strong reducing agent such as hydrous hydrazine as expected since Ir nanoparticles could be formed and this characteristic gives another indication that the activity displayed by the heterogeneous material is related to the presence of Ir^0 or Ir in low oxidation state.

4.2.5. Reusability tests

In Chapter 3, section 3 the studies on the reusability of the Ir/ CeO_2 prepared by deposition-precipitation with NaOH, Ir/ CeO_2 DP 600, are reported, which from the catalytic tests reported in this chapter is among one of the best performing catalytic materials second only to the Ir/NiO. Most of the materials, with the exception of the Ir/NiO, have similar structural and chemical proprieties to Ir/ CeO_2 DP 600. The attention was therefore focused on Ir/NiO prepared by sol-immobilisation method with THPC to test if the different properties, which have led to the increase in the catalytic performance in batch reaction conditions, influence also the long-term stability of the material over time.

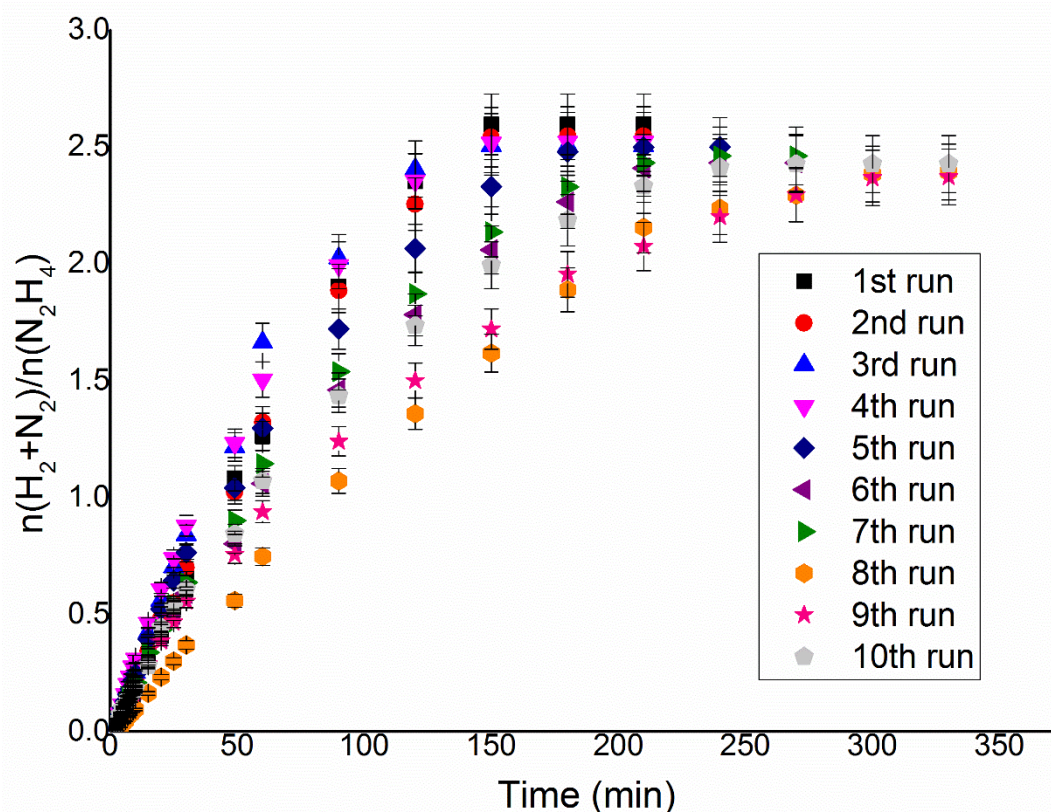


Figure 4.15. $n(\text{H}_2+\text{N}_2)/n(\text{N}_2\text{H}_4)$ versus time for hydrous hydrazine decomposition over Ir/NiO prepared by sol-imm. with THPC for ten consecutive runs using 0.3mL of 3.3M hydrazine monohydrate in 8mL 0.5M of NaOH solution, at 50°C and 76.2 mg of catalyst, with a stirring rate of 1050 rpm.

As it can be seen in Figure 4.15, from the reusability tests, the Ir/NiO sample exhibited a remarkable improvement in terms of stability compared to the Ir/CeO₂. Over the course of ten recyclable reactions, performed by adding fresh aqueous hydrous hydrazine to the mixture at the end of the reaction, the final yield toward molecular hydrogen decreased after 10 cycles from 84.8% to 78.5%, with relative loss of 7.4% in final yield from the first and the final reaction, as shown in Figure 4.16. The presented activity based on TOF_{50%}, on the other hand, tend to fluctuate more during the catalytic tests, nevertheless, the value of 138 h⁻¹ at the final reaction was observed, which is slightly higher the initial value 118 h⁻¹, as shown in Table 4.4. The better stability shown by the Ir/NiO sample is probably associated with the higher final yield toward hydrogen of this sample. The production of ammonia and its successive absorption on the metal surface can be correlated to the deactivation of the iridium catalysts due to the high desorption energy of this molecule that can remain on the surface and block the active sites of the catalyst, therefore, poisoning it, as described by the DFT calculation in Chapter 3 Section 3.5. . To explain the increase in the activity exhibited in

the first few runs, reaching the maximum value of $\text{TOF}_{50\%}$ in the fourth run (181 h^{-1}), two possible cases could be considered: first, the surface of the metal nanoparticle can be reconstructed during the reaction because of the exposure to the high pH of the reaction environment; second, since this material is reduced at lower temperature than the others, the nanoparticles can maintain a small amount of iridium oxide which is then reduced during the reaction, in this way increasing the number of metallic iridium active sites and the activity of the catalyst with it. A final conclusion on the exact reason of the increase in activity during the reusability tests could not be reached due to the overlapping of the high intensity Ni 3p peaks that for NiO is at binding energy, BE, of 67.9 eV that will be discussed later in the chapter, and it precludes a clear quantification of the iridium species on the surface. Equally, the presence of small mean particle size of the Ir nanoparticles makes it difficult to identify any significant variation in the morphology of the nanoparticles. ICP-MS analysis on the solution of reaction remained after the tenth reaction showed limited leaching for Ir, only 2.2% of the total iridium used in ten reactions, and almost no Ni was found in solution, 0.01% of the initial Ni used for the reaction. This is another indication of high stability of Ir/NiO for the decomposition of hydrous hydrazine.

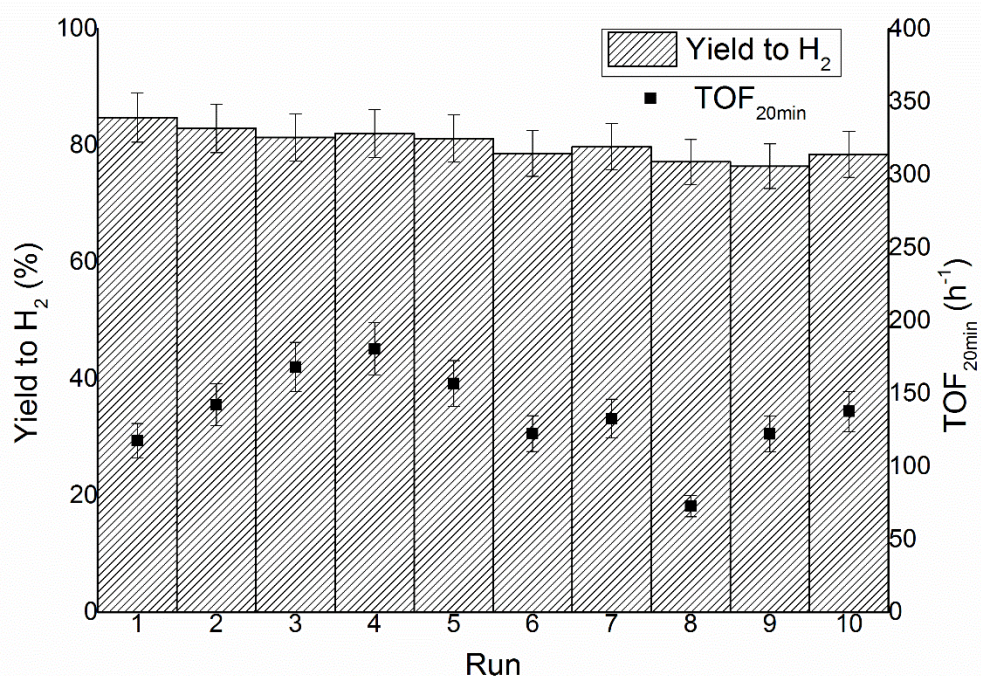


Figure 4.16. Yield toward molecular hydrogen and $\text{TOF}_{20\text{min}}$ over the reusability tests on Ir/NiO using 0.3 mL of 3.3 M hydrazine monohydrate in 8 mL 0.5 M of NaOH solution, at 50°C and 76.2 mg of catalyst, with a stirring rate of 1050 rpm.

Table 4.4. TOF and final yield toward molecular hydrogen during the reusability tests using Ir/NiO_{THPC} as catalyst

Reaction	TOF _{20min} (h ⁻¹)	Yield (%)
1	118	84.8
2	142	82.9
3	168	81.4
4	181	82.0
5	157	81.2
6	123	78.6
7	133	79.8
8	77	77.2
9	122	76.4
10	138	78.5

4.2.6. Analysis of gaseous products by Mass Spectroscopy

To control and verify the accuracy of the measurements made by the water displacement method used for this reaction in the literature as a reliable method, the gases produced during selected reactions were analysed by mass spectroscopy, MS. As reported in Chapter 2 section 2.3.3., the analysis by MS of the gas mixture was performed on the gaseous products collected during the reactions in a sealed gas bag previously purged with inert gas. In order to be certain that the reaction was completed over chosen reaction time, the final reaction time was set at 30 min longer than the typical reaction time needed followed by water displacement to reach the plateau in the following gas evolution graphs. The analysis of the gases produced can be used to quantify the final yield of the reaction toward molecular hydrogen, in particular from the ratio between H₂ and N₂ in the final gas mixture. Therefore, the reaction was performed under Ar gas as inert instead of N₂ like in the water displacement method. In this way the N₂ produced by the reaction was quantifiable. The yield can be calculated using these equations:

$$\frac{n(N_2H_4)_{hyd}}{n(N_2H_4)_{initial}} = yield \quad (Eq. 4.1)$$

At full conversion initial amount of mole of hydrazine is equal to the total hydrazine moles converted at the end of the reaction, therefore:

$$\frac{n(N_2H_4)_{hyd}}{n(N_2H_4)_{cons}} = yield \quad (Eq. 4.2)$$

$$nH_2 = 2 \cdot n(N_2H_4)_{hyd} = 2 \cdot (N_2H_4)_{cons} \cdot yield \quad (Eq. 4.3)$$

$$\begin{aligned} nN_{2amm} &= \frac{1}{3} \cdot [n(N_2H_4)_{cons} - n(N_2H_4)_{hyd}] = \frac{1}{3} \cdot [n(N_2H_4)_{cons} - yield \cdot n(N_2H_4)_{cons}] = \\ &= \frac{1}{3} \cdot n(N_2H_4)_{cons} \cdot (1 - yield) \end{aligned} \quad (Eq. 4.4)$$

$$nN_{2hyd} = n(N_2H_4)_{hyd} = (N_2H_4)_{cons} \cdot yield \quad (Eq. 4.5)$$

$$\begin{aligned} \frac{nH_2}{nN_{2tot}} = ratio &= \frac{2 \cdot (N_2H_4)_{cons} \cdot yield}{(N_2H_4)_{cons} \cdot yield + \frac{1}{3} \cdot n(N_2H_4)_{cons} \cdot (1 - yield)} = \\ &= \frac{2 \cdot yield}{yield + \frac{1}{3} \cdot (1 - yield)} = \frac{6 \cdot yield}{2 \cdot yield + 1} \end{aligned} \quad (Eq. 4.6)$$

$$6 \cdot yield - 2 \cdot yield \cdot ratio = ratio \quad (Eq. 4.7)$$

$$yield = \frac{ratio}{6 - 2 \cdot ratio} \quad (Eq. 4.8)$$

In the Equations 4.1-4.8, $n(N_2H_4)_{initial}$ are the initial moles of hydrous hydrazine, $n(N_2H_4)_{hyd}$ are the moles of hydrous hydrazine that are converted to hydrogen, $n(N_2H_4)_{cons}$ are the total moles of hydrous hydrazine converted, nH_2 are the moles of hydrogen produced, nN_{2amm} are the moles of nitrogen produced from the decomposition of hydrous hydrazine to ammonia, nN_{2hyd} are the moles of nitrogen produced from the decomposition of hydrous hydrazine to hydrogen, nN_{2tot} are the total moles of nitrogen produced from the decomposition of hydrous hydrazine. Equations 4.1 and 4.2 are the definitions of yield and yield at full conversion. Combining equation 4.2 with the reaction equation 1.18 and 1.19 it is possible to calculate the moles of nitrogen and hydrogen produced by each of the two reaction pathways as function of the yield at full conversion and the moles of hydrazine converted, Eq. 4.3-4.5. Finally, in equations 4.6-4.8 using the ratio between moles of hydrogen and nitrogen produced and the equations 4.3-4.5, correlate the yield to the ratio of the gases, which is a

value that can be measured by the mass spectroscopy on the gases produced during the reaction.

Table 4.5. Quantification of hydrogen and nitrogen amount through mass spectroscopy and yield calculated by the MS analyses and from water displacement method for Ir/CeO_{2 400}, Ir/CeO_{2 600} and Ir/NiO.

Catalyst	Hydrogen (ppm)	Nitrogen (ppm)	H ₂ /N ₂ ratio	Yield from MS (%)	Yield from W-D (%)
Ir/CeO _{2 THPC 400}	32935	55135	0.597	12.4 ± 0.4	11.6 ± 0.7
Ir/CeO _{2 THPC 600}	83885	85770	0.978	24.2 ± 0.6	23.9 ± 0.4
Ir/NiO _{THPC}	137470	73144	1.879	83.9 ± 1.1	84.2 ± 0.3

The catalysts used with the test for the MS analyses to confirm the validity of the water displacement method were two; 0.7 wt.% Ir/CeO_{2 400}, Ir/CeO_{2 600}, and the 1 wt.% Ir/NiO. These samples were chosen as representative of the Ir on metal oxide catalysts with low yield range to H₂, Ir/CeO_{2 400}, medium yield range, Ir/CeO_{2 400}, and high yield, Ir/NiO. As it can be seen in Table 4.5 there is a small discrepancy between the value of yield obtained by the water displacement method and by the analysis of the gases with the MS, but the difference between the value is in the range of the experimental error of the measurements of the two techniques, therefore the water displacement method can be considered reliable by the analysis of the gaseous products presented.

The analysis of the gaseous products was also used to obtain vital information about the mechanism of the reaction that takes place during the liquid-phase decomposition of hydrous hydrazine over Ir catalysts. These studies were performed using hydrazine monohydrate labelled with 98% ¹⁵N atoms. Using hydrazine with different nitrogen isotopes will produce molecular nitrogen with different molecular mass that can be detected by the mass spectrometer. In particular, using a pure ¹⁴N₂H₄ and ¹⁵N₂H₄ the reaction will produce only ¹⁴N¹⁴N and ¹⁵N¹⁵N respectively, displaying on the MS analysis only peaks for mass 28 and 30. More interesting is the use of mix ¹⁴N₂H₄ and ¹⁵N₂H₄ since in this case the possible peaks in the mass spectrum are 28 and 30 but also 29, from the possible presence of ¹⁴N¹⁵N. The presence of ¹⁴N¹⁵N is an indicator of a reaction mechanism in which the N-N bond of the hydrazine molecule is broken and the N adsorbed atom is free to move on the surface and therefore recombine with other N atoms originated from another hydrazine molecule. On the

contrary, the absence of this particular molecular nitrogen isotopic combination does not exclude the cleavage of the N-N bond, but it indicates that if the cleavage takes place the surface can accommodate only one molecule of hydrazine at the time so that the recombination of the N atoms can take place only between atoms originated from the same hydrazine molecule.

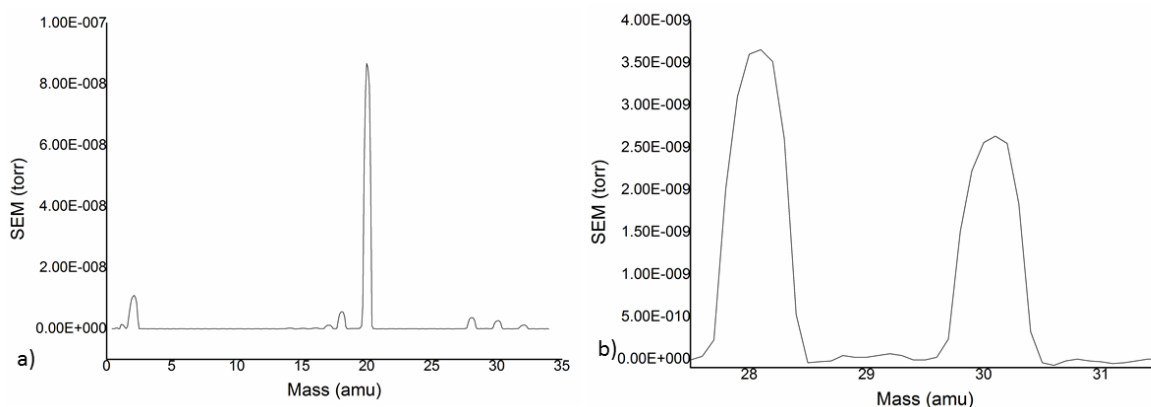


Figure 4.17. a) Mass Spectrum of the gaseous product of the reaction of decomposition of hydrous hydrazine using ^{15}N labelled hydrazine monohydrate as reagent. b) Magnification of the region between 27 and 31 atomic mass unit of the spectrum.

As it can be seen in Figure 4.17a, when the reaction was performed using only $^{15}\text{N}_2\text{H}_4$ as the reagent, the mass spectrum exhibits only peaks at 30 and 28, which can be related to the peak at 32 indicating a small contamination from the air. The labelled reagent has 98% of ^{15}N , therefore a small amount of $\text{H}_2^{14}\text{N}^{15}\text{NH}_2$ and $^{14}\text{N}_2\text{H}_4$ was still present in the reagent mixture. The catalytic test on pure isotopic labelled hydrazine monohydrate was used as a test on the sensibility of the MS to naturally occurring fragments with mass 29, since the presence of ^{14}N is higher in this compound, 2%, than the presence of ^{15}N in the common hydrous hydrazine, where its natural occurrence is 0.4%. In Figure 4.17b, the region of the spectrum between 26 and 31 m/z is enlarged and a small peak of maximum value $4.45 \cdot 10^{-11}$ torr is centred at 29, while the peak at 30 has an $1.42 \cdot 10^{-9}$ torr so with a ratio between the two peaks of 31.9, 30/29.

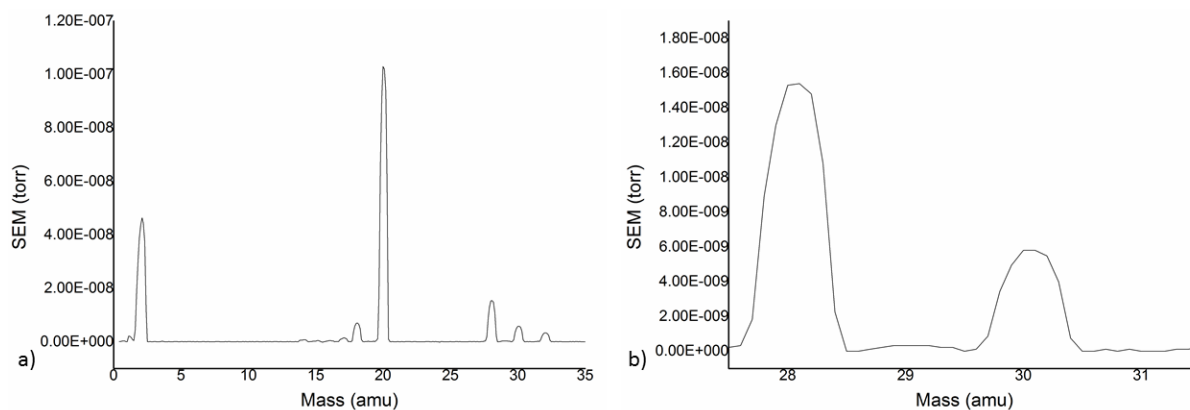


Figure 4.18. Mass Spectrum of the gaseous product of the reaction of decomposition of hydrous hydrazine using a mixture of ^{15}N labelled hydrazine and non-labelled hydrazine monohydrate as reagent. b) Magnification of the region between 27 and 31 atomic mass unit of the spectrum.

Figure 4.18a display the mass spectrum of the gas products of a mixture 1:1 in mole of labelled hydrazine monohydrate and non-labelled hydrazine. As can be seen in the graph the fragments present in the gas mixture are similar, with a higher intensity for the fragment at 28 m/z due to the nitrogen produced by the reaction. In Figure 4.18b the region between 26 and 31 m/z is enlarged and it can be noticed the higher intensity of the peak at 29 m/z, with a maximum of $2.35 \cdot 10^{-10}$ torr, respect the peak at 30 which has a maximum of $3.15 \cdot 10^{-9}$ torr. In this case, the ratio between the 30 and 29 peaks decreased to 13.4. Therefore, the use of the mixture of the two reagent increases the presence of N_2 formed by two different isotopes respect to the use of pure $^{15}\text{N}_2$ hydrazine monohydrate, from 31.9 to 13.4. This increase can indicate that at least a small part of the hydrous hydrazine undergoes to the split of the N-N bond and rearrange the N atoms between atoms derived from different hydrazine molecules. Nevertheless, the area of the fragment at 29 m/z is low and if the N-N bond is broken the mobility of the N atoms is limited so that they can only interact with the other N atom of their original molecule.

4.3. Characterisation of the catalytic materials

Ir nanoparticles as suitable candidates for the catalytic liquid-phase decomposition of hydrous hydrazine were identified. With the empirical data of the catalytic performance of materials prepared using different chemical methods and supports, the characterisation performed were focused on the identification of the structural differences between the materials tested. This with the aim to better comprehend the mechanism of reaction and how to improve further the synthesis of these catalytic materials in the near future.

In particular, in this chapter (I) oxidation state of Ir on the surface, (II) mean particle/crystallite size of Ir and particle size distribution and (III) adsorption on the surface have been analysed.

4.3.1. Powder X-ray diffraction (p-XRD)

The most representative materials have been analysed using the p-XRD in order to determine if the structural differences between their syntheses lead to changes in the crystalline structure of the synthesised Ir nanoparticles. As reported in Chapter 3, Section 3.4.2., the Ir/CeO₂ prepared by deposition-precipitation with NaOH reduced at 400°C under H₂/Ar flow for 3 hours, Ir/CeO₂ DP 400, did not exhibit any of the characteristic diffraction peaks of metallic iridium, at $2\theta = 40.8^\circ$, 47.2° , 69.1° and 83.6° corresponding to the (111), (200), (220) and (311) planes,¹³ or IrO₂, at $2\theta = 28.1^\circ$, 35.0° , 39.8° and 55.3° respectively for (110), (101), (200) and (211) planes.¹⁴ The absence of diffraction peaks of the iridium species was then explained, following the analysis of TEM images of Ir/CeO₂ DP 400, with the small mean particle size, 1.0 ± 0.2 nm, which lead to broad peaks that cannot be distinguished by the background using p-XRD.

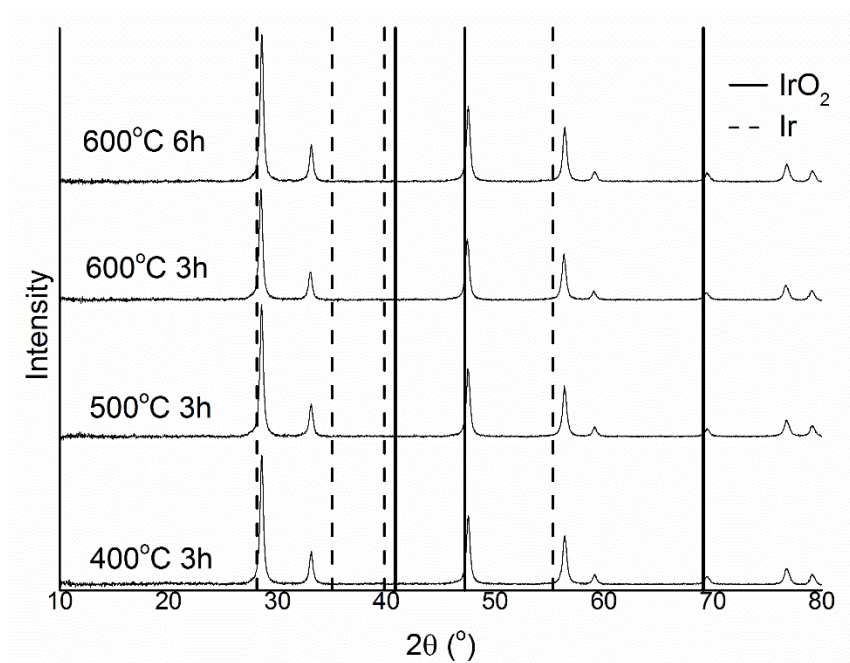


Figure 4.19. p-XRD patterns for Ir/CeO₂ DP 400, Ir/CeO₂ DP 500, Ir/CeO₂ DP 600, Ir/CeO₂ DP 600 6h. (—) represent the position of the IrO₂ diffraction peaks and (- -) represent the position of the Ir diffraction peaks reported in literature.

In this chapter, the effect of the temperature of the reduction treatment was studied. High-temperature heat treatment is known to facilitate the growth of deposited nanoparticles both

by coalescence of nanoparticles and by Ostwald-Ripening.¹⁵ These phenomena take place to a higher extent when the heat treatment is performed in the presence of oxygen, but they can also occur in reductive environments such as the one used in the protocol of reduction for Ir nanoparticles. In Figure 4.19 the diffractograms for the Ir/CeO₂ prepared by deposition-precipitation with NaOH and reduced at different temperature and for different times are reported. As it can be seen the four samples displayed only the characteristic diffraction peaks of cerium oxide as previously reported in Chapter 3. Also Ir/CeO₂ DP 600 6h, that underwent a heat treatment at 600°C for 6 hours instead of the typical 3 hours used for the other sample, did not exhibit any of the diffraction peaks of the iridium species indicating that, even if sintering phenomena took place, the growth of the Ir nanoparticles is limited under reductive environment and final crystallite size remained below 5 nm. Therefore, the increase in catalytic performance observed with the reduction at high temperature can be related mainly to the increase in metallic iridium on the surface, as reported in Chapter 3, by the results of XPS and TPR analyses, and not to a significant increase in particle size of Ir.

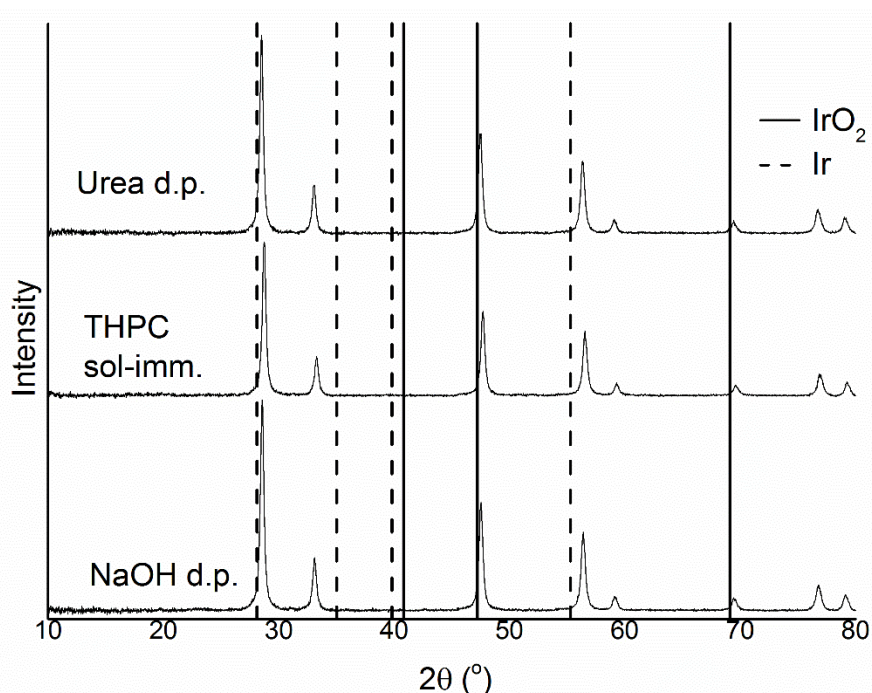


Figure 4.20. p-XRD pattern for Ir/CeO₂ DP 600 6h, Ir/CeO₂ urea 600 6h and Ir/CeO₂ THPC 600 6h. (—) represent the position of the IrO₂ diffraction peaks and (- -) represent the position of the Ir diffraction peaks reported in literature.

As it is known, different preparation methods can produce nanoparticles with different mean particle size. Therefore, the Ir/CeO₂ prepared by different preparation methods tested in this chapter were also analysed by p-XRD in order to compare the crystallite size and possibly the

nature of those crystallites. In Figure 4.20 the diffractive pattern of the Ir/CeO₂ prepared by various synthesis methods tested in this chapter are reported. Among the Ir/CeO₂ samples, sol-immobilisation with THPC, Ir/CeO₂ THPC 600 6h, formed very small Ir nanoparticles as observed by the UV/vis analysis on the Ir colloidal solution, reported later. On the other hand the deposition-precipitation with urea, Ir/CeO₂ urea 600 6h, with an experimental protocol established using a calcination step at 300°C under flow of air which could lead to faster growth of the Ir nanoparticles that can be detected in the diffractogram. Nonetheless, as it can be seen in Figure 4.20, neither Ir/CeO₂ urea 600 6h, did not exhibit any of the typical diffraction peaks of iridium species, indicating that also during the calcination step the crystallite size of Ir did not grow above the 5 nm. Therefore, the lower catalytic performance presented cannot be related mainly to the mean particle/crystallite size of Ir since the range of variation of crystallite size of Ir was small. Therefore, other parameters should be considered, such as the oxidation state of Ir and surface exposure of Ir.

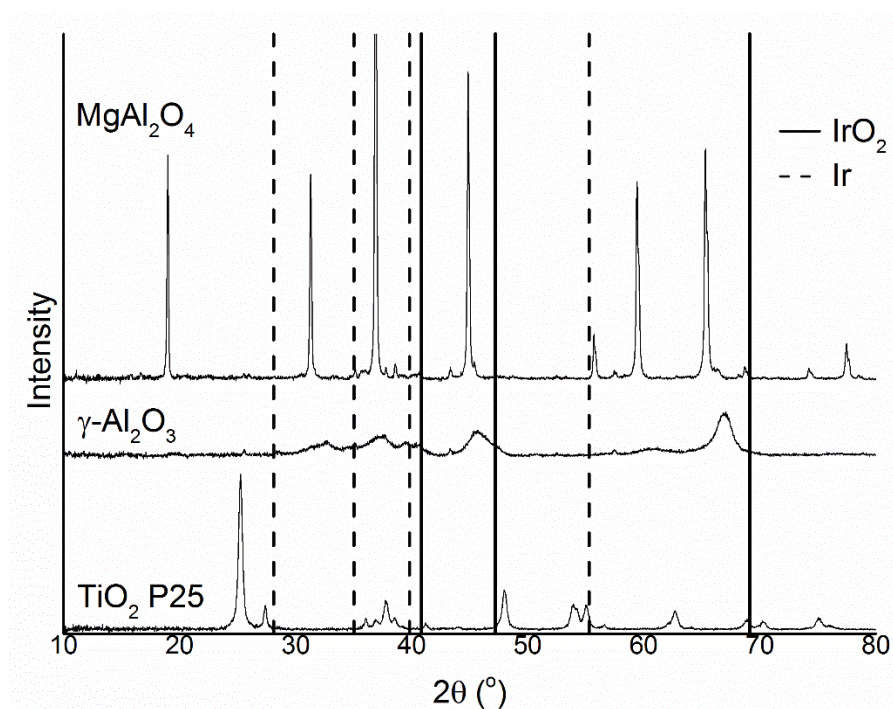


Figure 4.21. p-XRD pattern for Ir/TiO₂ urea 600, Ir/Al₂O₃ 600, and Ir/MgAl₂O₄ 600. (—) represent the position of the IrO₂ diffraction peaks and (- -) represent the position of the Ir diffraction peaks reported in literature.

Figure 4.21 reports the p-XRD patterns of Ir nanoparticles deposited on various supports using urea. These analyses were meant to prove the stability of the Ir nanoparticles under high-temperature treatment or, in case of negative results, to identify a stabilising action played by the CeO₂ as support. The Ir/TiO₂ and Ir/Al₂O₃ materials presented broader diffraction peaks

that can be assigned to the small particle size of the metal oxides used as support without the presence of any of the characteristic diffraction peaks of Ir species. Ir/MgAl₂O₄ presented sharper diffraction peaks that can be assigned to the characteristic structure of spinel metal oxide, but there are also smaller diffraction peaks at 37.7°, 38.5° and 43.4° that cannot be assigned to the support or to the presence of Ir nanoparticles. These diffraction peaks can be due to impurity in the structure of the mixed oxide or due to the presence of other metal ions in the spinel crystallites. Since none of the samples exhibited the characteristic diffraction peaks of Ir species it can be concluded that the stability during high-temperature heat treatment is a feature of these supported Ir nanoparticles not strictly related to the support on which these are deposited on. It is also noteworthy that in all the analyses reported in this section no characteristic diffraction peaks of Ir were visible, strongly implying that Ir nanoparticles tend to form Ir crystallites of dimension below 5 nm independently from preparation method and support with high stability to sintering at high temperature, especially in the case of using oxides.

4.3.2. Scanning Electron Microscopy (SEM) and Energy Disperse X-ray Spectroscopy (EDS)

In addition to the p-XRD analyses, the samples were analysed by scanning electron microscopy to obtain additional structural information about their morphological properties. As explained in Chapter 3, Section 3.4.4., SEM can be used to study the morphology of the metal oxide support, while EDS analyses performed in combination with it can give additional information about the metal loading and the dispersion of the active metal on the surface. In this chapter catalysts prepared by different experimental protocols and with different metal oxide used as support have been tested as possible catalysts for the liquid-phase decomposition of hydrous hydrazine, therefore, these materials were analysed to control the effective loading of the active metal on the surface since every support interacts differently to the various preparation method, which could lead to difficulties in the immobilisation or deposition of the Ir nanoparticles.

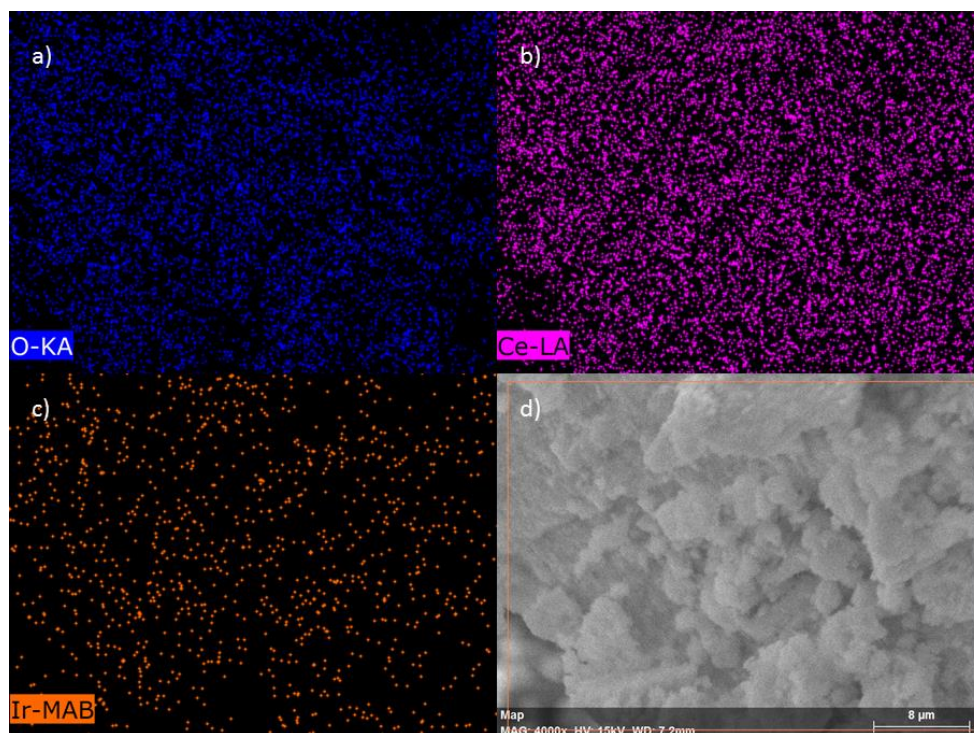


Figure 4.22. Representative SEM images, *d*, with EDX mapping of Ir/CeO₂ urea 600 sample for different elements such as O, a, Ce, b, and Ir, c.

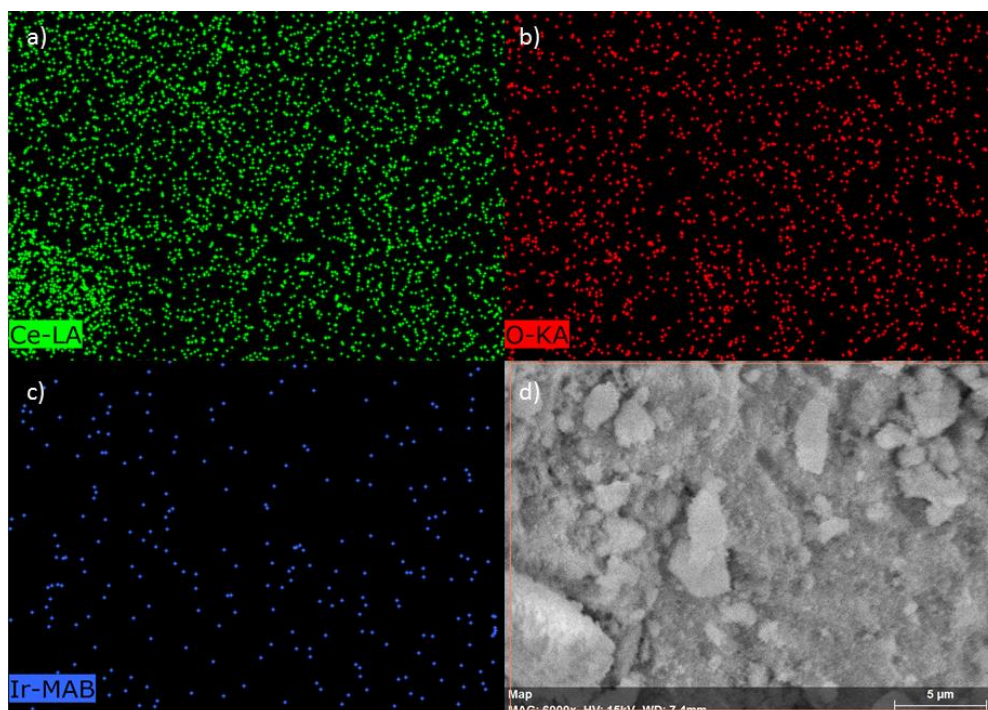


Figure 4.23. Representative SEM images, *d*, with EDX mapping of Ir/CeO₂ THPC 600 sample for different elements such as O, a, Ce, b, and Ir, c.

As reported in Chapter 3 the Ir/CeO₂ prepared by deposition-precipitation with NaOH presented a real loading of 0.7 wt.% instead of the nominal 1 wt.%. In Figures 4.22 and Figure

4.23 some representative images for the catalysts prepared by deposition-precipitation with urea, Ir/CeO₂_{urea 600}, and sol-immobilisation with THPC on CeO₂, Ir/CeO₂_{THPC 600}, are reported. As can be seen, the Ir nanoparticles are well dispersed on the surface on both the samples. As reported in Table 4.6 the data from the EDX quantification of the elements on the surface are 0.98 ± 0.06 wt.% for Ir/CeO₂_{urea 600} and 0.97 ± 0.10 wt.% for Ir/CeO₂_{THPC 600}; these results are in agreement with the nominal values of 1 wt.%, calculated by the amount of metal precursor utilised for the synthesis. Therefore, it is possible to conclude that, contrary to the deposition-precipitation by NaOH, the other preparation methods managed to deposit or immobilise completely the iridium on the surface of the support. The improved loading can be achieved at a lower pH of the aqueous solution during the preparation methods. In fact, where the deposition-precipitation with NaOH requires a pH of 10, the sol-immobilisation with THPC was achieved at a pH value between 7.5 and 8.5 in the final stages of the immobilisation starting from lower values and during deposition-precipitation with urea increased from a pH value of 2 to 7 due to the decomposition of the precipitation agent. After this consideration it can be concluded that the interaction between Ir nanoparticles and the CeO₂ is optimal at values of pH below 10, therefore, preparation methodologies that require lower pH deposition or immobilisation steps are to be preferred for the preparation of Ir/CeO₂ catalysts, keeping in mind that pH values below 4 for prolonged time periods can lead to the partial dissolution of the support. This last condition excluded the use of sol-immobilisation with polyvinyl alcohol which requires the use of concentrated H₂SO₄ to increase the immobilisation of the Ir nanoparticles on the surface.

Table 4.6. Catalysts loading calculated by SEM-EDX analyses.

Catalysts	Ir loading (wt. %)
<i>Ir/CeO₂ THPC 600</i>	1.0 ± 0.1
<i>Ir/TiO₂ urea 600</i>	0.5 ± 0.2
<i>Ir/CeO₂ urea 600</i>	1.0 ± 0.1
<i>Ir/Al₂O₃ urea 600</i>	1.1 ± 0.1
<i>Ir/MgAl₂O₄ urea 600</i>	1.0 ± 0.1
<i>Ir/NiO</i>	1.0 ± 0.1

For similar reasons, the Ir catalysts prepared by deposition precipitation with urea using different supports were analysed to obtain a real quantification of Ir loading of the samples. As reported in Table 4.6 the samples prepared on $\text{Ir}/\text{Al}_2\text{O}_3_{\text{urea } 600}$ and $\text{Ir}/\text{MgAl}_2\text{O}_4_{\text{urea } 600}$ present a calculated value of Ir loading of 1.1 ± 0.1 wt.% and 1.0 ± 0.1 wt.% respectively, while the sample prepared on $\text{Ir}/\text{TiO}_2_{\text{urea } 600}$ had a loading of only 0.5 ± 0.2 wt.% and for this reason it was not considered a suitable material for catalytic testing. Similar materials prepared by sol-immobilisation with THPC were tested in the same context, but due to a temporary “shut down” of the scanning electron microscope an analysis of those samples were not possible, therefore the loading of those samples were quantified by analysis of mass spectroscopy on the filtrated solution and these analyses will be reported later in this chapter.

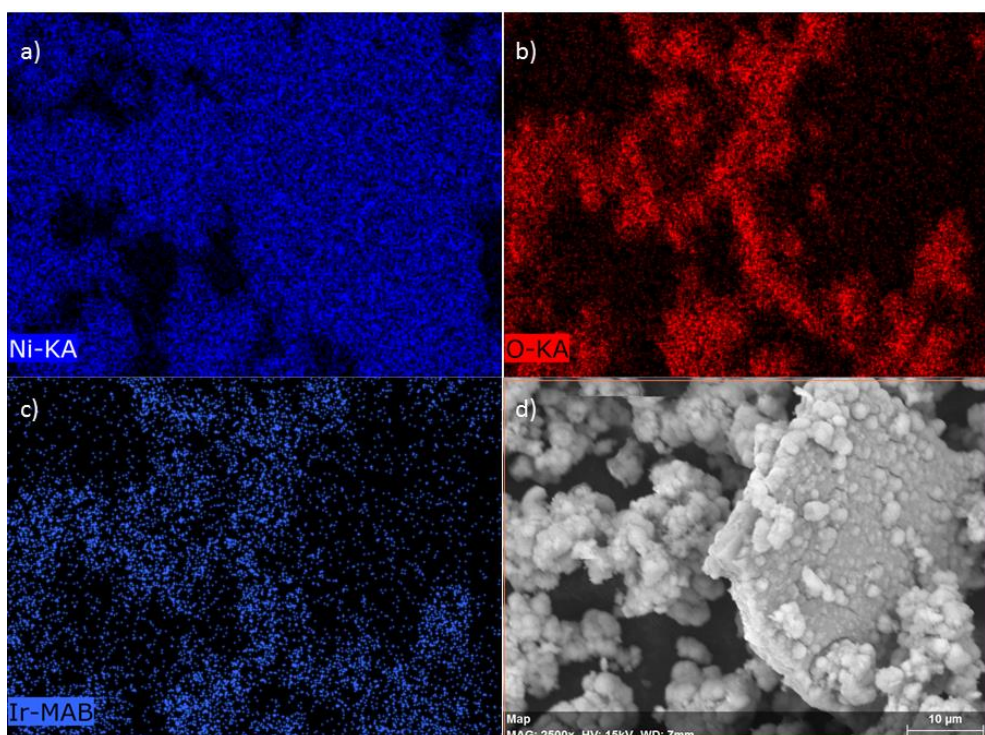


Figure 4.24. Representative SEM images, *d*, with EDX mapping of Ir/NiO sample for different elements such as O, *a*, Ce, *b*, and Ir, *c*.

In Figure 4.24 some representative SEM images of the Ir/NiO prepared by sol-immobilisation with THPC are reported. As it can be observed, the NiO present some clumps on the surface of bigger and more regular particles of oxide. From the mapping, it can be noticed that the Ir nanoparticles tend to prefer to deposit on these clumps than on more regular surface of bigger oxide particles. This preference can be associated with the presence of a higher number of defects on the surface of these clumps that can facilitate the stabilisation of the Ir

nanoparticles deposited. The Ir loading calculated by the EDS spectrum is 1.0 ± 0.1 wt.% is in agreement with the nominal value of 1 wt.% obtained by the amount of the Ir precursor used during the synthesis.

In a following section, section 4.3.5., are reported images, Figure 4.31 and 4.32, collected by transmission electron microscopy (TEM) and in particular the TEM images of an Ir/CeO₂ prepared by sol-immobilisation with THPC. For one part of the catalyst an additional heat treatment step was carried out; a calcination step at 500°C prior the reduction at 600°C for 6 hours under flow of H₂/Ar using the same reduction treatment followed by the part of the sample that was not calcined. From the TEM images, it was possible to calculate the mean particle size of Ir for the material that was only reduced while the material that underwent the calcination step did not exhibit a high number of Ir nanoparticles to allow sufficient counting with a good statistical value. Therefore, to understand the discrepancy between the two samples they were analysed with field emission gun-scanning electron microscopy, FEG-SEM, that has higher resolution than the Hitachi TM3030PLUS SEM used for the quantification of the Ir loading, to control the presence of Ir nanoparticles on the calcined sample as well as the morphology of Ir nanoparticles after the heat treatment under oxidative environment. Figure 4.25 displays some representative images of two samples; one calcined-reduced and only reduced. In the images of the only reduced sample, no visible nanoparticles of Ir could be observed and while the presence of Ir was confirmed by EDX spectrum and it was well dispersed. For the calcined-reduced sample, Ir sintered nanoparticles with particle size in the range between 50-200 nm were observed. The larger Ir nanoparticles are an indication that a sintering process occurred during the calcination step. This increase of the nanoparticle size of Ir can explain the decrease in yield displayed by this sample compared with the same sample that was not calcined, 7.4% of the final yield compared to 29.5%.

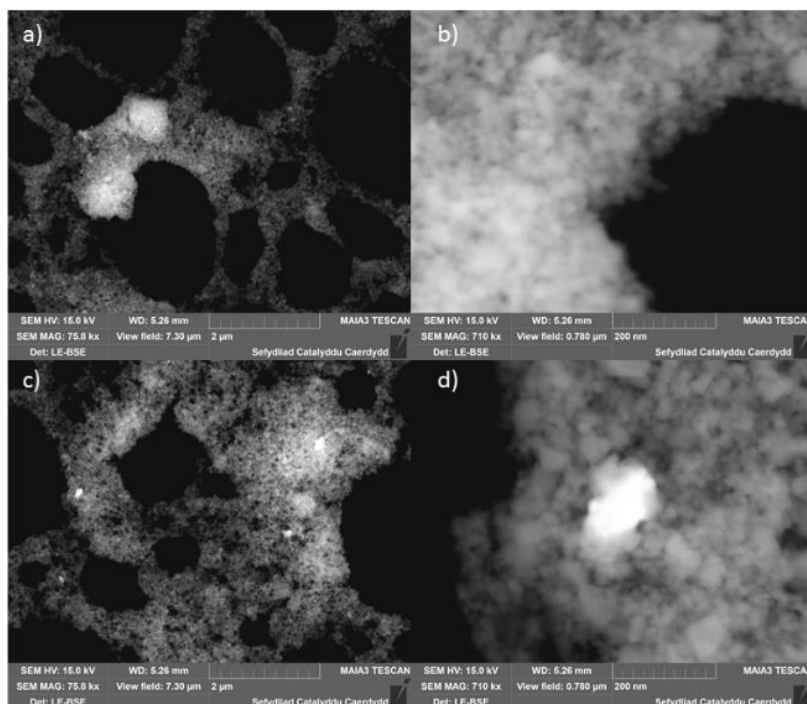


Figure 4.25. FEG_SEM images of Ir/CeO₂ THPC 600 only reduced, a and b, and calcined and reduced, c and d.

4.3.3. Inductively Coupled Plasma – Mass Spectrometry (ICP-MS)

As explained in the previous section ICP-MS was used to confirm the Ir loading of some of the samples prepared by sol-immobilisation with THPC on TiO₂, Ir/TiO₂ THPC 600, Al₂O₃, Ir/Al₂O₃ THPC 600, and MgAl₂O₄, Ir/MgAl₂O₄ THPC 600. The analyses were performed on a part of the filtrated solution before the final washing of catalyst. The use of ICP-MS allows to detect minimal traces of the investigated Ir species in the order of ppb or ppt level. In the filtrate solution of Ir/TiO₂ THPC 600 were present 1.113 mg of iridium from the 10 mg of metal derived from the Ir precursor so the final loading of iridium on the surface was 0.89 wt.%, achieving higher Ir loading than the low loading reported in the previous section for the Ir/TiO₂ prepared by deposition-precipitation with urea. Nonetheless, for the Ir/Al₂O₃ THPC 600 and Ir/MgAl₂O₄ THPC 600, the Ir amount still present in the filtrated solution is 2.96 and 7.39 mg respectively for the two syntheses. From the amount of the Ir in the filtrated solution, the Ir loading in the final catalysts was calculated as 0.70 wt.% for the Ir/Al₂O₃ THPC 600 and 0.26 wt.% for Ir/MgAl₂O₄ THPC 600. Therefore, it can be concluded that in the case of Al₂O₃ and MgAl₂O₄ the deposition-precipitation with urea provided a higher final Ir loading, therefore it is preferable as synthesis methodology than the sol-immobilisation with THPC, while in the case of TiO₂ the sol-

immobilisation is preferable even if also this methodology does not allow to reach complete immobilisation of the preformed Ir nanoparticles.

ICP-MS was performed to quantify Ir and Ni in solution after the tenth consecutive reaction performed with Ir/NiO. The analysis found a concentration of, in 11 mL of the final solution, 1.63 mg/L of Ir and 0.50 mg/L of Ni. Considering the total mass of Ir and Ni used were 0.762 mg and 47.9 mg respectively. Therefore, the final loss of metals during the reusability test can be quantified as 2.2% for Ir and 0.01% for Ni.

4.3.4. Transmission Electron Microscopy (TEM)

As explained in Chapter 3 section 3.4.5. the Ir/CeO₂ material are difficult to analyse by transmission electron microscopy due to the poor contrast between the Ir nanoparticles and the support and because the Ir nanoparticles produced by the deposition-precipitation method have mean particle size of Ir below 2 nm, reaching values close to the maximum resolution of the instrument, that are difficult to distinguish in conditions of not perfect contrast. Therefore, in order to obtain better information on the final structure of Ir nanoparticles, TEM analyses were performed on Ir preformed colloidal solutions via the collaboration with prof. Chris Kiely at Lehigh University, and Dr Thomas Chamberlain at Leeds university and the results are presented in Figure 4.26 and Figure 4.27 respectively. Figure 4.26 displays that Ir nanoparticles in the colloidal solution are present as sub-2nm particles and also some Ir nanoclusters could be observed. Similar results are exhibited by Figure 4.27e and the mean particle size of Ir was 1.94 ± 0.24 nm with a narrow particle size distribution.

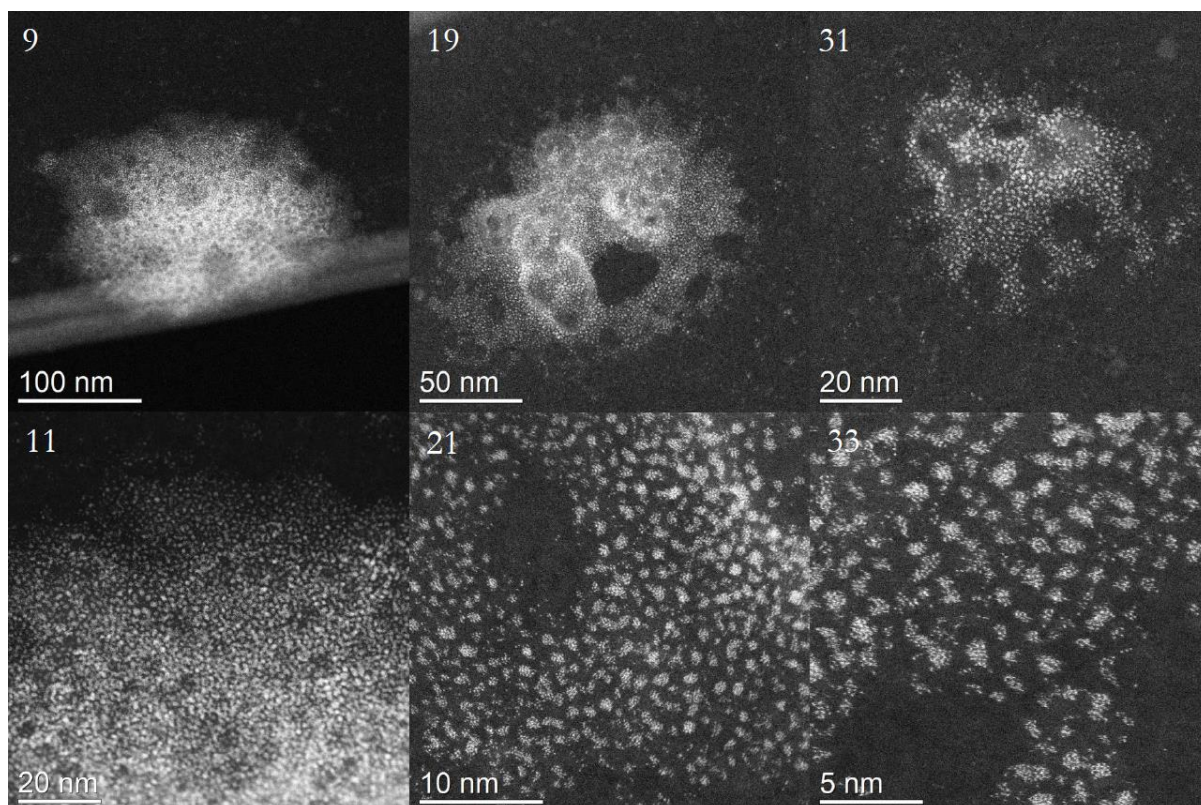


Figure 4.26. a-f) HAADF-STEM images of a solution of Ir nanoparticles, showing particles size distribution of ≈ 2 nm.

To increase the structural information on the active catalysts used and understand better the nature of Ir morphology on the synthesised catalysts, an Ir/CeO₂ prepared by sol-immobilisation with THPC, Ir/CeO₂_{THPC 600}, was further prepared and analysed by TEM. Figure 4.28 displays some representative TEM images of Ir/CeO₂_{THPC 600} and it can be observed that the Ir nanoparticles were well dispersed across the surface of CeO₂ nanoparticles. The mean particle size calculated based on 127 Ir nanoparticles was 1.00 ± 0.24 nm, similar to the value calculated for the Ir/CeO₂ prepared by deposition-precipitation with NaOH, Ir/CeO₂_{DP 400}, 0.90 ± 0.23 nm. Since the two catalysts, when reduced at 600°C, exhibited similar final yields in the catalytic tests reported it is possible that mean particle size of Ir is “key” for higher final yield exhibited by these samples, 36.6% and 38.9% respectively. The mean particle size of Ir was lower for Ir/CeO₂_{THPC 600 6h} than the corresponding Ir colloidal samples prepared by sol-immobilisation with THPC. This is probably due to the poor stability of the Ir colloidal solution as a function of time and the period of time past between the preparation of the Ir colloidal solution and the TEM analysis, few months. In the sol-immobilisation method with THPC, as explained in Chapter 2, the stabilisation of the nanoparticles is electrostatic and it results less

effective over time, but after immobilisation on the support, the particles have a surface more accessible to the reagents compared to the one prepared using steric stabilisers.

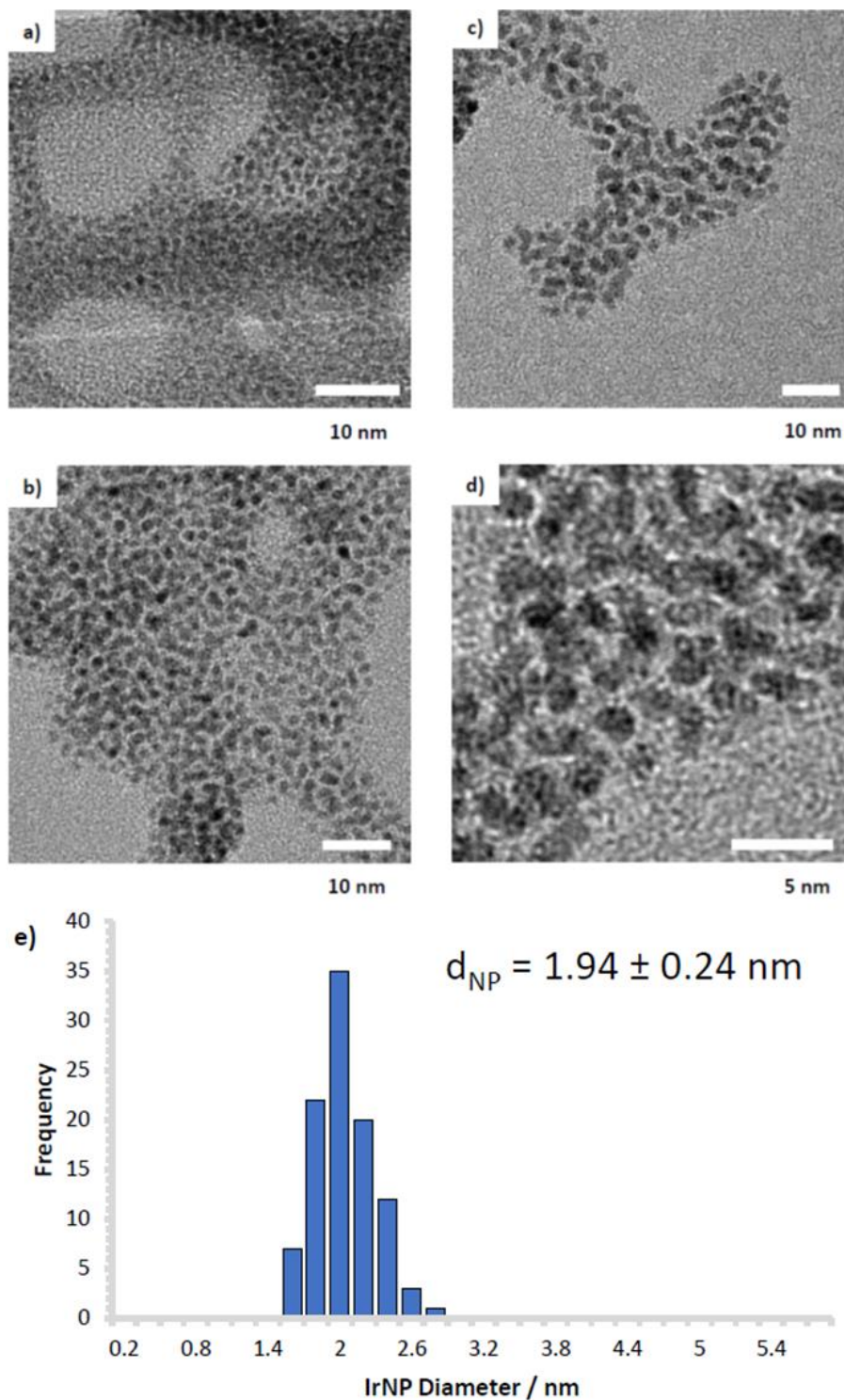


Figure 4.27. a-d)HR-TEM images of a colloidal solution of Ir nanoparticles. e) particle size distribution for the colloidal solution.

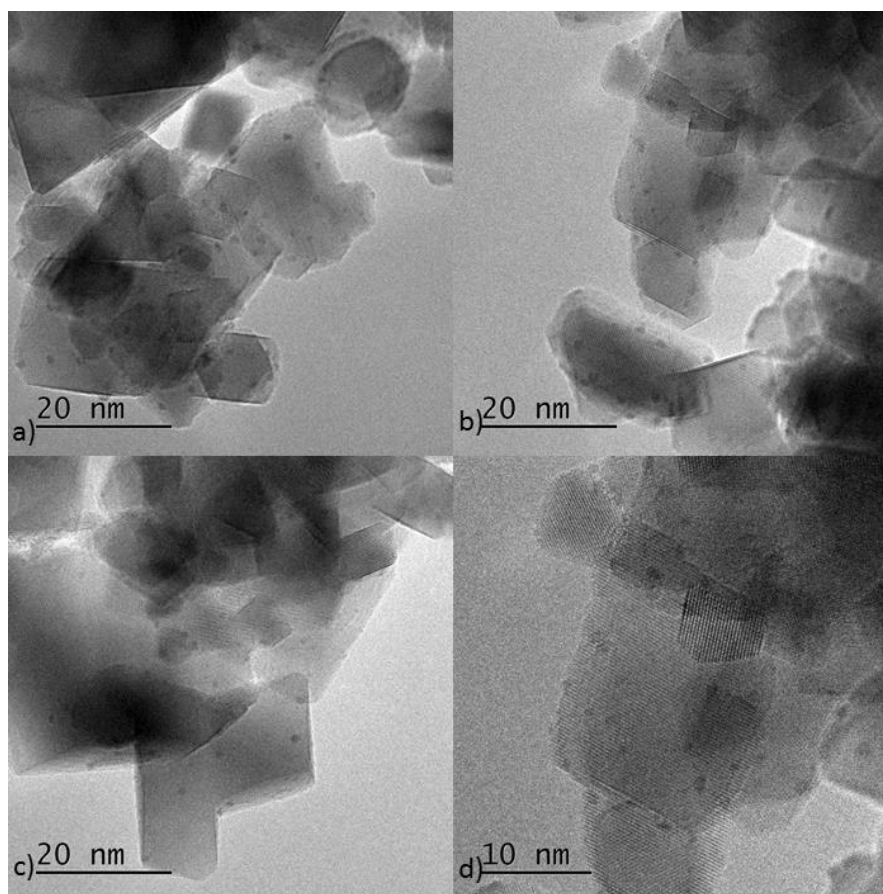


Figure 4.28. Representative HR-TEM images of Ir/CeO₂ prepared by sol-immobilisation with THPC and reduced at 600°C in H₂/Ar flow .

Because one of the main issues to obtain reliable and statistically valid data for Ir nanoparticles is the poor contrast with the CeO₂ as the chosen support, two Ir/TiO₂ prepared by sol-immobilisation with THPC samples were analysed by TEM. TiO₂ is a lighter support and can provide better contrast with supported Ir nanoparticles, and, therefore, it is easier to identify even the presence of smaller Ir nanoparticles and measure and calculate mean particle size of Ir in a more accurate way. It is not entirely correct to compare nanoparticles immobilised on different supports since the surface can influence the stabilisation and wetting of the nanoparticles and influence the mean particle size and particle size distribution to a certain degree. However, by using preformed Ir colloidal nanoparticles with the same mean particle size of Ir, during the immobilisation step the final particle size could be controlled better. Figure 4.29 displays some representative TEM images of Ir/TiO₂_{THPC 600}, the mean particle size of Ir was 1.25 ± 0.21 nm (counting 260 Ir nanoparticles). The sample had a mean particle size of Ir slightly higher than the corresponding Ir/CeO₂_{THPC 600} $1.00 \text{ nm} \pm 0.24$ nm, but still in good agreement. The calcined Ir/TiO₂ was analysed to check the growth and

therefore the stability of Ir nanoparticles at heat treatment at 300°C, like the one followed in the deposition-precipitation with urea. In Figure 4.30, TEM mages are shown, it is a Ir/TiO₂ calcined at 300°C before been reduced at 600°C, and it exhibited that mean particle size of Ir was 1.38 ± 0.17 nm from a sample of 233 nanoparticles and a good the particle distribution was observed.

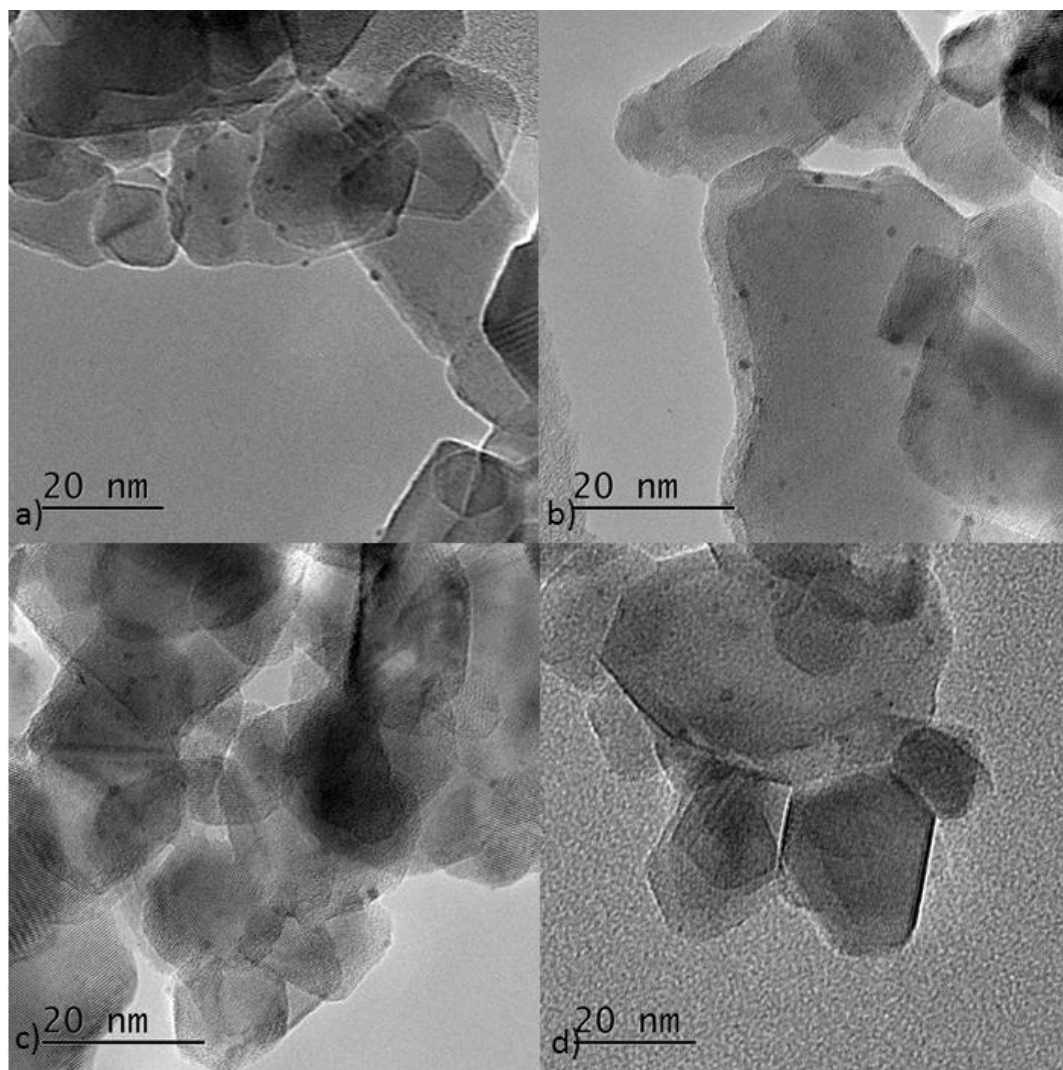


Figure 4.29. Representative TEM images of Ir/TiO₂ prepared by sol-immobilisation with THPC and reduced at 600°C in H₂/Ar flow.

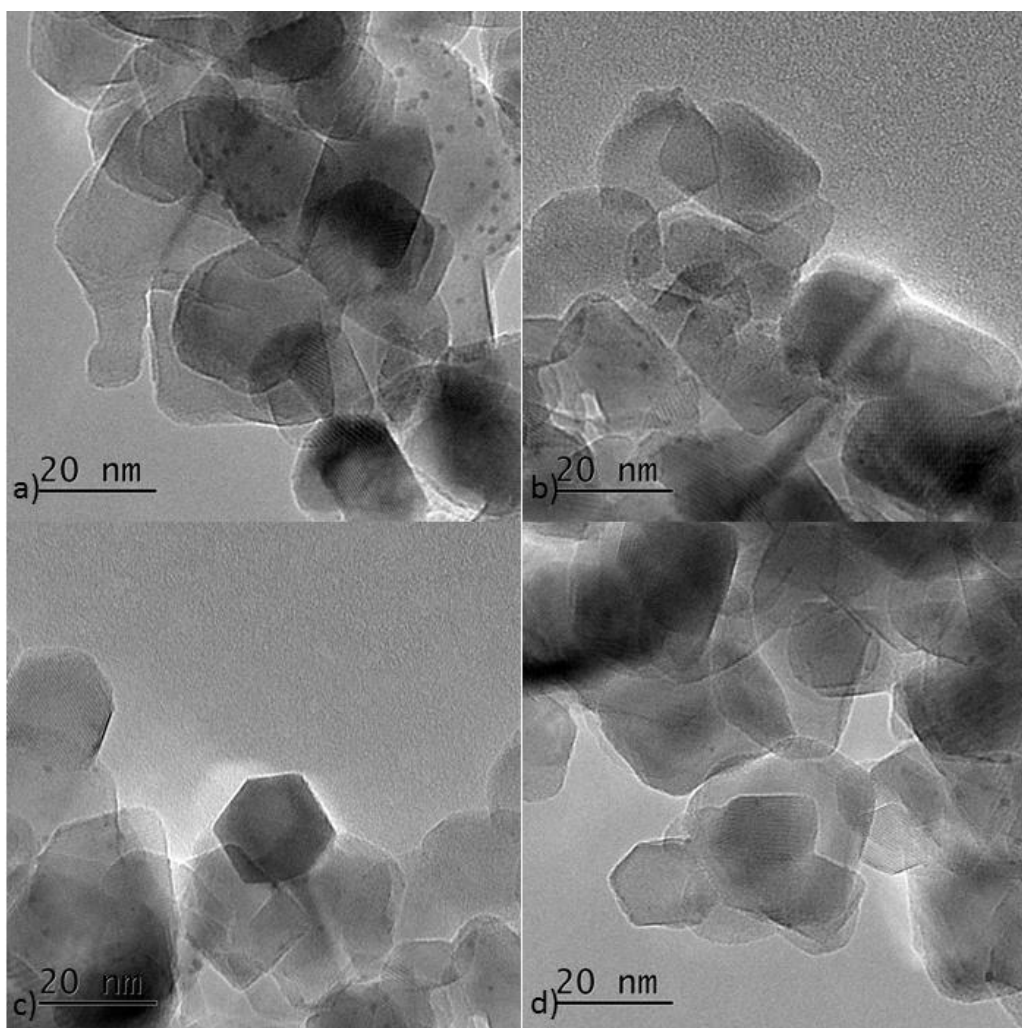


Figure 4.30. Representative TEM images of Ir/TiO₂ prepared by sol-immobilisation with THPC and calcined at 400°C before the reduction at 600°C in H₂/Ar flow.

To conclude the analysis of the TEM studies, Figure 4.31 shows some representative images of an Ir/CeO₂ prepared by sol-immobilisation with THPC a part of which underwent only to a reduction step, while the rest of the sample was first calcined at 500°C and after reduced at 600°C. Figure 4.31 displays TEM images with well-dispersed Ir nanoparticles and a mean Ir particle size 1.14 ± 0.35 nm which is in agreement with the analysis done on similar prepared sample. Interestingly the calcined sample in Figure 4.32 did not display visible Ir nanoparticles on the surface of CeO₂. These TEM images and the analysis by FEG-SEM that has shown Ir nanoparticles in the range of 50-200 nm seems to indicate that the heat treatment at 500°C in air flow leads to the growth and agglomeration of the supported Ir nanoparticles. These bigger Ir nanoparticles were not distinguishable from the support in the TEM images explaining the absence of Ir nanoparticles in Figure 4.32.

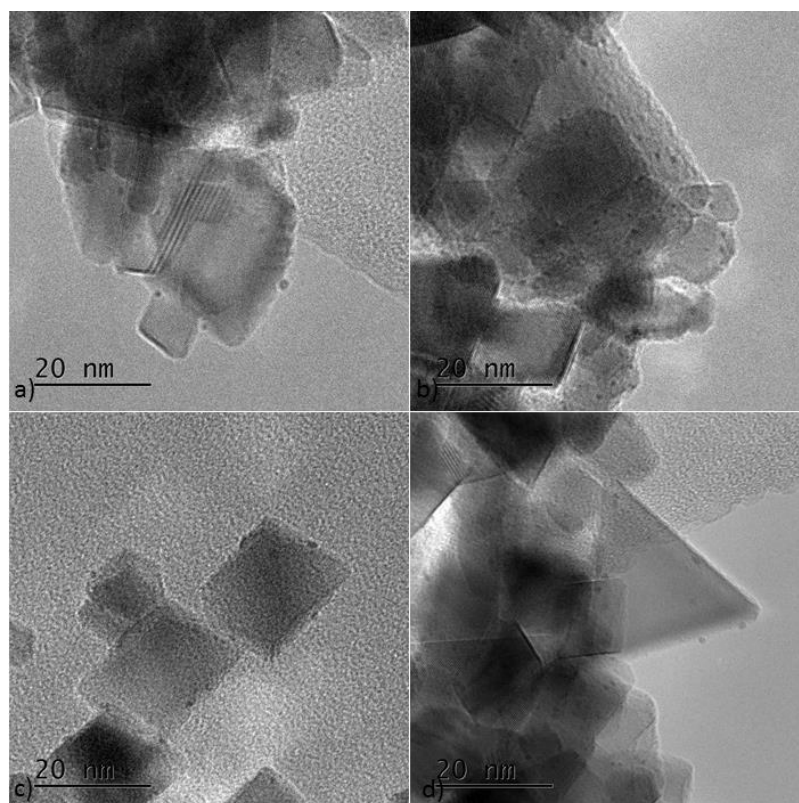


Figure 4.31. Representative TEM images of Ir/CeO₂ prepared by sol-immobilisation with THPC and reduced at 600°C in H₂/Ar flow.

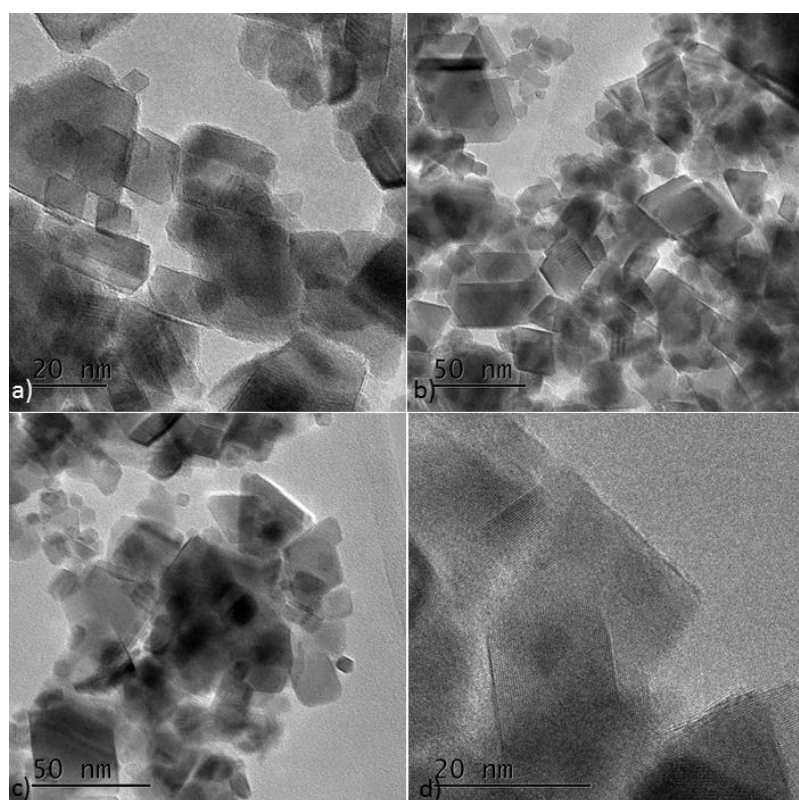


Figure 4.32. Representative TEM images of Ir/CeO₂ prepared by sol-immobilisation with THPC and calcined at 500°C before the reduction at 600°C in H₂/Ar flow.

4.3.5. X-ray Photoelectron Spectroscopy (XPS)

Other than the importance of Ir nanoparticle size in terms of influencing catalytic performance, of great importance for the catalytic properties of the Ir materials are the oxidation state of the Ir nanoparticles and the atomic surface coverage. As reported in Chapter 3, Section 3.5., the IrO₂ surface is not adapted to sustain a catalytic decomposition of hydrous hydrazine since most of the intermediate species involved in the mechanism of reaction bind irreversibly on the surface, as displayed by the DFT calculations. The strong interaction with IrO₂ can lead to a rapid coverage of the surface by ammonia and the poisoning of the catalytic material. As said before Ir⁰, from literature, displays a peak for Ir 4f_{7/2} at 60.9 eV, while for IrO₂ the same peak is reported at 62.0 eV.¹⁶

The effect of heat-treatment temperature of the reduction step has been discussed in Chapter 3, Section 3.4.7 on a series of Ir/CeO₂ samples prepared by deposition-precipitation with NaOH. In these series, the main difference analysed by XPS among the samples is an increase in the percentage of metallic iridium on the surface when the temperature and duration of the reduction step increase.

Table 4.7. XPS values for the Ir species binding energy (BE), atomic ratios on the total Ir and total atom surface coverage of Ir for a series of Ir catalysts. *Overlap of Ti 3s orbital does not allow exact quantification. †Overlap of Ni 3s orbital does not allow exact quantification.

Sample	Ir 4f _{7/2} (eV)		Metal coverage (%)		Ir atomic surface coverage (%)
	Ir ⁰	Ir ^{IV}	Ir ⁰	Ir ^{IV}	
Ir/CeO ₂ DP 400	61.6	62.1	42.9	57.1	0.53
Ir/CeO ₂ DP 600	61.5	62.5	87.6	12.4	0.40
Ir/CeO ₂ DP 600 6h	61.6	n.d.	100	0	0.28
Ir/CeO ₂ DP 500	61.6	62.3	77.9	22.1	0.35
Ir/CeO ₂ THPC dry	61.3	62.3	8.6	91.4	0.78
Ir/TiO ₂ THPC 600 6h	60.9*	n.d.*	100	0	0.39*
Ir/CeO ₂ THPC 600 6h	61.7	62.6	87.1	12.9	0.86
Ir/CeO ₂ urea 600 6h	61.0	62.0	70.6	29.4	0.41
Ir/Al ₂ O ₃ THPC 600 6h	61.0	62.0	70.8	29.2	0.20
Ir/MgAl ₂ O ₄ THPC 600 6h	61.1	62.3	82.8	17.2	2.00
Ir/TiO ₂ urea 600 6h	61.2*	n.d.*	100	0	0.19*
Ir/Al ₂ O ₃ urea 600 6h	61.2	n.d.	100	0	0.12
Ir/MgAl ₂ O ₄ urea 600 6h	61.3	62.4	80.1	19.9	2.50
Ir/CeO ₂ THPC calc 400	n.d.	62.0	0	100	0.46
Ir/CeO ₂ THPC calc 400 red	61.3	62.3	58.2	41.8	0.40
Ir/NiO	60.9†	62.5†	9.9	90.1	1.27†
Ir/NiO USED	60.9†	62.0†	46.7	53.3	0.26†
Ir/CeO ₂ THPC calc 500 red	61.0	62.0	84.0	16.0	0.31

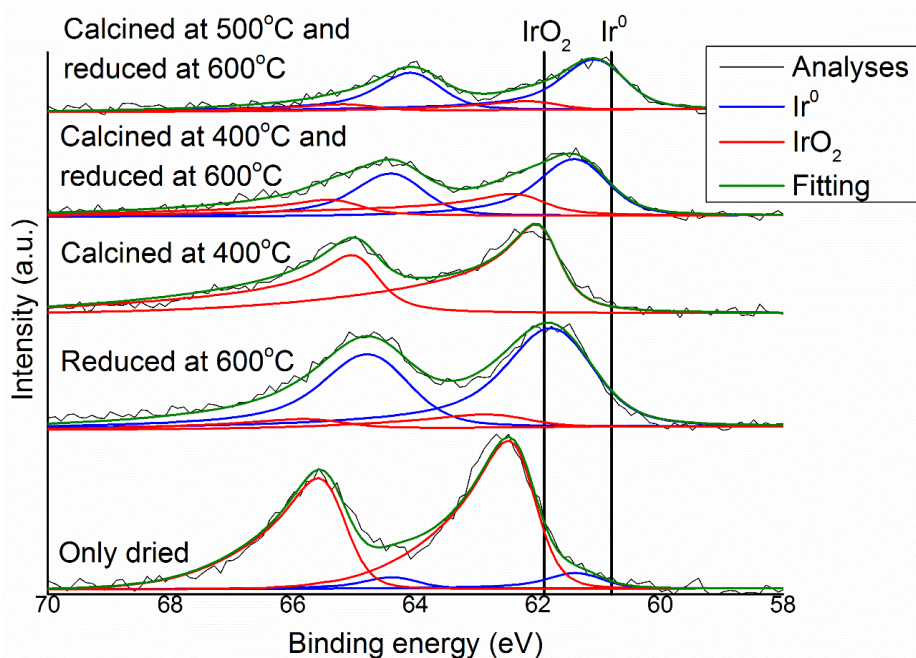


Figure 4.33. XPS spectra of Ir 4f region for Ir/CeO₂ prepared by sol-immobilisation with THPC which underwent different heat treatment: only drying step, reduced at 600°C under H₂/Ar, calcined at 400°C in air, calcined at 400°C in air and reduced at 600°C under H₂/Ar and calcined at 500°C in air and reduced at 600°C under H₂/Ar. In the graph are also reported graphically the binding energies of Ir⁰ and IrO₂ reported in literature.

Later in the project, a series of Ir/CeO₂ prepared by sol-immobilisation with THPC method were analysed by XPS to study the effect of different heat treatment on the supported nanoparticles and the XPS spectra are reported in Figure 4.33. Ir/CeO₂_{THPC dry} was only dried, so no high-temperature reduction process was performed to increase the percentage of metallic iridium on the surface. The high amount of IrO₂, 91%, observed, can be explained by the drying step at 90°C in static air overnight. This prolonged heat treatment in an oxidative environment, air, may induce superficial oxidation. The binding energy of metallic Ir 4f_{7/2} is at 61.3 eV lower than the samples reduced at a high temperature which may indicate a weaker interaction between the Ir nanoparticles and the surface. The low gas production observed by catalytic tests of Ir/CeO₂_{THPC dry} can be due to the presence of high amount of iridium oxide on the surface either of the Ir nanoparticles and support, that, as explained before, could decompose hydrous hydrazine initially, however as the reaction was prolonged, Ir catalyst can quickly poisoned by the product of the reaction, Figure 4.7. The Ir/CeO₂_{calc 400} was analysed after a heat treatment at 400°C for 3 hours before the final reduction step. The Ir 4f region of this sample exhibited the presence of only IrO₂ with a binding energy of 62.0 eV. To conclude the study on the effect of the heat treatment three samples were compared. The first sample was reduced at 600°C for 6h (I) after the drying step, (II) the second sample was

reduced after 3 hours of calcination at 400°C and (III) the third one was reduced after 3 hours of calcination at 500°C. The most noticeable difference between these samples, except the lower amount of Ir⁰ in Ir/CeO₂ THPC calc 400 red, 58.2%, probably due to interference during the reduction process, is that the binding energy for the Ir⁰ peak decreases from 61.7 eV to 61.3 eV and 61.0 eV when calcination step at higher temperature was performed before the reduction of the materials. From the FEG-SEM and TEM analyses was confirmed that the calcination step at 500°C lead to the sintering of the Ir nanoparticles changing the distribution and forming large Ir nanoparticles in the range of 50-200 nm. Therefore, we can associate the up-shift of the Ir 4f_{7/2} metallic peak to the small dimensions of the Ir nanoparticles that create partial positive charge on the surface of the Ir nanoparticles. On the other hand, high-temperature heat treatments, that induce sintering of the Ir nanoparticles, reduce significantly the aforementioned up-shift of the peaks as it is shown in the case of Ir/CeO₂ THPC calc 500 red. The decrease of this up-shift phenomenon is associated to the decrease in catalytic performance, as it has been discussed for Ir/CeO₂ THPC calcined and non-calcined, but it is still unclear if the catalytic performance is due to the combination of the superficial charge induced on the surface and the presence of small Ir mean particle size or only one of the two parameters.

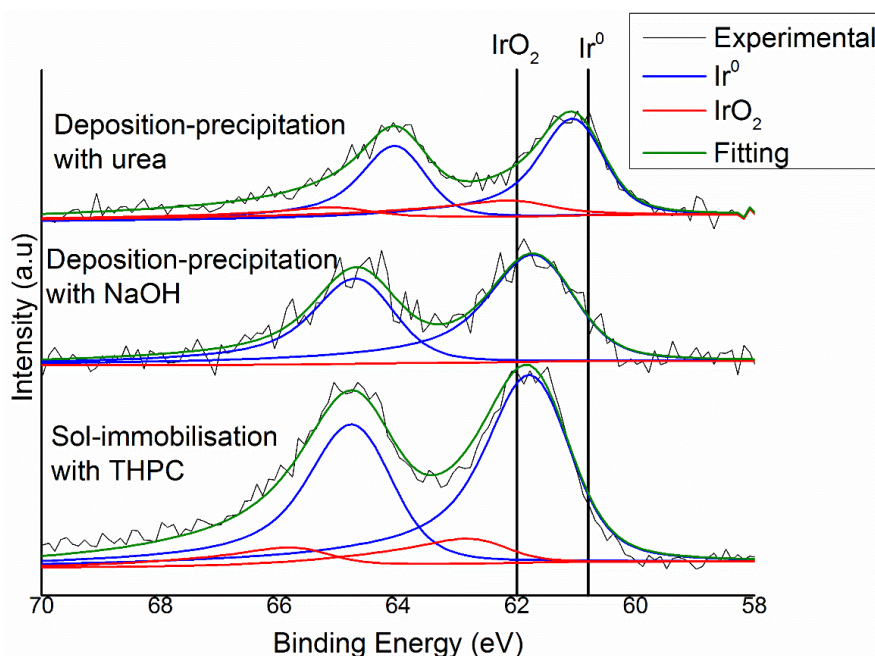


Figure 4.34. XPS spectra of Ir 4f region for Ir/CeO₂ prepared by different preparation methods: Sol-immobilisation with THPC, deposition-precipitation with NaOH and deposition-precipitation with urea. In the graph are also reported graphically the binding energies of Ir⁰ and IrO₂ reported in literature.

Different preparation methods have been tested for the production of Ir/CeO₂ and in Figure 4.34 the XPS of Ir/CeO₂ prepared by deposition-precipitation with urea, Ir/CeO₂_{urea 600}, is exhibited with the previously reported Ir/CeO₂ prepared by deposition-precipitation with NaOH, Ir/CeO₂_{DP}, and by sol-immobilisation with THPC, Ir/CeO₂_{THPC 600}. For Ir/CeO₂_{urea 600}, the XPS results displayed, suggest the presence of lower binding energy, 61.0 eV, which can be linked to the calcination step required by the preparation method as it was discussed before in this section which can increase the mean particles size.

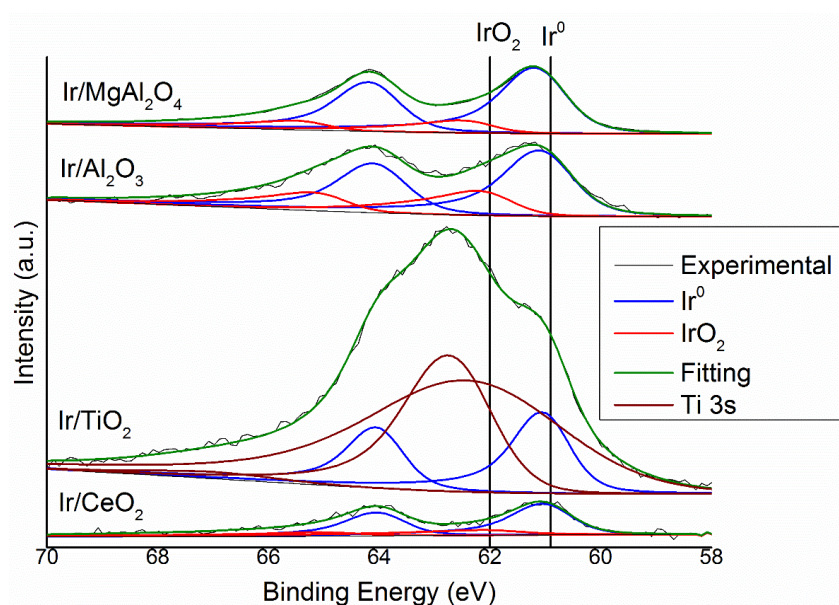


Figure 4.35. XPS spectra of Ir 4f region for Ir catalysts prepared by deposition-precipitation with urea on different support: Ir/CeO₂, Ir/TiO₂, Ir/AlO₃ and Ir/MgAl₂O₄. In the graph are also reported graphically the binding energies of Ir⁰ and IrO₂ reported in literature.

In Figure 4.35 the XPS spectra of the iridium catalyst prepared by deposition-precipitation with urea on different supports are reported. From the XPS data reported in Table 4.7 it can be seen that for all the samples prepared by deposition precipitation with urea on CeO₂, TiO₂, Al₂O₃ and MgAl₂O₄ have similar binding energies, close to the standard 60.9 eV of metallic Ir. Ir/CeO₂, Ir/Al₂O₃ and Ir/MgAl₂O₄ have also similar percentage of metallic iridium on the surface. These analyses could explain the similar catalytic activity between the different supports used for the deposition of Ir (CeO₂, Al₂O₃ and MgAl₂O₄) and catalytic tests reported previously. To be noticed that due to the presence of the peak associated with Ti 3s orbital an accurate quantification of the Ir 4f peaks is difficult.

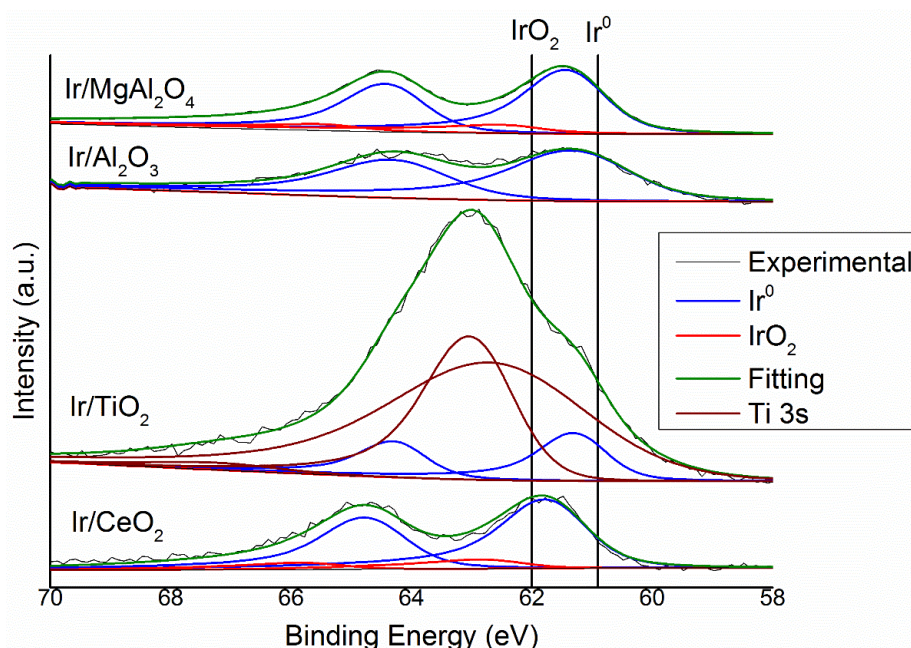


Figure 4.36. XPS spectra of Ir 4f region for Ir catalysts prepared by sol-immobilisation with THPC on different support: Ir/CeO₂, Ir/TiO₂, Ir/AlO₃ and Ir/MgAl₂O₄. In the graph are also reported graphically the binding energies of Ir⁰ and IrO₂ reported in literature.

In Figure 4.36 the XPS spectra of the iridium catalyst prepared by sol-immobilisation with THPC on different supports are reported. As described previously, a series of samples, Ir/CeO₂, Ir/TiO₂, Ir/Al₂O₃ and Ir/MgAl₂O₄ were compared. In Table 4.7, it can be seen that all the described samples exhibited a degree of up-shift of the metallic Ir 4f_{7/2} peak. As reported previously the up-shift was substantial in the case of CeO₂, +0.7 eV, while for the other supports the up-shift was limited to +0.2-0.3 eV. The difference in up-shift can follow the same trend of the catalytic performance where Ir/CeO₂ reached 32.4% of final yield to molecular hydrogen, while Ir/TiO₂ reached 4.5%, whereas Ir/Al₂O₃ and Ir/MgAl₂O₄ had a final yield toward molecular hydrogen close to 0%. The lower up-shift of the Ir peaks on supports different from CeO₂ is an indication that the possible positive charge on the surface is due also to the interaction between the support and the Ir nanoparticles, being CeO₂ known as a metal oxide with good strong metal-support interaction (SMSI). This combination of the presence of low particle size of Ir and SMSI seems to be the key to the catalytic performances of Ir/CeO₂ catalysts.

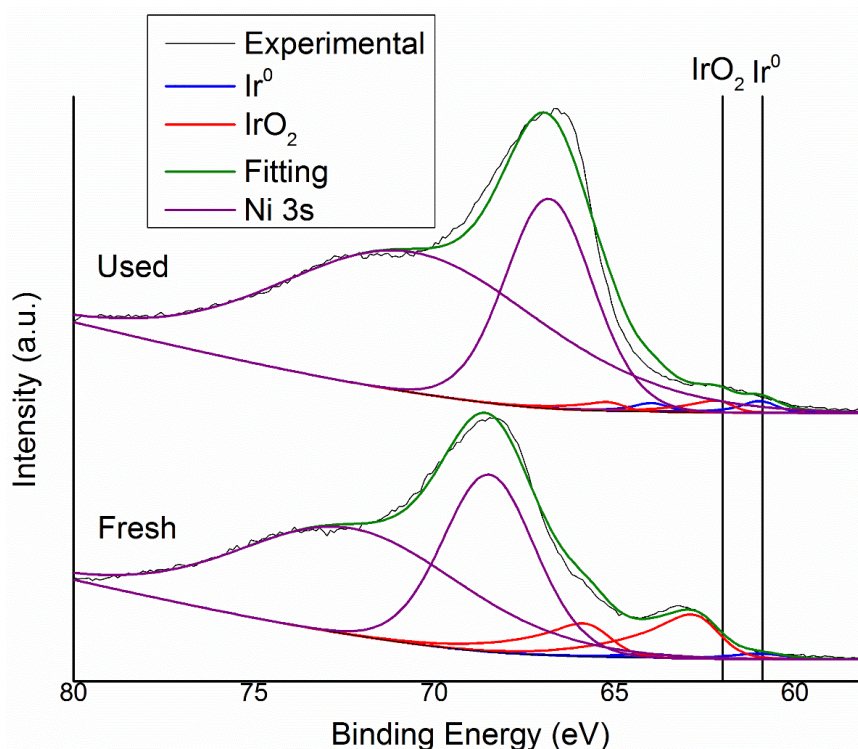


Figure 4.37. XPS analyses of the Ir 4f region for Ir/NiO prepared by sol-immobilisation with THPC before and after the reaction of decomposition of hydrazine in aqueous solution. In the graph are also reported graphically the binding energies of Ir⁰ and IrO₂ reported in literature.

To conclude this section, the XPS analysis on the Ir/NiO was performed for the fresh and on the used catalyst, as it is shown in Figure 4.37. Ir/NiO was the catalyst that exhibited the highest final yield toward molecular hydrogen among the materials catalytically tested. From Table 4.7, it can be seen how the fresh Ir/NiO, contrary to other Ir nanoparticles supported on different metal oxides, presented a lower percentage of metallic iridium, only, 9.9%, and there was no up-shift of the Ir 4f_{7/2}. This is a clear indication that the mechanism on this particular catalyst is different from the other Ir supported metal oxide catalysts presented, where the presence of small Ir nanoparticles and SMSI are necessary to achieve high final yield to H₂, and these characteristics were not present on the fresh Ir/NiO. However, the used catalyst presented a percentage of metallic Ir closer to 50% and this is due to the reducing effect of hydrous hydrazine, indicating a restructuring and in situ reduction of Ir species during the liquid-phase decomposition of hydrous hydrazine. Unfortunately, a more accurate quantification of the iridium species is challenging due to the presence in the region of Ir 4f of the peak associated with orbital 3s of Ni. The Ni 3s in the used catalyst is shifted from a

value of 68.5 eV of the fresh to 66.8 eV, this shift can be related to a reduction of the superficial Ni, which can be assumed to be due to the contact with hydrous hydrazine.

4.3.6. UV/Visible Spectroscopy

UV/Vis spectroscopy is a useful and versatile technique and can be applied for both quantification of chemical species and collection of qualitative information about specific samples.

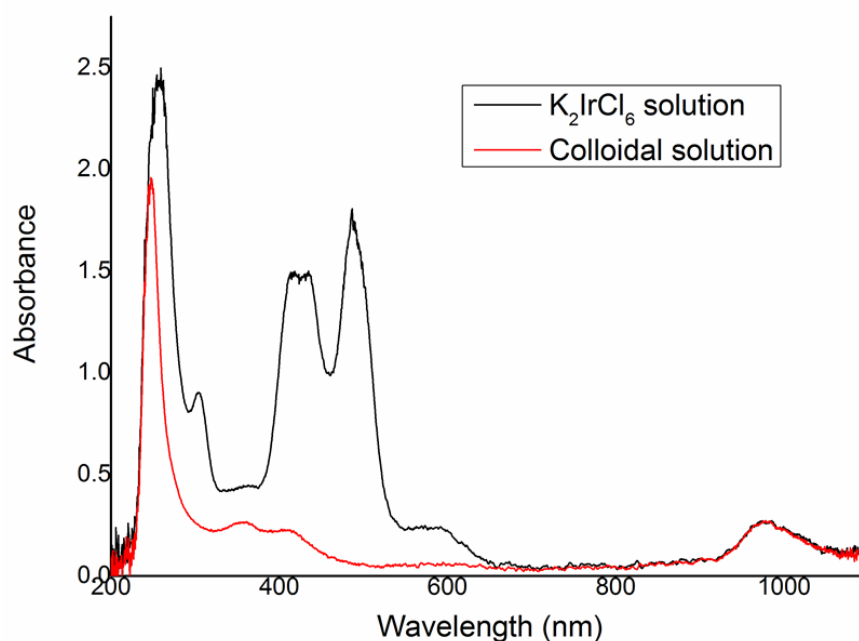


Figure 4.38. UV/vis spectra of K_2IrCl_6 solution in NaOH solution in water before the reduction by THPC and of the Ir colloidal solution 25 min after the addition of THPC.

In Figure 4.38 a representative example of UV/Vis absorption spectra of a colloidal solution of Ir recorded before the immobilisation on the designed support and a solution of Ir precursor is reported. The comparison between the two spectra demonstrate the reduction of the K_2IrCl_6 , which absorption spectra disappear after the addition of the reducing agent, THPC, which make disappear the precursor UV/vis spectrum in favour of the one of the colloid. The absorption spectrum of the Ir colloidal solution presents a small peak in the near UV region, 300- 400 nm, that is in agreement with the colourless Ir colloidal solution obtained by the synthesis and the spectrum calculated by Creighton *et al.* ¹⁷

UV/Vis was also used to have first confirmation of the immobilisation of the nanoparticles. In Figure 4.39 is reported the spectrum of the filtrated solution from the preparation of Ir/CeO₂

prepared by sol-immobilisation with PVA which displayed the characteristic plasmonic peak indicating a low immobilisation of the effectiveness of the preparation.

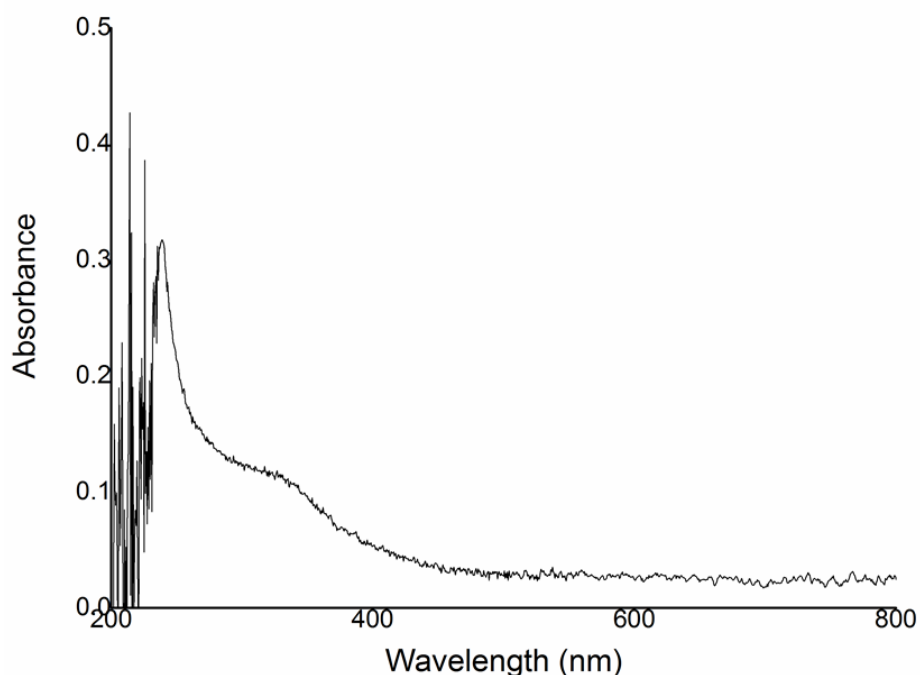


Figure 4.39. UV/vis spectrum of the filtrate solution from the synthesis of Ir/CeO₂ prepared by sol-immobilisation with PVA.

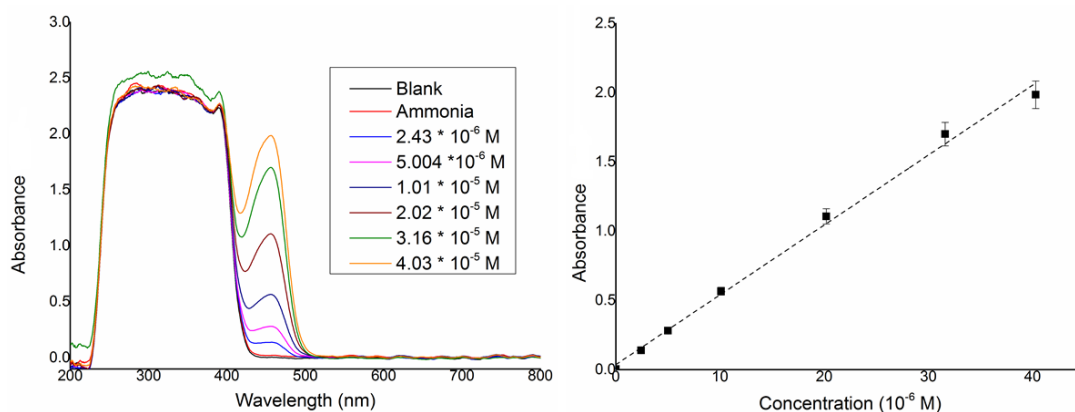


Figure 4.40. a) UV/Vis Absorption spectra of solution of 4-(dimethyl)aminobenzaldehyde with different concentration of hydrous hydrazine and ammonia. b) Linear plotting of the absorption at 456 nm versus the concentration of hydrous hydrazine in solution.

UV/Vis spectroscopy was also used to quantify the remaining hydrous hydrazine at the end of the reaction. The experimental protocol as described in Chapter 2 was developed in later stages of the thesis project, but some key reactions were performed to validate the assumption that at the end of the reaction, the stop of the gas production coincided with the complete decomposition of hydrous hydrazine. In Figure 4.40 is reported the absorption

spectra of the 4-(dimethyl)aminobenzaldehyde azine and the calibration of the response of absorption at the maximum peak 456 nm with concentration.¹⁸ The response factor was found to be 54284. In Figure 4.41 the colourimetric analyses of a reaction performed with Ir/NiO and one performed with bare CeO₂ are reported. As it can be seen the colourimetric test confirmed the complete decomposition of hydrous hydrazine when the production of gaseous products completed, while reactions that did not produce gaseous products did not decompose hydrous hydrazine in a practical way. These tests confirmed the total decomposition of hydrous hydrazine at the end of the reaction for the majority of the catalysts and validate the assumption made at the beginning of the project.

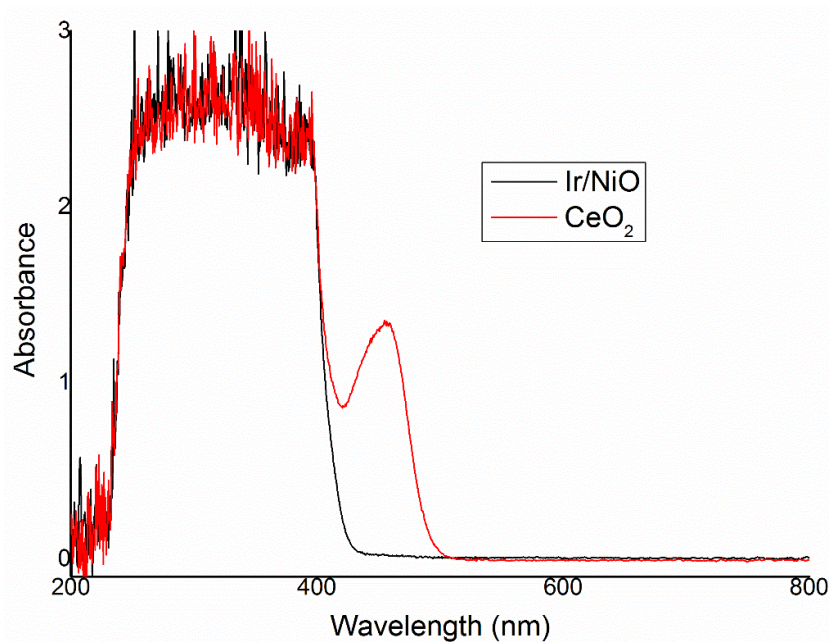


Figure 4.41. UV/vis Absorption spectra of the reaction solution after that the plateau in gas production is reached for a reaction with Ir/NiO and bare CeO₂ during the decomposition of hydrous hydrazine in aqueous solution.

4.3.7. *In situ* Attenuated Total Reflectance Infrared Spectroscopy (ATR-IR)

During the visit at the Paul Scherrer Institute in Villigen, CH, infrared absorption spectra for hydrazine adsorbed on some representative catalytic material were recorded. *in situ* ATR-IR spectra allow to identify species adsorbed on the surface during the reaction, therefore, the ATR-IR can give important information about the mechanism of reaction. These results can then be compared with the DFT calculation and studies with the labelled ¹⁵N hydrazine monohydrate in order to obtain a deeper insight into the reaction of decomposition of

hydrous hydrazine. The ATR-IR spectra were recorded using a fine layer of catalyst powder deposited on the ZnSe crystal to perform the analysis and the desired solution was flowed over the catalyst layer continuously during the analysis. ATR-IR can give information on the structure of the catalysts based on the adsorption of the chemical species on the surface of the active metal. In particular, comparing the adsorption spectra of hydrous hydrazine on materials with different catalytic behaviour can give important information such as the variation in the strength of the bonds between the active metal and the adsorbed species or difference in the adsorbed species that can indicate different reaction pathways, which can later be compared with the DFT calculations.

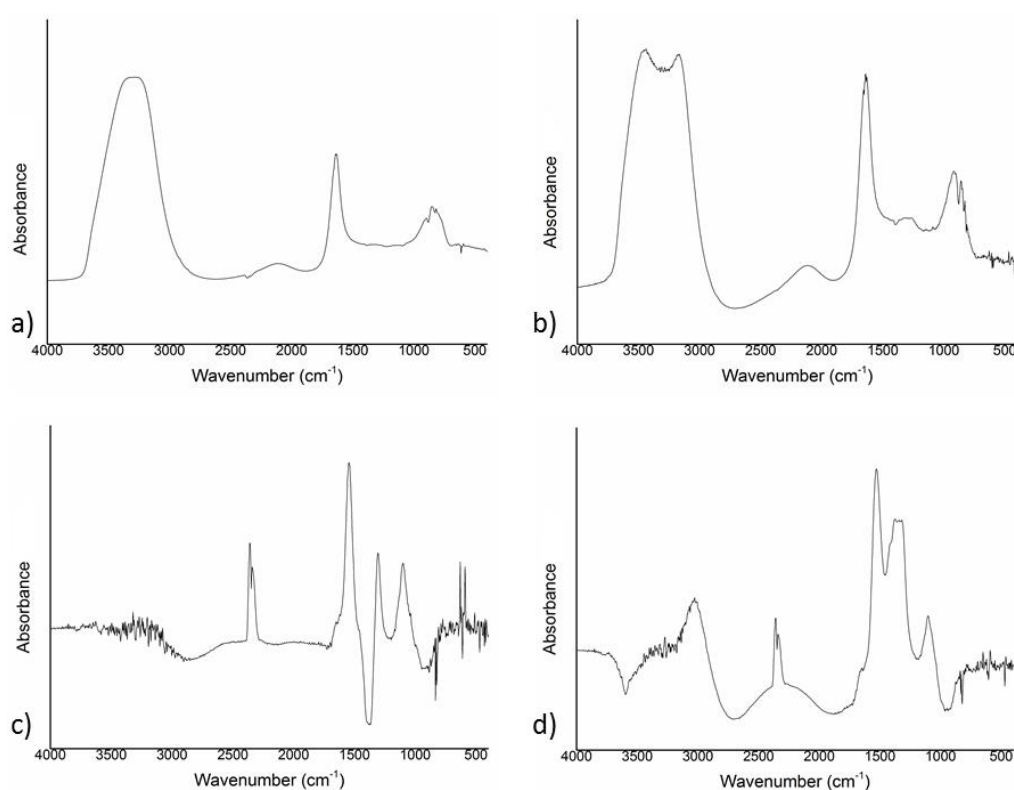


Figure 4.42. ATR-IR spectra recorded at 50 °C with CeO₂ deposited on a ZnSe crystal with different solution flowing on the catalysts: a) water; b) 0.1M NaOH solution; c) 0.02M hydrous hydrazine solution in water; d) 0.02M hydrous hydrazine 0.1M NaOH solution in water.

In the first instance, the ATR-IR spectra of various solution on bare CeO₂ have been recorded in order to have a reference for the study of the Ir/CeO₂ materials later on. In Figures 4.42a and 4.42b, the ATR-IR spectra of water and a solution 0.1 M of NaOH in water are reported. Figure 4.42c displays the adsorption of an aqueous solution of hydrous hydrazine with three characteristic peaks at wavenumbers of 1544, 1307 and 1099 cm⁻¹. Figure 4.42d displays, the

ATR-IR spectrum of hydrous hydrazine in a solution of NaOH. This absorption spectrum is similar to one recorded in neutral conditions with one extra peak at a wavenumber of 1374 cm^{-1} , while the other slightly shift at 1529 , 1320 and 1099 cm^{-1} .

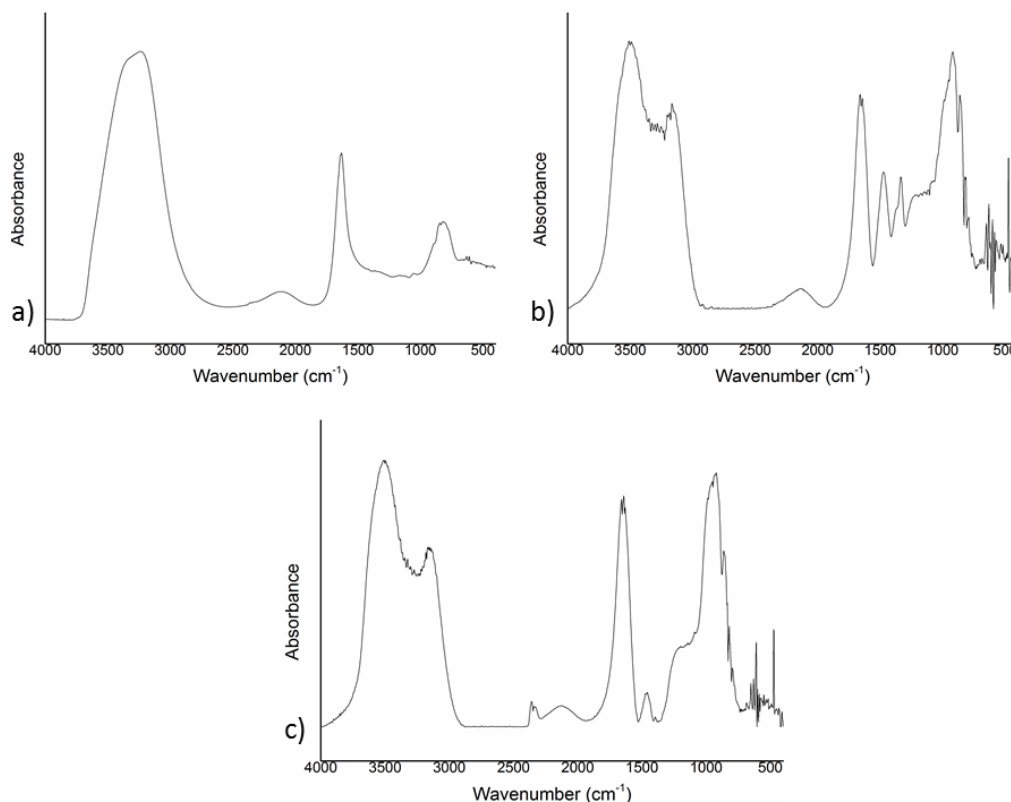


Figure 4.43. ATR-IR spectra recorded at $50\text{ }^{\circ}\text{C}$ with Ir/CeO_2 prepared by deposition-precipitation with urea deposited on a ZnSe crystal with different solutions flowing on the catalysts: a) water; b) 0.02M hydrous hydrazine solution in water; c) 0.02M hydrous hydrazine 0.1M NaOH solution in water.

Figure 4.43 exhibits the absorption spectra of Ir/CeO_2 prepared by deposition-precipitation with urea. $\text{Ir}/\text{CeO}_2^{\text{urea } 600}$ was chosen as a representative example of an Ir/CeO_2 with a low final yield toward molecular hydrogen. Figure 4.43b shows the absorption spectrum of a solution of hydrous hydrazine in water and four main peaks were observed at wavenumbers of 1660 , 1471 , 1335 and 920 cm^{-1} . The last peak showed a shoulder at 1202 cm^{-1} . Figure 4.43c shows the adsorption of hydrous hydrazine in an aqueous NaOH solution and displayed comparable peaks at 1642 , 1458 and 920 cm^{-1} with the absence of the peak at 1335 cm^{-1} .

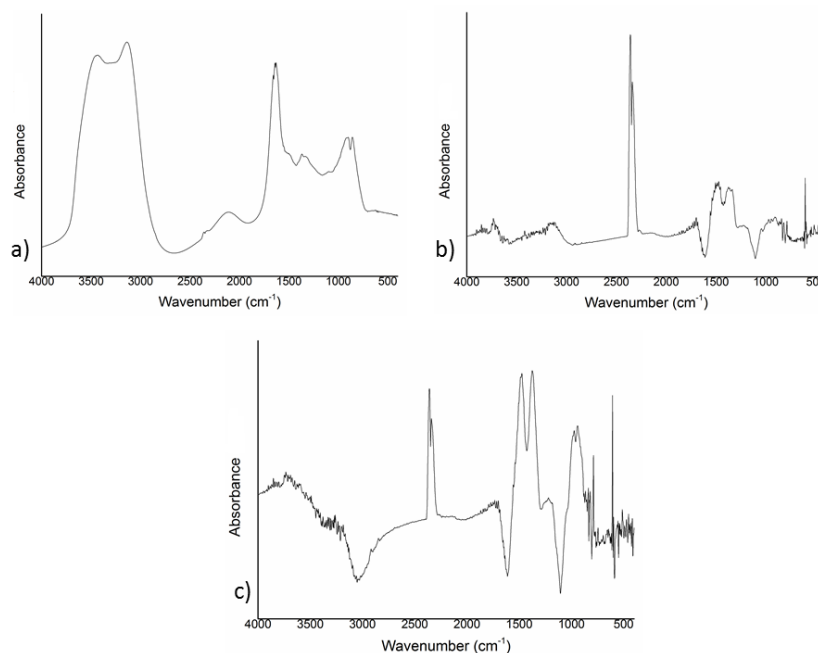


Figure 4.44. ATR-IR spectra recorded with Ir/CeO₂ prepared by Sol-immobilisation with THPC deposited on a ZnSe crystal with different solutions flowing on the catalysts: a) water; b) 0.02M hydrous hydrazine solution in water; c) 0.02M hydrous hydrazine 0.1M NaOH solution in water.

Ir/CeO₂ prepared by sol-immobilisation with THPC underwent the same *in situ* analyses as the bare support and Ir/CeO₂ urea 600, as shown in Figure 4.44, as representative material with higher final yield toward hydrogen, 29.5%. The absorption spectrum of the hydrous hydrazine solution in water on Ir/CeO₂ THPC 600, as shown in Figure 4.44b, exhibited peaks at 1489 and 1363 cm⁻¹. Figure 4.44c shows the adsorption on the surface of Ir from a mixed solution of hydrous hydrazine and NaOH with peaks at 1474, 1373 and 974 cm⁻¹.

From the analysis of the ATR-IR spectra and the theoretical calculations of the vibrational wavenumbers of the different adsorbed species. Reported in Chapter 3 Section 3.5.6., it is possible to assign the peaks reported in the ATR-IR spectra presented using different solutions of hydrous hydrazine in the absence and presence of NaOH and catalysts. Since the ATR-IR spectra recorded are of aqueous solution of hydrous hydrazine the stretching of the N-H bonds, which is present in most of the intermediate species as well as ammonia and hydrous hydrazine, could not be detected clearly due to the large peak related to the O-H bond of water in the same region of the spectrum, 3200-3600 cm⁻¹. The ATR-IR spectra reported for hydrous hydrazine solution underwent the subtraction of the background, eliminating, therefore, most of the peaks related to the ATR-IR spectrum of H₂O. To be noticed, in addition, the ATR-IR peaks of H₂O around 1600 and 900 cm⁻¹ can affect the reading and the correct

interpretation of the ATR-IR peaks close to them. Taking into account considerations, the ATR-IR spectra of the hydrous hydrazine solution over Ir catalysts present: (I) ATR-IR peak at a wavenumber between 1489 and 1458 cm^{-1} and (II) ATR-IR peaks at 1373-1335 cm^{-1} and 974-920 cm^{-1} . These last two ATR-IR peaks were also presented in the ATR-IR spectra recorded over bare CeO_2 with similar intensity and position that may indicate that these ATR-IR peaks are due to chemical species deposited on the surface of the support. A variation in wavenumber, around 50 cm^{-1} , can derive from the presence of Ir nanoparticles on the surface of the support. Moreover, the heat-treatment carried out during the synthesis of the catalysts could modify the surface of the oxide leading to small changes in the chemical strength of the surface (CeO_2 and Ir nanoparticles) and the adsorbed species. In addition, from the theoretical calculations, none of the chemical species that can be adsorbed on the surface should present vibrational peaks close to 1350 cm^{-1} and N_2H_3 , which has a peak at 933 cm^{-1} , as calculated from the DFT, should present as well, other ATR-IR vibrational bands at 1104 and 1555 cm^{-1} that are not present in the recorded spectra. On the other hand, the vibrational band at 1489-1458 cm^{-1} could be assigned, considering the simulated spectra, to the following chemical species: NNH and NH_2 . The simulated NNH species adsorbed on Ir (111) surface presented another vibrational peak at 1232 cm^{-1} that was not presented in the operando ATR-IR study. NH_2 presented a vibrational peak at 609 cm^{-1} and in some of the ATR-IR spectra recorded a vibration peak near 600 cm^{-1} was observed and considering that the region below 800 cm^{-1} suffered from higher signal/noise ratio. It can be concluded that on the surface of the Ir nanoparticles the most stable chemical intermediate adsorbed species is NH_2 , while other chemical species were contemporaneously adsorbed on the CeO_2 . This statement is supported by the simulated IR spectra presented and with the DFT calculations. DFT calculations suggest as the main preferential reaction pathway, the initial breaking of the N-N bond in the hydrous hydrazine molecule, which can lead to the formation of two NH_2 adsorbed, Chapter 3 Section 3.5. . Moreover, the catalytic tests performed using isotopic labelled hydrous hydrazine agreed with the scission of that N-N bond, Section 4.2.6. .

4.4. Conclusions

In this chapter, Ir supported nanoparticles using a range of metal-oxide supports were studied to evaluate and optimise their catalytic performance and understand how it is feasible, to design better catalysts for the liquid-phase decomposition of hydrous hydrazine. Initially, it

was examined, how the methodology used to synthesise the Ir supported nanoparticles can have a significant influence on the catalytic performance in the liquid-phase decomposition of hydrous hydrazine. It was found that the catalytic performance exhibited by the Ir/CeO₂ prepared by deposition-precipitation with NaOH was better than the one exhibited by the other materials. While the catalyst prepared by deposition-precipitation with urea showed slightly higher TOF, 1712 h⁻¹ against 1564 h⁻¹, it displayed poor final yield toward molecular hydrogen, of 0.7%. On the contrary, the Ir/CeO₂ prepared by sol-immobilisation with THPC had a lower TOF value of 727 h⁻¹ and the final yield is similar to the one displayed by the sample prepared by deposition-precipitation with NaOH, 36.6% and 38.9% respectively. The preparation method by deposition-precipitation with NaOH was capable to deposit only 70% of the Ir used during the synthesis, in line with the expectation due to the mechanism of deposition. Therefore, due to the high price per gram of iridium the other preparation methods were chosen as reference for the successive tests since a higher Ir loading was achieved. From the characterisation studies performed on the samples, it was possible to understand and evaluate the effect of Ir particle size in terms of influencing catalytic performance. Ir/CeO₂ catalysts prepared by DP with NaOH and sol-imm. with THPC presented the higher final yield toward molecular hydrogen, 38.9 % and 36.6% respectively, with similar Ir mean particle size, 0.9 nm and 1.0 nm, which could suggest that the Ir particle size has a significant play role in affecting and improving the yield to H₂, of the Ir/CeO₂ catalysts.

Ir/CeO₂ was the best performing catalysts when comparing among materials prepared by the same preparation method on different supports. In particular, in the case of the sol-immobilisation method, Ir/CeO₂ exhibited a final yield toward H₂, almost eight times higher than the analogous Ir/TiO₂, with yield to H₂ of 36.6% and 4.5%, respectively. The supports tested had a wide range of points of zero charge indicating that the increase in final yield to H₂ is not related acid-base properties of the metal-oxides used as supports. The increase in yield is more likely related to the redox properties of CeO₂, since it is known to exchange O atoms with metal nanoparticles most than other oxides, creating vacancies on the surface. This strong metal-support interaction, as it has been shown by the effect of the calcination and reduction heat-treatment. The reduction temperature increased catalytic activity and final yield to H₂, this is related due to the further reduction of the cerium oxide around the Ir nanoparticles as shown in Chapter 3 Section 3.4.6. . The increased concentration of vacancies

near the Ir nanoparticles may be one significant parameter for the improved catalytic performance exhibited by Ir/CeO₂ materials. It was also shown, that (I) small mean Ir particle size and with narrow particle size distribution and (II) the strong Ir interaction with the surface of the support created a higher up-shift in the metallic Ir 4f peaks as presented in the XPS analysis. The up-shift of the metallic iridium Ir 4f peaks suggests the formation of partial positive charge on the surface of the Ir nanoparticles. As discussed previously, this phenomenon is related with the presence of small particle size as proven by the sample prepared by sol-immobilisation with THPC calcined at 500°C and then reduced, Ir/CeO₂ THPC calc 600, that has particles between 50 and 200 nm and do not present up-shift, while the same material only reduced, Ir/CeO₂ THPC 600, as an up-shift of 0.8 eV and sub-2nm cluster of Ir. The phenomenon is associated with the interaction of Ir nanoparticles with the support since it has been also shown for the Ir/Metal oxide samples prepared by sol-immobilisation with THPC. However, a lower up-shift of the peak of metallic Ir by 0.3-0.4 eV was observed, than in the case of Ir/CeO₂. To support this statement, from the catalytic evaluation of soluble Ir salts and water-stable Ir complexes it was also shown that Ir species reacted firstly with hydrous hydrazine to produce Ir nanoparticles and then the “in-situ” synthesised Ir nanoparticles (during the reaction with hydrous hydrazine) performed the catalytic decomposition of hydrous hydrazine.

Taking into account the above information, it can be deduced that improving the yield to H₂ during the catalytic decomposition of hydrous hydrazine in aqueous solution on Ir monometallic catalysts requires the presence of small nanoparticles of Ir (1-2 nm) and have a strong metal-support interaction. These requirements also influence the partial surface charge of the nanoparticle, after possible charges of the surface due to the effect of the X-ray gun were compensated. Therefore, the position of the peaks of Ir 4f and the upshift of the signal can be used to predict the availability of Ir/CeO₂ catalysts for the decomposition of hydrazine to hydrogen.

Moreover, another important characteristic of the catalytic materials that influence the final yield of the reaction is the oxidation state of the Ir on the surface of the nanoparticles. The DFT calculations have shown that IrO₂ binds strongly with all the intermediates and products leading to rapid poisoning of the material. This indication is confirmed by the experimental

catalytic tests on materials that possess a high percentage of iridium oxide on the surface, due to the fact that these materials showed improved catalytic activity only when the surface of the supported Ir nanoparticles were reduced by the hydrous hydrazine in solution. Moreover, the catalytic activity of reduced sample increased with the increase of the atomic percentage of metallic iridium after XPS analysis.

Mass spectrometry analysis was used during the catalytic decomposition of hydrous hydrazine using selected catalysts. It was performed using labelled ^{15}N hydrazine in order to obtain information about the reaction mechanism of the decomposition reaction of hydrous hydrazine. A small increase in fragment with mass 29, $^{14}\text{N}^{15}\text{N}$, when using a mixture of labelled and not labelled hydrous hydrazine indicated a cleavage in the N-N bond of the hydrazine molecule and successive recombination of the N adsorbed atom on the surface. The low entity of the increase in the peak of the fragment at 29 amu suggested that the N atoms on the surface have low probability to interact with atoms originated from other molecules of hydrazine. The identification of the scission of the N-N bond of hydrazine is in agreement with the DFT calculations presented, and, moreover, is additionally supported by the *in situ* ATR-IR analysis which showed the absorption of NH_2 , at wavenumber 1470 cm^{-1} , on the surface of the Ir/CeO₂ materials.

Ir/NiO prepared by sol-immobilisation with THPC was also tested as a potential catalyst for the liquid-phase decomposition of hydrous hydrazine in aqueous solution. This material exhibited an outstanding final yield of 84.2% toward hydrogen, higher than any other monometallic iridium catalysts reported in the literature. The catalytic activity, reported as TOF of 132 h^{-1} , is lower than the other materials presented in the literature, but the higher amount of hydrogen produced and, therefore, the lower amount ammonia produced, by-product that can damage the fuel cell, indicates that Ir/NiO can be appealing catalyst for the decomposition reaction of hydrous hydrazine at mild reaction conditions. Moreover, during the reusability tests, the Ir/NiO sample displayed good stability over the course of 10 consecutive reactions with the final yield of hydrogen less than a 10% of the initial value of the fresh catalyst, to 78.5%, and retaining the same value of TOF, 138 h^{-1} . The characterisation performed on this material displayed a good dispersion of Ir nanoparticles on the surface of NiO and confirmed the nominal loading of active metal on the surface, from the SEM-EDX

analysis. XPS analysis showed that did not display the up-shift of metallic Ir that was present on the Ir/CeO₂ and presented a higher amount of IrO_x species than previously reported active samples. Ni is a known active metal for the decomposition of hydrous hydrazine. Therefore, in Chapter 5 and 6 supported bimetallic Ir-Ni samples have synthesised and the catalytic performance has been investigated.

4.5. References

- 1 R. Zanella, L. Delannoy and C. Louis, *Appl. Catal. A Gen.*, 2005, **291**, 62–72.
- 2 J. L. Hueso, V. Sebastian, A. Mayoral, L. Uson, M. Arruebo and J. Santamaria, *RSC Adv.*, 2013, **3**, 10427–10433.
- 3 L. Prati and A. Villa, *Catalysts*, 2012, **2**, 24–37.
- 4 F. Porta, L. Prati, M. Rossi, S. Coluccia and G. Martra, *Catal. Today*, 2000, **61**, 165–172.
- 5 A. Aguirre, C. E. Barrios, A. Aguilar-Tapia, R. Zanella, M. A. Baltanás and S. E. Collins, *Top. Catal.*, 2016, **59**, 347–356.
- 6 R. Zanella, S. Giorgio, C. H. Shin, C. R. Henry and C. Louis, *J. Catal.*, 2004, **222**, 357–367.
- 7 H. Yen, Y. Seo, S. Kaliaguine and F. Kleitz, *ACS Catal.*, 2015, **5**, 5505–5511.
- 8 C. L. Bianchi, S. Biella, A. Gervasini, L. Prati and M. Rossi, *Catal. Letters*, 2003, **85**, 91–96.
- 9 S. Li, Y. Xu, Y. Chen, W. Li, L. Lin, M. Li, Y. Deng, X. Wang, B. Ge, C. Yang, S. Yao, J. Xie, Y. Li and X. Liu, *Angew. Chemie Int. Ed.*, 2017, **56**, 10761–10765.
- 10 L. He, B. Liang, L. Li, X. Yang, Y. Huang, A. Wang, X. Wang and T. Zhang, *ACS Catal.*, 2015, **5**, 1623–1628.
- 11 S. K. Singh, Z. H. Lu and Q. Xu, *Eur. J. Inorg. Chem.*, 2011, 2232–2237.
- 12 S. K. Singh, X. Zhang and Q. Xu, 2009, **131**, 9894–9895.
- 13 X. Yan, T. Ai, X. Su, Z. Wang, G. Sun and P. Zhao, *MATEC Web Conf.*, 2016, **2**, 1–5.
- 14 D. F. Abbott, D. Lebedev, K. Waltar, M. Povia, M. Nachtegaal, E. Fabbri, C. Coperet and T. J. Schmidt, *Chem. Mater.*, 2016, **28**, 6591–6604.
- 15 T. W. Hansen, A. T. Delariva, S. R. Challa and A. K. Datye, *Acc. Chem. Res.*, 2013, **46**, 1720–1730.
- 16 S. J. Freakley, J. Ruiz-Esquius and D. J. Morgan, *Surf. Interface Anal.*, , DOI:10.1002/sia.6225.
- 17 J. A. Creighton and D. G. Eadont, *J. Chem. Soc. Faraday Trans*, 1991, **87**, 3881–3891.
- 18 G. W. Watt and J. D. Chrisp, *Anal. Chem.*, 1952, **24**, 2006–2008.

5. Investigation of Ni nanoparticles for catalytic decomposition of hydrous hydrazine in aqueous solution

5.1. Introduction

In Chapters 3 and 4, the potential of Ir supported nanoparticles was investigated as a potential catalyst for the liquid-phase decomposition of hydrous hydrazine. Except Ir as a potential material for the studied reaction, in literature is reported that Ir, Rh and Ru catalysts usually present high activity for the liquid-phase decomposition of hydrous hydrazine, but the selectivity/yield reported for these catalysts lead toward the generation of ammonia and not H_2 .^{1,2} On the other hand, first row transition metals such as Ni, Fe and Cu present lower activities, requiring longer reaction time to achieve full decomposition of the reagent, but exhibit higher selectivity/yield to the production of molecular hydrogen.²⁻⁴ Therefore, Ni was chosen as the desirable candidate to investigate and understand the decomposition of hydrous hydrazine toward H_2 . Therefore, a series of supported Ni nanoparticles were synthesised, characterised and tested for the reaction.

If in the case of Ir-based catalysts the main goal of the research was to improve primarily the yield of the reaction to the production of hydrogen, due to the fact that rate of reaction was not the primary issue of Ir catalysts. In the case of Ni-based catalysts was vital to improve the activity as well as the yield to molecular hydrogen.

Considering the catalytic results reported in the literature for the hydrous hydrazine liquid-phase decomposition it is possible to see that colloidal solution of Ni nanoparticles tend to not to display any catalytic activity, where supported Ni nanoparticles are more reactive.⁴⁻⁶ On the contrary, as reported in the literature and then verified during the tests reported in Chapter 4, Ir colloidal solutions are catalytically active for the liquid-phase decomposition of hydrous hydrazine. This different behaviour is probably associated to the lower stability of

colloidal solutions of a first-row transition metal, such as Ni, that can result in agglomeration of the nanoparticles and faster formation of oxides on the surface of the nanoparticles.

For this reason, in this chapter, the optimisation of supported Ni nanoparticles was studied, and comparison was made, comparing, as it was presented in Chapter 4 for Ir supported nanoparticles. For example, the effect to the catalytic performances of following parameters was studied: (I) changes of metal oxide used as support, (II) heat treatment and (III) changes of preparation method applied for the synthesis of the catalysts. The optimisation of the catalysts and the structural and catalytic data collected during this process can be used afterwards to design better active and selective materials for this reaction.

5.2. Results and discussion

In this chapter, supported Ni nanoparticles have been synthesised and tested as potential catalysts for the catalytic decomposition of hydrous hydrazine in aqueous solution. It was decided to begin the study of the Ni-based materials by depositing preformed Ni nanoparticles on CeO₂ using the sol-immobilisation method. The reasons for this decision was based on the following facts: (I) the optimisation work presented on Ir/CeO₂ and reported in Chapters 3 and Chapter 4 and (II) the work of He *et al.* which strongly indicated an interaction between Ni and CeO₂ to improve both selectivity/yield and activity.⁷ The work of He *et al* is in agreement with the results presented in our case between Ir and CeO₂ in this thesis.

The experimental conditions used for Ir/CeO₂ linked to fluid dynamics were validated also for the Ni catalysts, allowing to perform the reaction under kinetic regime for these catalysts.

The catalytic tests were performed following the experimental procedure reported in Chapter 2, Section 2.3. .

5.2.1. Initial catalytic screening of Ni/CeO₂ catalysts prepared by sol-immobilisation with THPC

Initial studies were carried out to evaluate the catalytic performance of Ni-based catalysts using as reference material, Ni/CeO₂ prepared by sol-immobilisation with THPC. The choice was due to the fact that this material has a similar preparation method to the Ir/CeO₂ catalyst with the on the best catalytic performance, with yield toward hydrogen of 36.6% and TOF of 726.9 h⁻¹. In the case of Ir, the catalyst had a small mean particle size of Ir (1.0 ± 0.2 nm) as it

was shown in Chapter 3 and after the heat treatment reduction presented strong metal-support interaction with the metal oxide. Since literature suggests that the SMSI can be present as well as in case of Ni-based catalysts for the liquid-phase decomposition of hydrous hydrazine, the Ni/CeO₂ prepared by sol-immobilisation with THPC was chosen as an ideal reference catalyst to initiate catalytic studies and performance.

Sol-immobilisation with THPC/NaOH as the reducing agent is a particularly interesting preparation method since the stabilisation of the preformed colloidal nanoparticles is mainly electrostatic, opposite to other sol-immobilisation methods, where the usage of polymers as effective ligands can provide steric stabilisation.^{8,9} Electrostatic stabilisation can facilitate and improve the accessibility of the surface of colloidal nanoparticles to the reactants after the immobilisation step, however, colloidal nanoparticles prepared with this method can be less stable over time and more susceptible to collapse and agglomeration by the presence of a small amount of free ions. The easiest way to monitor that the synthesis produces metal colloidal nanoparticles is by colourimetric control of the colloidal metal solution. For example, NiCl₂, the chosen precursor and source of Ni atoms, when it is dissolved in water, has a bright green colour. The disappearance of this colouration in the presence and addition of THPC and NaOH, reducing agent and stabiliser, can indicate a change in the presence of Ni species in aqueous solution. By using UV-vis analysis and from the work of Creighton *et al.*, it can be seen that Ni colloidal solution should present a small shoulder peak in the near UV region of the spectrum, giving a colourless colloidal Ni solution.¹⁰ Therefore, the first indication of successful preparation of a colloidal Ni solution is the disappearance of the green colouration of the solution which was confirmed by the UV/vis spectrum of the solution recorded before the immobilisation step, by the absence of the peaks at 395, 655 and 720 nm.¹¹

The success of the preparation method and final immobilisation of preformed Ni colloidal nanoparticles on the support, was also confirmed later by the calculated Ni loading by the SEM-EDX analyses giving a loading of 1.06 ± 0.18 wt.%, which is in agreement with the theoretical loading used, as shown in Chapter 5, Section 5.3.3. .

After the reduction at 600°C under flow of H₂/Ar of the material obtained by the sol-immobilisation of Ni colloid, the catalyst was ready to be tested for the liquid-phase decomposition of hydrous hydrazine. The reaction was repeated at least three times to

control the reproducibility of the method and the stability of the catalysts. As mentioned before, Ni-based catalysts are reported, in contrast to the higher selectivity to hydrogen, to display lower activity with respect to Ir-based catalysts. Therefore, the substrate/metal molar ratio was decreased to a value of 38 in order to decrease the total time of reaction but without compromising the hydrodynamic properties of the reaction solution and using an amount of catalyst (152.2 mg). The chosen amount is in the range tested during the optimisation of the reaction conditions with Ir catalysts presented in the previous chapters, therefore not increasing the impact of mass transfer phenomena and working in kinetic chemical regime. Nonetheless, the reaction required longer reaction time to decompose completely the hydrous hydrazine. The reaction was prolonged up to 24h and consequently the reaction was left overnight and in the following day, the reaction was stopped when the volume of gas was remained constant for at least one hour.

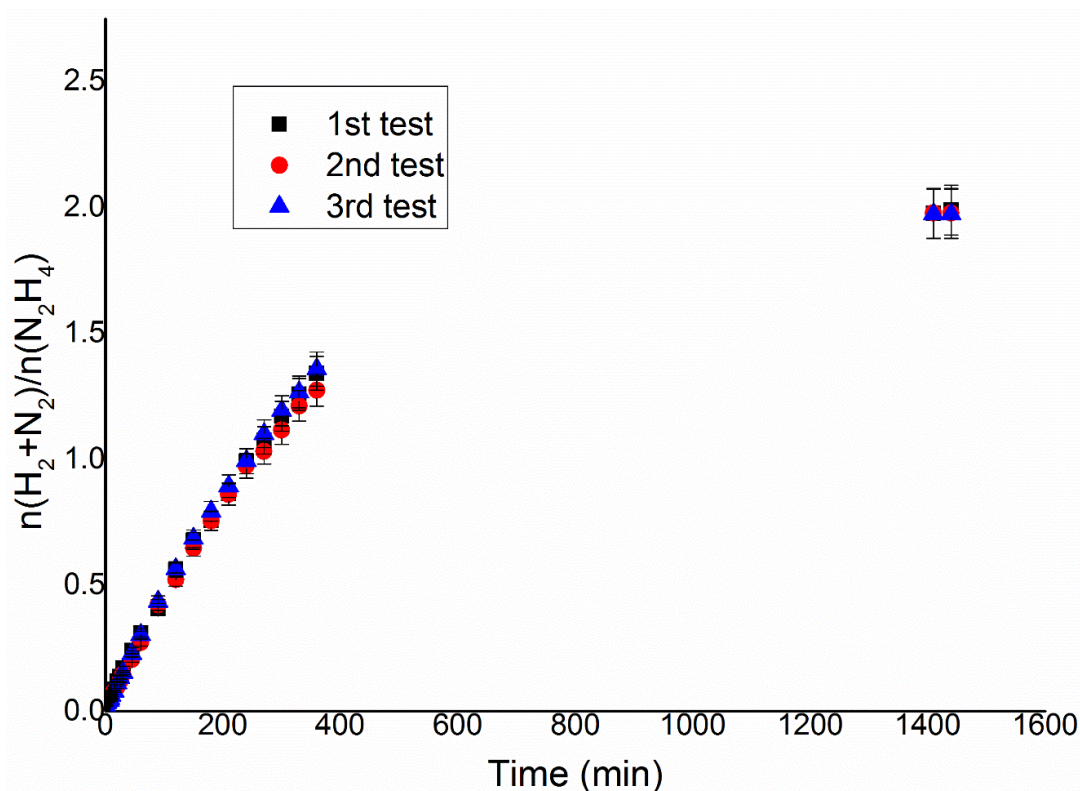


Figure 5.1. $n(\text{H}_2+\text{N}_2)/n(\text{N}_2\text{H}_4)$ versus time for hydrous hydrazine decomposition over Ni/CeO₂ prepared by sol-immobilisation with THPC reduced at 600 °C using 0.3mL of 3.3 M hydrazine monohydrate in 8 mL of 0.5 M NaOH solution, at 50°C, 1050 rpm of stirring rate and 38:1 substrate to metal molar ratio. Repeated three times using fresh catalyst.

In Figure 5.1 the volume of gas production as a function of time and the yield of gaseous products overtime for three reactions performed with Ni/CeO₂ prepared by sol-

immobilisation with THPC reduced at 600°C in H₂/Ar flow, at 50°C and 1050 rpm with a substrate/metal molar ratio of 38 are reported. The reactions were reproducible, with differences inside the margin of experimental error of the analyses, below 1% of the $n(\text{H}_2+\text{N}_2)/n(\text{N}_2\text{H}_4)$ final value. The value of the calculated final yield to hydrogen was 60.9%, while the TOF_{50%} was 4.6 h⁻¹. These results gave a good starting insight into the possible activity and yield of Ni-based catalysts and ensured the reproducibility of the reaction system.

5.2.2. Effect of the Reduction Treatment

Once proven the reproducible catalytic activity of Ni/CeO₂ prepared by sol-immobilisation with THPC as a reference catalyst for the decomposition of hydrous hydrazine in aqueous solution the catalyst was optimised in order to increase yield to hydrogen and TOF. The first approach was to improve the interaction between the Ni nanoparticles and the surface of the support, by varying and studying the effect of temperature of the reductive heat treatment on the catalyst.

From the temperature-programmed reduction (TPR), reported in Section 5.3.1., it could be observed, that the Ni was reduced between 300 °C and 350°C with a small shoulder peak at 400 °C. For this reason, a series of samples prepared by reducing the Ni/CeO₂ prepared by sol-immobilisation with THPC at different heat-treatment temperatures was carried out, in order to study how the difference in the temperature of the heat treatment can affect the catalytic performance of the synthesised materials.

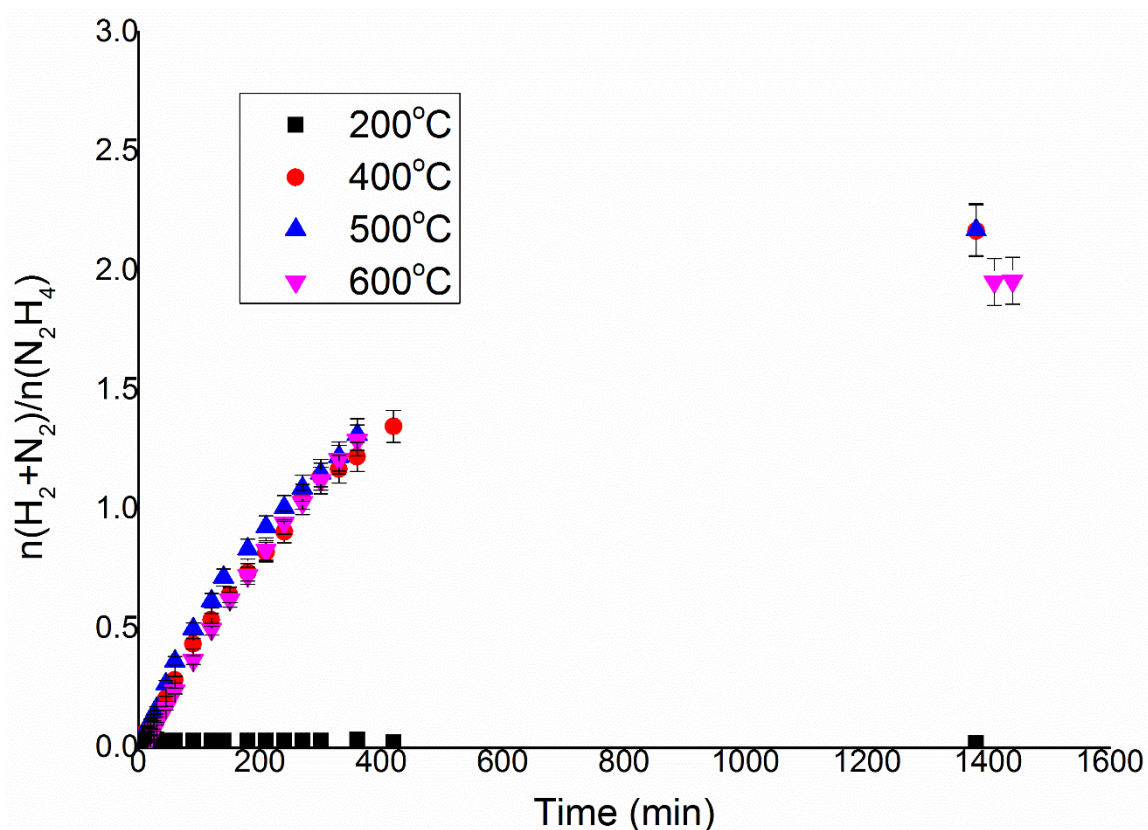


Figure 5.2. $n(\text{H}_2+\text{N}_2)/n(\text{N}_2\text{H}_4)$ versus time for hydrous hydrazine decomposition over Ni/CeO_2 prepared by sol-immobilisation with THPC reduced at 200°C, 400°C, 500°C and 600°C using 0.3 mL of 3.3 M hydrazine monohydrate in 8 mL of 0.5 M NaOH solution, at 50°C, 1050 rpm of stirring rate and 38:1 substrate to metal molar ratio.

Figure 5.2 shows the effect of heat-treatment temperature on the series of Ni/CeO_2 catalysts. The Ni/CeO_2 reduced at 200°C did not exhibit catalytic activity for the decomposition of hydrous hydrazine, without producing gaseous products over the 24h period of reaction. In contrast, the samples reduced at a temperature higher than 400°C, higher than the temperature of reduction found by the TPR analysis, were active and showed formation of gaseous products, exhibiting yield toward molecular hydrogen. To be noticed is that, while the TOF values remained practically constant, 4.1-4.6 h^{-1} , among the high temperature reduced samples, the yield toward molecular hydrogen decreased for the sample reduced at 600°C, with value of 60.9%, compared with the samples reduced at 400°C and 500°C, with values of 68.8% and 68.9%, respectively. The observed differences, higher than the error of the measurements, between reduced samples may be related to a growth in the mean particle size of Ni that alter the surface area of the nanoparticles and, in particular, the preferentially exposed nickel facet. Unfortunately, since Ni is a lighter atom than Ir, TEM analysis wasn't able to find the presence of Ni nanoparticles and p-XRD did not exhibit

characteristic Ni peaks so there is no way to prove that the growth of the Ni nanoparticles by the heat treatment is the main reason for the decrease in yield.

Table 5.1. $TOF_{50\%}$ for the activity and final yield to H_2 for Ni/CeO₂ catalysts prepared by sol-immobilisation with THPC reduced at different heat-treatment temperature. N.d. for not determined

Samples	Reduction temperature (°C)	Final yield toward H ₂ (%)	TOF _{50%} (h ⁻¹)
Ni/CeO ₂ THPC 200	200	n.d.	n.d.
Ni/CeO ₂ THPC 400	400	68.8	4.1
Ni/CeO ₂ THPC 500	500	68.9	4.4
Ni/CeO ₂ THPC 600	600	60.9	4.6

The XPS data, reported in Section 5.3.4., showed that the samples, also after the reduction at high temperature with H₂, still present the majority of the surface covered by oxidised Ni species. The reduction of nickel happens below 400°C, from TPR analysis, so it can assume the complete reduction of Ni during the heat treatment. This oxidation of the surface of the Ni nanoparticles is probably due to the interaction with air after the heat treatment and low resistance of Ni nanoparticles to oxidation, in contrast to bulk Ni which tend to passivate and resist to further oxidation. In this case, the inactivity of the sample reduced at 200 °C and the activity of the other Ni/CeO₂ could be related to an *in situ* activation of the surface process by the hydrous hydrazine, which requires that the core of the nanoparticles is reduced firstly at higher reduction temperature and therefore to be effective. This activation of the surface is also further supported by the reaction profile of the gas production in the first minutes of the reaction, which displayed an increase after the first 10 minutes of reaction, as shown in Figure 5.3.

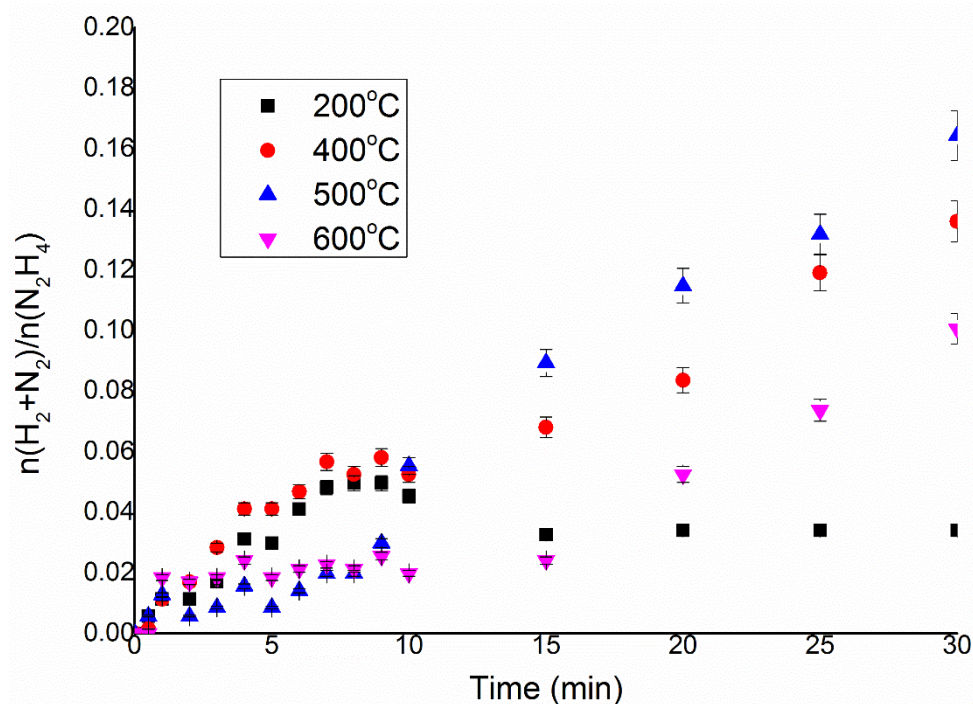


Figure 5.3. $n(\text{H}_2+\text{N}_2)/n(\text{N}_2\text{H}_4)$ versus time for hydrous hydrazine decomposition over Ni/CeO₂ prepared by sol-immobilisation with THPC reduced at 200°C, 400°C, 500°C and 600°C using 0.3 mL of 3.3 M hydrous hydrazine in 8 mL of 0.5 M NaOH solution, at 50°C, 1050 rpm of stirring rate and 38:1 substrate to metal molar ratio.

5.2.3. Influence of the preparation method on the catalytic activity of Ni/CeO₂ catalysts

As explained in Chapter 4, the experimental methods used for the synthesis of supported metal nanoparticles can have a great impact on the catalytic performance of a material based on the same combination of active metal and support. Different preparation methods can produce metal nanoparticles with different mean particle size, particle size distribution, can present different preferential facets and finally have different accessibility for reagent to the surface.

To investigate this aspect, 2 wt. % Ni/CeO₂ material was prepared by deposition precipitation with NaOH method and was compared with the 1 wt. % Ni/CeO₂ prepared by sol-immobilisation method. It was decided to increase the metal loading of the active metal deposited on the surface in the attempt to increase the response and sensitivity of the sample at the characterisation performed. For the comparison of the catalytic performance, the substrate/metal molar ratio was maintained the same value of 38 by using half of the mass of the catalyst used for the catalytic tests with respect to the sol-immobilisation samples.

The Ni/CeO₂ prepared by deposition precipitation method was then reduced at 400 °C under H₂/Ar flow since it was observed that the optimal increase in catalytic performance was achieved at this heat-treatment temperature.

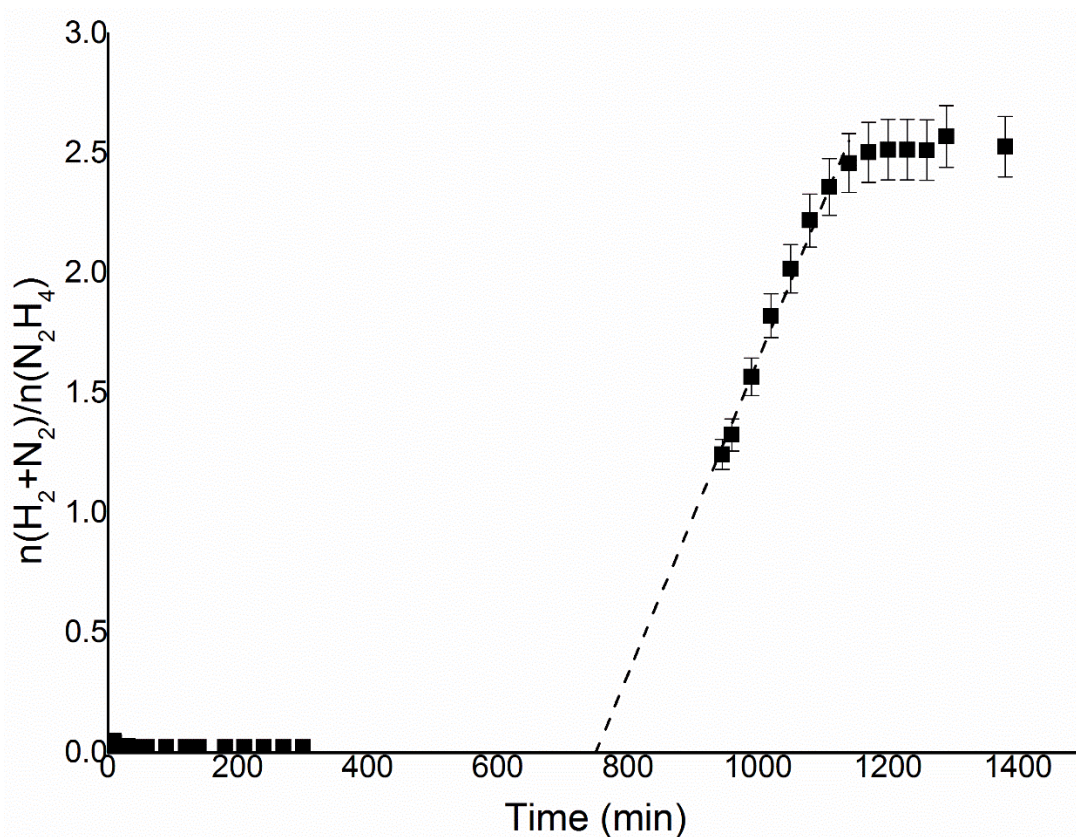


Figure 5.4. $n(\text{H}_2 + \text{N}_2) / n(\text{N}_2\text{H}_4)$ versus time for hydrous hydrazine decomposition over 2 wt. % Ni/CeO₂ prepared by deposition-precipitation reduced at 400°C using 0.3 mL of 3.3 M hydrazine monohydrate in 8 mL of 0.5 M NaOH solution, at 50°C, 1050 rpm of stirring rate and 38:1 substrate to metal molar ratio.

In Figure 5.4, it can be observed that during the first 5 hours of reaction the catalyst did not display the production of gaseous products. The reaction mixture was left overnight for checking the possibility of producing gaseous products and the next morning it was found the production of gaseous products after 15 hours from the starting of the reaction. These results indicate *in situ* activation of the samples prepared by deposition-precipitation as in the case of the sample prepared by sol immobilisation. However, the reaction time required for this activation increased considerably by a few minutes to several hours. An approximate duration of the induction period was extrapolated by the data obtained at the end of the reaction. For this reason, the calculation of the TOF for this material is not possible in an accurate way. Nevertheless, considering a starting point after 13 hours of reaction from the addition of the

hydrous hydrazine solution in the reaction, an approximate TOF of 5.0 h^{-1} was calculated, which is in line with the values recorded for the Ni/CeO₂ prepared by sol-immobilisation.

It should be noticed also that the final yield to hydrogen recorded with the catalyst prepared by deposition-precipitation was 82%, higher than the 68.8% recorded by the sol-immobilisation sample. The higher yield to molecular hydrogen and the longer activation time may indicate the formation and presence of narrower particle size distribution and smaller mean nanoparticle size of Ni. In this way, the reduction of Ni in basic solution could be decreased and therefore it could increase the extension of the interface between Ni nanoparticles and the cerium oxide and therefore to increase the entity of the metal support interaction.

5.2.4. Influence of the support material

The studies on Ir-based catalysts indicated that the interaction of the active metal with the cerium oxide used as support plays a key role in the catalytic performance displayed by the materials tested. The first tests reported in this chapter on Ni/CeO₂ seem to indicate that a similar interaction is vital also for Ni-based catalysts. In order to study and control the influence of the support in terms of activity and yield toward H₂, a series of Ni-metal oxide catalysts were prepared. Ni/Al₂O₃ and Ni/MgAl₂O₄ catalysts prepared by deposition precipitation with NaOH and a Ni/Al₂O₃ catalyst prepared by sol-immobilisation with THPC were tested using the same experimental reaction conditions of the Ni/CeO₂ catalyst.

From the TPR analysis of the Ni/Al₂O₃ prepared by sol-immobilisation THPC, and reported in Section 5.3.1., it was possible to observe how the reduction temperature of Ni on Ni/Al₂O₃ increased compared with the Ni/CeO₂ reaching an effective temperature of reduction between 350° and 400°C. Therefore, the materials were reduced at 400°C in H₂/Ar flow for 3 hours in order to achieve the complete reduction of the metal. As it is shown in Figure 5.5, the samples prepared by deposition-precipitation retained a light colourisation, while the one prepared by sol-immobilisation changed to a darker grey colour. The darker colour as seen for the CeO₂ is an indication of the reduction of the Ni nanoparticles on the surface of the support.

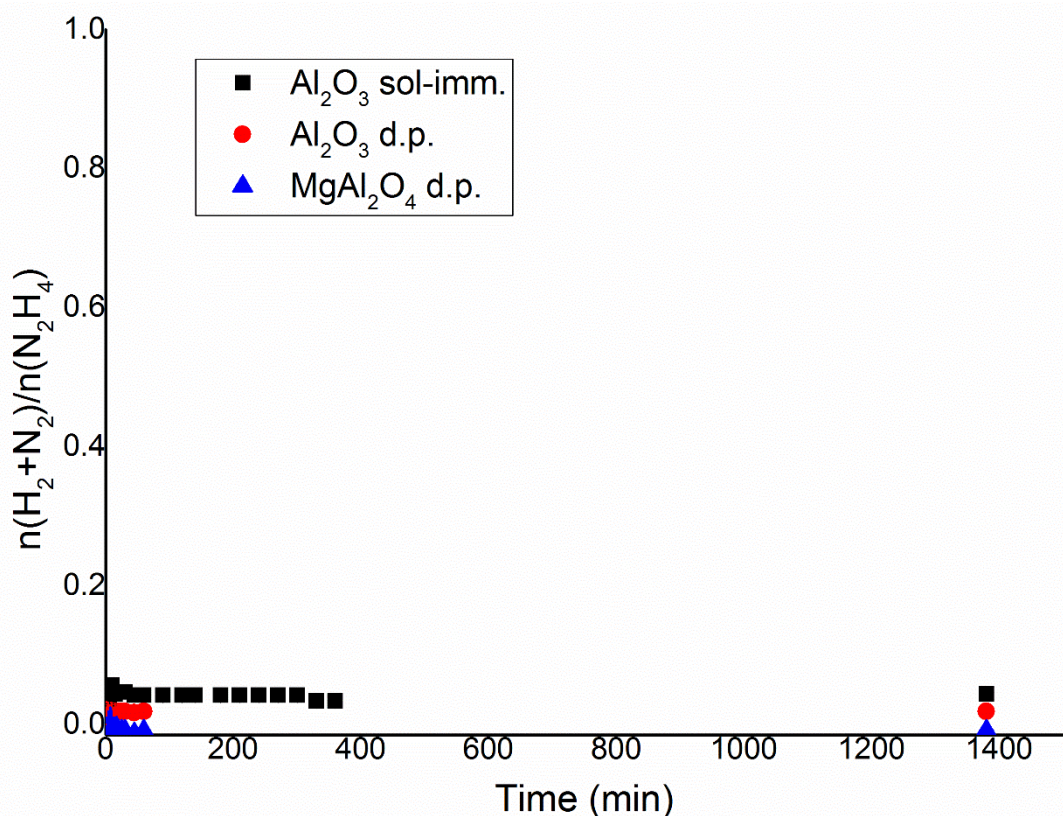


Figure 5.5. $n(\text{H}_2+\text{N}_2)/n(\text{N}_2\text{H}_4)$ versus time for hydrous hydrazine decomposition over Ni/Al₂O₃ prepared by sol-immobilisation with THPC, Ni/Al₂O₃ prepared by deposition-precipitation and Ni/MgAl₂O₄ prepared by deposition-precipitation reduced at 400°C using 0.3 mL of 3.3 M hydrazine monohydrate in 8 mL of 0.5 M NaOH solution, at 50 °C, 1050 rpm of stirring rate and 38:1 substrate to metal molar ratio.

Figure 5.5 shows that none of the supported Ni nanoparticles different from CeO₂ as the chosen support previously, were catalytically active for the decomposition of hydrous hydrazine in aqueous solution as confirmed by the colourimetric quantification of hydrazine at the end of the reaction. These results clearly indicate the key role played by the interaction between Ni and CeO₂ for the catalytic decomposition of hydrous hydrazine.

5.2.5. Effect of the reaction temperature

To conclude the studies on Ni-based catalysts, the Ni/CeO₂ prepared by sol-immobilisation with THPC reduced at 400°C was chosen as reference material since after the previous studies have shown to be the most effective catalytic material and the effect of reaction temperature of the reaction in terms of catalytic performance.

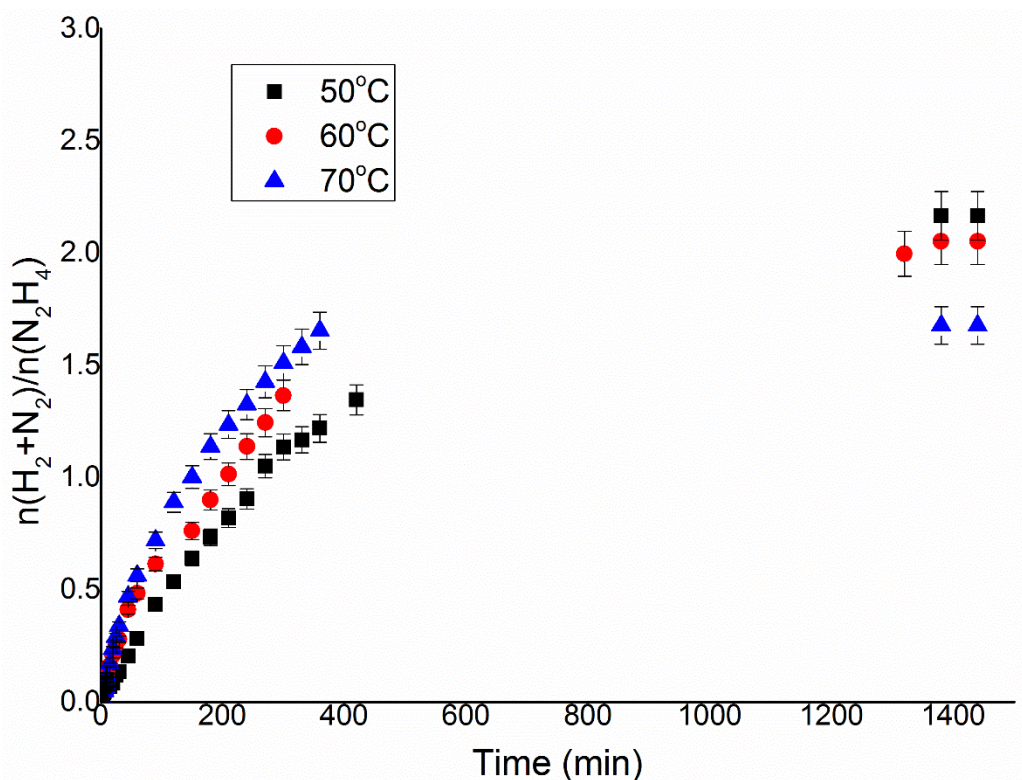


Figure 5.6. $n(\text{H}_2+\text{N}_2)/n(\text{N}_2\text{H}_4)$ versus time for hydrous hydrazine decomposition over Ni/CeO₂ prepared by sol-immobilisation with THPC reduced at 400°C using 0.3 mL of 3.3 M hydrous hydrazine in 8 mL of 0.5 M NaOH solution, 1050 rpm of stirring rate and 38:1 substrate to metal molar ratio performed at 50°C, 60°C and 70°C.

Since Ni-based catalysts require longer reaction times to completely decompose the hydrazine than Ir-based catalysts, the range of temperature tested for Ni/CeO₂ was 50°C, 60°C and 70°C. The reaction at 30°C was excluded to avoid 48 hours long reactions.

Figure 5.6 shows the gas evolution versus time. As expected, the activity growth with the reaction temperature from a TOF of 4.1 h⁻¹ at 50°C to 10.1 h⁻¹ at 70°C, Table 5.2. As in the case of Ir catalysts, the final yield to hydrogen decreases with temperature, from 68.8% to 50.4%. The change in selectivity of the reaction is related to the different kinetics of the two competitive decomposition reactions and the increase in ammonia production indicates that the activation energy of the reaction that leads to ammonia is higher than one that leads to hydrogen, therefore it is affected more by the increase of temperature.

Table 5.2. $TOF_{50\%}$ for the activity and final yield to H_2 for Ni/CeO₂ catalyst prepared by sol-immobilisation with THPC reduced at 400 °C for reaction performed at 50°C, 60°C and 70°C.

Temperature (°C)	Final Yield to H ₂ (%)	TOF _{50%} (h ⁻¹)
50	68.8	4.1
60	64.4	5.4
70	50.4	10.1

5.3. Characterisation of the catalysts

From the catalytic studies presented before, only some of the Ni-based catalysts were catalytically active with the Ni/CeO₂ prepared by deposition-precipitation to exhibit a long activation period at the beginning of the reaction. To understand better the parameters for synthesising and producing active Ni catalysts and therefore improve later the design of Ni-based catalysts that do not require a prolonged activation period, a series of characterisation methods have been performed to understand the nature of Ni-based catalysts, synthesised and tested in this chapter.

The characterisation data of SEM-EDX, XRD, XPS and TPR analyses are reported to evaluate and compare the following parameters: (I) surface area, (II) quantification of the Ni species on the surface, (III) identification of species on the surface and (IV) identification of crystallite size and phase in the for the different materials discussed in this chapter.

5.3.1. Temperature Programmed Reduction (TPR)

During the synthesis of the material, TPR analyses were performed to find the ideal temperature to reduce effectively the supported Ni nanoparticles and therefore form metallic Ni nanoparticles on the surface of the chosen support. Factors like the mean particle size of Ni and the Ni interaction with the support can increase the reactivity of the nickel oxide with hydrogen. Therefore, by decreasing the heat-treatment temperature necessary for the effective reduction of NiO to metallic Ni, from the almost 400°C heat-treatment temperature reported in the literature.¹² Using high heat-treatment temperature of reduction can increase the sintering of the formed Ni nanoparticles, and therefore increasing the mean particle size of Ni and therefore modifying the reactivity of the catalytic material for the studied reaction.

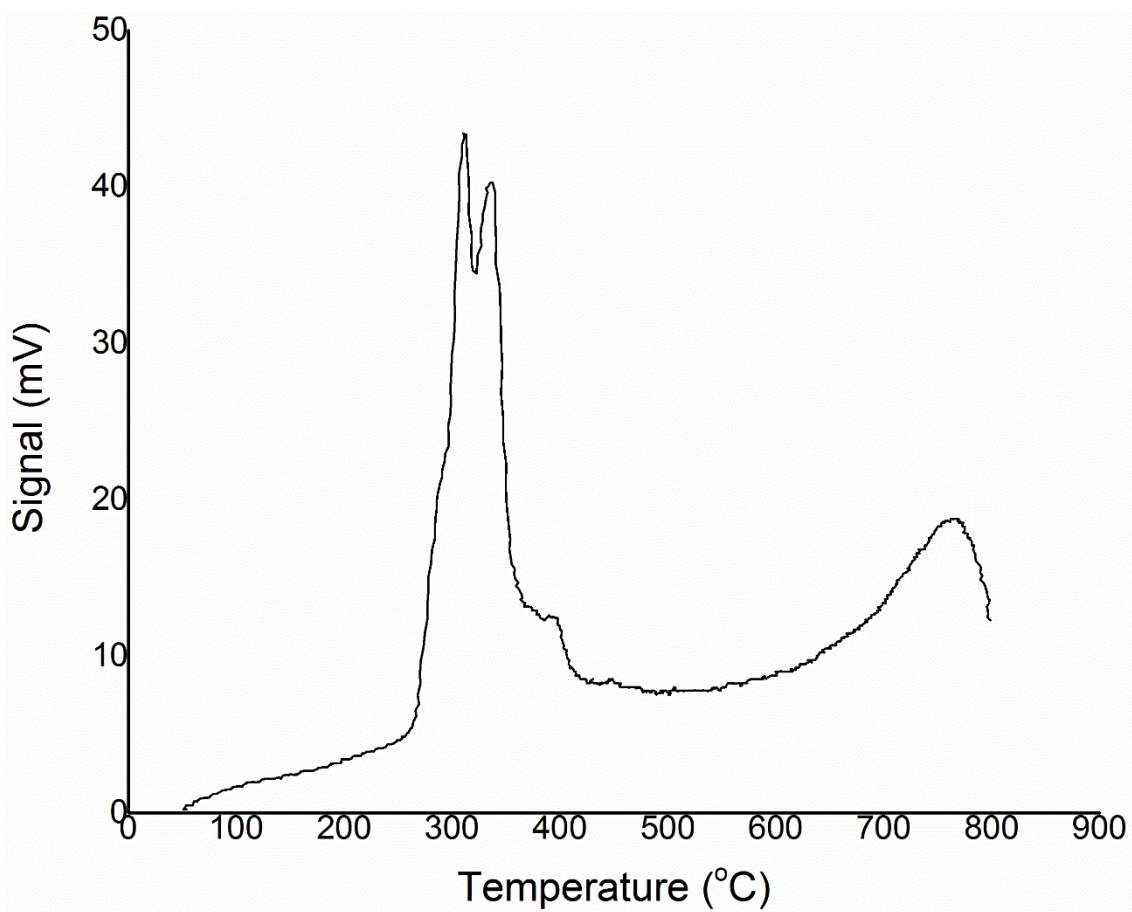


Figure 5.7. Temperature Programmed Reduction of Ni/CeO₂ prepared by sol-immobilisation with THPC.

In Figure 5.7 the reduction profile with temperature of Ni/CeO₂ is reported. Two main peaks are present at 311°C and 336°C and a smaller shoulder at 394°C. The two main peaks can be associated to the presence of small Ni nanoparticles and the split of the peaks may be an indication of a bimodal particle size distribution where the smaller Ni nanoparticles can be reduced at a slightly lower temperature.¹² The presence of a small shoulder at around 394 °C may have two possible explanations: (I) the presence on the surface of bulk nickel oxide¹² and (II) the reduction of CeO₂ around the Ni nanoparticles, where the reduction is facilitated by the presence of metal nanoparticles like in the case of Ir/CeO₂.¹³

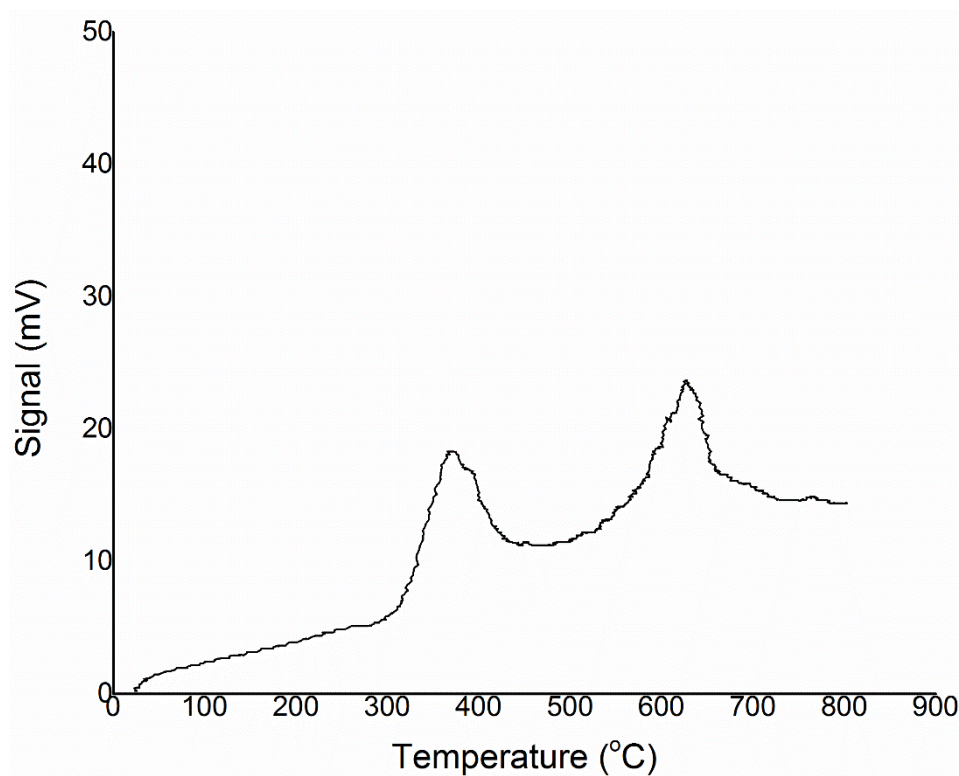


Figure 5.8. Temperature Programmed Reduction of Ni/Al₂O₃ prepared by sol-immobilisation with THPC.

In Figure 5.8 the reduction profile of Ni/Al₂O₃ presents a peak at 372°C and another at 627°C is reported. A reduction behaviour similar to one reported in the literature was observed.¹² However, the exact nature of the second reduction peak is not clear, therefore, the reduction was carried out at 400°C.

5.3.2. Powder X-Ray Diffraction (p-XRD)

p-XRD analysis was performed on the Ni/CeO₂ prepared by sol-immobilisation and deposition-precipitation to study the nature and possible dimensions of the Ni crystallites. For the analysis of Ni/CeO₂ the main characteristic diffraction peaks assigned to CeO₂, were presented at $2\theta = 29.3^\circ$, 33.1° , 47.5° and 57.6° and corresponding to (111), (200), (220) and (311) planes, respectively.¹⁴ The diffraction peaks at $2\theta = 44.5^\circ$, 51.9° and 76.4° could be assigned to (111), (200) and (220) planes of metallic Ni,¹⁵ respectively. The diffraction peaks at $2\theta = 37.2^\circ$, 43.2° , and 62.8° correspond to (111), (200), and (220) planes of NiO, respectively.¹⁶

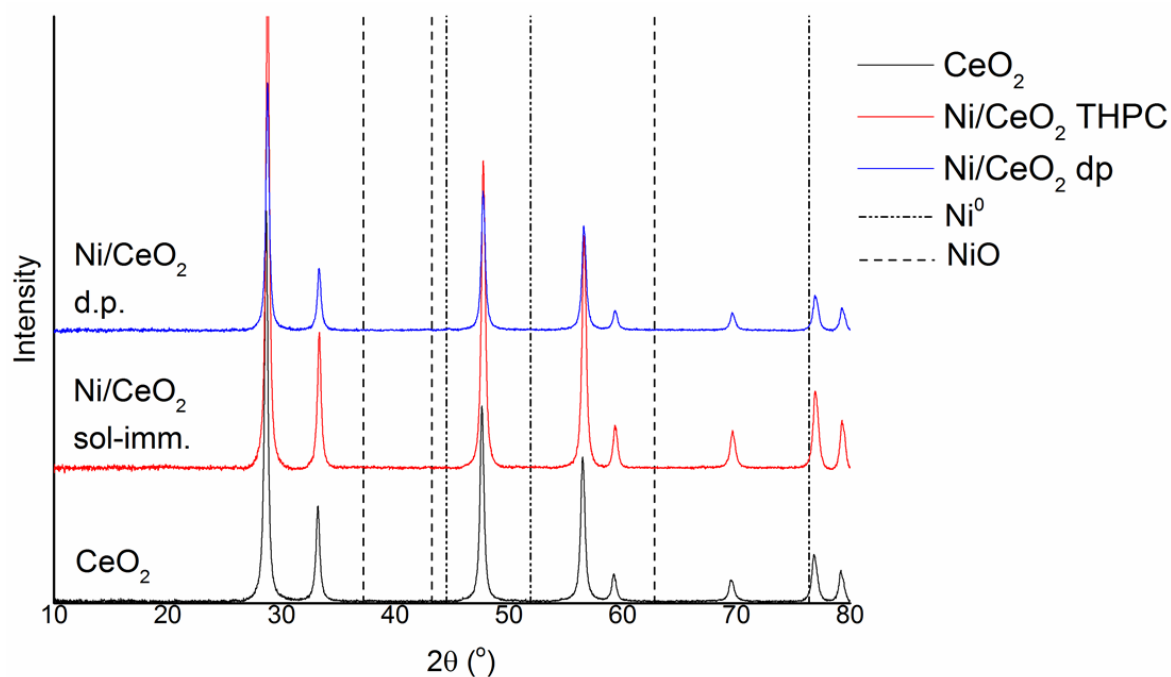


Figure 5.9. p-XRD patterns for CeO_2 , Ni/CeO_2 prepared by sol-immobilisation and Ni/CeO_2 prepared by deposition-precipitation. (---) represent the expected diffraction for NiO , while (.....) is the diffraction pattern of Ni^0 from literature.

Figure 5.9 shows the p-XRD patterns for the bare CeO_2 , Ni/CeO_2 samples prepared by sol-immobilisation and deposition-precipitation. As it can be seen in none of the samples any of the characteristic diffraction peaks of Ni species can be observed from the p-XRD pattern of CeO_2 . The absence of the diffraction peaks can be due to two different reasons; (I) the amorphous nature of the Ni nanoparticles, especially in the case of oxidised species and (II) the presence of Ni nanoparticles below 5 nm in diameter, since small dimensions broaden the diffraction peaks, until the diffraction peaks cannot be distinguished from the background. From XPS analysis reported later in the chapter, only small amounts of metallic Ni have been found on the surface of the support. Therefore, both of the suggested explanations for the lack of diffraction peaks of NiO or metallic Ni, displayed by Ni/CeO_2 can be correct and no further structural information related to the crystallite/particle size can be obtained from the p-XRD patterns.

5.3.3. Scanning Electron Microscopy (SEM) and Energy Dispersed X-Ray Spectroscopy

Scanning electron microscopy was used to obtain information about the real loading of nickel and its dispersion on the surface of the supports.

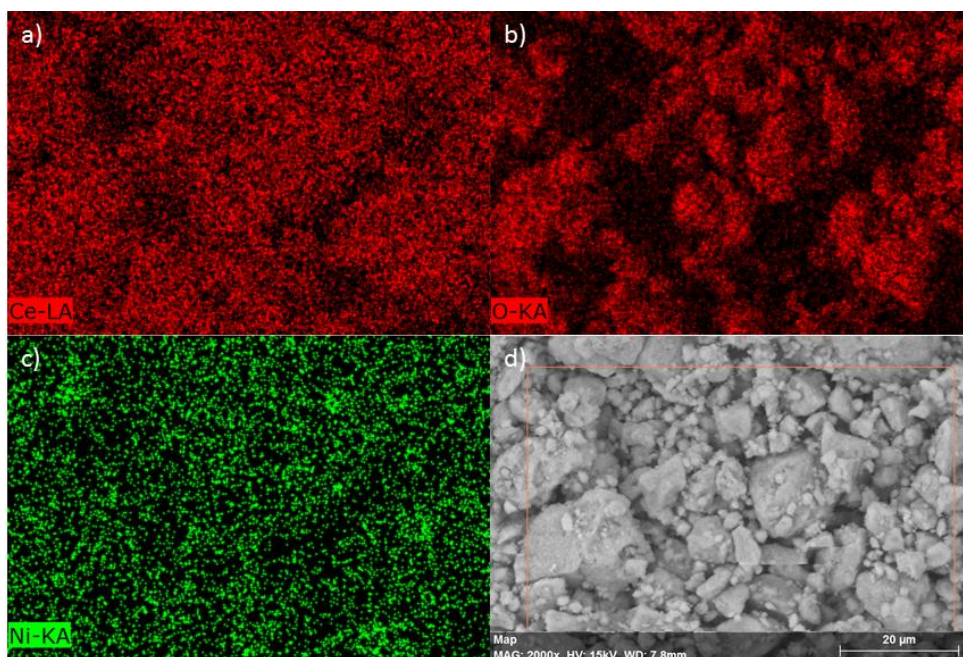


Figure 5.10. d) Representative SEM images of Ni/CeO₂ prepared by sol-immobilisation with TPHC reduced at 200°C, with EDX mapping for Ce, a), O, b), and Ni, c), showing homogenous distribution of the element on the sample.

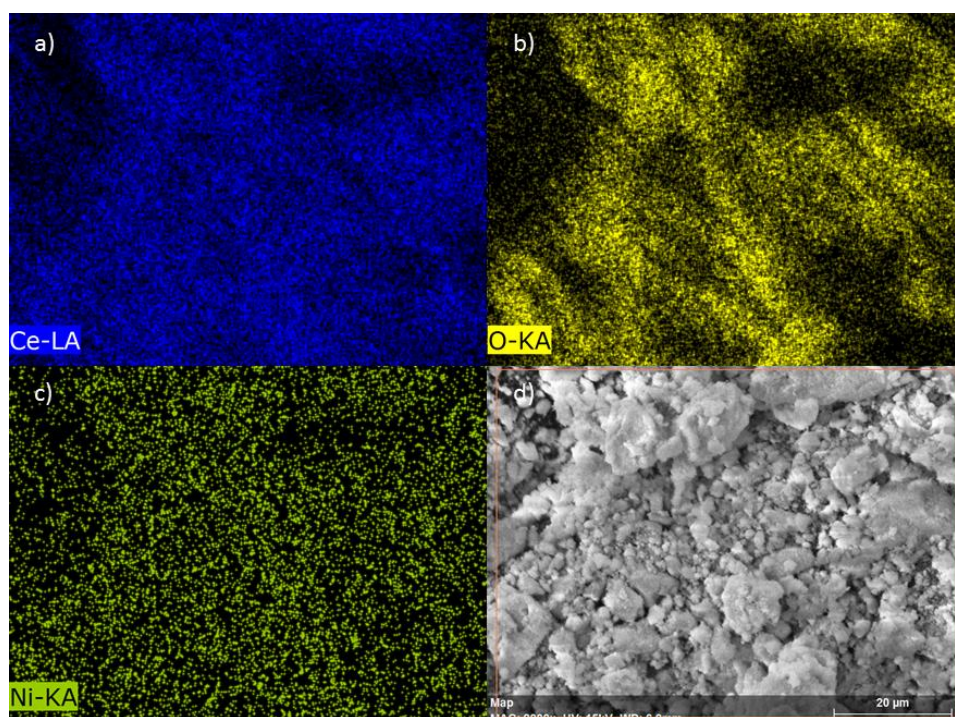


Figure 5.11. d) Representative SEM images of Ni/CeO₂ prepared by sol-immobilisation with TPHC reduced at 600°C, with EDX mapping for Ce, a), O, b), and Ni, c), showing homogenous distribution of the element on the sample.

Figure 5.10 and Figure 5.11 show some representative SEM images of Ni/CeO₂ prepared by sol-immobilisation and then reduced at 200°C and 600°C, respectively. The SEM images show

that Ni species were distributed uniformly on the surface of cerium oxide and the morphology of the oxide seems to be same after the heat-treatment at higher temperature. The Ni loading calculated from the EDX analysis for the materials reduced at 200°C was 1.1 ± 0.2 wt.%, while the one reduced at 200 °C had a Ni loading of 1.1 ± 0.2 wt.%, therefore the nominal loading values for Ni are confirmed for these materials.

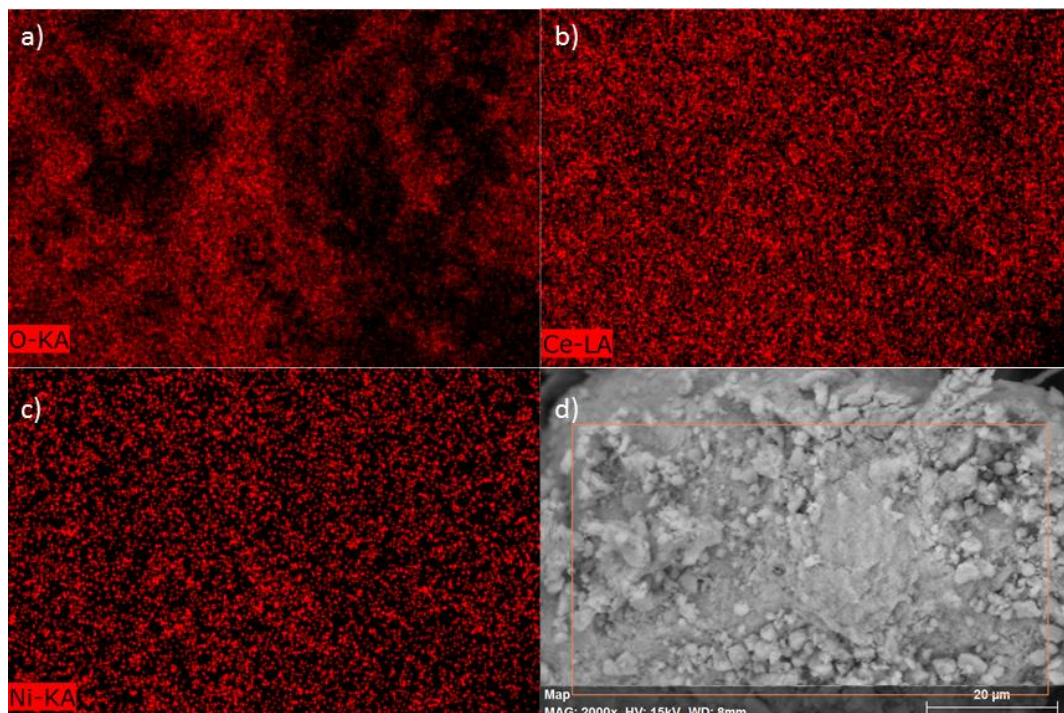


Figure 5.12. d) Representative SEM images of Ni/CeO₂ prepared by deposition-precipitation with NaOH reduced at 400°C, with EDX mapping for O, a), Ce, b), and Ni, c), showing homogenous distribution of the element on the sample.

Figure 5.12 shows the surface of the Ni/CeO₂ prepared by deposition-precipitation by NaOH and confirming an even distribution of Ni on all the surface of the cerium oxide. The EDX analysis calculated a real Ni loading of 2.3 ± 0.3 wt.%, which is within the margin of error with the nominal loading of 2 wt. %.

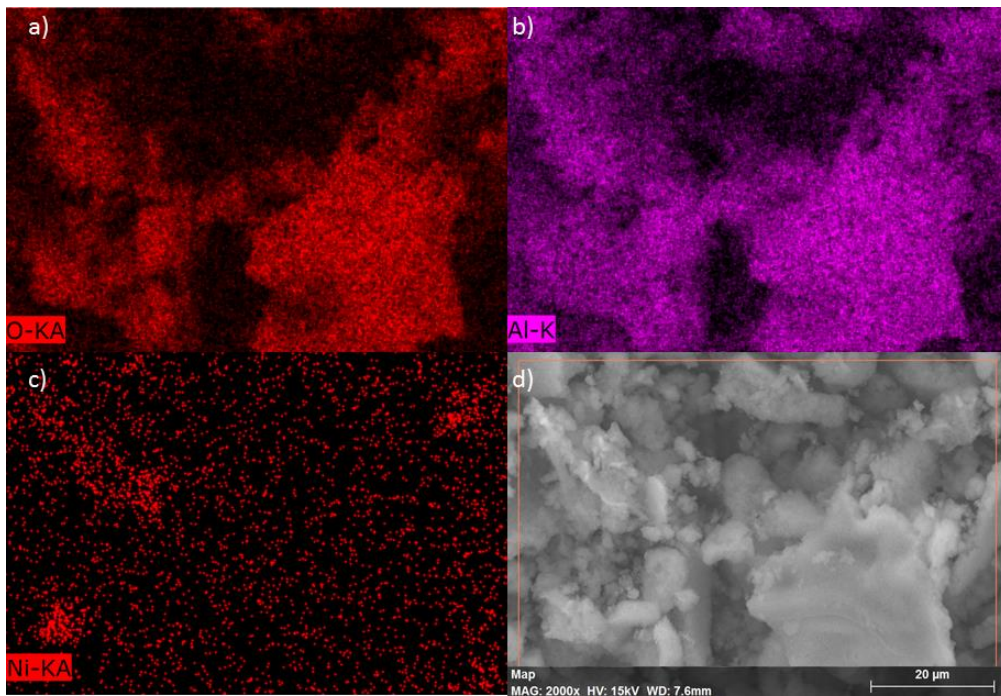


Figure 5.13. d) Representative SEM images of $\text{Ni}/\text{Al}_2\text{O}_3$ prepared by deposition-precipitation with NaOH reduced at 400°C , with EDX mapping for O, a), Al, b), and Ni, c), showing homogenous distribution of the element on the sample.

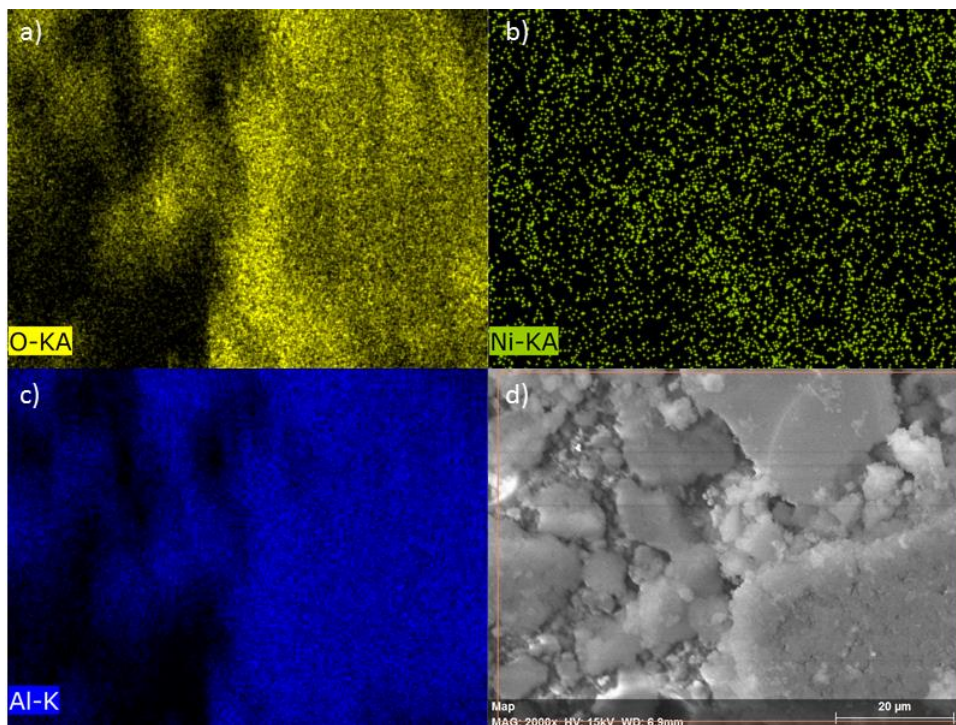


Figure 5.14. d) Representative SEM images of $\text{Ni}/\text{Al}_2\text{O}_3$ prepared by sol-immobilisation with THPC reduced at 400°C , with EDX mapping for O, a), Ni, b), and Al, c), showing homogenous distribution of the element on the sample.

Figure 5.13 and Figure 5.14 are representative images of the $\text{Ni}/\text{Al}_2\text{O}_3$ prepared by deposition-precipitation and by sol-immobilisation, respectively. The sample prepared by deposition-

precipitation presented a good distribution of Ni on the surface of the support. From the EDX mapping of the sample prepared by sol-immobilisation, it was observed that some regions showed the presence of a higher density of Ni indicating agglomeration of the Ni nanoparticles. The calculation of the Ni loading from EDX confirmed the 1 wt.% nominal loading for the deposition-precipitation sample, with a value of 1.0 ± 0.1 wt.%. The sample prepared by sol-immobilisation displayed a lower Ni loading of 0.8 wt.% with a large error margin, probably related to the uneven Ni distribution.

Table 5.3. Catalysts loading calculated by SEM-EDX analysis

Materials	Reduction temperature (°C)	Loading (wt.%)
Ni/CeO ₂ THPC 200	200	1.1 ± 0.2
Ni/CeO ₂ THPC 200	600	1.1 ± 0.2
Ni/CeO ₂ DP 400	400	2.3 ± 0.3
Ni/Al ₂ O ₃ DP 400	400	1.0 ± 0.1
Ni/Al ₂ O ₃ THPC 400	400	0.8 ± 0.5

5.3.4. X-Ray Photoelectron Spectroscopy (XPS)

To identify the oxidation state of Ni species and, therefore, help to understand which are the active species for the catalytic decomposition of hydrous hydrazine over Ni catalysts, XPS analysis was performed on the Ni/CeO₂ prepared by sol-immobilisation reduced at 400°C and 500°C. Quantification of Ni species by XPS is more difficult than in the case of Ir since Ni 2p_{3/2} displays satellite peaks that make the peaks irregular and hard to fit properly. Therefore, in order to fit the peaks, standard reference materials were recorded and used for example dry commercial NiO and hydrate NiO as references.

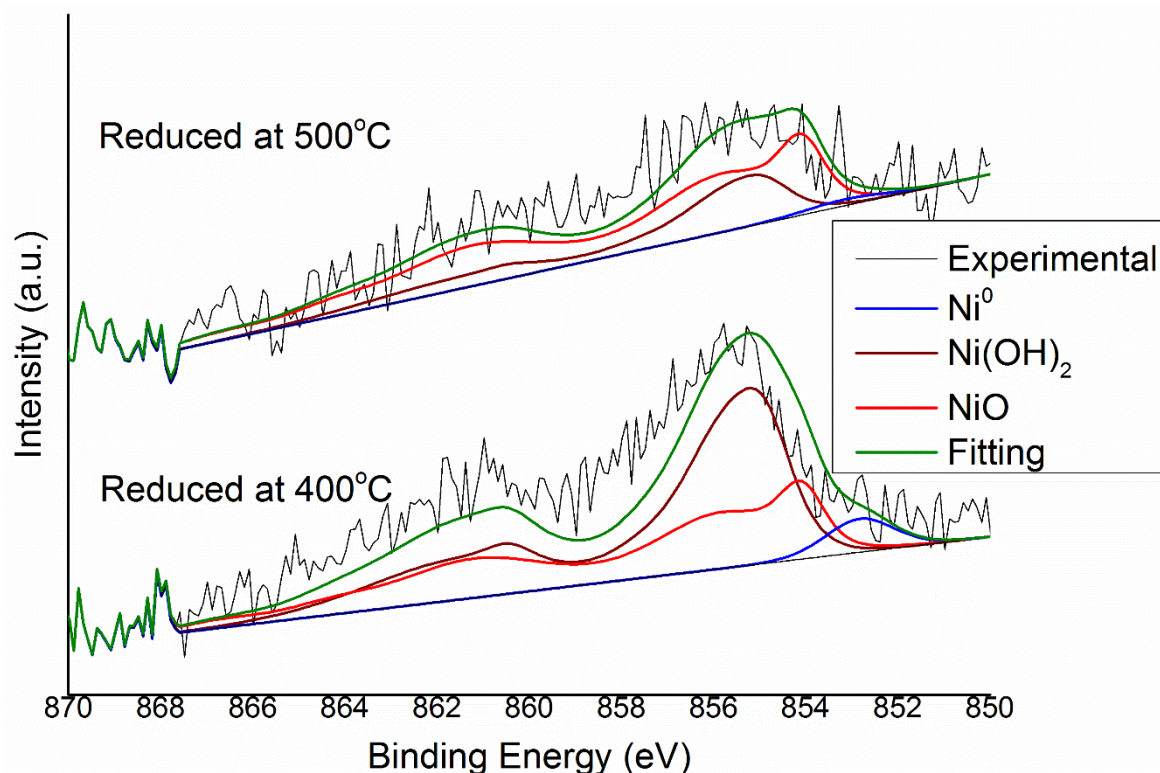


Figure 5.15. XPS spectra of the Ni $2p_{3/2}$ region for Ni/CeO₂ prepared by sol-immobilisation with THPC reduced at 400°C and 500°C.

Figure 5.15 shows that Ni/CeO₂ is composed mainly of a mixture of NiO and Ni(OH)₂, irregular and fitted with model from standard materials,¹⁷ with only 1.9% of nickel in metallic form for the sample reduced at 400 °C and 5.0% when the temperature of reduction is raised to 500 °C.¹⁸ Since the active species is metallic Ni, these analyses indicate that the active species (metallic Ni) should be formed during the reaction by direct reduction with hydrous hydrazine.

5.3.5. UV/visible spectroscopy

To monitor the formation of the Ni colloid, UV/vis spectroscopy was performed onto the solution to establish the disappearance of the peaks, at 355, 695 and 720 nm, related to the presence of NiCl₂ used as precursor.¹¹

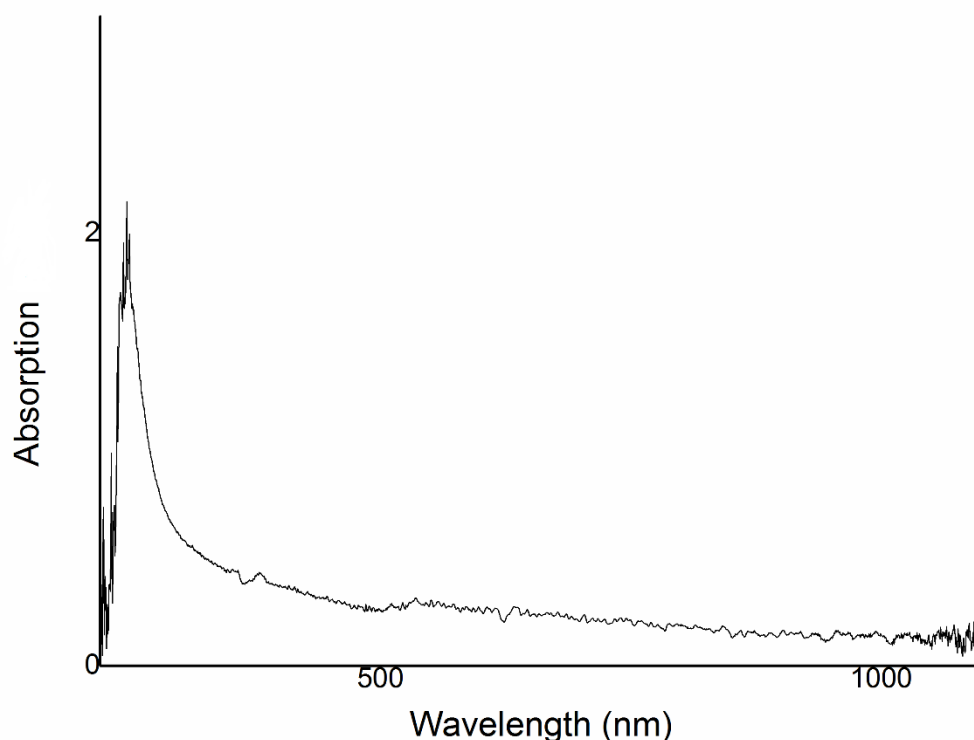


Figure 5.16. UV/vis spectrum of the Ni colloidal solution prepared with THPC method.

In Figure 5.16 displays the colloidal solution of Ni prepared with THPC method, without peaks that can be assigned to Ni^{2+} species. The spectrum is in good agreement with the calculation done by Creighton *et al.* for which colloidal solution should absorb in the UV region with a shoulder peak at 400nm, confirm the reduction of Ni.¹⁰

5.4. Conclusions

In this chapter, the catalytic performance of a series of Ni-based catalysts was investigated in order to study the liquid-phase decomposition of hydrous hydrazine using a number of different approaches. From the literature, it has been shown that iridium can be an active catalyst with a poor selectivity to the production of hydrogen, while nickel-based catalysts are reported to be less active but showing higher production of hydrogen. Therefore, the improvement in terms of catalytic activity for Ni-based catalysts is a challenging task.

To begin catalytic studies base on Ni catalysts, a 1 wt. % Ni/CeO₂ prepared by sol-immobilisation with THPC was synthesised and then it was reduced at 600°C under H₂/Ar flow as a direct comparison with similar samples of Ir/CeO₂ that have been synthesised with the same preparation method and showed high catalytic activity and yield to H₂. The material presented a final yield toward hydrogen of 60.9%, almost double of the 36.6% of the similarly

prepared Ir/CeO₂. From the yield point of view, the result is promising since the production of hydrogen significantly increased whereas the by-product, which is harmful to the fuel cell, ammonia, was reduced significantly. In terms of activity, a TOF of 4.6 h⁻¹ against 727 h⁻¹, for Ni/CeO₂ prepared by DP with NaOH and reduced at 500°C, displays an issue for a practical application in day to day life of this material since it requires large amounts of catalysts to be used and therefore complete the liquid-phase decomposition of the hydrous hydrazine in reasonable amount of time. In fact, even if the substrate/metal molar ratio was decreased from the 250 used for Ir-based catalysts to 38, the completion of reaction was over 20 hours with Ni/CeO₂, while the Ir/CeO₂ required less than one hour.

TPR analysis performed on the Ni/CeO₂ prepared by sol-immobilisation displayed how the reduction of the Ni nanoparticles occurred at a temperature between 300°C and 400°C. Therefore, the high-temperature heat treatment was varied in order to obtain information about its effect on the effective reduction of Ni nanoparticles and therefore on the catalytic performance of the reduced materials. When the Ni/CeO₂ was reduced at 200°C, below the reduction temperature indicated by the TPR analysis, the material did not display any catalytic activity for the decomposition of hydrous hydrazine in aqueous solution. The samples reduced at 400 °C and 500 °C, instead, presented similar catalytic performances, both in terms of activity, with TOF values of 4.1 and 4.4 h⁻¹ respectively, and yield, 68.8% and 68.9%, respectively. It is interesting to note that the sample reduced at 600 °C gave a yield of only 60.9%. The lower yield of the sample reduced at higher temperature may be an indication of modification of the surface (growth of Ni nanoparticles and/or encapsulation of Ni nanoparticles by the support, strong support-metal interaction) due to the heat treatment temperature effect. The XPS analysis of the samples showed that the surface of the Ni nanoparticles were re-oxidised possible after the reduction with H₂, by the O₂ in the air. However, the activity found seem to be related to the presence of metallic Ni species, which are formed by the interaction with the hydrous hydrazine during the reaction. This in situ activation of the Ni nanoparticles was also supported by the presence of an induction period of a few minutes at the beginning of the reaction, after which the gas production increased. This activation mechanism probably requires for the core of the Ni nanoparticles to still be metallic and the shell to be in oxidised form, as a possible explanation for the lack of initial activity of the sample reduced at high temperature.

The *in situ* activation of the catalysts was also further supported by the catalytic results of the Ni/CeO₂ prepared by deposition-precipitation and reduced at 400 °C. In fact, this catalyst did not produce gaseous products in the first hours of the reaction. However, after 24 hours and at the completion of the reaction with a final yield of 82%, which is higher than the value obtained with the Ni/CeO₂ prepared by sol-immobilisation. A starting point of the reaction can be extrapolated around the 13 hours from the addition of hydrous hydrazine.

To study the effect of metal-oxide supports, Al₂O₃ and MgAl₂O₄ were chosen as potential candidates and evaluated as supports for the deposition/immobilisation of Ni nanoparticles, as an alternative to the CeO₂. The materials prepared with Al₂O₃ and MgAl₂O₄ did not produce gaseous products after the addition of hydrous hydrazine to the reaction mixture. This lack of activity displayed by nickel catalysts on supports different from CeO₂ or reduced at a temperature below the reduction temperature of Ni/CeO₂ can be considered an indication that the activity is related to the interaction between metallic nickel and CeO₂. Interaction that was showed also by the Ir/CeO₂, but in the case of Ir seems to mainly lead to an increase in yield toward the production of hydrogen, while in the case of Ni it is vital for the activity of the catalysts. These conclusions agree with the results in literature where unsupported Ni nanoparticles are reported almost inactive, while CeO₂, even in traces, drastically increases the activity of nickel.^{7,19}

The characterisation of the samples showed that the reductions were performed at a temperature high enough to completely reduce the Ni nanoparticles, as observed from TPR analysis. However, these supported Ni nanoparticles are later re-oxidised, at least on the surface, by the oxygen contained in the air, as displayed by low metallic content shown at the XPS. It is well-known as well that small Ni nanoparticles have high affinity for re-oxidation. The actual loading of Ni and its even dispersion on the support surface were confirmed by the SEM-EDX analyses for most of the samples. It was not possible to obtain structural information in terms of particle size of Ni due to the poor contrast at the TEM and no detection of diffraction peaks from nickel from the XRD patterns.

5.5. References

- 1 M. Zheng, R. Cheng, X. Chen, N. Li, L. Li, X. Wang and T. Zhang, *Int. J. Hydrog. Energy*, 2005, **30**, 1081–1089.
- 2 A. K. Singh, M. Yadav, K. Aranishi and Q. Xu, *Int. J. Hydrog. Energy*, 2012, **37**, 18915–18919.
- 3 H. Wang, L. Wu, Y. Wang, X. Li and Y. Wang, *Catal. Commun.*, 2017, **100**, 33–37.
- 4 S. K. Singh, A. K. Singh, K. Aranishi and Q. Xu, *J. Am. Chem. Soc.*, 2011, **113**, 19638–19641.
- 5 H. Wang, L. Wu, A. Jia, X. Li, Z. Shi, M. Duan and Y. Wang, *Chem. Eng. J.*, 2018, **332**, 637–646.
- 6 J. Wang, X.-B. Zhang, Z.-L. Wang, L.-M. Wang and Y. Zhang, *Energy Environ. Sci.*, 2012, **5**, 6885–6888.
- 7 L. He, B. Liang, L. Li, X. Yang, Y. Huang, A. Wang, X. Wang and T. Zhang, *ACS Catal.*, 2015, **5**, 1623–1628.
- 8 J. L. Hueso, V. Sebastian, A. Mayoral, L. Uson, M. Arruebo and J. Santamaria, *RSC Adv.*, 2013, **3**, 10427–10433.
- 9 F. Porta, L. Prati, M. Rossi, S. Coluccia and G. Martra, *Catal. Today*, 2000, **61**, 165–172.
- 10 J. A. Creighton and D. G. Eadont, *J. Chem. Soc. Faraday Trans*, 1991, **87**, 3881–3891.
- 11 E. Y. Vasilyeva, V. I. Prokhorenkov, A. P. Puzyr and V. S. Bondar, *J. Biomater. Nanobiotechnol.*, 2016, **7**, 214–224.
- 12 J. Jehng and C. Chen, *Catal. Letters*, 2001, **77**, 147.
- 13 G. Ranga Rao, *Bull. Mater. Sci.*, 1999, **22**, 89–94.
- 14 Y. H. Liu, J. C. Zuo, X. F. Ren and L. Yong, *Metalurgija*, 2014, **53**, 463–465.
- 15 A. S. Lanje, S. J. Sharma and R. B. Pode, *Arch. Phys. Res.*, 2010, **1**, 49–56.
- 16 H. Yan, D. Zhang, J. Xu, Y. Lu, Y. Liu, K. Qiu, Y. Zhang and Y. Luo, *Nanoscale Res. Lett.*, 2014, **9**, 1–7.
- 17 A. Di Michele, A. Dell’Angelo, A. Tripodi, D. Motta, N. Dimitratos, E. Bahadori, F. Sanchez, I. Rossetti and G. Ramis, *Int. J. Hydrogen Energy*, 2019, **44**, 952–964.
- 18 A. Villa, C. E. Chan-Thaw, G. M. Veith, K. L. More, D. Ferri and L. Prati, *ChemCatChem*, 2011, **3**, 1612–1618.
- 19 Y. Qiu, H. Yin, H. Dai, L. Gan, H. Dai, P. Wang, A. Y. Qiu, H. Yin, H. H. Dai, L. Gan and H. H. Dai, *Chem. Eur. J.*, 2018, **24**, 4902–4908.

6. Investigation of supported bimetallic Ir-Ni nanoparticles for the catalytic decomposition of hydrous hydrazine in aqueous solution

6.1. Introduction

In Chapters 3, 4 and 5 the catalytic properties of monometallic Ir and Ni nanoparticles toward the decomposition of hydrous hydrazine solutions were presented and discussed. Ir-based catalysts have displayed higher activity while the yield of the hydrogen was low, having a maximum final yield of less than 40%. In contrast, Ni-based catalysts have displayed higher yield, with yield up to 82%, however, with low TOF, requiring almost a full day to reach full decomposition of hydrous hydrazine even using a lower substrate/metal molar ratio. These catalysts seem to be unsuitable, at this moment, for real-world applications combined with fuel cell technologies. In fact, fuel cells require a constant feed of clean hydrogen gas to function correctly. A low activity would require a large amount of catalyst utilised; this is not only an issue for the cost of the system but mainly for the volume to be allocated at the catalyst in the system. On the other hand, a catalyst that displays low yield and selectivity to hydrogen is unsuitable for the application due to the lower amount of hydrogen produced. Moreover, the decrease in yield to H₂ means an increase of the production of ammonia as a side product and this is detrimental for the stability of the fuel cell itself.

Therefore, the final goal of the project is to find a catalytic material capable to convert the hydrous hydrazine to hydrogen and nitrogen, with the highest possible yield and with the lower amount of catalyst possible. In literature, a suggested solution for this issue is the combination of heavier metals, such as Ir and Rh, and first row transitional metals, such as Ni, Cu, and Fe. As a consequence, the studies discussed so far on supported monometallic Ir and

Ni nanoparticles, it was decided to investigate the catalytic performance of supported bimetallic Ir-Ni nanoparticles.

The synthesis and usage of supported bimetallic nanoparticles as potential catalysts adds to the usual challenges of optimising the structure of nanoparticles, such as (I) controlling the mean particle size of the bimetallic nanoparticles, (II) tuning the morphology of the particles (alloy versus core-shell structures) and (III) maintaining high accessibility to them (effect of ligand, choice of support). One of the most important challenges is the control of the surface composition of the bimetallic nanoparticles. In fact, by changing the synthesis method for the synthesis of nanoparticles, such as, the choice of reducing agent, order of addition of the metal precursor, amount of metal precursor, choice of ligand can affect the nucleation, growth of nanoparticles and the ratio of the two metals in every step of the synthesis.^{1,2} Moreover, bimetallic nanoparticles differ from each other for the way the atoms of different metals are arranged in the individual nanoparticles, from mixed alloys to core-shell structures and adjacent clusters, as it is shown in Figure 6.1.

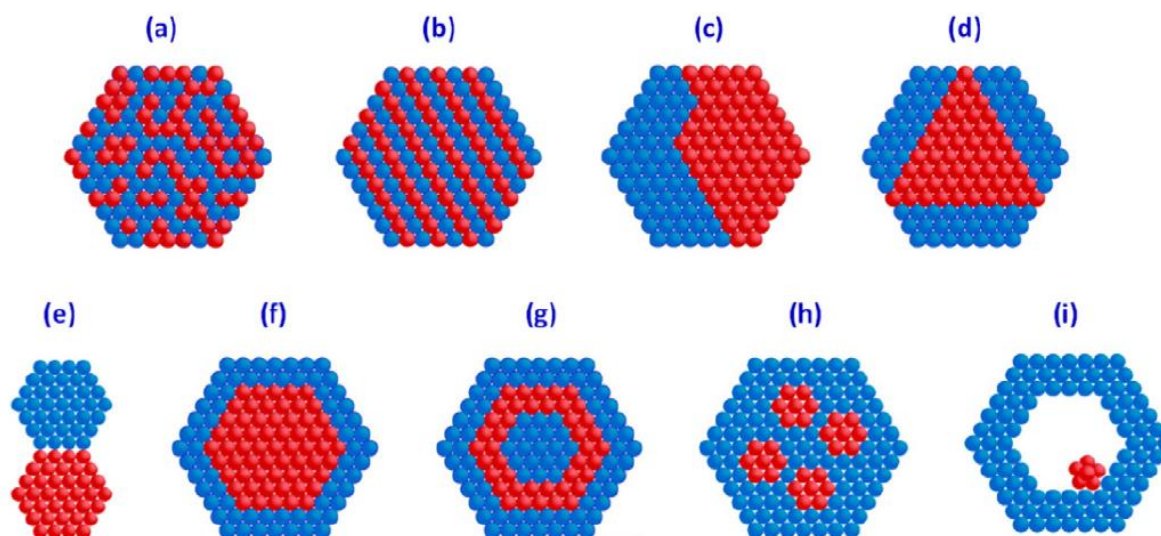


Figure 6.1. Structures of bimetallic nanoparticles: (a) mixed alloys; (b) random alloys; (c) subclusters with two interfaces (d) subclusters with three interfaces; (e) subclusters with small number of A–B bonds; (f) core-shell nanoparticles; (g) multishell core-shell nanoparticles; (h) multiple small core material coated by single shell material, (i) movable core within hollow shell material.¹

For these reasons, studies on bimetallic nanoparticles tend to be more complicated due to the increased number of variables that can affect the final catalytic performance of the material. In addition, the identification of the actual mechanism of reaction is more difficult to be predicted, due to the variety of surfaces possible on the nanoparticles. Nevertheless,

bimetallic nanoparticles have shown promising catalytic results in a range of catalytic applications, in terms of activity, yield, selectivity to desired products and finally stability due to intimate interaction between the metals.²⁻⁶ Similarly, in the case of catalytic decomposition of hydrous hydrazine, this phenomenon is reported.⁷⁻¹¹ A series of characterisation methods, such as XPS and TEM, have been used and described in this chapter to study the morphology of the synthesised supported bimetallic catalysts, in terms of particle size of the bimetallic nanoparticles, oxidation state and the chemical species on the surface.

6.2. Results and discussion

In this Chapter, the studies on supported bimetallic Ir-Ni nanoparticles were performed using the same preparation method, sol-immobilisation with THPC, in order to reduce the variables of the following studies. The Ir-Ni nanoparticles were synthesised varying the atomic ratio between the two metals and varying the time of addition of the metal precursor during the synthesis. The reactions have been performed following the procedure detailed in Chapter 2, Section 2.3. .

6.2.1. Initial tests on IrNi/CeO₂ prepared by sol-immobilisation with THPC

As it was previously discussed, it was decided to test supported Ir-Ni bimetallic nanoparticles with different Ir:Ni atomic ratio for the catalytic decomposition of hydrous hydrazine. Therefore, an Ir-Ni/CeO₂ was prepared by sol-immobilisation with THPC, using the amount of precursor calculated to obtain 0.5 wt.% loading for each of the metal the atomic ratio between Ni and Ir is 3.27, therefore the sample will be referred to as Ir₁Ni_{3.3}/CeO₂ hereafter. The Ir-Ni/CeO₂ was then reduced at 600°C under H₂/Ar flow like in the case of Ir/CeO₂ catalysts tested previously and reported in chapters 4 and 5.

The first step was to determine the reproducibility of the catalytic system and obtain an initial evaluation of the possible catalytic performances of bimetallic Ir-Ni catalysts. The amount of catalyst used in the reactions was calculated in order to have a substrate/metal molar ratio of 250, similar to the tests performed on monometallic Ir catalysts after the optimisation tests. Since Ni has an atomic weight lower than Ir using any bimetallic catalyst with the same weight loading in the same conditions would require a lower mass of catalyst. For this reason

and for the fact that the support is used, the optimised reaction conditions found for Ir/CeO₂, in Chapter 3, are considered to be valid also for the Ir-Ni/CeO₂, since the mass of catalyst used was in the range of the kinetic regime for the reaction, at 50°C, 1050 rpm of stirring and using 0.5 M NaOH solution. At the end of the reaction, colourimetric analyses were performed to confirm the complete catalytic decomposition of hydrous hydrazine.

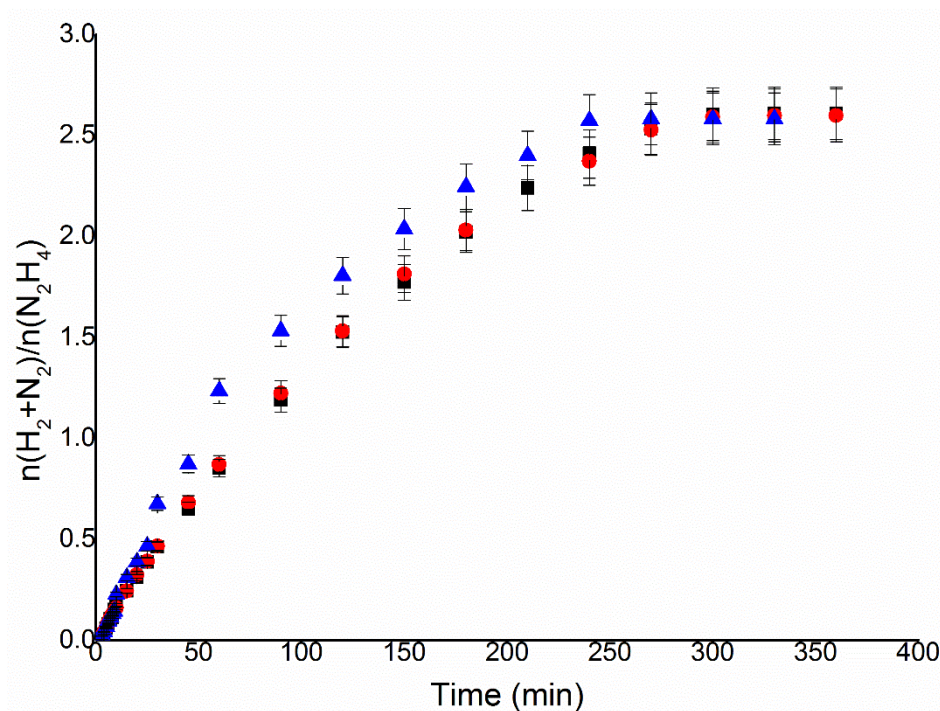


Figure 6.2. $n(\text{H}_2+\text{N}_2)/n(\text{N}_2\text{H}_4)$ versus time for hydrous hydrazine decomposition over Ir₁Ni_{3.3}/CeO₂ prepared by sol-immobilisation with THPC reduced at 600°C using 0.3 mL of 3.3 M hydrazine monohydrate in 8 mL of 0.5 M NaOH solution, at 50°C, 1050 rpm of stirring rate and 250:1 substrate/metal molar ratio.

In Figure 6.2 the yield of gaseous products for three tests performed with Ir₁Ni_{3.3}/CeO₂_{THPC} at 50°C is reported. As can be seen, the reaction is reproducible and the differences among the tests are inside the margin of error of the analysis, below 1% error on the value of final yield to hydrogen. The final yield toward molecular hydrogen observed for Ir₁Ni_{3.3}/CeO₂ in the tests was 84.8% with a TOF of 77 h⁻¹. Comparing the activity of Ir₁Ni_{3.3}/CeO₂_{THPC} with the results of the analogue monometallic catalysts, (Ir/CeO₂ and Ni/CeO₂ prepared by sol-immobilisation with THPC reduced at 600°C), the bimetallic catalyst showed higher final yield to H₂, with respect to Ir and Ni monometallic catalysts, 36.6% and 60.9% respectively. The activity was lower than in the case of Ir, 727 h⁻¹, but it was higher than Ni, 4.6 h⁻¹. These results were promising for the use of supported bimetallic nanoparticles as potential catalysts since it has been improved the low activity of Ni-based catalysts, even if it did not match the activity of

monometallic Ir, and overpassed the best performances from any monometallic catalysts prepared by sol-immobilisation method in this project.

6.2.2. Effect of the Ir:Ni ratio in the synthesis of nanoparticles

Once it was established, that supported bimetallic Ir-Ni nanoparticles are suitable for the catalytic decomposition of hydrous hydrazine, the preparation method has been investigated in order to obtain information for the intelligent design of future materials. Firstly, it was decided to vary the atomic ratio between the two metals maintaining the weight nominal loading of the total active metal on the surface. A series of 1 wt. % IrNi/CeO₂ were prepared, with Ir:Ni atomic ratio of 9:1, 3:1, 1:1 and 1:9, in addition to the already mentioned 1:3.3. To prepare these catalysts the amount of precursor solution used for the synthesis was varied in accordance with the calculation for the desired 1 wt. % nominal loading and the atomic ratio between the two metals. At the same time the amount of reducing agent, THPC, used was adapted to maintain the same total metal:THPC molar ratio. While the volume of the solution of NaOH was adjusted to 1.5 times the volume of THPC used.

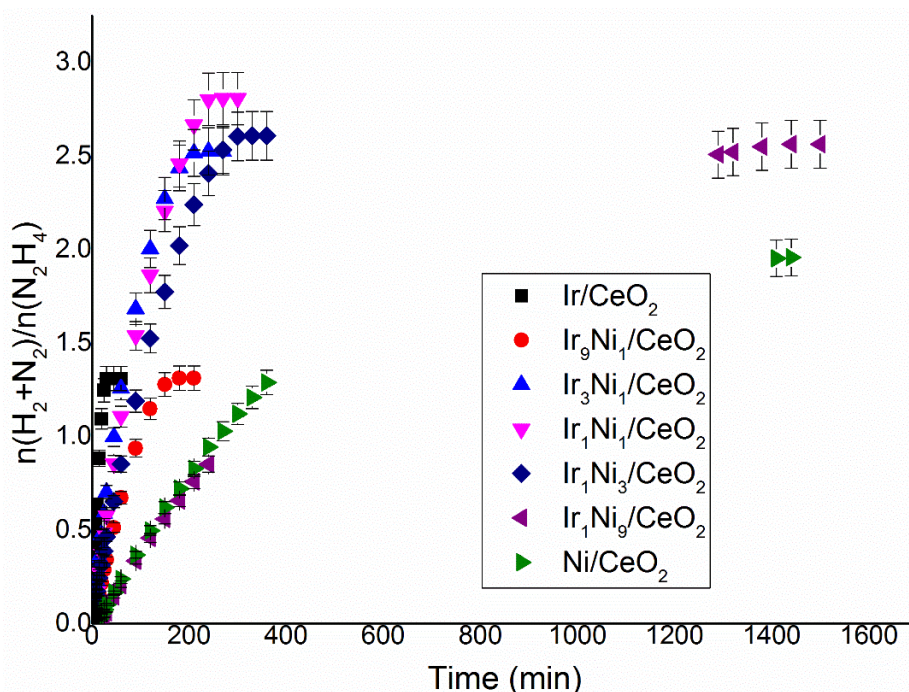


Figure 6.3. $n(\text{H}_2+\text{N}_2)/n(\text{N}_2\text{H}_4)$ versus time for hydrous hydrazine decomposition over $\text{Ir}_x\text{Ni}_y/\text{CeO}_2$ prepared by sol-immobilisation with THPC reduced at 600°C with different Ir:Ni atomic ratios using 0.3 mL of 3.3 M hydrazine monohydrate in 8 mL of 0.5 M NaOH solution, at 50°C, 1050 rpm of stirring rate and 250:1 substrate/metal molar ratio (with the exception of Ni/CeO₂ where the substrate/metal molar ratio used was 38). Displaying the higher yield displayed by Ir₁Ni₁/CeO₂.

Figure 6.3 exhibits the production of gases during the reaction of the various $\text{Ir}_x\text{Ni}_y/\text{CeO}_2$ prepared by sol-immobilisation with THPC reduced at 600°C under H_2/Ar flow. From the values of the final yield to hydrogen and the $\text{TOF}_{50\%}$, reported in Table 6.1, it can be seen that the trend of the final yield to hydrogen follows a bell shape trend with maximum, among over data, at an atomic ratio of 1 to 1 of the two metals used. On the other hand, the TOF values decrease with the decreasing content of Ir in the nanoparticles. Therefore, it seems that where selectivity/yield of the reaction, a key feature of Ni-based catalysts, benefits from the interaction of the two metals the higher activity is the only prerogative of Ir and there is no significant gain from this point of view in the use of bimetallic catalysts.

Table 6.1. Yield to molecular hydrogen and TOF values for different $\text{Ir}_x\text{Ni}_y/\text{CeO}_2$ prepared by sol-immobilisation with THPC reduced at 600 °C, using a substrate/metal molar ratio of 250. *Substrate/metal molar ratio of 38.

Catalyst	Ir:Ni molar ratio	Yield to H_2 (%)	$\text{TOF}_{50\%}$ (h^{-1})
Ir/CeO_2 THPC 600 6h	Only Ir	36.6	727
$\text{Ir}_9\text{Ni}_1/\text{CeO}_2$ THPC 600 6h	9:1	36.7	126
$\text{Ir}_3\text{Ni}_1/\text{CeO}_2$ THPC 600 6h	3:1	81.8	109
$\text{Ir}_1\text{Ni}_1/\text{CeO}_2$ THPC 600 6h	1:1	92.8	90
$\text{Ir}_1\text{Ni}_{3.3}/\text{CeO}_2$ THPC 600 6h	1:3.3	84.8	77
$\text{Ir}_1\text{Ni}_9/\text{CeO}_2$ THPC 600 6h	1:9	83.6	20
Ni/CeO_2 THPC 600 6h	Only Ni	60.9	4.6

These considerations are done based on the atomic nominal ratio between the two metals used during the preparation of the bimetallic nanoparticles. In reality, a small percentage of the metal (surface of the metal) can be active in the reaction. Therefore, better understand the structural differences among the catalysts the surface of the metal nanoparticles was studied using XPS analysis, as reported in Section 6.3.4. of this chapter.

6.2.3. Modifications of the catalyst preparation protocol

After the identification of the most efficient atomic ratio between Ir and Ni, it was decided to further modify the catalyst to understand how the structure of the synthesised supported bimetallic nanoparticles can affect the catalytic performances. The catalysts reported in this chapter till now are prepared by sol-immobilisation with THPC and the addition of the metal

precursors was carried out by using an aqueous solution containing both the metal precursors. In this way, the addition of the metal was simultaneous, if the two metals are capable to produce alloys, can produce a random mixed or ordered alloys, or in alternative sub-clusters aggregates and core-shell structures if the reduction rate of the two metal is significant differences. From TEM-EDX analyses, Section 6.3.3., on both colloidal Ir-Ni solution and supported Ir-Ni nanoparticles suggest that the nanoparticles formed are for the most cases, random alloys. Another experimental procedure was used, by modifying the previous one for synthesising core-shell structures. In the modified experimental procedure, the Ni precursor was added only at the beginning with part of the reducing agent, forming a Ni colloid. Then the Ir precursor and the rest of the reducing agent were added to the solution to finally form the bimetallic Ir-Ni nanoparticles. In this way, Ni preformed colloidal nanoparticles should be formed and when the Ir metal precursor with the reducing agent is added should start to reduce on the surface of the Ni nanoparticles. In this way, the second metal added can cover partially or completely the core Ni nanoparticles, creating a core-shell structure. To conclude the studies, an additional experimental procedure was used. Preformed Ni colloid was immobilised on cerium oxide. The synthesised Ni/CeO₂ was then dried and used as support for the immobilisation of the Ir nanoparticles prepared in a different colloidal solution. This method should allow immobilising separated nanoparticles on the surface or on the surface of the preformed nanoparticles, that with the heat treatment can form alloy or core-shell. These three methods should allow to investigate if the increase in catalytic performance are related to a two sites mechanisms, in which the hydrazine reacts on neighbour Ir and Ni atoms (most likely on alloys), or to change in electronic properties of a metal induced by the other (on core-shell and sub-cluster) or the independent activity of the two metals (co-immobilised segregated nanoparticles).

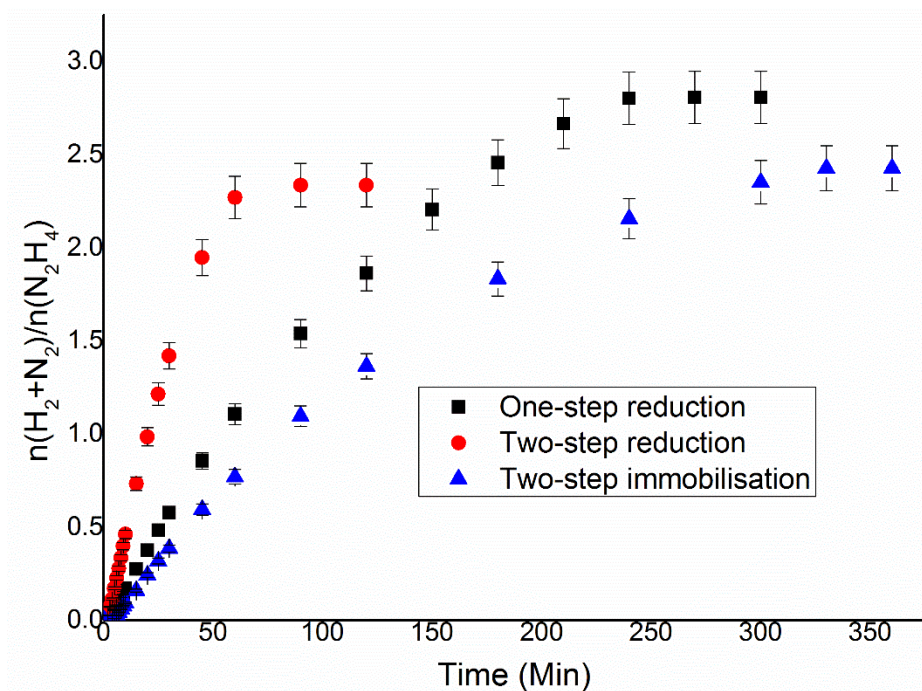


Figure 6.4. $n(\text{H}_2+\text{N}_2)/n(\text{N}_2\text{H}_4)$ versus time for hydrous hydrazine decomposition over $\text{Ir}_1\text{Ni}_1/\text{CeO}_2$ prepared by sol-immobilisation with THPC reduced at 600°C with different synthesis procedures using 0.3 mL of 3.3 M hydrazine monohydrate in 8 mL of 0.5 M NaOH solution, at 50°C , 1050 rpm of stirring rate and 250:1 substrate/metal molar ratio.

In Figure 6.4 are represented the reactions of the $\text{Ir}_1\text{Ni}_1/\text{CeO}_2$ prepared by sol-immobilisation with THPC by standard procedure, by two-step reduction and two-step immobilisation,. As can be seen, the catalyst prepared by the standard method still presents the highest yield between the catalysts tested, with the other modified procedure catalysts displaying only 75.1% for two-step reduction and 78.5% for the two-step immobilisation sample, Table 6.2. Considering the activity, the catalyst prepared by two-step reduction present the highest activity on the range of monometallic Ir/CeO_2 , 307 h^{-1} , this may be due to the fact that the surface of the particles is supposed to be pure Ir while the yield is enhanced by the influence of Ni in contact with Ir.

Table 6.2. Yield to molecular hydrogen and TOF values for different $\text{Ir}_1\text{Ni}_1/\text{CeO}_2$ prepared by sol-immobilisation with THPC reduced at 600°C , using a substrate/metal molar ratio of 250.

Catalyst	Method	Selectivity to H_2 (%)	TOF _{50%} (h^{-1})
$\text{Ir}_1\text{Ni}_1/\text{CeO}_2$ 600h	Standard	92.8	90
$\text{Ir}_1\text{Ni}_1/\text{CeO}_2$ 600h TSR	Two-step reduction	75.1	307
$\text{Ir}_1\text{Ni}_1/\text{CeO}_2$ 600h TSI	Two-step immobilisation	78.5	69

6.2.4. Effect of the reaction temperature

$\text{Ir}_1\text{Ni}_1/\text{CeO}_2$ was used as standard material for the study of the effect reaction temperature on the catalytic performances of bimetallic IrNi catalysts due to its higher final yield to molecular hydrogen.

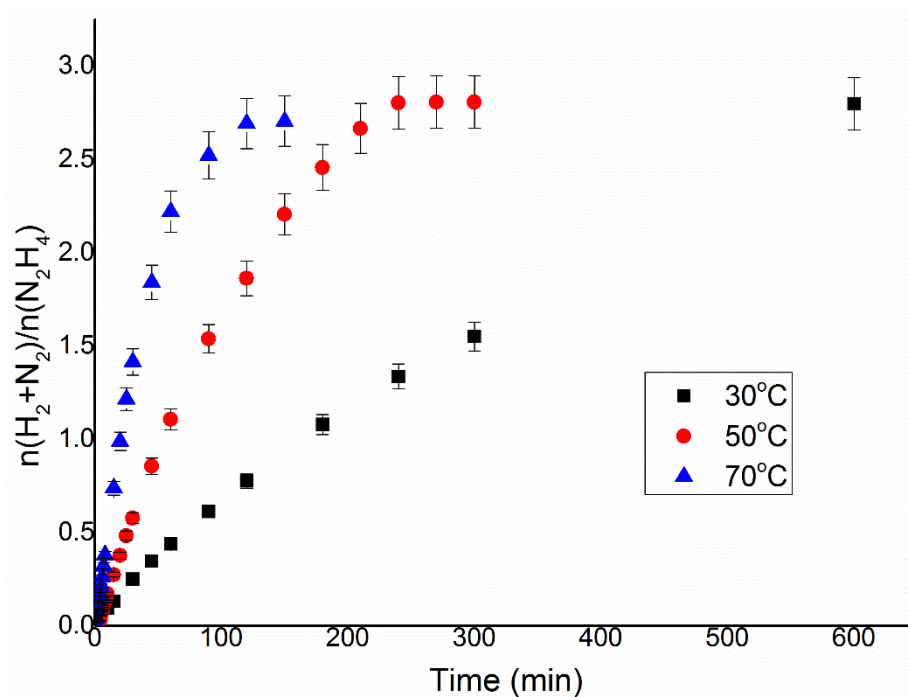


Figure 6.5. $n(\text{H}_2+\text{N}_2)/n(\text{N}_2\text{H}_4)$ versus time for hydrous hydrazine decomposition over $\text{Ir}_1\text{Ni}_1/\text{CeO}_2$ prepared by sol-immobilisation with THPC reduced at 600°C using 0.3 mL of 3.3 M hydrazine monohydrate in 8 mL of 0.5 M NaOH solution, at 30°C , 50°C and 70°C , 1050 rpm of stirring rate and $250:1$ substrate/metal molar ratio.

Figure 6.5 shows the evolution of gaseous products over time at different reaction temperatures. As expected, the activity measured by the TOF value increases with the increase of the temperature, from 29 h^{-1} to 257 h^{-1} in the range from 30°C to 70°C . More interesting is the trend displayed by the selectivity of the reaction. The previous tests performed on the influence of the reaction temperature on the decomposition of hydrous hydrazine using monometallic Ir or Ni catalysts have displayed a decrease in final yield to hydrogen with the increase of the reaction temperature. In the case of bimetallic $\text{Ir}_1\text{Ni}_1/\text{CeO}_2$, if the final yield diminishes to 88.9% when the reaction is performed at 70°C , the yield slightly increases between 30°C , 92.3% , and 50°C , 92.8% . However, this apparent increase in the final yield is well-within the experimental errors, therefore, it is not possible to add further considerations on the difference of the catalytic proprieties between 30°C and 50°C for this material.

6.2.5. Preliminary reusability tests

Another key parameter to control during the investigation for possible application of a catalyst for hydrous hydrazine decomposition is catalyst stability since a crucial requirement for the catalyst application is the ability to be active for a long time after the deployment. To test the stability of $\text{Ir}_1\text{Ni}_1/\text{CeO}_2$ during the hydrous hydrazine decomposition reaction, the catalyst was tested in a series of consecutive reactions. $\text{Ir}_1\text{Ni}_1/\text{CeO}_2_{600}$ was chosen since it is the Ir-Ni/CeO₂ catalysts among the ones synthesised to the best catalytic performance. The reusability tests were performed following the same experimental procedure of the standard batch reaction with the addition of fresh hydrous hydrazine solution when the gas evolution was completed.

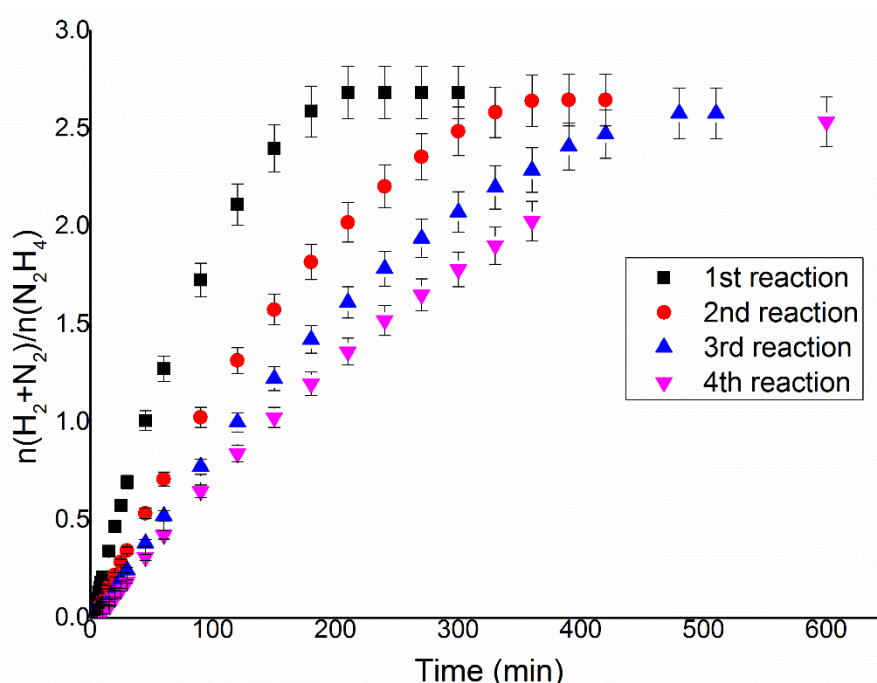


Figure 6.6. $n(\text{H}_2+\text{N}_2)/n(\text{N}_2\text{H}_4)$ versus time for hydrous hydrazine decomposition over $\text{Ir}_1\text{Ni}_1/\text{CeO}_2$ prepared by sol-immobilisation with THPC reduced at 600°C reused by using fresh 0.3 mL of 3.3 M hydrazine monohydrate in 8 mL of 0.5 M NaOH solution to start a new reaction, at 50°C, 1050 rpm of stirring rate and 250:1 substrate/metal molar ratio.

In Figure 6.6 the gas products evolution versus reaction time for the four consecutive reactions performed using $\text{Ir}_1\text{Ni}_1/\text{CeO}_2$ as the reference catalyst are reported. The final yield slowly decreased from 88.1% to 82.6%, while the activity followed a more drastic decrease during the reusability tests, from 117 h⁻¹ to 38 h⁻¹, as shown in Figure 6.7. Only four consecutive reactions were performed, due to the reaction time required to reach full catalytic decomposition at the fourth reaction. Further reactions would have required

modification to the reaction procedure in order to be reproducible and the data to be compared properly. In fact, the main issue displayed by these first preliminary reusability tests is the rapid decline in activity which would not allow the continued use of this catalyst without a reactivation process between the usages.

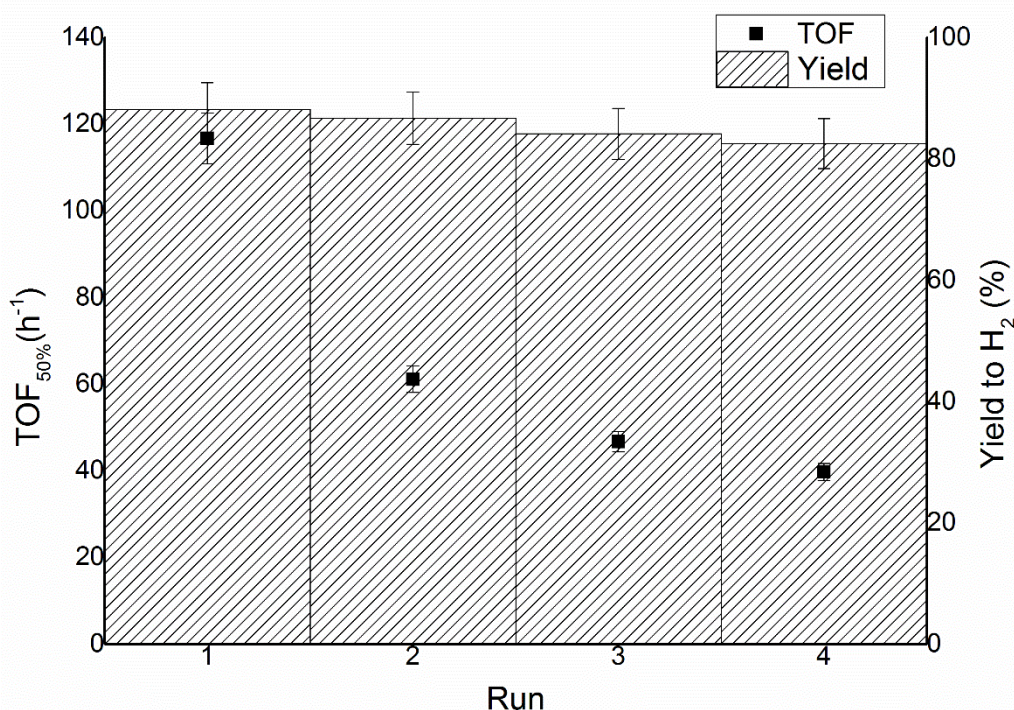


Figure 6.7. TOF_{50%} and final yield toward molecular hydrogen for over consecutive hydrous hydrazine decomposition reactions by Ir₁Ni₁/CeO₂ prepared by sol-immobilisation with THPC.

The final yield of the fresh using Ir₁Ni₁/CeO₂_{THPC} in this reproducibility test is lower than the data reported for the reaction performed with the same catalyst reported in the previous sections of this chapter, 92.8%, and a higher activity compared to the same reaction, 90 h⁻¹. This change in catalytic performances can be explained by the fact that the between the first reactions and the reproducibility test the catalyst was store at room temperature in a desiccator, so the surface of the catalyst may be modified by the action of O₂ from the air. Therefore, both the decrease in activity showed during this preliminary reusability tests and the change in performance when stored in air for a long period of time indicate instability of the nanoparticles structure that needs to be improved before any actual application is feasible.

6.3. Characterisation of the catalysts

As it was discussed in Chapter 6.2, in the case of bimetallic nanoparticles characterisations are of particular importance to determine the exact nature of the active surface onto which the reaction take place. For this reason, various characterisations have been performed on the bimetallic catalysts in order to determine (I) mean particles size, (II) superficial species and oxidation state, (III) metal loading and (IV) crystallinity.

6.3.1. Powder X-ray Diffraction (p-XRD)

$\text{Ir}_1\text{Ni}_3/\text{CeO}_2$ was analysed by p-XRD to study the crystallite size and possibly the metal species. In order to do so, CeO_2 was previously characterised to obtain the X-ray pattern of the support material. Cerium oxide is characterised by peak related to (111), (200), (220) and (311) planes at $2\theta = 29.3^\circ$, 33.1° , 47.5° and 57.6° , respectively. $\text{Ir}_1\text{Ni}_3/\text{CeO}_2$ has two active metals and the main possible species that can be found are Ni metallic, which has diffraction of (111), (200) and (220) planes at $2\theta = 44.5^\circ$, 51.9° and 76.4° ,¹² NiO, which has the diffraction of (111), (200), and (220) at $2\theta = 37.2^\circ$, 43.2° , and 62.8° ,¹³ Ir, which has diffraction of (111), (200), (220) and (311) planes at $2\theta = 40.8^\circ$, 47.2° , 69.1° and 83.6° ,¹⁴ and IrO_2 , which has diffraction of (110), (101), (200) and (211) planes at $2\theta = 28.1^\circ$, 35.0° , 39.8° and 55.3° .¹⁵

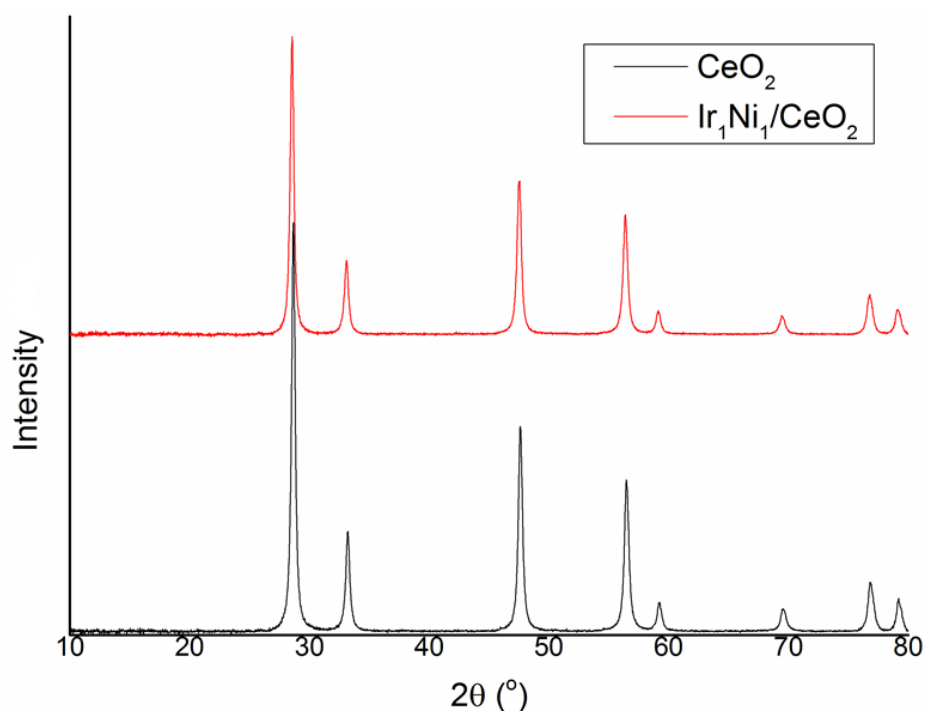


Figure 6.8. XRD pattern for $\text{Ir}_1\text{Ni}_1/\text{CeO}_2$ prepared by sol-immobilisation with THPC and CeO_2 . The patterns do not exhibit differences between the catalysts and the bare support.

Figure 6.8 displays, as was it was shown for the case for Ir/CeO₂ and Ni/CeO₂ prepared by sol-immobilisation, the absence of diffraction peaks that can be associated with iridium or nickel species and the diffraction peaks can be assigned to CeO₂. This absence can be explained with the presence of small particle size which broadens the diffraction peaks until the point that the diffraction peaks are not distinguishable from the background of the analysis. These results have been confirmed by TEM images reported later in the chapter, Section 6.3.3. . Therefore, additional characterisation techniques are necessary to determine accurate particle size and species presents on the surface of the bimetallic catalysts, such as TEM or XPS.

6.3.2. Scanning Electron Microscopy (SEM) and Energy Disperse X-ray Spectroscopy (EDS)

To control the effectiveness of the synthesis of the catalysts and the morphology of the samples, SEM-EDS analyses were performed.

Table 6.3. Iridium and nickel metal loading calculated by SEM-EDS for different 1 wt. % Ir_xNi_y/CeO₂.

Catalysts	Nominal ratio (Ir:Ni)	Preparation procedure	Ir loading (wt.%)	Ni loading (wt.%)	Calculated ratio (Ir:Ni)
Ir ₁ Ni _{3.3} /CeO _{2 600}	1:3.3	One-step reduction	0.55	0.53	1:3.13
Ir ₁ Ni ₁ /CeO _{2 600}	1:1	One-step reduction	0.63	0.23	1:1.18
Ir ₁ Ni ₉ /CeO _{2 600}	1:9	One-step reduction	0.26	0.90	1:11.7
Ir ₁ Ni ₁ /CeO _{2 600} TSR	1:1	Two-step reduction	0.81	0.23	1:0.92
Ir ₁ Ni ₁ /CeO _{2 600} TSI	1:1	Two-step immobilisation	0.73	0.24	1:1.10

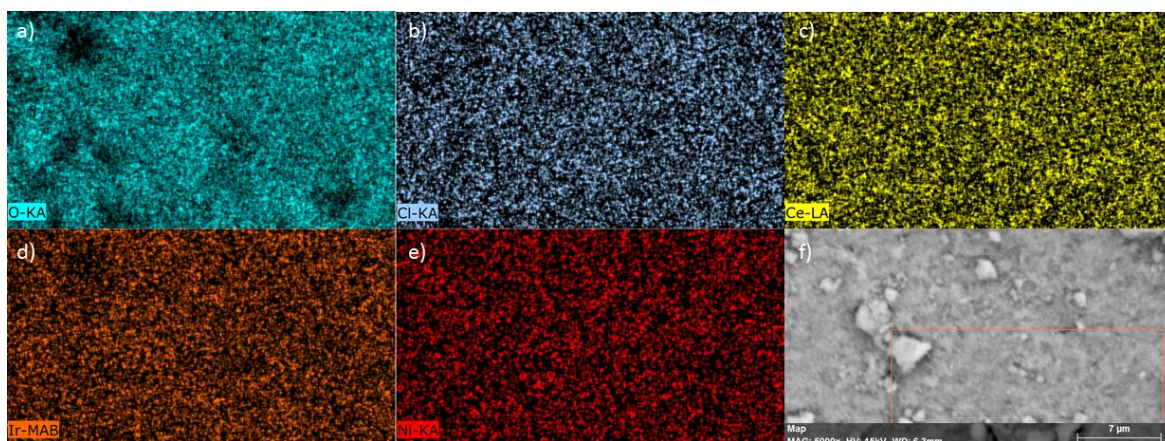


Figure 6.9. Representative SEM images, *f*, with EDX mapping of $\text{Ir}_1\text{Ni}_{3.3}/\text{CeO}_2$ 600 sample for different elements such as O, *a*, Cl, *b*, Ce, *c*, Ir, *d*, and Ni, *e*.

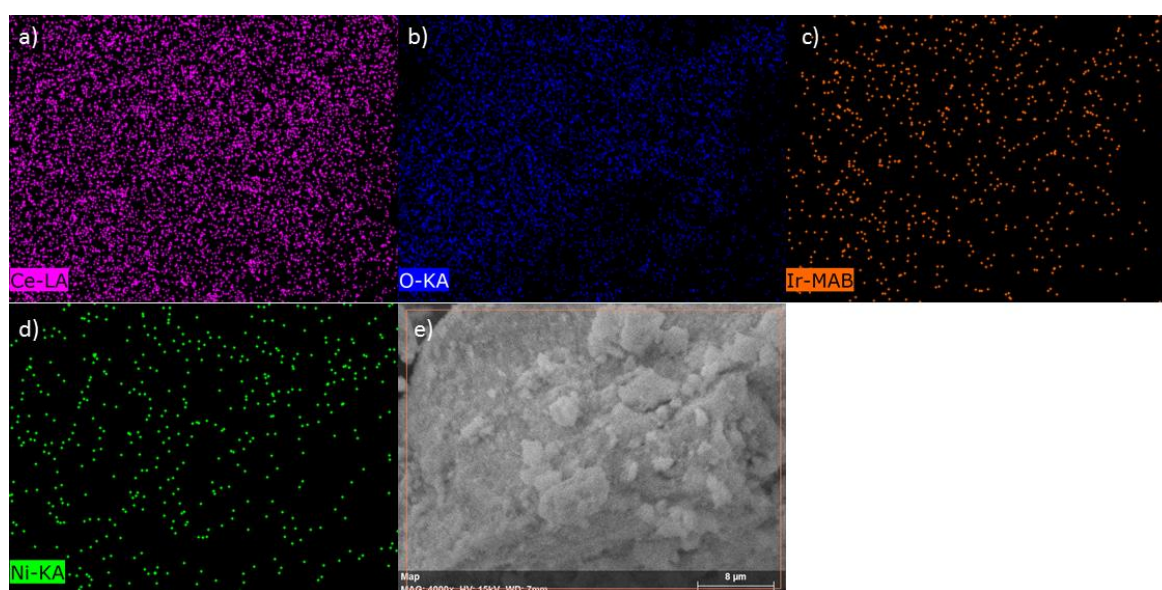


Figure 6.10. Representative SEM images, *e*, with EDX mapping of $\text{Ir}_1\text{Ni}_1/\text{CeO}_2$ 600 sample for different elements such as O, *a*, Ce, *b*, Ir, *c*, and Ni, *d*.

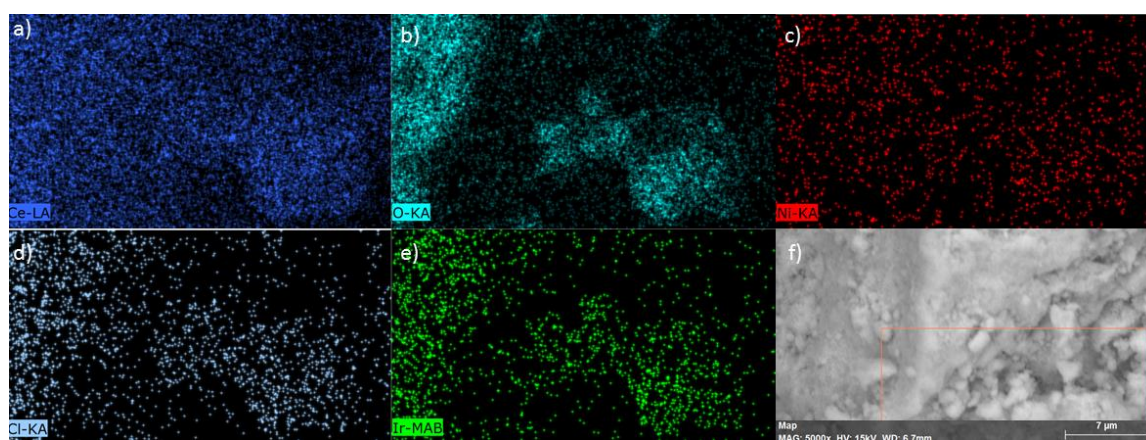


Figure 6.11. Representative SEM images, *f*, with EDX mapping of $\text{Ir}_1\text{Ni}_9/\text{CeO}_2$ 600 sample for different elements such as Ce, *a*, O, *b*, Ni, *c*, Cl, *d*, and Ir, *e*.

Figures 6.9 – 6.11 illustrate representative SEM images of selected catalysts with different Ir/Ni atomic ratio presented in this chapter. The SEM images display that the bimetallic nanoparticles are well dispersed on the surface of the support. As it can be noticed from Table 6.3, the total metal loading in wt.% varies from 0.9 to 1.2%. This large margin of error is due to the low values of individual metal loadings. In fact, for low wt.% SEM-EDX analyses suffer from a high signal/noise ratio that results in a higher error margin for the analysis itself, ICP-MS on digested catalysts can decrease the margin of uncertainty. The molar ratios calculated from the SEM-EDX quantification for these samples agree, within the margin of error, with the nominal value calculated from the masses of metal precursor salts used during the synthesis of the catalysts, as it is shown in Table 6.3.

6.3.3. Transmission Electron Microscopy (TEM) and Energy Disperse X-ray Spectroscopy (EDS)

The aforementioned characterisations gave little information about the nature of the individual bimetallic nanoparticles. In order to obtain a deeper insight of these materials, HAADF-STEM-EDS analyses were performed on colloidal and supported on cerium oxide Ir₁Ni₃ nanoparticles.

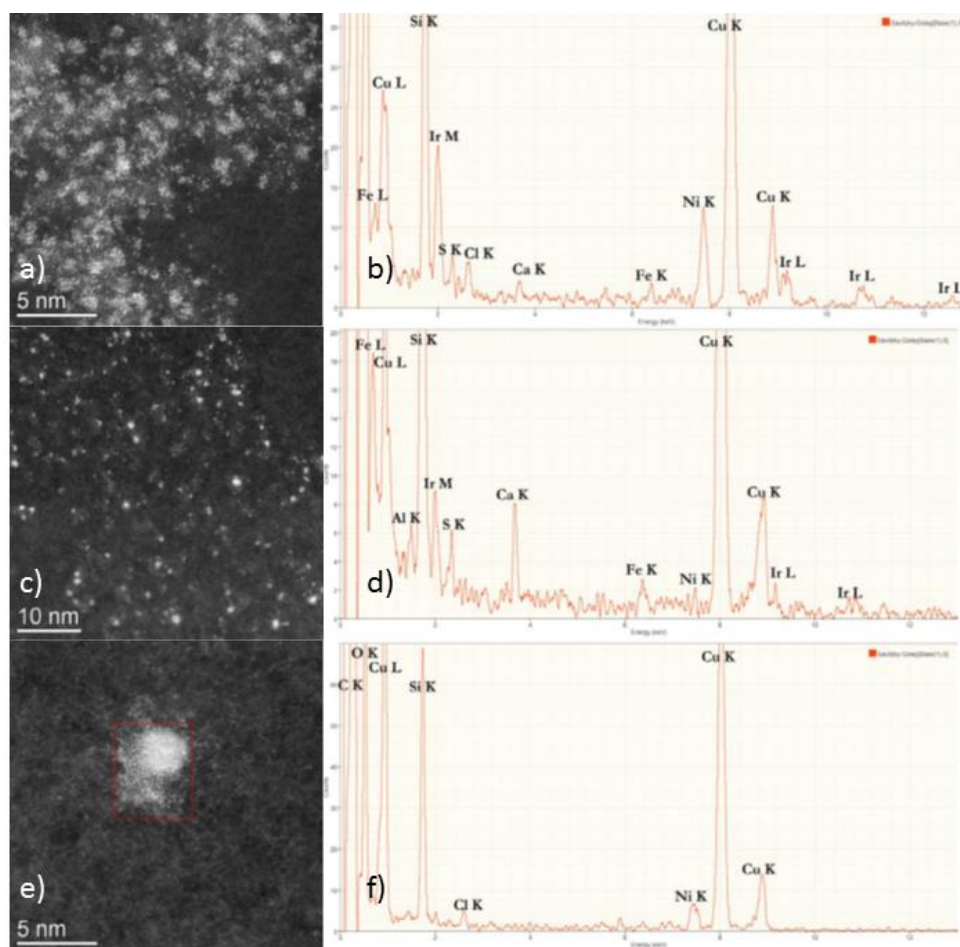


Figure 6.12. a), c) and e) HRTEM images of Ir_1Ni_3 colloidal solution, and respectively EDS analyses b), d) and f). Showing different composition for particles of different size.

In collaboration with the group of Prof. Kiely at Lehigh University, HAADF-STEM images of an Ir_1Ni_3 colloidal solution have been recorded. It was decided to perform the HAADF-STEM on the colloidal Ir-Ni solution because of the poor contrast of the support nanoparticles on the support. Ce, with an atomic number of 58, is a heavier element than Ni, atomic number 28, and, therefore, it interacts more than Ni with the electron beam used to record the images. This lower interaction with the electron beam by the Ni atoms results in poor contrast of this metal when deposited on cerium oxide, especially if the dimensions of particles are small (shorter optical pathway). In the case of iridium, that is heavier than cerium, the main cause of the poor contrast are the small mean particle size, that giving a shorter pathway for the transmission of the electron beam and resulting in lowering the chances to sufficient interaction between the beam itself and the atoms of the Ir nanoparticles. Therefore, in order to gain data on the bimetallic nanoparticles and knowing the possibility of formation of monometallic particles during the synthesis of the bimetallic colloids, some preliminary tests

with TEM were performed on the colloidal bimetallic solution. Figures 6.12 a) and 6.12 b) show that the majority of the nanoparticles are sub-2 nm nanoparticles. EDX analysis of individual nanoparticles confirmed the presence of both metals used in the synthesis. However, smaller bimetallic nanoparticles, as shown in Figures 6.12 c) and 6.12 d), seems to contain a lower amount of Ni, that in this case is barely detectable by the EDX coupled with the HAADF-STEM. On the other hand, larger nanoparticles, such as the ≈ 5 nm nanoparticle displayed by Figures 6.12 e) and 6.12 f), appear to be monometallic Ni, with no Ir detected. The tendency of bimetallic nanoparticles to have the composition dependent on the nanoparticle size is a known phenomenon, reported, for example, for AuPd nanoparticles.¹⁶ This non-homogeneity of the nanoparticles in the colloidal solution may derive (I) from the low stability of THPC colloids and Ostwald-ripening occurring over time especially for Ni and/or (II) from the difference of reduction and nucleation rate between the two metals.

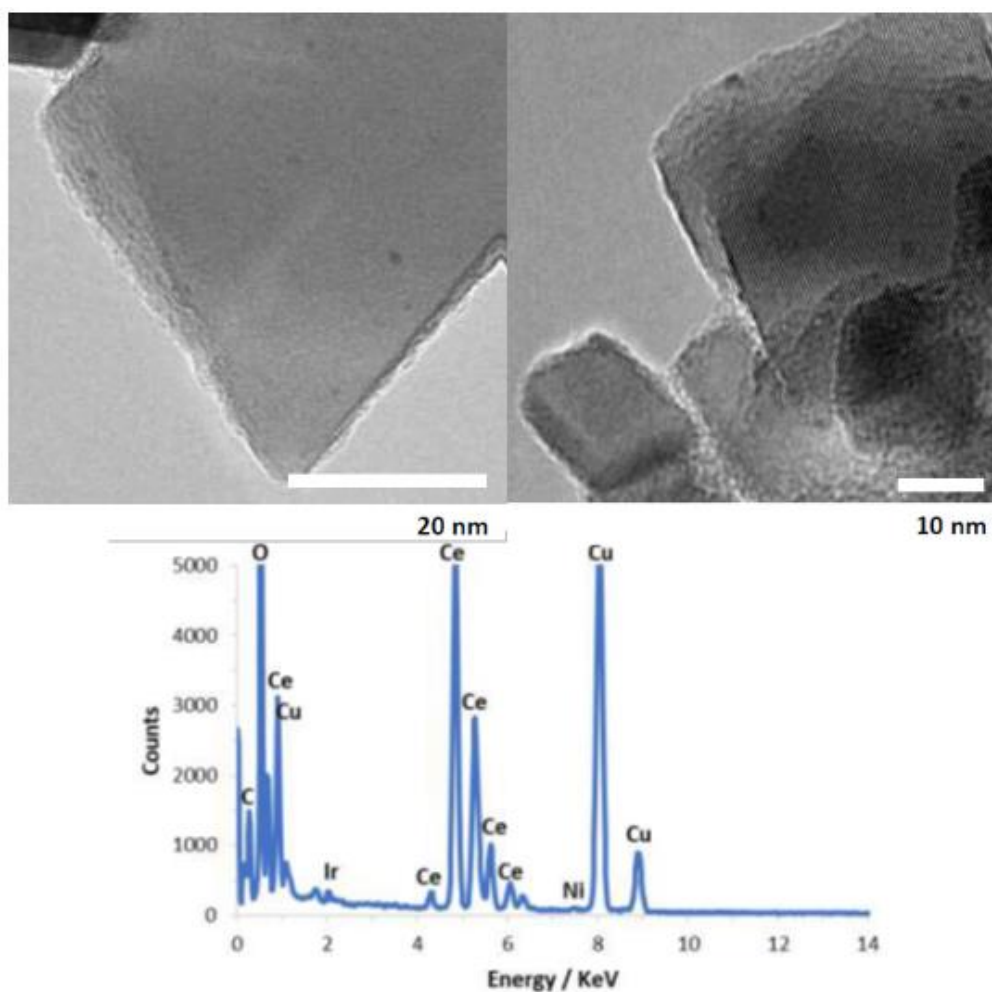


Figure 6.13. TEM images of $\text{Ir}_1\text{Ni}_3/\text{CeO}_2$, top, and EDS spectra of the samples, bottom.

Moreover, during the collaboration with Dr Chamberlain at Leeds University, HRTEM-EDS analyses were performed on Ir₁Ni₃/CeO₂. The immobilised bimetallic nanoparticles on CeO₂, as shown in Figure 6.13, displayed a homogeneous nanoparticle size distribution. The mean particle size seems to be lower than 2nm, but the number of analysed nanoparticles was too small to give statistically valid counting. No areas of segregated bimetallic nanoparticles were detected. The EDS analysis detected both metals on the catalyst and the signals on the EDS spectra were low because of the 1 wt. % metal loading. The higher homogeneity of particles displayed by the immobilised catalyst can be associated with an improved stabilisation of the bimetallic nanoparticles by the cerium oxide which avoids agglomerations and dissolution/redeposition processes. The main conclusions of the HRTEM-EDS, STEM/HAADF-EDS studies is that the Ir-based bimetallic catalyst possesses a small nanoparticle size below 2 nm, with narrow particle size distribution and the presence of bimetallic alloy Ir-Ni nanoparticles and individual segregated Ir and Ni nanoparticles.

6.3.4. X-ray Photoelectron Spectroscopy (XPS)

Another important aspect of bimetallic catalysts is the actual surface composition of the nanoparticles deposited onto the support. Due to the difference in reducibility and stability on the surface of the two metals, the nanoparticles may create a composition gradient, therefore the surface composition is not represented by the total ratio between the metals. In this chapter, the production of the core-shell structure was also attempted. For all these reasons, XPS analysis on the samples assumed a crucial role in the understanding of the catalytic material surface and then association with the activity of the catalysts. Ni 2p present peaks with shapes that are non-regular, therefore, model fitting was created from the analysis of standard NiO and Ni(OH)₂,^{17,18} while Ir 4f fitting was performed by using previously reported fitting parameters.¹⁹

Table 6.4. XPS data for 1 wt.% $\text{Ir}_x\text{Ni}_y/\text{CeO}_2$ catalysts reported as metal atomic coverage (at.%), percentage of Ir^0 on total Ir amount (%), percentage of Ni^0 on total Ni amount (%), Binding Energy, BE, for different Ir and Ni species (eV).

Catalyst	Atomic ratio Ir:Ni	Ir (at.%)	Ni (at.%)	Ir^0 (%)	Ni^0 (%)	BE Ir 4f _{7/2} (eV)	BE Ni 2p _{3/2} (eV)
$\text{Ir}_9\text{Ni}_1/\text{CeO}_2$ 600	9:1	0.52	0.57	37.0	12.2	61.6 (Ir^0)	852.4 (Ni^0)
						62.3 (IrO_2)	854.0 (NiO)
							855.0 (Ni(OH)_2)
$\text{Ir}_3\text{Ni}_1/\text{CeO}_2$ 600	3:1	0.47	0.75	71.0	11.1	61.3 (Ir^0)	852.6 (Ni^0)
						62.1 (IrO_2)	853.8 (NiO)
							855.0 (Ni(OH)_2)
$\text{Ir}_1\text{Ni}_1/\text{CeO}_2$ 600	1:1	0.24	1.30	60.8	2.6	61.5 (Ir^0)	852.3 (Ni^0)
						62.2 (IrO_2)	853.5 (NiO)
							855.8 (Ni(OH)_2)
$\text{Ir}_1\text{Ni}_{3.3}/\text{CeO}_2$ 600	1:3.3	0.30	0.75	75.2	7.5	61.3 (Ir^0)	852.5 (Ni^0)
						62.1 (IrO_2)	853.9 (NiO)
							855.8 (Ni(OH)_2)
$\text{Ir}_1\text{Ni}_9/\text{CeO}_2$ 600	1:9	0.05	0.76	86.4	11.4	61.2 (Ir^0)	852.8 (Ni^0)
						62.0 (IrO_2)	853.8 (NiO)
							855.0 (Ni(OH)_2)
$\text{Ir}_1\text{Ni}_1/\text{CeO}_2$ 600 TSR	1:1	0.66	0.65	78.4	9.3	61.0 (Ir^0)	852.0 (Ni^0)
						62.0 (IrO_2)	853.9 (NiO)
							855.3 (Ni(OH)_2)
$\text{Ir}_1\text{Ni}_1/\text{CeO}_2$ 600 TSI	1:1	0.93	0.92	83.7	12.6	60.9 (Ir^0)	851.9 (Ni^0)
						62.0 (IrO_2)	853.8 (NiO)
							855.6 (Ni(OH)_2)

Figure 6.14 and 6.15 report the XPS spectra for the IrNi/CeO_2 prepared by sol-immobilisation with THPC, with the two-metals reduced contemporaneously in order to obtain alloys, with different metal molar ratios. The metal composition of the samples reported is calculated based on the atomic coverage on the surface. The results show that a higher amount of nickel

is presented than the nominal values from the metal precursors, Table 6.4. This phenomenon can be explained by the fact that Ir is more easily reducible than Ni, therefore, this can create a gradual change in surface composition, with a core of metal richer in Ir, which is reduced faster, and a shell of metal richer in Ni. Moreover, the Ir⁰ peaks for Ir 4f_{7/2} showed an up shift of 0.2-0.6 eV, like one presented by the monometallic Ir catalysts prepared with the same method. This indicates that the hypothesised stabilisation of partial positive charges on the surface of nanoparticles by the combination of small particle dimensions and strong metal-support interaction, (SMSI), may be still valid also for the bimetallic nanoparticles and, therefore, the influence of the use of CeO₂ as support as well in this case.²⁰

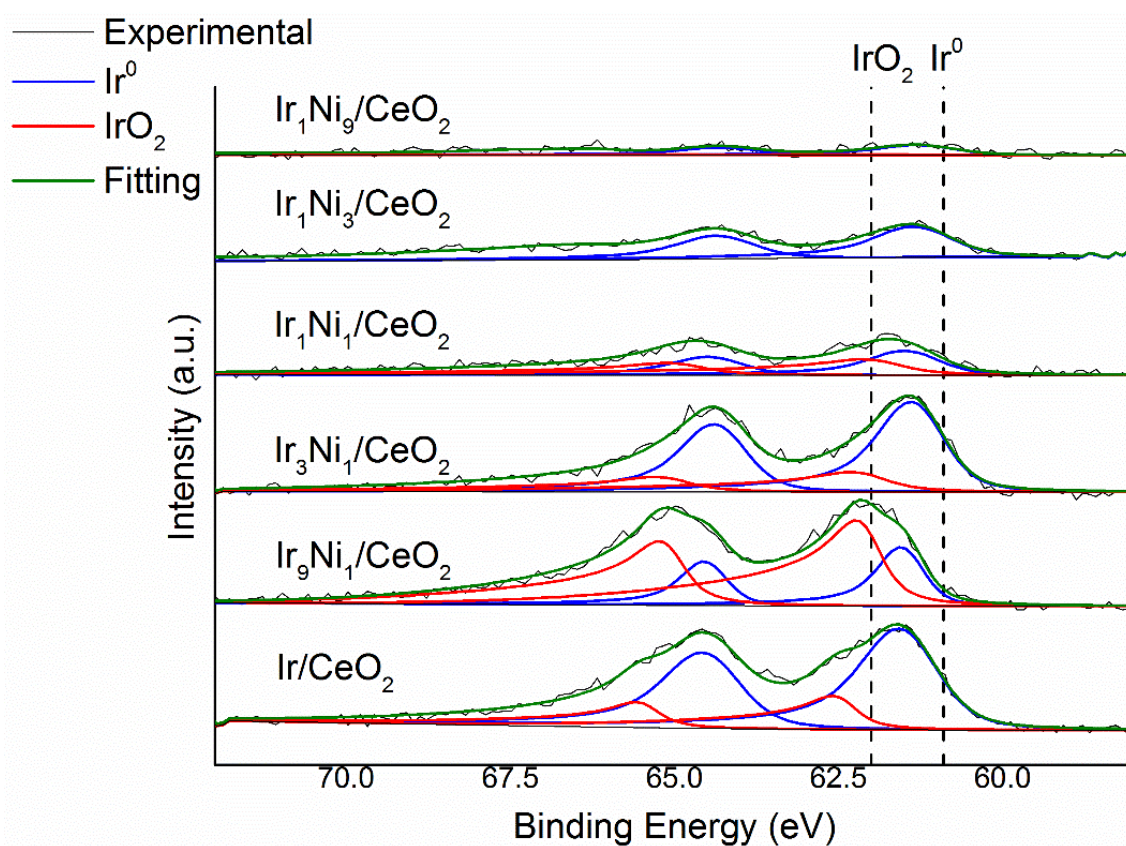


Figure 6.14. XPS spectra of Ir 4f region of Ir_xNi_y/CeO₂ prepared by sol-immobilisation with THPC. In the picture the position of Ir⁰ and IrO₂ from literature are reported, shift of the Ir⁰ signal are visible for the sample.

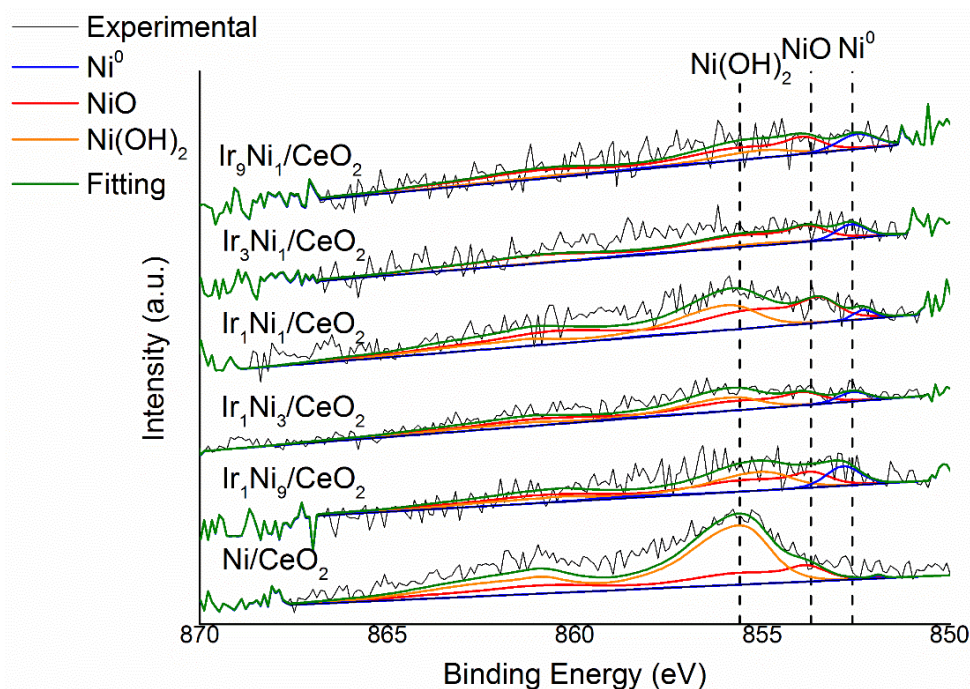


Figure 6.15. XPS spectra of Ni 2p region of $\text{Ir}_x\text{Ni}_y/\text{CeO}_2$ prepared by sol-immobilisation with THPC. The position of Ni^0 , NiO and Ni(OH)_2 from previous modelling is added as comparison to control eventual shifting.

Figure 6.16 and 6.17 displays the XPS spectra for $\text{Ir}_1\text{Ni}_1/\text{CeO}_2$, which showed the best performances, prepared using sol-immobilisation with THPC with modified procedures. In the case of the sample prepared by the standard experimental procedure, one-step reduction, showed a surface Ir:Ni ratio of 0.18 instead of the 0.84 calculated by SEM-EDX analysis. In the case of the catalysts prepared by a two-step reduction procedure and a two-step immobilisation procedure, which aim was to produce core-shell particles, showed a surface Ir:Ni atomic ratio of 1.01 close to the nominal value. The two-step immobilisation procedure have a surface ratio of 1 between the two metals suggesting the production of separated monometallic nanoparticles on the surface or randomly mixed alloys formed during the high-temperature heat treatment. For the two-step reduction procedure, instead, the goal was to cover the Ni nanoparticles produced during the first reduction with Ir. A core-shell structure would have revealed a higher surface amount of Ir than Ni because the shell layer would have been the part of the particles analysed. This ratio of 1, instead, it indicates that the Ir particles did not cover the Ni, but it creates Ir nanoparticles or clusters which are immobilised separately or perfectly mixed alloys formed during the high-temperature heat treatment. The possible formation of segregated nanoparticles of Ir and Ni would explain the lower yield obtained by the modified procedures, $\approx 75\text{-}78\%$ compared with the standard

procedure, were alloys are formed, 92.8%. This can be an indication of the better catalytic performances of alloyed supported Ir-Ni nanoparticles compared to separated supported Ni and Ir nanoparticles.

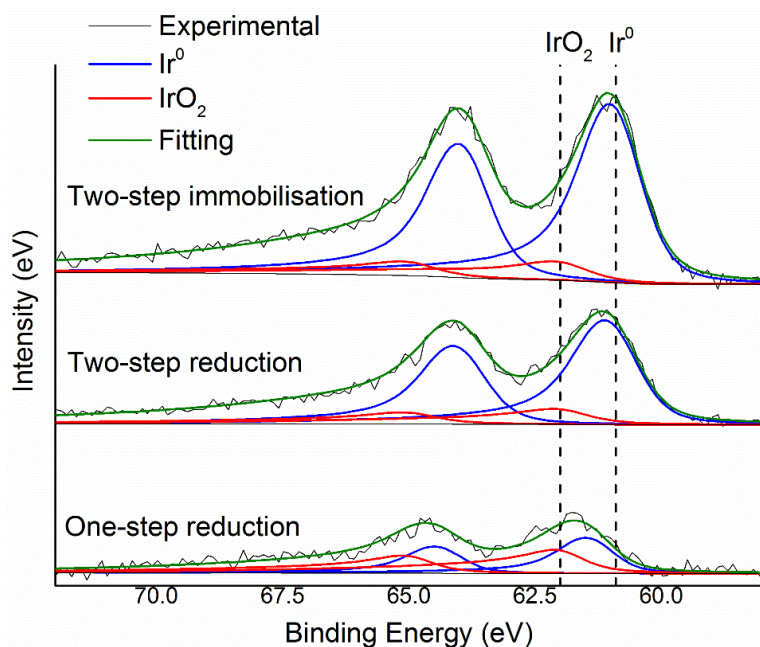


Figure 6.16. XPS spectra of Ir 4f region of $\text{Ir}_1\text{Ni}_1/\text{CeO}_2$ prepared by sol-immobilisation with THPC using different preparation procedures. In the picture the position of Ir^0 and IrO_2 from literature are reported, shift of the Ir^0 signal are visible for the sample.

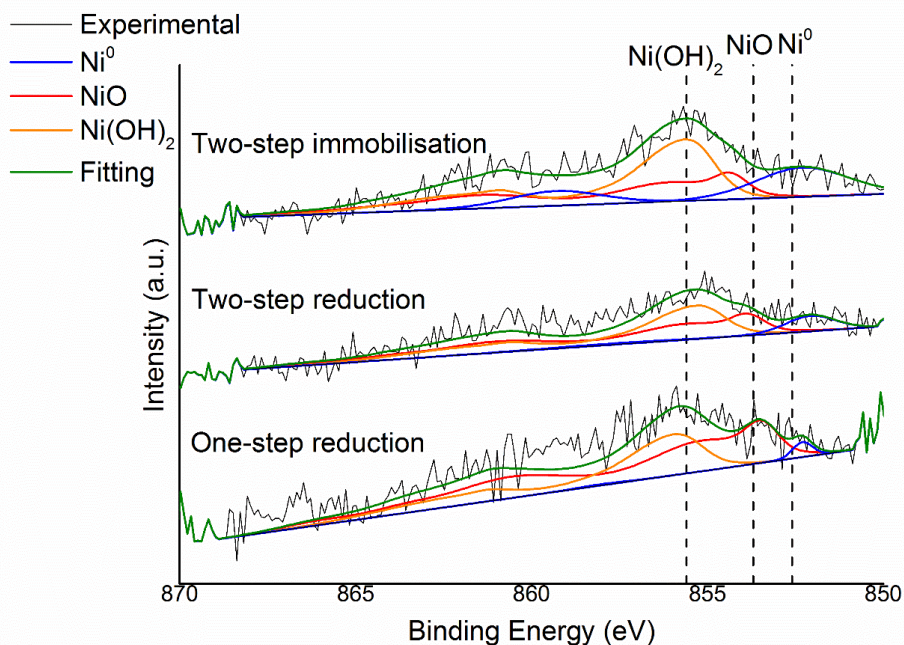


Figure 6.17. XPS spectra of Ni 2p region of $\text{Ir}_1\text{Ni}_1/\text{CeO}_2$ prepared by sol-immobilisation with THPC using different preparation procedures. The position of Ni^0 , NiO and Ni(OH)_2 from previous modelling is added as comparison to control eventual shifting.

6.3.5. *In situ* Attenuated Total Reflectance Infrared Spectroscopy (ATR-IR)

As reported in Chapter 4 Section 4.3.7. *in situ* ATR-IR can be used to identify the intermediate species adsorbed on the surface of the catalyst during a reaction. This analysis can give vital information about the mechanism of reaction for the decomposition of hydrazine over IrNi nanoparticles. Ir₁Ni₁/CeO₂ prepared by sol-immobilisation with THPC was analysed as representative of the bimetallic catalysts. Figure 6.18b display the absorption spectra of a solution of hydrazine in water which presents peaks at 1481 and 1367 cm⁻¹, this last peak can be attributed to the adsorption of species on CeO₂ while the other can be related to adsorbate on the active metal. The spectrum of the solution of hydrazine and NaOH flowed over Ir₁Ni₁/CeO₂ 600, Figure 6.18c, present similar peaks at 1479, 1379 and 1335 cm⁻¹. The peak at ≈1480 cm⁻¹ cannot be attributed with certainty since the DFT calculation on a similar surface were not performed, but it can be hypothesised that similar to the Ir (111) surface the peak is due to the NH₂ on the surface.

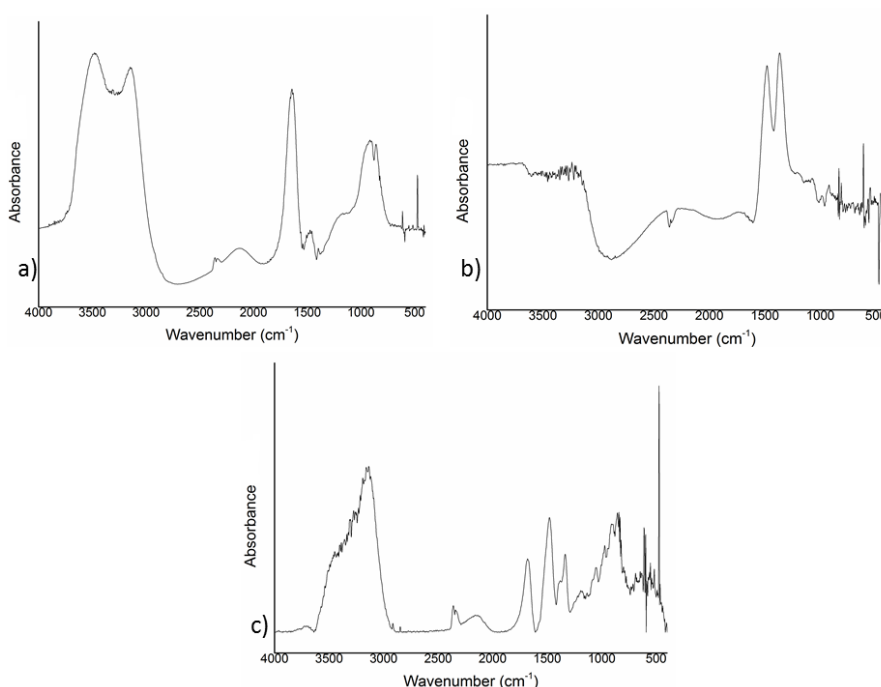


Figure 6.18. ATR-IR spectra recorded with Ir₁Ni₁/CeO₂ prepared by sol-immobilisation with THPC deposited on a ZnSe crystal with different solution flowing on the catalysts: a) water; b) 0.02 M hydrazine solution in water; c) 0.02 M hydrazine 0.1 M NaOH solution in water.

6.4. Conclusions

In this chapter, the catalytic performances of supported Ir-Ni nanoparticles have been explored for the catalytic decomposition of hydrous hydrazine in aqueous solution. For preliminary catalytic studies, an IrNi/CeO₂ with 0.5wt.% in Ni and 0.5 wt.% in Ir nominal weight loading by sol-immobilisation with THPC was synthesised to study the applicability of bimetallic supported Ir-Ni nanoparticles as catalysts. These initial tests, other than confirming the reproducibility of the experimental reactions in batch, showed that the bimetallic catalyst displayed a final yield to molecular hydrogen, 84.8%, higher than the similarly prepared Ir/CeO₂ and Ni/CeO₂, 36.6% and 60.9%, reduced at the same heat-treatment temperature of 600°C under flow of H₂/Ar. The bimetallic catalyst exhibited lower activity compared to the monometallic Ir, 77 h⁻¹ and 727 h⁻¹ respectively, nonetheless, the higher yield to H₂ is a promising result for the utilisation of supported bimetallic Ir-Ni nanoparticles as potential catalysts. This is due to the fact that for actual applications or initial exploitations a higher efficient hydrogen production can translate to a higher level of energy, possibly produced by the same amount of hydrous hydrazine solution and the significantly lower amount of ammonia produced that can degrade the polymer membrane of the fuel cell. HAADF-SEM/HRTEM analysis revealed that the synthesised Ir-Ni nanoparticles produced with this method have similar particle size with the Ir colloidal nanoparticles, with sub-2nm nanoparticles, which are stabilised by the immobilisation on the surface of CeO₂. Ir-Ni colloidal solution seems to be less stable and displayed how in these bimetallic nanoparticles composition and particle size seems to be related, with bigger particles being Ni-rich while smaller ones are richer in Ir content.

Once the activity of bimetallic IrNi/CeO₂ was demonstrated, the effect of changes of atomic ratio between the two metals was studied. The catalysts were prepared with Ir:Ni ratio of 9:1, 3:1, 1:1, 1:3 and 1:9 and in all of the cases the synthesis followed was sol-immobilisation with THPC and then the catalysts were reduced at 600°C. Among these catalysts, the Ir₁Ni₁/CeO₂ was the one displaying the highest final yield to hydrogen, 92.8%, and moderate activity of TOF 90 h⁻¹. When the values of yield and activity are compared using the nominal Ir-Ni ratio as reference, no clear relationship between them and the composition of the nanoparticles emerge from the data. Instead, when using the atomic coverage data obtained from the XPS analysis it can be seen that the activity, measured by the TOF values, is directly related with

the Ir atomic coverage of the surface, while the final yield to H₂ increases with the value of Ni atomic coverage of the surface in a non-linear relationship that tend to a plateau to the 100% yield at higher Ni at%. From these two relationships it can be concluded that in order to produce a highly active and selective catalyst, the atomic coverage of the surface by the two metals has to be the highest possible. This can be achieved by reducing the mean particle size and, therefore, increasing the exposed surface of the alloy nanoparticles immobilised on the surface of the catalyst. Moreover, a deeper systematic study on the correlation between total metal ratio and surface ratio composition can help to tune the catalytic performances of the system.

In a following study, the procedure of the sol-immobilisation synthesis was then modified in the attempt to change the structure of the bimetallic nanoparticles (alloy versus core-shell nanoparticles) in order to investigate the possibility of developing optimised bimetallic Ir-Ni structures for the catalytic decomposition of hydrous hydrazine in aqueous solution to molecular hydrogen. In a first modification to the standard protocol reported in Chapter 2 Section 2.2.1.1. the reduction of the metals was separated, by adding first the Ni precursor solution and carrying out the reduction step using the desired amount of the reducing agent, (calculated in relation to the number of moles of Ni added). After 30 minutes the rest of the desired reducing agent and the Ir precursor were added to complete reduction and the nanoparticles so formed are immobilised on CeO₂. This modification of the reaction procedure was an attempt to produce core-shell Ni@Ir structure, by reducing Ir on the surface of preformed Ni nanoparticles in colloidal solution. However, XPS analysis shows a surface atomic coverage similar for the two metal that agrees with the total Ir:Ni metal atomic ratio, calculated from the moles of metal precursor used during the synthesis and then confirmed by SEM-EDX of 1:1. The data from the XPS quantification on the surface indicate that, instead of the formation of a core-shell structure, segregated domains of Ir and Ni were more likely formed since in the case of core-shell nanoparticles the quantification of the metal constituting the shell, Ir in this case, would have been higher than the nominal value. However, the formation of random alloy during high-temperature heat treatment cannot be excluded without further characterisation, such as XAS. Another experimental procedure was used for the synthesis of core-shell structures, by firstly immobilising the Ni colloidal nanoparticles on the CeO₂, and then using the synthesised monometallic Ni/CeO₂ as support

that can act as nucleation centre for the immobilisation of Ir nanoparticles. In this case, the goal was to immobilise on the surface separated Ir and Ni monometallic nanoparticles in order to study the catalytic performances of separated nanoparticles. The two Ir₁Ni₁/CeO₂ catalysts prepared by modified sol-immobilisation with THPC method displayed higher final yield to H₂, 75.1% for the two-step reduction and 78.5% for the two-step immobilisation, compared to the monometallic Ir/CeO₂ or Ni/CeO₂ catalysts prepared by sol-immobilisation, 36.6% and 60.9% respectively. This higher final yield can be explained in two possible ways (I) interaction between adjacent nanoparticles of different metals or (II) incorporation of Ni atoms into the structure of Ir nanoparticles during both the synthesis and the high-temperature reduction of the materials. The final yield to H₂ of the samples prepared with modified procedures is lower than the one exhibited by the alloy Ir₁Ni₁/CeO₂ prepared by the “standard” sol-immobilisation with THPC and this indicates that higher final yields can be achieved by increasing the interaction between the two metals in the formed nanoparticles.

The catalytic performances obtained by the bimetallic catalysts are in line with the results obtained from Ir/NiO reported in Chapter 4, with yield up to 84.2% and TOF of 132 h⁻¹. This similarity between the catalytic performances of Ir/NiO and bimetallic Ir-Ni catalysts seems to confirm the hypothesis that Ni atoms were incorporated to a certain degree into the crystalline structure of Ir nanoparticles as in the case Ir/NiO, therefore, enhancing the catalytic performances of the material by involuntary creating a bimetallic catalyst.

Ir₁Ni₁ was used then as reference material for studying the effect of the reaction temperature on the catalytic performances of the material and the stability of the catalyst. The decrease in final yield to H₂ associated to the increase of the reaction temperature reported for the monometallic catalysts was less pronounced in the case of the bimetallic catalyst, being 92.3%, 92.8% and 88.9% at 30°, 50° and 70°C, respectively. The lower decrease of yield with the increase of the reaction temperature can be an indication that the gap in activation energy between the two competitive reactions is smaller than in the case of monometallic catalysts, however, computational calculation on bimetallic surface are necessary to clarify this assumption. The TOF for Ir₁Ni₁/CeO₂ increased almost tenfold, from 29 to 257 h⁻¹, in the range from 30°C to 70°C.

The stability of Ir₁Ni₁/CeO₂ was analysed by performing reusability tests. Four consecutive reactions were performed by adding fresh hydrous hydrazine water solution when the gas evolution stopped at the end of each reaction. The yield to hydrogen slowly decreased from 88.1% to 82.6% and higher decrease in TOF from 117 h⁻¹ to 38 h⁻¹ was observed which is associated to a three-fold increase in the time necessary for the complete catalytic decomposition of hydrous hydrazine. This decrease in activity may be due to a reconstruction of the surface or a selective poisoning by ammonia of Ir active sites, which are responsible for the higher activity of the catalyst. To conclude, it is also noteworthy that the catalytic performance of the fresh catalyst is to some extent different from the performance recorded for the same catalyst in the initial tests and this difference may be related to the interaction of the nanoparticles with the O₂ contained in the air over time, therefore, oxidation of the supported Ir-Ni nanoparticles. Finally, more detailed characterisations, such as XAS, are required for identification of the actual structure of the bimetallic Ir-Ni catalysts in order to design catalysts with higher activity, yield to H₂ and stability in the future.

6.5. References

- 1 A. Zaleska-Medynska, M. Marchelek, M. Diak and E. Grabowska, *Adv. Colloid Interface Sci.*, 2016, **229**, 80–107.
- 2 M. Sankar, N. Dimitratos, P. J. Miedziak, P. P. Wells, C. J. Kiely and G. J. Hutchings, *Chem. Soc. Rev.*, 2012, **41**, 8099–8139.
- 3 H.-L. Jiang, T. Umegaki, T. Akita, X.-B. Zhang, M. Haruta and Q. Xu, *Chemistry*, 2010, **16**, 3132–3137.
- 4 P. Verma, K. Yuan, Y. Kuwahara, K. Mori and H. Yamashita, *Appl. Catal. B Environ.*, 2018, **223**, 10–15.
- 5 Z. Wei, J. Sun, Y. Li, K. Datye and Y. Wang, *Chem. Soc. Rev.*, 2012, **41**, 7994–8008.
- 6 A. B. Vysakh, C. L. Babu and C. P. Vinod, *J. Phys. Chem. C*, 2015, **119**, 8138–8146.
- 7 S. K. Singh, A. K. Singh, K. Aranishi and Q. Xu, *J. Am. Chem. Soc.*, 2011, **113**, 19638–19641.
- 8 L. He, Y. Huang, X. Y. Liu, L. Li, A. Wang, X. Wang, C. Y. Mou and T. Zhang, *Appl. Catal. B Environ.*, 2014, **147**, 779–788.
- 9 M. Liu, Y. Zheng, S. Xie, N. Li, N. Lu, J. Wang, M. J. Kim, L. Guo and Y. Xia, *Phys. Chem. Chem. Phys.*, 2013, **15**, 11822–11829.
- 10 A. K. Singh, M. Yadav, K. Aranishi and Q. Xu, *Int. J. Hydrog. Energy*, 2012, **37**, 18915–18919.
- 11 N. Firdous, N. K. Kausar, I. Qazi and M. H. S. Wattoo, *Int. J. Hydrogen Energy*, 2016, **41**,

- 984–95.
- 12 A. S. Lanje, S. J. Sharma and R. B. Pode, *Arch. Phys. Res.*, 2010, **1**, 49–56.
 - 13 H. Yan, D. Zhang, J. Xu, Y. Lu, Y. Liu, K. Qiu, Y. Zhang and Y. Luo, *Nanoscale Res. Lett.*, 2014, **9**, 1–7.
 - 14 X. Yan, T. Ai, X. Su, Z. Wang, G. Sun and P. Zhao, *MATEC Web Conf.*, 2016, **2**, 1–5.
 - 15 D. F. Abbott, D. Lebedev, K. Waltar, M. Povia, M. Nachtegaal, E. Fabbri, C. Coperet and T. J. Schmidt, *Chem. Mater.*, 2016, **28**, 6591–6604.
 - 16 J. Pritchard, L. Kesavan, M. Piccinini, Q. He, R. Tiruvalam, N. Dimitratos, J. A. Lopez-sanchez, A. F. Carley, J. K. Edwards, C. J. Kiely and G. J. Hutchings, *Langmuir*, 2010, **26**, 16568–16577.
 - 17 A. Villa, C. E. Chan-Thaw, G. M. Veith, K. L. More, D. Ferri and L. Prati, *ChemCatChem*, 2011, **3**, 1612–1618.
 - 18 A. Villa, G. M. Veith, D. Ferri, A. Weidenkaff, K. A. Perry, S. Campisi and L. Prati, *Catal. Sci. Technol.*, 2013, **3**, 394–399.
 - 19 S. J. Freakley, J. Ruiz-Esquiús and D. J. Morgan, *Surf. Interface Anal.*, 2017, **49**, 794–799.
 - 20 S. Li, Y. Xu, Y. Chen, W. Li, L. Lin, M. Li, Y. Deng, X. Wang, B. Ge, C. Yang, S. Yao, J. Xie, Y. Li and X. Liu, *Angew. Chemie Int. Ed.*, 2017, **56**, 10761–10765.

7. Conclusions and Recommended future work

7.1. Conclusions

Reliance on fossil fuels is becoming one of the most problematic aspects of modern society. Over the course of time, humankind found new and innovative ways to generate and transform energy. Currently, the research for alternative sources of energy is paramount for the continuity of society in a sustainable way. Sources of energy utilised nowadays are slowly depleting and poisoning the environment, therefore, new renewable and sustainable energy sources are the goal of many research groups worldwide. Hydrogen has caught many attentions in recent years as an energy vector due to the possibility to generate energy at location and store it as chemical. Using hydrogen as energy vector requires technology to use the energy that it contains, this has been identify in fuel cells. These devices, especially proton exchange membranes, are attractive replacement for traditional technologies due to the high effectiveness of energy generations and the production of water as only by-product. Nonetheless, the utilisation of hydrogen in large scale is limited by its low density, which requires large volumes or a large amount of energy to be stored, and safety risks. Therefore, liquid hydrogen storage materials are studied and among them hydrous hydrazine as a potential candidate, is one of the most promising due to its high hydrogen content, reactivity and production of nitrogen as the only by-product.

This thesis is focused on the catalytic decomposition of hydrous hydrazine in liquid phase as a model reaction for hydrogen generation. In **Chapter 3** the investigation began with the synthesis of supported Ir nanoparticles. For example, Ir/CeO₂ catalyst prepared by deposition-precipitation with NaOH, that was then used as reference material for the decomposition reaction. The reaction conditions were optimised in order to perform the catalytic test under kinetically limited regime of reaction. This catalyst achieved full conversion of hydrazine with a 23.9% yield toward molecular hydrogen and a TOF of 1018 h⁻¹.

Characterisations were performed to understand the nature of the catalyst synthesised. In particular, temperature-programmed reduction showed how the presence of Ir nanoparticles on the surface of cerium oxide decreases the reduction temperature of surface Ce^{4+} to Ce^{3+} creating a vacancy on the support.¹ The creation of these vacancy combined with small particle size stabilised partial positive charge on the surface of Ir nanoparticles detected by XPS analyses as an up-shift in the binding energy of the peak of metallic Ir 4f.

Preliminary reusability test, performed on batch reactions, exhibits deactivation of the catalyst after an initial high activity and good yield to hydrogen. The yield decreased from 26.9% to 3.6%, indicating, therefore, poor stability of Ir/CeO₂ to be further improved.

From DFT calculations is found that the IrO₂ surface irreversibly binds with reagent and products which would lead to rapid deactivation of the catalyst. On the Ir(111) surface from these calculations, the first step to take place is the cleavage of the N-N bond of the hydrazine adsorbed on Ir(111) lead to the formation of NH_2^* species. Afterwards, NH_2^* may interact with different N_2H_x ($x = 1-4$), assisting the extraction of H and producing, therefore, NH_3^* and subsequently leaving N_2^* . Another possible mechanism is the interaction between NH_2^* and NH_x^* ($x = 1-2$) to produce NH_3^* and ad-atom N on the surface. On Ir(111) the recombination of ad-atoms H has a high energy barrier that limits the production of molecular hydrogen on this particular surface at mild conditions.

The ATR-IR spectrum and analysis of gases produced during the decomposition of ¹⁵N labelled hydrazine monohydrate reported in **Chapter 4** helped to understand the mechanism of reaction suggested by the computational calculations. ATR-IR showed that the main species adsorbed on the surface of Ir during the reaction is NH_2 validating the mechanism of adsorption of hydrazine and rapid breaking of the N-N bond of hydrazine. The production of a higher amount of ¹⁴N¹⁵N, when a mixture of labelled and non-labelled hydrous hydrazine was used, also indicated that cleavage of the N-N bond of hydrazine is a predominant elementary step in the mechanism of the decomposition.

A series of Ir monometallic catalysts are tested to optimise the properties of the catalysts such as mean particles size, oxidation state and metal distribution. The preparation method and high-temperature heat treatment have great influence on the catalytic performances of the material since the presence of small metallic nanoparticles increases the final yield to

hydrogen in the case of Ir/CeO₂. Studying the influence of different metal oxides as supports for Ir, the need for small Ir nanoparticles is clarified by the presence in the case of Ir/CeO₂ of strong metal-support interaction. This was evident by the increase of the reduction of cerium oxide on the surface, from TPR analysis, and stabilisation of partially charge Ir nanoparticles, resulting in shift to higher binding energy for the Ir⁰ peaks in the XPS spectra. This interaction is the “key” of improving the final yield to hydrogen of Ir/CeO₂ prepared by DP with NaOH, (38.9%), with an activity of 1564 h⁻¹. These results are in line with recently reported Ir/meso-CeO₂ where yield to hydrogen was 34% and with TOF activity of 8571 h⁻¹ using high loading Ir catalysts, approximately 27 wt.%, and low substrate/metal molar ratio of 20, an order of magnitude lower than the one utilised in this thesis.² Ir/NiO catalysts prepared by sol-immobilisation method, on the other hand, exhibited a final yield of 84.2% toward hydrogen, higher than any other monometallic iridium catalysts reported in this Thesis, and activity reported as TOF of 132 h⁻¹. The higher yield to the desired product makes of this material a more promising material despite the lower activity. Reusability tests also prove that Ir/NiO is more stable than the Ir/CeO₂ at the presented reaction conditions, decreasing the yield of less than 10% over course of ten reactions maintaining the same level of activity, and low level of Ir leaching, less than 2% of the total metal deposited on the support.

In **Chapter 5** the catalytic properties of Ni monometallic catalysts are explored. Ni presented similar interaction with CeO₂ increasing the activity and yield of Ni-based catalysts. The Ni/CeO₂ prepared by DP with NaOH showed an activity of TOF 4.4 h⁻¹ and final yield to hydrogen of 68.9%. The preparation method and choice of support were then optimised to better evaluate and understand the role of the active metal and the support in the specific reaction. Ni/Al₂O₃ and Ni/MgAl₂O₄ are not active for the decomposition of hydrous hydrazine, indicating the importance of CeO₂ as the essential support for the improved catalytic properties of Ni catalysts. When sol-immobilisation is used to prepare the Ni/CeO₂ after an induction period of approximately 13 h decomposition of hydrous hydrazine was completed with an activity of 5 h⁻¹ and final yield of 82% higher than what reported in the literature for similar Ni/meso-CeO₂ of 67% but with the activity of 13 h⁻¹.

In order to combine activity and selectivity/yield of the two active metals, bimetallic nanoparticles catalysts were prepared and studied in **Chapter 6**. The optimisation of the

molar ratio between the two metals (Ir, Ni) in the bimetallic particle is performed by synthesising and using catalysts produced by contemporaneous reduction of the two metals by sol-immobilisation method. The best performing material is the catalysts with a molar ratio of 1 between the two metals which reached a final yield to hydrogen of 92.8% with an activity of 90 h^{-1} . The XPS analyses performed on the series of bimetallic catalysts exhibit two trends for the catalytic performances with the surface contents of the metals in the catalysts prepared. The activity increased linearly with the iridium atomic surface content, while the final yield to hydrogen is in relation to the Ni atomic surface content.

To obtain different morphology of the bimetallic particles the experimental protocol of the sol-immobilisation method was modified. Segregated particles are decomposing hydrous hydrazine with lower yield than alloy Ir-Ni nanoparticles, indicating that the intimate contact of the two metals achieved by the mixed alloy particle is beneficial for the production of hydrogen.

Reusability tests performed on the best performing bimetallic catalyst exhibited that the stability of this material is not enough for long terms applications. The final yield decreases from 88.1% to 82.6% in four reactions, but most importantly the activity decreases from 117 h^{-1} to 38 h^{-1} .

7.2. Recommended future works

Some challenges of the hydrogen generation from hydrous hydrazine have been tackled in this work and combination of experimental and computational studies have shed some light on the mechanism of reaction, nevertheless, new research challenges have been opened.

The yield above 30% obtained with Ir/CeO₂ was not expected in the light of the DFT calculation on the mechanism of reaction of hydrazine on Ir (111). This facet is the most common in nanoparticles of medium size, and the reactivity foreseen from the simulation is in agreement with Ir/CeO₂ that presented particle of 50-200 nm. Sub 2 nm particles, such as the ones produced by DP with NaOH or sol-immobilisation, present different facets that can explain the unexpected behaviour of some Ir/CeO₂ catalysts. Therefore, additional calculations on other Ir facets could be performed, like (110) or (116), or Ir clusters deposited on CeO₂ can provide new information which can enlighten the mechanism of formation of hydrogen. If a

particular facet or cluster is responsible for the higher generation of hydrogen, then preparation of the catalysts can be optimised to increase the presences of nanoparticles with that particular morphology. This work could lead to the preparation of more selective Ir catalysts which can have an application in hydrogen generation if the amount of ammonia produced is below concentration harmful for PEMFC because the high activity of noble metals, which can decrease the mass of catalysts necessary making them competitive with other catalysts cheaper but less active.

Similarly, DFT studies on bimetallic Ir-Ni nanoparticles can help in identifying the optimal facet and molar ratio of the metal to perform the catalytic decomposition of hydrous hydrazine. In this work bimetallic catalysts had high yield to hydrogen and in literature are reported examples of bimetallic Ir-Ni catalysts able to achieve full conversion to hydrogen, therefore, in this case, the study should be focused on the increment of the reaction rate.

The main drawback of the Ir/CeO₂ and Ir-Ni/CeO₂ used in this thesis is the progressive deactivation of the catalysts in the reaction conditions. A deeper investigation on the causes of this deactivation would help understand and avoid the phenomenon in new material, making of the hydrous hydrazine decomposition a competitive technology for the hydrogen economy. One of the mechanisms of the deactivation can be associated to the strong adsorption of ammonia on the surface, performing TPD and TPD-NH₃ analyses on fresh and used catalysts would allow identifying if the ammonia remains bind on the surface after the reaction and in case quantify the energy of the bond. This should provide information for the optimisation of the catalysts.

Another possible mechanism of deactivation is the restructuring of the nanoparticles. This phenomenon has been reported for Ir-Ni unsupported nanoparticles. Small particle size and poor contrast with CeO₂ make analysis by common TEM difficult to interpret, but the use of more accurate instrument can give indication on the morphology of single particles. XANES and EXAFS analyses could also help to understand the geometry and oxidation of the atoms in the particles and in this way find a modification of their structure.^{3,4}

XAS analysis could also elucidate the nature of Ir/NiO catalysts, the most promising among the tested catalysts from the aspect of stability. The analysis would clarify the doubt about monometallic/bimetallic nature of its Ir nanoparticles.³ Moreover, the study of the region

around the nanoparticle and the comparison with the Ir/CeO₂ could provide crucial information also about the deactivation mechanism. *In-situ/operando* studies in the case of the monometallic and bimetallic supported Ir-Ni nanoparticles using a combination of EXAFS/XANES/DRIFTS studies could be useful to elucidate the reaction mechanism and in real-time the interaction of adsorbate/intermediate on the active sites of the catalysts.

Finally, the long-run reusability tests in a continuous flow reactor is required in order to achieve realistic conditions for long-term stability measurements. The batch reactions are practical for lab tests and study on kinetic parameters, but flow reactors are preferred for application in everyday-life technologies. The conditions in continuous flow are different, for example the exposure to fresh hydrazine prevent re-oxidation of the nanoparticle in the basic environment of the end of the reaction and as well as, fresh hydrous hydrazine could also help the desorption of strongly adsorbed species like ammonia and help with the stability of the catalysts. On the other hand, continuous exposure to basic fluid could increase recombination of nanoparticles structure. Therefore, tests in continuous flow should be paramount for future application of this catalytic technology.

Finally, the synthesis of CeO₂ with different facets and the synthesis of NiO/CeO₂ oxides varying Ni/Ce atomic ratio could be explored based on our positive results of the utilisation of NiO as the chosen support. Moreover, (photo)catalytic applications for the decomposition of hydrous hydrazine at UV and visible light can be studied using Au, Ag and Cu as the chosen plasmonic metals and using colloidal methods for performing colloidal metal nanoparticles with controlled size and shape.

7.3. References

- 1 G. Ranga Rao, *Bull. Mater. Sci.*, 1999, **22**, 89–94.
- 2 Y. Qiu, H. Yin, H. Dai, L. Gan, H. Dai and P. Wang, *Chem. Eur. J.*, 2018, **24**, 4902–4908.
- 3 H. N. Nong, T. Reier, H. Oh, M. Gliuch, P. Paciok, T. Ha, T. Vu, D. Teschner, M. Heggen, V. Petkov, R. Schlögl, T. Jones and P. Strasser, *Nat. Catal.*, 2018, **1**, 841–851.
- 4 Y. Lee, Y. Jeon, Y.-D. Chung, K.-Y. Lim, C.-N. Whang and S.-J. Oh, *J. Korean Phys. Soc.*, 2000, **37**, 451–455.

Publications

Mechanistic study of hydrazine decomposition on Ir(111)

Xiuyuan Lu, Samantha Francis, Davide Motta, Nikolaos Dimitratos and Alberto Roldan, Phys. Chem. Chem. Phys., 2020, **22**, 3883-3896

Acknowledgements

In first place, I would like to thanks Nikos that presented me to possibility of CDT course and later gave me the chance to do this PhD in his group. His experience and guided me during the work. Moreover, the lovely time and great environment that he helped create in the group.

A special thanks to Ceri, for the help and guidance always valuable during this work.

I would like thanks also Davide Ferri for the opportunity to visit and work at the Paul Scherrer Institute.

A thanks also to Alberto Roldan for his patience and support all the way through the DFT studies.

Another thanks to the EPSRC, the CDT in catalysis and Cardiff University for the life-changing opportunity of this PhD.

And finally, a special to all the people who shared with me this (country) road throughout this work.